UNIVERSITE DE LIMOGES

ECOLE DOCTORALE Sciences et Ingénierie pour l'information

FACULTE DES SCIENCES ET TECHNIQUES

Equipe de recherche Xlim MINACOM

Thèse N° 40

Thèse

pour obtenir le grade de

DOCTEUR DE L'UNIVERSITÉ DE LIMOGES

Discipline: Electronique des Hautes Fréquences et Nanotechnologie

présentée et soutenue par

Christophe Brun

le 29 Octobre 2013

Carbon nanotubes based nanopackaging dedicated to innovative high frequency interconnections

Thèse dirigée par Dominique Baillargeat et Stéphane Bila

JURY:

S. VERDEYME	Professeur des Universités, Xlim Limoges	Président
G. DAMBRINE	Professeur des Universités, IEMN Lille	Rapporteur
S. Ravi P. SILVA	Professor, University of Surrey, United Kingdom	Rapporteur
D. BAILLARGEAT	Professeur des Universités, Xlim Limoges	Examinateur
H. T. E. TEO	Assistant Professor, NTU, Singapore	Examinateur
G. POUPON	Conseiller scientifique, CEA Grenoble	Examinateur
Y. MANCUSO	Expert ingénieur, TSA Elancourt	Examinateur
S. BILA	Chargé de Recherche, Xlim Limoges	Invité

Dédicace à ma famille et mes amis

“The real voyage of discovery consists not in seeking new lands but seeing with new eyes.”

—Marcel Proust

Acknowledgements

Je tiens à remercier en premier lieu mes parents, mon frère et ma famille pour leur soutien constant durant mes quatre années d'études. Ils m'ont encouragé et soutenu dans tous le moments difficiles. Leur aide me fut précieuse, et je dois ma réussite en parti grâce à eux.

Je remercie le professeur Dominique Baillargeat, mon directeur de thèse qui a su me guider pendant toutes les années de ma thèse, m'aider à concrétiser mes objectifs et m'a permis d'évoluer au rang de docteur. Ses précieux conseils, sa grande pédagogie et son importante expérience en recherche m'ont été d'une aide indispensable. Enfin, je lui dois cette merveilleuse aventure que fut Singapour pendant plusieurs années, un enseignement riche sur les cultures du monde et des expériences inoubliables. Nous avons commencé l'aventure CINTRA à ces débuts et grâce a lui, je suis fier de tout ce qui a été concrétisé jusqu'à aujourd'hui. Par la même occasion, je souhaiterais remercier mon co-superviseur de thèse Stéphane Bila pour son soutien lors de mes phases de travaux à Xlim à Limoges.

Je remercie mes collègues du laboratoire Xlim de Limoges pour leur important soutien et toutes les connaissances qu'ils ont pu généreusement m'enseigné : Michel Aubourg, Nicolas Delhote, Kamel Frigui, Arnaud Pothier, Olivier Tantot, Serge Verdeyme, Damien Passerieux et Valérie Madrangeas.

I would like to thanks the EEE school in NTU, and more precisely his Professor Tay Ben Kang for his great support, and for supplying me all the necessary equipment to succeed our common projects. I also met a great person with invaluable advices for the progress of my studies.

I send a special thanks to Yap Chin Chong, a colleague and a friend for 4 years who worked with me like a very motivated person. Both of us, we successfully concretized all our projects and I own him a lot of our results. He also taught me with patience and generosity all the material science knowledge, an indispensable material for the realization of this thesis.

I also thank all my team in Singapore who worked with me for 4 years, composed by Philippe Coquet, Dunlin Tan, Edwin Teo, Li Hong, Chow Wai Leong, Pierre Franck and Tan Chang Wai. This large amount of different skills helps us to make most of our projects and ideas become a reality. Since I met this motivated team, I learnt a lot from them. They also

taught me how to work hand-in-hand with an international team, a great lesson of life and humility.

Finally, I would like to have a thought to all these special friends with who I had these unforgettable memories and experiences, and who helped me during the hard times and enjoyed the great times with me. I will try to remember all: Melisa Hisoler, Florian Pinalie, Lisa Blanchard, Léo Dumy, Jeremy Fabre, Emmanuel Sevin, Charles Berthoty, Christophe Wilhelm, Pierre Baudin, Gladys Lee, Lenaic Bonneau, Navany Khim, Zeineb Ben Aziza, Vj, Pacchini Sebastien, Charles Altuzarra, Aurelien Olivier, Vivien Hang, Romain Dauliat, Paul Leshauris, Nicolas Jolly, Yoann Marchives, Samuel Ngoho, Carlos Alberto Paragua and Jerome Andrieux.

Je finirai mes remerciements en pensant à la région Limousin et l'université des sciences et techniques de Limoges dont leur financement ont permis la réalisation et l'aboutissement de mes travaux.

Outline

Acknowledgements 2
Outline 4
Introduction 8
Chapter I 13
I. Carbon nanotubes properties 14
1. Physics of carbon nanotubes 14
A. General structure 14
a) Composition 14
b) Chirality vector 15
c) Particularities and defects 16
B. Single-wall carbon nanotube 17
a) General properties 17
b) Semi-conducting properties 18
C. Multi-wall carbon nanotube 19
c) Number of shells in MWCNTs 20
d) Number of conducting channels in MWCNTs 21
D. Double-wall carbon nanotube 23
E. Carbon nanotube fibers 24
2. Intrinsic properties of carbon nanotubes 25
A. Electrical properties [6, 16] 25
a) Electron transport: Ballistic conduction versus Diffusive [3] 25
b) Mean free path in CNTs (MFP) [20, 21] 26
c) General properties of CNTs 28
B. Thermal properties 29
C. Mechanical properties 30
a) CNT strength 30
b) Flexibility of the CNTs 30
II. Carbon nanotubes fabrication 32
1. Arc discharge [41] 32
2. Laser ablation [42] 33
3. Chemical vapor deposition (CVD) 34
A. Thermal chemical vapor deposition (TCVD) 36
a) Principle 36
b) Catalyst preparation [44] 37
i. Choice of catalyst material 38
ii. Catalyst deposition method – Ebeam process 39
iii. Catalyst deposition method – Underlayer and pre-treatment 40
c) Bottom and Top CNT growth 41
i. Principle 41
ii. CNT morphologies and effect on their structure 43
d) The choice of hydrocarbon (also called CNT precursors) 44
e) Growth mechanisms and control [49] 45
f) Summary of CVD method to grow CNTs: Pros and Cons 47
B. Plasma enhanced chemical vapor deposition (PECVD) 48

a) Principle 49
b) Catalyst preparation and selection 50
c) The choice of hydrocarbon 50
d) The plasma 51
e) Summary of CVD method to grow CNTs: Pros and Cons 52
4. Conclusion 53
III. Carbon nanotubes modeling 56
1. Microwave properties of CNTs versus DC 56
2. Carbon nanotube modeling for high frequency electronics applications 57
A. Analytical modeling of carbon nanotube for DC 57
a) Contact resistance R_C 58
b) Quantum resistance R_Q 59
c) Carbon nanotube resistance R_{CNT} 61
B. Analytical modeling of carbon nanotube for RF 62
a) Modeling of a single-wall carbon nanotube (SWCNT) 62
b) Modeling of multi-wall carbon nanotube (MWCNT) 64
c) Modeling of a bundle of CNTs 66
d) Application and determination of the CNT parameters by experiments (work with Chow Wai Leong) 68
i. Fabrication of the structure and CNT growth 68
ii. DC characterization and resistance extractions 70
iii. High frequency measurements and analytical model extraction 72
C. Electromagnetic (EM) modeling of carbon nanotube for RF 76
a) SWCNT modeling 76
b) MWCNT modeling 79
c) Bundle of CNTs modeling 80
i. Bundle of three SWCNTs 80
ii. Bundle of twenty-one SWCNTs 84
iii. Bundle of MWCNTs 87
iv. Bundle with an unlimited number of SWCNTs 88
D. Conclusion 90
IV. High frequency applications based on carbon nanotubes (state of the art) 91
1. Transistor [85] 91
2. Gas sensor [90, 91] 92
3. Thermal management 92
4. Antennas 93
5. Other applications 93
6. Conclusion 94
Chapter II 95
I. Interconnections using carbon nanotubes 96
1. Second level of interconnection using CNTs (also called level 0) [7, 101] 97
A. Local interconnections using CNTs [102] 97
a) Local interconnects: properties and issues 97
b) Local interconnects: performance of CNTs (SW vs. MW) 98
B. Semi-global interconnections using CNTs 99
C. Global interconnections using CNTs 100
D. Conclusion 101
2. First level of interconnection using CNTs (also called level 1) [2, 104-107] 102
A. Wire bonding 103
B. Hot-Via [63, 108, 109] 104

C. Flip-Chip 106
a) Flip-Chip fabrication process 106
b) Flip-Chip limitations 107
c) Flip-Chip using CNTs (state of the art) 108
II. Interconnections based on carbon nanotubes for flip-chip technology 110
1. Design and fabrication of a test structure with CNT bumps working up to 40 GHz 111
A. Problems to solve 111
a) Experimental details 112
b) Results and discussion 113
i. Influence of the PECVD process on the Au metallization and the RF performance 113
ii. Influence of the barrier layer on the CNT growth 116
iii. Influence of the barrier layer on the CNT quality 118
iv. Conclusion 119
B. Flip-chip structure under test 120
a) Design and fabrication of the flip-chip test structure based on CNT bumps 120
i. Design of the device 120
ii. Photolithography process 122
iii. CNT bundle growth by PECVD 124
iv. Flip-chip bonding 126
b) Results and discussion 127
i. Fabrication results 127
ii. DC measurements 132
iii. Repeatability of the flip-chip contact 135
iv. High frequency measurements 136
v. Discussion: pros & cons compared 141
2. Modeling and model extraction of the flip-chip structure 142
A. Full EM modeling of the flip-chip structure 143
B. Contact resistance $R_{CNT-CNT}$ between two CNTs extraction by full EM modeling. 147
C. Hybrid EM/analytical modeling of the flip-chip structure 149
D. Parametric study of the flip-chip using the hybrid EM/analytical model 153
i. Parametric study on the CNT resistance R_{CNT} 155
ii. Parametric study on the CNT contact resistance $R_{CNT-CNT}$ 156
iii. Parametric study on the CNT density (N_{MWCNT}) 158
3. Remarks and observations on the flip-chip working up to 40 GHz 159
A. CNT bundle resistance issue 159
B. Mechanical bond issue [159, 160] 161
4. Conclusion 165
5. Design and fabrication of a test structure with CNT bumps working up to 110 GHz 166
A. Design of the updated flip-chip 167
i. Flip-chip with 20-µm-bump size: FC1 167
ii. Flip-chip with 100-µm-bump size: FC2 173
B. Fabrication of the devices 180
C. Conclusion 180
Chapter III 182
I. Wireless interconnections based on carbon nanotubes 183
1. Wireless interconnections based on carbon nanotubes 183
A. Wireless on-chip interconnects based on CNTs for optical range 184
B. Wireless chip-to-chip interconnects based on CNTs for high frequency range 186
C. Wireless interconnects: their applications 187

2. CNTs-based-wireless interconnection for chip-to-chip communication 188
A. Principle 188
a) Definition of a monopole antenna 188
b) Principle of the monopole antenna based on CNTs 191
B. First prototype working at 40 GHz 195
a) Design of the monopole interconnection using a KOH etching 195
C. Second prototype working at 200 GHz 200
a) Monopole interconnection alone 200
b) Final design of the monopole interconnection 202
c) Final design simulation results at 200 GHz 203
D. Third prototype working from 100 to 300 GHz 206
a) Design and principle of the monopole interconnection using a single-plane 206
b) Wireless interconnection at 100 GHz 207
c) Wireless interconnection at 200 GHz 210
d) Wireless interconnection at 300 GHz 213
e) Conclusions and observations 216
f) Transmission simulation tests 218
i. First approach 218
ii. Second approach with reflectors 220
g) Fabrication of the device 222
h) Conclusion 223
Conclusion and outlook 225
List of publications 228
Appendix 244
Appendix 1 245
Appendix 2 246
Appendix 3 247
Appendix 4 248
Table of figures 250
Tables 258

Introduction

Infinity small and infinity big, two important topics that researchers have looked for answers for many years. Today, we are going to study the nano-world, one billion times smaller than a meter. How could an entity ten thousands times smaller than a hair be used everyday in electronics devices? Carbon nanotubes are the main interest of this report. Carbon nanotubes are very simple structural material and they are only composed by one kind of atom: the carbon.

Carbon is a main element that composing the universe and the 6th element in the Mendeleev table. The carbon is everywhere and we are able to find this atom in many occasions everyday in the world surrounding us, such as in a pencil (graphite), in jewelry (diamond), or in petrol. Massive quantities of carbon atoms are also created in the big star center, where the helium fusion happens. Only in our galaxy, astrophysicists estimated the number of stars equal to 234 billions, which is an inexhaustible source of carbon atoms. So why does this element is particular and how its properties can find an interest in electronics for high frequencies?

In this thesis, we will try to answer this important question on a particular topic. Carbon has six electrons and four of them are on the valence layer. This unique property allows the carbon to have four covalent liaisons and create a large number of different structures such as: diamond, graphite, lonsdaleite, fullerenes (C60, C540, C70), amorphous carbon, carbon nanotube (Figure 1). All of these structures have specific behaviors and properties. Some of them will be an isolator such as the diamond or a semi-conductor for electronics such as the graphene or conductor such as the carbon nanotubes. All these properties and much more will be presented and we will see how this large panel of unique properties composing the carbon nanotubes will be used for each application in high frequency electronics.

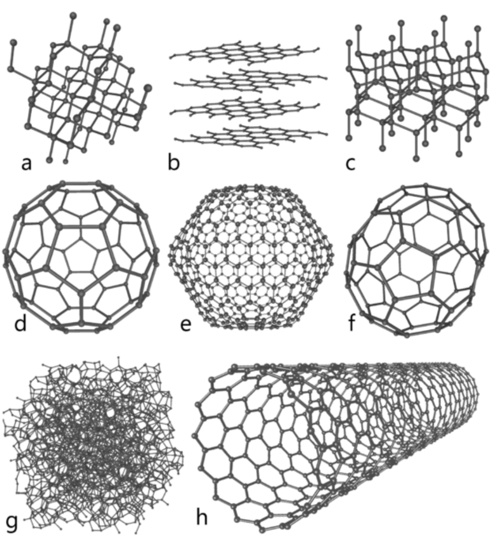

Figure 1: carbon allotropes: diamond (a), graphite (b), lonsdaleite (c), fullerenes (C60 (d), C540 (e), C70 (f)), amorphous carbon (g), carbon nanotube (h).

After the discovery of the electromagnetism by William Gilbert in 1600, works on wave propagations started with Michael Faraday, James Maxwell and Heinrich Hertz during the 19th century. From these works with big devices such as the Hertz's oscillator for proving their theories, a large panel of applications using the wave propagation has been developed. Today, most of the world is using electronics devices for high frequencies. As example, we can cite the mobile phone, radio, computer, television, etc. If we take a look on all of these applications, one tendency can be highlight: a constant wish of increasing the compactness. However, we will see that metal-based devices have a limit of size due to their physics and soon a limit of compactness will be reached in electronics if we don't find new alternatives or materials to outperform the limitations of current physics based on metal devices.

The demand of RF and microwave applications has increased very fast since a decade because of the emergent wireless applications such as the radar, telecommunications (wimax, wifi, 3G, 4G, etc), etc. Moreover, the demand for increasingly higher rates of data transmission requires the use of technologies at higher frequencies. Indeed, the bandwidth is closely related to the resonant frequency of the electronics components: BW=f/Q. However, by increasing the working frequency, we decrease the wavelength, meaning the electronics components scale is reduced. The current material commonly used in electronics such as copper, gold and other metals will meet scale issues with electromigration and surface and grain boundary scatterings. The nano-scales of the carbon nanotubes with their unique and excellent electrical properties will permit to overcome the limitation existing in bulk materials.

Band No.	Designation	Frequency	Wavelength	Applications
7	HF (high frequency)	3–30 MHz	100–10 m	Telephone, telegraph
8	VHF (very high frequency)	30–300 MHz	10–1 m	TV, FM broadcast
9	UHF (ultra high frequency)	300–3000 MHz	100–10 cm	TV, satellite links, cellular communication
10	SHF (super high frequency)	3–30 GHz	10–1 cm	Radar, microwave links
11	EHF (extremely high frequency)	30–300 GHz	1–0.1 cm	Radar, military applications
13	P Band	0.23–1 GHz	130–30 cm	Cellular phone band
14	L Band	1–2 GHz	30–15 cm	Global positioning systems
15	S Band	2–4 GHz	15–7.5 cm	Wireless local area network
16	C Band	4–8 GHz	7.5–3.75 cm	Global digital satellite
17	X band	8–12.5 GHz	3.75–2.4 cm	Ground based radar, navigation
18	Ku Band	12.5–18 GHz	2.4–1.67 cm	VSAT networks
19	K Band	18–26.5 GHz	1.67–1.13 cm	Satellite TV
20	Ka Band	26.5–40 GHz	1.13–0.75 cm	Special telecom services
21	Millimeter wave	40–300 GHz	7.5–1 mm	Collision avoidance radar

All along this thesis, we will keep in mind this problematic and want to show how the use of carbon nanotubes can be alternative approach to classical ones, in order to solve future electronics issues and open a new physics for future devices.

Our work has been conducted between two research laboratories: CINTRA, located in Singapore and XLIM, located in Limoges France. I spent a total of two years and half at CINTRA in order to learn the carbon nanotube growth, mechanisms and properties.

CINTRA UMI 3288 is a French-Singaporean international joint laboratory between three major partners, the French National Centre for Scientific Research (CNRS) - Institute for Engineering and systems Science -, the Nanyang Technological University (NTU) and Thales (the French electronics giant and global leader in aerospace, space, defense, security and transportation industries). Nanyang Technological University is the fastest-rising university in the world's top 50. NTU provides a high-quality global education to more than 33500 undergraduate and postgraduate students with 3800 teaching and research staff. In CINTRA, PhD students and interns are in strong association with more than 15 host NTU professors. Currently, more than 50 people are members of CINTRA. The lab is divided into 3 research axes: Carbon based nanotech; Nanowire based nanotech and Photonic materials and Nanostructures. I was working in the carbon based nanotech research axis. The team from EEE school composed by Tay Beng Kang, Edwin Teo, Yap Chin Chong, Dunlin Tan, Li Hong, Chow Wai Leong and Tan Chang Wai helps me to improve my knowledge on the carbon nanotube material and support me during all my PhD. (Address: Research Techno Plaza, 50 Nanyang Drive, Border X Block, Level 6, Singapore 637553).

XLIM UMR CNRS 7252 is a Mixed Research Unit of the University of Limoges and the CNRS, which combines more than 460 research lecturers, researchers of the CNRS, administrative staff and PhD students in computer science, mathematics, photonics, electro-magnetism and electronics. The laboratory is divided into 6 departments and I was working in the department of Micro and Nanotechnologies for Optoelectronic and Microwave components (MINACOM). The people from Xlim brought most of my knowledge in high frequency designs, simulations and measurements. (Address: 123, avenue Albert Thomas - 87060 LIMOGES CEDEX).

Our PhD work is focused on nanopackaging. This new field of research concerns the use of nanomaterials applied to the packaging of electronics or photonic components. That can be for interconnect, thermal, mechanical, etc managements. In this work, I mainly focused on two main applications: interconnections based on CNTs for flip-chip technology and wireless interconnections using CNT monopole.

The first chapter of this report will be dedicated to the description of carbon nanotube properties. The objective is to present the CNT composition and the different type of CNTs that can be grown with their respecting properties. We will also show what are the interest and advantages of using CNTs for high frequency applications. Several methods to grow CNTs will be described and a focus on the two mains methods (TCVD and PECVD) employed our work will be conducted. Advantages and limitations of each method will be detailed. Finally, all methods to model a carbon nanotube for high frequency will be presented. Two approaches will be presented: analytical and electromagnetic. A study on the coupling between CNTs will be performed.

In the second chapter, we will present an innovative approach to interconnect by flip-chip two bundles of CNTs. The first objective of this part is to demonstrate the feasibility of these new interconnected CNTs up to 40 GHz. In the second time and after fabrication of the device using CNTs, the performance will be tested and compare to the current technologies using metal bumps. A full modeling of the structure will be performed by full electromagnetic approach and a hybrid analytical/electromagnetic approach. The two methods will be compared and CNTs properties such as the contact resistance between two CNTs will be extracted. Finally, after we will show all the issues encountered with our first flip-chip prototype, a second prototype with better optimization and improved performance (up to 100 GHz) will be presented.

In the third and last chapter, we will present a second innovative approach to interconnect chips. The objective is to avoid the ohmic contacts existing in current interconnections by replacing them with wireless interconnections at high frequency. The wireless interconnection presented here will be composed by a CNT monopole. Only simulation works will be presented and the behaviors of such CNT monopole will be studied from 40 GHz to 300 GHz. We will show that due to quantum effects, a size reduction of the monopole length and diameter can be obtained by replacing the metal such as gold by a bundle of CNTs. Thus, we will present several monopole configurations in order to get a full understanding of our device and in order to achieve realistic designs. Finally, few CNT monopoles will be fabricated.

At last, we will conclude and present future works.

Chapter I

I. Carbon nanotubes properties

1. Physics of carbon nanotubes

In this part, carbon nanotubes (CNTs) will be presented. The general structure of CNTs, their composition and their respective properties will be detailed. We will see that CNTs have quite uncommon properties for electronics, which makes them a unique material for many applications in high frequency.

A. General structure

a) Composition

Carbon nanotubes have been officially discovered by Sumio Iijima from NEC in 1991 and can be assimilate as a one-atom-thick layer of carbon (also called graphene) rolled up around a hollow cylinder [1]. This 1 layer arrangement is a 1-D structure. The new physics compared to more conventional 3-D materials will be explained on the next section “Electrical properties on page (25)” and gives the interest of using carbon nanotubes instead of metal on many applications in micro-/nano-electronics, spintronics, optics, as well as material science, mechanical and biological fields [2] (see section “Electron transport: Ballistic conduction versus Diffusive on page (25)”). As shown on Figure 2, carbon atoms in a hexagonal arrangement compose graphene (e) and carbon nanotubes (d) but are also able to form various allotropes like the well known Diamond and Graphite. Sp^2 bonds link the carbon atoms each other. Instead of the graphene with two dimensions in space (2-D) for the electron/hole propagations, carbon nanotubes are one-dimensional. Indeed, because of its small cylinder diameter, generally between 1 to 100 nm [2, 3], electrons and holes can only propagate in the direction of the nanotube. Instead, in a 3-D material, an electron will adopt a diffusive transport randomly on the three directions. Further details will be given on the next section “Electron transport: Ballistic conduction versus Diffusive on page (25)”.

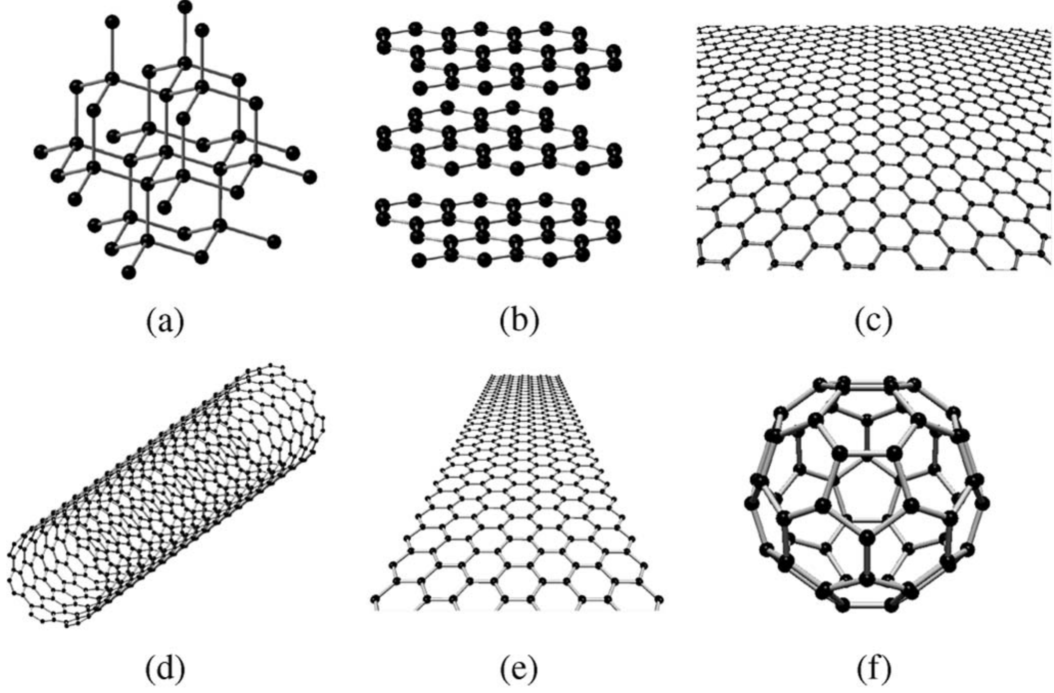

Figure 2: The different allotropes structures from carbon atoms. Different dimensionalities can be obtained from 1-D structure such as (d) and (e) to 3-D with (a) and (b). (c) is 2-D and (f) is 0-D. (a) is the diamond, (b) is the graphite, (c) is the graphene, (d) is a single-wall carbon nanotube and (e) is a nanoribbon. Source: [2]

b) Chirality vector

Moreover, CNTs electrical properties depend on the direction that the monolayer of carbon atoms has been rolled up. This parameter, which indicates the nanotube folding direction, is called the chirality vector $\overrightarrow{C_h}$. Pair of indices (n and m are integers) defines the vector $\overrightarrow{C_h}$. The integers n and m indicate the number of unit vectors along two directions ($\overrightarrow{a_1}$ and $\overrightarrow{a_2}$) in the honeycomb crystal lattice of graphene (Figure 3). The following scalar is obtained: $\overrightarrow{C_h} = n\overrightarrow{a_1} + m\overrightarrow{a_2}$. This range of configuration allows three different carbon atoms arrangement among the CNT structure and two electrical behaviors. If m = 0, the nanotube is a “zigzag” configuration. If n = m, an “armchair” configuration is realized while all other values of n and m return a “chiral” nanotube structure. We will see later the differences in the electric behavior according to the configuration. The control of the chirality is CNTs is an important field of research since its discovery. However, since the CNT growth mechanisms are not fully understood yet as we will see in section “Carbon nanotubes fabrication on page (32)”, researchers don’t know how to control the CNT chirality during the growth. Some works will be presented later (section “Single-wall carbon nanotube on page (17)”), showing some groups who succeed the growth of 99% of one CNT type under specific growth conditions. However, again, growth mechanisms weren’t fully understood.

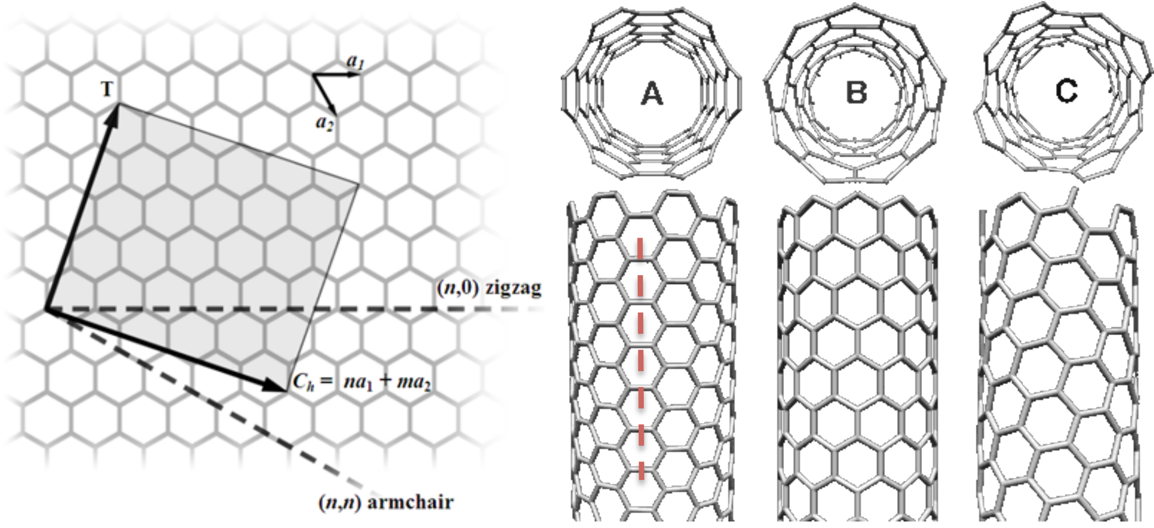

Figure 3: On (a), definition of the chirality vector $\overrightarrow{C_h}$ represented on a graphene mesh structure. On (b), the three different configurations, which can be encountered: "A" represents the armchair configuration, "B" the zig-zag configuration and "C" a random chiral configuration. Source: [4]

c) Particularities and defects

Finally, carbon nanotubes have a high aspect ratio between their length and their diameter. As already explained, a CNT has usually a diameter from 1 to 100 nm while the range of length that researchers are able to obtain is from few nanometres and can reach up to several millimetres. A ratio up to 132,000,000:1 can be reached with carbon nanotubes [5]. However, a perfect structured carbon nanotube as shown on Figure 3 is very difficult to achieve. In reality, even if the carbon atoms arrangement in CNTs is highly perfect, most of them have few defects on their structure. These defects appear during the CNT growth where other chemical components are also present. These other components and the stability of the process (temperature, pressure, time, etc) will also affect the CNT quality. As we will see in the section "Carbon nanotubes fabrication on page (32)", for example, process temperature is a very important parameter to control in order to get CNTs with low impurities. We can denote four main defects on the structure: topological (introduction of ring sizes other than hexagons), rehybridization (ability of carbon atom to hybridize between sp^2 and sp^3 bonds), incomplete bonding defects (vacancies, dislocations,...) and doping with other elements than carbon. All impurities in carbon arrangements will affect their electrical performance, as we will see later. Also CNT extremities play an important role in the CNTs properties.

B. Single-wall carbon nanotube

a) General properties

A carbon nanotube with a unique shell is called a single-wall carbon nanotube (SWCNT). The diameter of a SWCNT ranges between 1 and 10 nm. The smallest theoretical SWCNT identified as far has a chirality of (6,0) and a 0.47 nm diameter [6]. Equation (1) allows us to determine the SWCNT diameter according to the chirality vector presented previously:

$$D = \frac{\sqrt{3}}{\pi} \times b \times \sqrt{m^2 + mn + n^2} \qquad (1)$$

With b the distance between 2 carbon atoms (b = 0.142 nm).

A SWCNT has the particularity to be able to become metallic or semiconductor according to its chirality (armchair, zigzag or chiral). Indeed, a SWCNT is conductor if $(2n + m)$ is multiple of 3. In all other cases, the CNT will be semiconducting. The particularity of an armchair SWCNT is they are always metallic since $m = n$, which implies the equation $(2n + n) = 3n$ is always respecting the criteria. Indeed, if we take a look on the Figure 3, we observe the carbon lattice of the CNT is rolled up following the orthogonal C-C bond orientation (the red dash line). This special arrangement helps the electrons to propagate along the CNT hexagonal structure and hence to become conductor. Other chirality returns a random type of CNTs, either metallic or semiconducting. However, a tendency of 1/3 metallic and 2/3 semiconductor in a bundle of single-wall carbon nanotubes has been found after CNTs growth [7]. Some growth technics exist to get up to 90 % of semiconductor SWCNT [8, 9]. These technics employ different chemical components to enhance the selectivity of SC or conductor carbon nanotubes. Indeed, in this first work [9], it has been shown that the use of methanol during the growth on the ST-cut quartz substrate can increase the number of SC-CNTs obtained. They suspect the methanol etch the metallic CNTs more than the SC ones because of a smaller ionization potential. The substrate (quartz in their case) also plays an important role in the achievement of SC or conductor CNTs since it has been shown that the lattice of the substrate can interact with the carbon nanotube lattice.

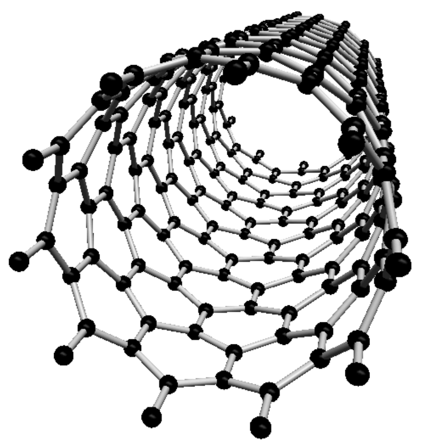

Figure 4: SWCNT with a (6,0) chirality.

b) Semi-conducting properties

As already explained in the previous part, single wall carbon nanotube can be semiconducting according to the chirality vector. In this report, we will briefly talk about this SWCNT property because in this PhD work, metallic ones are our main interest. The main question with SC is: what is the bandgap structure of carbon nanotubes? Indeed, even if it is not necessary to master and understand this physics part, the CNT band gap structure is the fundamental reason, which gives to CNTs their unique electrical properties. This point becomes fundamental for SC CNTs. On the Figure 5, we are showing the 6 cones representing the electron energy dispersion of graphene E-k [10]. With graphene band structure, the E-k relation is linear for lowest energy at the 6th corners (Figure 5a). Due to this linear dispersion, electrons and holes near these six points behave like relativistic particles described by the Dirac equation for spin 1/2 particles [2]. If we now slice the graphene structure according to a periodic distance (2/D) and a direction, which depends on the CNT chirality, we model the periodic boundary conditions appearing in CNTs around their circumference. At this point, two cases can appear for a given chirality and diameter CNT:

- a slice intercepts the apex of the cones. No bandgaps will exist between the valence and conduction bands. The CNT is metallic.

- no interception exists between the slices and the cones. A bandgap is created between the valance and conduction bands. The CNT is seminconducting. In order to calculate the band gap between the valence gap and the conduction gap in semiconducting SWCNT, we use the equation (2):

$$E_g = \frac{(2\gamma b)}{D} \quad (2)$$

With b the distance between the carbon atoms = 0.142 nm, D is the SWCNT diameter and γ = 2.5 – 3.2 eV. Thus, more the SWCNT diameter increases, more the gap decreases. With the equation (2), we have the confirmation that with the increase of diameter in MWCNTs, we obtain a too low bandgap to have a SC. That's a reason why MWCNTs are always conductor as we will detailed on the next part.

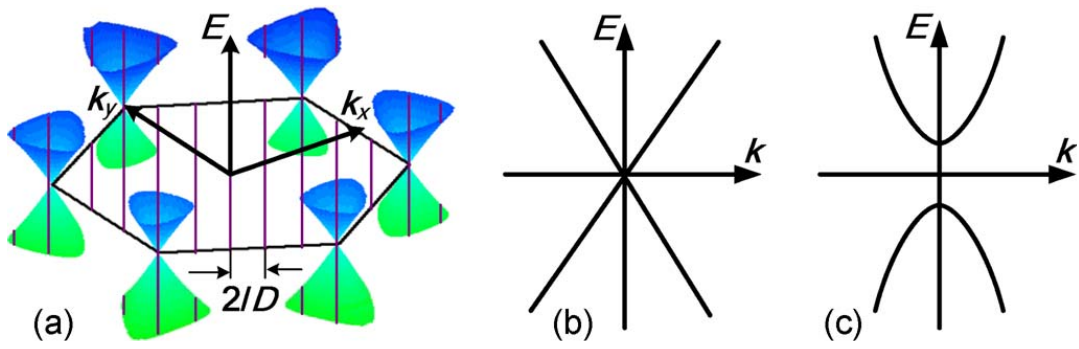

Figure 5: On left, E-k dispersion diagram of a metallic CNT. On right, E-k dispersion diagram of a SC CNT with a visible band gap between the conduction and valance bands. Source: [2]

These SC carbon nanotubes could be used for transistor application but not only. Indeed, SC SWCNTs have photoconductors capabilities that make them controllable by lights at some frequencies.

C. Multi-wall carbon nanotube

Another category of carbon nanotube is the multi-wall carbon nanotube (MWCNT). They are composed by several imbricated rolled up sheets of graphene (also called shell). Their diameter ranges usually between 10 and 100 nm. The interspace between the shells is equal to the Van der Waals length (0.34 nm) (VDW), which is the smallest distance possible between two atoms without creating a liaison/bond (inter-atomic) between them. The small distance existing between the shells allows MWCNTs to limit the number of impurities and scattering on inner shells. Indeed, it is proven that MWCNTs have less internal impurities than SWCNTs [2-4]. However, for the outer shell of a MWCNT, the problem remains the same and defects such as the ones described earlier can appear on their surface.

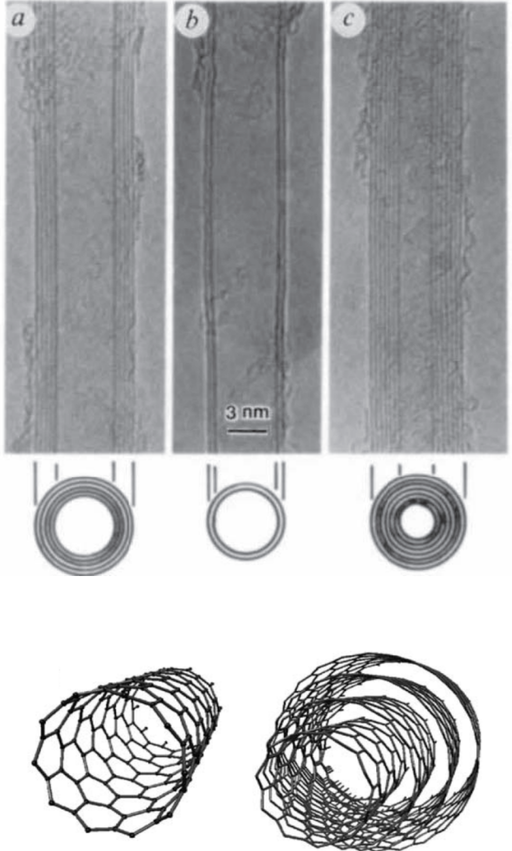

Figure 6: On the left, a representation of a single-wall carbon nanotube and a multi-wall NT. Transmission electron microscope (TEM) image of MWCNTs with several numbers of shell. Source: [1]

c) Number of shells in MWCNTs

In a MWCNT, the ratio between the inner tube diameter and the outer one is about ½ [2]. So, in order to estimate the number of shell in a MWCNT according to its diameter, we use the equation (3):

$$P = 1 + int\left(\frac{D_{max} - \frac{D_{max}}{2}}{2d}\right) \quad (3)$$

With D_{max} is the outer shell diameter; d is the gap distance between shells also calls VDW distance. As example, with a 10 nm diameter, 8 shells compose the MWCNT. The equation (3) can only be used from minimum diameter of 3 nm.

A MWCNT will be always considered as a conductor for two reasons: at least one shell is metallic and every time the outer shells (with diameter above 20 nm) are metallic because of their larger diameter. To give an explanation, we have to remember that a carbon nanotube is a rolled up sheet of graphene, which creates periodical boundaries on the band

gap structure depending on the CNT chirality. Some sort of slices cutting the hexagonal structural arrangement of CNTs can represent these boundaries (Figure 7). In fact, with the increase of the shell diameter, the number of slices increases (being inversely proportional to the diameter) and the slices cutting the band structure of the graphene (see Figure 7) get closer. A bigger number of slices also increase the chance to cut the apex of the cones in CNT band structure (Figure 7) and to obtain a metallic shell without bandgap between the conduction and valence bands [2]. Moreover, with large diameter, even if the apex of the cone is not crossed by a slice, the bandgap between two adjacent states would become negligible to consider the CNT as a semiconductor [11].

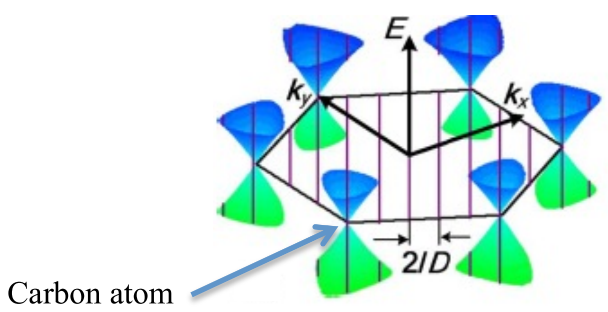

Figure 7: Representation of the periodical boundaries in carbon nanotubes with the hexagonal arrangement of carbon atoms. E-k dispersion diagram is also represented.

d) Number of conducting channels in MWCNTs

At nanoscale, the ohmic law is not applicable anymore because the conduction becomes quantized. In CNTs, conduction is quantized because of their nanoscale 1-D structures. Thus, an electron is able to propagate on a finite number of conduction channel, represented by the CNT sub-band on the Figure 8. By increasing the shell diameter, the number of conduction channel also increases (Figure 9). In contrast, a SWCNT has a fixed number of conducting channels, which is two, regardless to the diameter. Indeed, if we take a look on the equation (5), with diameter always below 10 nm, we always obtain a number of conducting channel N_i lower than 1. Thus, for SWCNTs, we only have two conducting channels. Each shell in a MWCNT hence has a different diameter, which implies different numbers of conducting channels. So, we must start to calculate the diameter of a specific shell in a MWCNT, by using the equation (4) [11]:

$$D_i = D_{max} - 2d(i-1) \quad \text{with} \quad 1 \leq i \leq p \tag{4}$$

With i the shell number; d is the gap distance between shells also called VDW distance. i=1 will correspond to the outer shell while i=p will be the inner shell in the MWCNT. Finally, in order to estimate the number of conducting channel in a specific shell, we use the equation (4) [2, 11]:

$$N_{i-channel/shell} = aD_i + b \quad \text{with} \quad D > 3 \text{ nm} \tag{5}$$

With a=0.0612 nm^{-1}, D_i: MWCNT selected shell diameter and b=0.425.

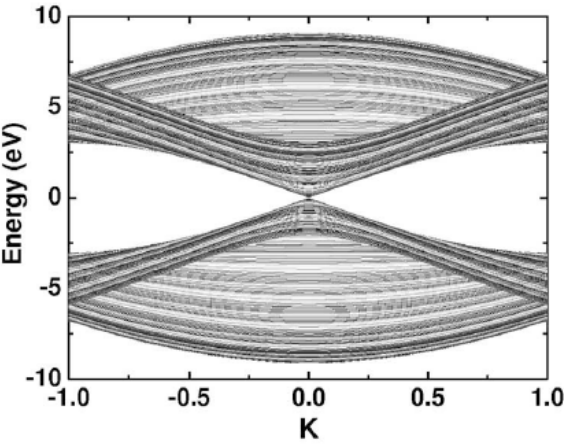

Figure 8: Band structure of a multi-wall carbon nanotube. Source: [11]

From these calculations, we can already observe that the MWCNT conduction will improve with the increase of its diameter and a larger number of conducting channels. Indeed, more conducting channels will help the CNT conduction and decrease the CNT electrical resistance. More discussion on CNT electrical conduction will be conducted on section “Electrical properties on page (25)”. But it is important to remember that MWCNTs start with a bigger advantage than SWCNTs for high frequency applications regarding to their electrical properties. Later in this report (section “Bundle of CNTs modeling on page (80)”), we will also see that the quantum effects existing in CNT goes down while the number of conducting channel increases.

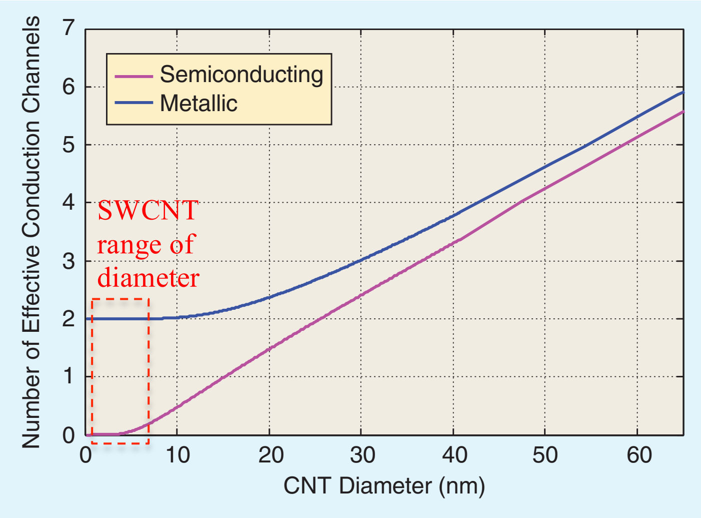

Figure 9: Number of conducting channel in function of the CNT diameter. With SWCNTs with diameter always below 10 nm, the number of conducting channel remains 2 (see equation (5)).

Finally, adjacent shells will interact each other by resistive, capacitive and inductive effects [11, 12]. However, assuming the random chirality of each shell, it can be assumed that the electrical properties of each shell will be kept constant.

D. Double-wall carbon nanotube

Double-wall carbon nanotubes are a special category of CNT. Naturally, two shells compose them and their diameter ranges near to the SWCNT diameters (Figure 10). Because of their small diameter, they share the electrical properties of SW and MW carbon nanotubes. Indeed, in a bundle of DWCNTs, we increase the proportion of metallic CNTs (because of their bigger diameter) compared to a SWCNT bundle and we keep the compactness of SWCNTs. However, a DWCNT can be still a semiconductor. Using DWCNT for conducting electronics components can be a very good compromise because of their high compactness and the good control of their diameter [13].

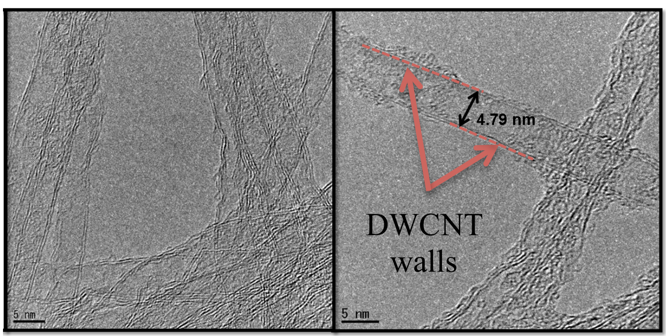

Figure 10: TEM images of DWCNTs fabricated at CINTRA by Chow Wai Leong.

E. Carbon nanotube fibers

In this last paragraph, some growth technics are discussed and for more information, section "Carbon nanotubes fabrication on page (32)" needs to be read. We show that we must be careful with the use of MWCNTs because we can denote two categories of carbon tube structures [14]. Indeed, according to the delta angle between the graphite shell and the direction of the tube, we obtain a multi-wall carbon fiber (MWCNF) if delta is non-zero and a multi-wall carbon nanotubes (MWCNTs) if delta=0 (Figure 11). In MWCNTs, all along the tubes, shells are not linked to each other; only an electromagnetic (EM) coupling can exist between them during the conduction. However, at the MWCNT extremities, bonding can be created by the catalyst particle left during the growth as shown on Figure 11. However, as it is clearly illustrated on the Figure 11, MWCNF won't be able to allow an optimal electron transport along the tube. Thus, MWCNTs will be preferred in this work and no MWCNF will be presented. That's the reason why it is very important to know with what kind of structure we are working on in order to get the best of the carbon nanotube electrical properties.

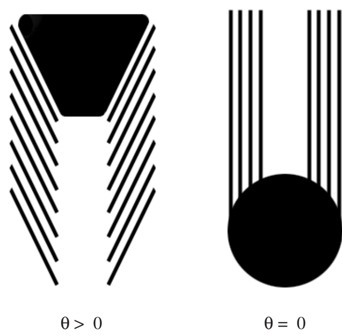

Figure 11: MWCNF versus MWCNT according to the delta angle representing the angle between carbon nanotube shells. Source: [15]

2. Intrinsic properties of carbon nanotubes

In this part, we will describe the general properties of carbon nanotubes such as the electrical transport in CNTs, the mechanical and the thermal properties. The RF properties of CNTs will be explained in the next part of this chapter (see section "Carbon nanotubes modeling on page (56)").

A. Electrical properties [6, 16]

a) Electron transport: Ballistic conduction versus Diffusive [3]

An important point to start with carbon nanotube is the conduction is quantized, meaning the electron moves through discrete conduction channels. We have already calculated the number of conducting channels in MWCNTs. In general, this conduction can be either ballistic or diffusive, but we will explain this point on the next paragraph. In SWCNTs, according to their small diameter between 1 and 10 nm, they will have 2 conducting channels from electron spins (spin up and spin down) and 2 additional conducting channels (presence of sub-band). As explained in the section "Multi-wall carbon nanotube on page (19)", MWCNTs have a bigger number of conducting channels regarding to the diameter of each shells composing the nanotube. However, for each shell, MWCNTs keep only 2 additional conducting channels from the electron spins. To explain the spin electron properties, electrons propagation in carbon nanotubes is considered to follow the fermion properties. Fermions have a ½ spin and they follow the Fermi-Dirac statistics, which gives a panel of equations to solve fermion distributions. So, SWCNT has two electron spins, meaning the electron has two possible spin states during its propagation along CNTs (see Figure 12). The particle spin is a quantum properties and both spins, the spin down and the spin up, are not correlated during a particle propagation and must be taken into account as two additional conducting channels either in SW or MW CNTs. Currently, the spintronic in CNTs is an important topic for future electronics applications and few works have been already done on that [17-19].

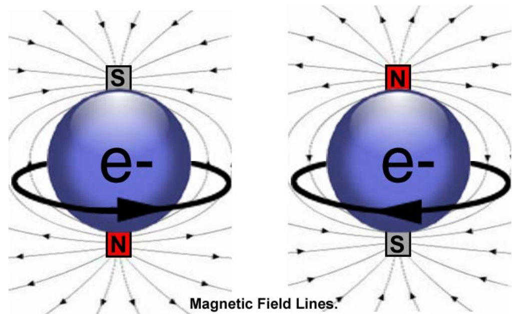

Figure 12: The two possible spin states for an electron (spin up and spin down). Magnetic field direction is changing with the spin.

b) Mean free path in CNTs (MFP) [20, 21]

In every conducting channel, electrons and holes in carbon nanotubes adopt an anisotropic ballistic (scattering free) transport for short distance, meaning the electron is able to propagate in only one direction, which is the nanotube direction (Figure 13). In CNTs, the electron motion is conducted by the Newton's second law in a material without scattering, meaning the electrons move at an equivalent to the speed of light (3.10^8 m/s). This particular propagation of the electron/hole gives us the value of the mean free path (MFP). The MFP is the distance that a particle is able to travel without collisions with another particle and, by definition, combines the effect of all scattering lengths. The MFP parameter will directly affect the resistance of the carbon nanotube, as we will see on the CNT modeling part (see section "Carbon nanotube resistance R_{CNT} on page (61)"). A long MFP (also called λ_{MFP}) between 1 and 25 µm exists in CNTs mainly because of a weak acoustic phonon scattering and a quasi-null optic phonon scattering at room temperature and a low voltage applied (lower than 1V). In bulk materials, such as metals, where the electron propagation is diffusive (Figure 13), MFP is about 38 nm in gold and about 40 nm in copper, which is extremely low compared to the case of CNTs. Indeed, in a bulk material, the electron is able to propagate in all directions and consequently MFP is low.

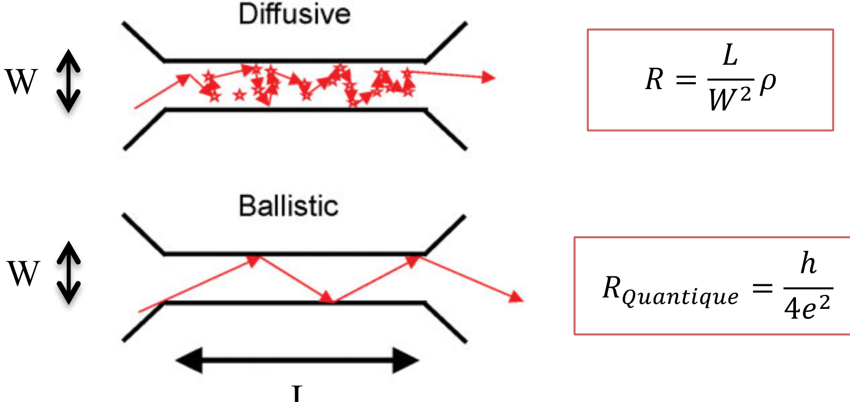

Figure 13: On top, the diffusive electron conduction in a 3-D material and the corresponding material electrical resistance definition. Below, the anisotropic ballistic transport of the electron existing in 1-D material such as carbon nanotube. In this case, a quantum resistance defines the equation of R. R is the material resistance, L is the material length, W is the material width and ρ is the material electrical resistivity. Source: [3]

In an ambient air, MFP is about 68 nm and can reach up to 1 km in a high vacuum atmosphere because of the poorness of particle. The others variations of MFP will depend on the scattering rate and mechanism. If we consider all scattering in CNTs, MFP is a combination of λ_{el-el} is the electron-electron scattering length, λ_{ap} is the acoustic phonon (emission and absorption) scattering length, $\lambda_{op,ems}$ is the optical phonon emission scattering length, $\lambda_{op,abs}$ is the optical phonon absorption scattering length, $\lambda_{impurity}$ is the electron-impurity scattering length, λ_{defect} is the electron-defect scattering length, and $\lambda_{boundary}$ is the electron scattering length with the boundary [20, 21]:

$$\frac{1}{\lambda_{MFP}} = \frac{1}{\lambda_{el-el}} + \frac{1}{\lambda_{ap}} + \frac{1}{\lambda_{op,ems}} + \frac{1}{\lambda_{op,abs}} + \frac{1}{\lambda_{impurity}} + \frac{1}{\lambda_{defect}} + \frac{1}{\lambda_{boundary}} \tag{6}$$

We are able to classify these scatterings in two main categories: electron-phonon scattering (in red) and impurity scattering (in blue). The physics behind the first category is well known and this combination of scatterings becomes significant with low voltage applications, such as the applications presented in our work. E-phonon scattering has been found about 1 µm for SWCNTs. The value depends mainly on the nanotube diameter (scaling at the inverse diameter) and the temperature. The second category of scattering source from impurities will obviously depends on the density of defects on the CNT structure. However, so far, there are no methods to efficiently characterize these impurities in CNTs, especially when we need to study a large amount in CNTs, such as in a bundle. Only a raman and TEM characterizations are able to give us the type of CNTs (SW or MW), however, these two

methods only map a small area. Mainly, the purity of the CNT structure depends on the method used to grow CNTs and the temperature reached during the process. More details will be given on section “Carbon nanotubes fabrication on page (32)”.

The carbon nanotubes usually have a high quality structure and so we expect the second category of scattering from impurities will remain low compared to the first category. Thus, since the acoustic phonon scattering is the main cause of losses in electron/hole propagation, we are able to simplify the MFP equation of CNTs by only indicate here the equation of λ_{AC}, the MFP from acoustic scattering:

$$\lambda_{AC} = 400.46 \times 10^3 \times \frac{D}{T} \quad (7)$$

with D the shell diameter and T the ambient temperature in Kelvin. With a 1 nm SWCNT diameter, we usually considerate a 1-µm MFP. Thus λ_{AC} can be approximate by $\lambda_{CNT} = \lambda_{AC} \approx 1000D$.

Thus, because of the ballistic transport of electron and the low phonon scattering existing in nanotubes, electrons/holes are able to travel a long distance without collisions, and MFP is able to reach up to 25 µm in MWCNTs [22]. The MFP is bigger in MWCNTs than SWCNTs as shown on Table 1. One reason is the MFP directly depends on the tube diameter as shown on equation (7) and the defects in the tubes. Moreover, as already explained in section “Multi-wall carbon nanotube on page (19)”, MWCNTs are more defect-free, decreasing hence the impurity MFP lengths category. Again, MWCNTs will be preferred for high frequency electronics applications [23-25]

c) General properties of CNTs

This high MFP value for a nanoscale component compared to bulk materials also explains the excellent electrical conductivity in carbon nanotubes. Indeed, a maximum current density greater than 10^9 A.cm² can be reached in carbon nanotubes and an electrical conductivity 6 times bigger than copper and gold has been demonstrated [7]. This current density is very high because of the important aspect ratio in CNTs. Indeed, as already explained, CNT is an optimal material for carrying an electron without collision at a nanoscale. The electron propagation at low scale (below 10 µm) is currently impossible with a bulk material such as gold [26, 27] because of important grain scatterings, producing

electromigration effects in them. Table 1 summarizes the mains CNTs properties compared to other materials.

Table 1: Carbon nanotube general properties compared to gold and copper materials. Best performances are highlight in red.

	Copper	Gold	SWCNT	MWCNT
Physical dimensions range /nm	Electromigration below 10 µm		0.7 – 5	10 - 100
Mean free path /nm (room temp)	40	38	1.10^3	25.10^3
Max current density /A.cm^2	10^5	10^{12}	10^9	
Thermal conductivity /W.mk	400	318	6000	3000
Electrical conductivity /Ω^{-1}.cm^{-1}	6.10^5	4.10^5	10^6 ~10^8	
Young's modulus /GPa	128	78	1500	

All these unique electrical properties indicate that CNTs have the potential to be used for next-generation electronics applications in order to replace classical metal-based structures.

B. Thermal properties

Graphite and Diamonds, two materials based on carbon are well known to have excellent thermal conductivity. So, based on the same carbon atoms root, carbon nanotubes are also known to have an excellent thermal conductivity (above 6000 W/mK). Several works [28-31] extracted a room-temperature thermal conductivity between 1750 and 5800 W/mK. This good thermal conductivity comes from the phonon vibrations/oscillations in carbon nanotubes that are able to absorb and transport the heat energy. Indeed, the phonon heat propagation dominates the electron heat propagation in carbon nanotubes. Instead, in metals, electrons heat propagation dominates. And more the temperature increase in CNTs, more the population of phonon modes increases dramatically (Bose–Einstein distribution). That large number of phonon modes gives the reason of an excellent thermal conductivity in CNTs. If we compare the thermal conductivity with other materials largely used in electronics such as silicon (84 W/mK), gold (318 W/mK) and copper (400 W/mK) [32], we see how carbon nanotubes can replace all of them for heat dissipation. Indeed, in interconnections, gold bumps are also used to dissipate the heat from the die; or in FET transistor, where the heat is a major issue, which can easily compromise the device performance or definitely break it. Thus,

by using the CNTs thermal properties, CNTs are able to outperform other material performances. If we take a look on an other work form Iwai's group [33], they use CNTs as interconnections and to dissipate heat from the die.

C. Mechanical properties

a) CNT strength

Carbon nanotubes are also known to be one of the hardest materials in the world. Indeed, if we take a look on its young modulus, which is equal to 1.5 TPa and compare it with other resistant materials such as Kevlar (0.15 TPa) and diamond (1 TPa), carbon nanotubes stay the best. Young modulus is the mechanical constraint we need to apply to the material in order to elongate by 100 % its original length. However, in reality, the material breaks or gets a permanent deformation before reaching the young modulus value. A material with a high young modulus is resistant and rigid. The reason of this hardness is the carbon sp^2 bonds composing the CNTs. Indeed, the sp^2 bond, which is linking two atoms of carbon, is stronger than the sp^3 bonds existing in diamond, one of the hardest materials. This same bond explains the good flexibility of CNTs, but this parameter will be shown in the last paragraph.

In this thesis, we mostly discuss about vertically carbon nanotubes, that's the reason why most of the work presented about CNTs will be done according to this disposition/arrangement. However, horizontally aligned CNTs are also largely used in many applications for electronics and others. Naturally, horizontally CNTs have different constraints on their structure than vertically aligned ones and only one topic can be treated in this work. We invite you to read these works [34-36] to have more details on horizontally aligned CNTs and mechanical properties.

Moreover, as it will be shown along the thesis, a large work have been done to increase the component integration for future electronics devices on high frequency by privileging 3-D CNTs-based devices. Based on this full integration idea, the use of CNTs made sense for our PhD work.

b) Flexibility of the CNTs

Finally, carbon nanotubes are flexible. Indeed, a CNT is able to be bended up to an angle greater than 45° [37, 38] without breaking (Figure 14). A MWCNT is able to bend up to

an angle of 110° without irreversible fracture. This property is interesting for many applications: a CNT placed on a flexible substrate or a CNT used for interconnection will have more durability than current metal-based materials. Moreover, it appears that when a CNT is bended by an external force, once the force is removed, the CNT goes back to its original position [38, 39]. NEMS (nano-electro-mechanical systems) can also be imagined as presented in these works [40]. Obviously, electrical performance is affected by bending the carbon nanotube.

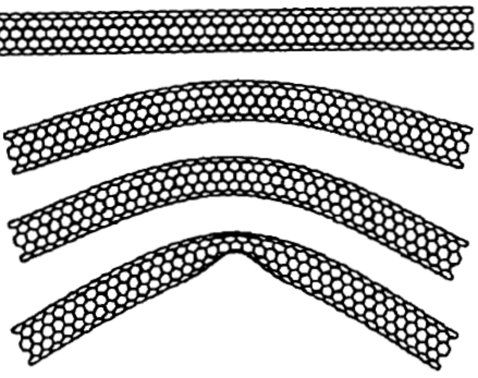

Figure 14: Single-wall carbon nanotube bended at 0, 30, 45 and 60°. We can see the deformation of the structure, which decreases the electrical performance of the carbon nanotube. Source: [37]

We have described all the important carbon nanotube properties for our electronics applications in high frequency. Carbon nanotubes present a quite unique composition at the nano-scale with a very good electrical conduction at this scale. Thus, a perfect structured CNT can be a good alternative to our current metal-based electronics components. However, as we will see on the next part, the fabrication of CNTs needs to be perfectly controlled. Several methods to grow CNTs exist, and four of them will be presented on the next part with their pros and cons.

II. Carbon nanotubes fabrication

1. Arc discharge [41]

The first time the carbon nanotube has been seen was by Iijima in 1991 and by using an arc discharge method. Hence, this method was the first one used for CNT synthesis and so far the most used for CNT production as it is rather simple to undertake. The method is simple: a direct current (DC or AC) is sent through two electrodes, the anode and the cathode, placed into a chamber filled by helium with low pressure (between 200 and 700 Torr) (see Figure 15). Both electrodes are approximately separated by 1 mm. A DC current will be preferred instead of an AC one in order to get a higher yield of carbon nanotubes. To fabricate SW nanotubes, a metal anode containing carbon and a graphite cathode are used whereas for MW nanotubes fabrication, both cathode and anode are made by graphite. With the current, anode and cathode surfaces will be heated by arc discharges, and a higher temperature about 4000 K will be reached by the anode whereas about 3500 K on the cathode. Thus, the carbon in the anode electrode will be evaporated to the cathode. Finally, the evaporated carbon will form carbon nanotube structures on the cathode [37].

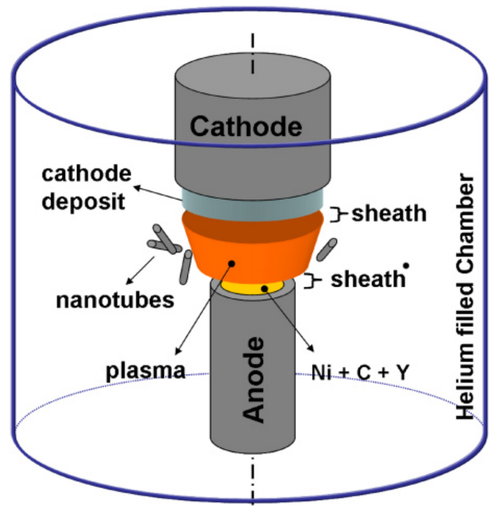

Figure 15: Arc discharge method principle to grow CNTs.

Since the arc discharge method is largely used around the world with a simple principle, why we won't use this method during this PhD work? The answer is simple and contains several points. First, the growth temperature is very high, up to several thousand of Kelvin, which is definitely not applicable to the nano-electronics. Secondly, this method fabricates non-homogeneous CNTs, meaning we obtain different CNT diameter and length on

the same process. Finally, a transfer of the fabricated CNTs to the electronics circuit/device needs to be done since the temperature is too high. Thus, vertically aligned CNTs cannot be obtained by this method. However, the arc discharge method is well known for fabricating the most pure or defect-free carbon nanotubes, especially because of the high temperature needed. Finally, arc discharge is an efficient method to produce a large quantity of CNTs. Table 2 summarizes the pros and cons of using arc discharge for the CNT growth in our applications.

Table 2: Summary of pros and cons of using arc discharge method to grow CNTs.

	Pros	Cons
Process difficulty	++	
Temperature process		- - -
CNT quality	+++	
CNT homogeneity and control		- -

2. Laser ablation [42]

Laser ablation was the last CNT growth method discovered. It was in 1995 by R.E. Smalley group. Again, the fabrication method is pretty simple. A pulsed laser beam (about few hundreds Joules and 532 nm wavelength) is sent on a metal-graphite composite target placed in a furnace chamber at a 1500 K temperature and a controlled pressure (Figure 16). The metal on the target is used as a catalyst for the CNT growth. We usually find Ni and Co as the best catalyst. The laser beam scans the target surface in order to get uniform carbon vaporization. Then, an argon gas is sent in the chamber. The argon flow permits to carry carbon particles outside the furnace on a water-cooled surface (usually copper) where the carbon nanotubes can be collected at the end of the process.

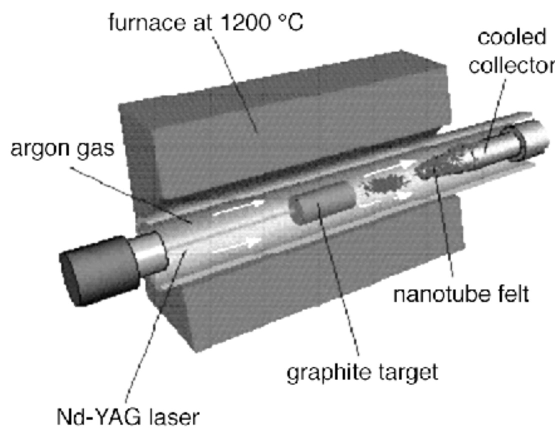

Figure 16: Laser ablation method principle to grow CNTs.

With this method, SW nanotubes are generally obtained and most of them are found agglomerated because of the Van Der Waals forces. For the same reasons than the arc discharge method, laser ablation won't be used in this PhD to grow carbon nanotube structure. Indeed, the temperature process is still very high (1500 K) and the CNTs obtained are placed randomly by bundle, which doesn't allow designing and fabricating well-ordered electronics structures. Hence, along the work on carbon nanotubes for electronics passive components presented here, we will focus on the CVD-based method in order to get well aligned CNTs with a lower temperature. Finally, laser ablation is the most expensive process and not efficient for scale-up production. Purity up to 90 % has been obtained with this method. Table 3 summarizes the pros and cons of using laser ablation for the CNT growth in our applications.

Table 3: Summary of pros and cons of using laser ablation method to grow CNTs.

	Pros	Cons
Process difficulty	++	
Temperature process		- -
CNT quality	++	
CNT homogeneity and control		-

3. Chemical vapor deposition (CVD)

The first report of CNT growth by CVD principle comes from M. José-Yacamán and his group [43] from Mexico in 1993. Since this period, a huge number of works have been

done to improve the repeatability and the direction, size, diameter control of the carbon nanotube growth. Even if now a large number of different methods based on chemical vapor deposition (CVD) principle have been developed, we can yield two main methods, which are mostly used in research because of their better control in CNT growth and their good understanding. Moreover, both of them can be homemade, as we will show in our PhD. Thus, the thermal CVD and the Plasma CVD are the two methods we choose to describe in this work. Therefore, only these two principles will be used to grow carbon nanotubes in all high frequency electronics applications studied in our PhD work.

We can already tell the main advantages of using CVD methods instead of the two, laser ablation and the arc discharge, methods previously explained. CVD principle is able to grow carbon nanotube on patterned locations with a certain control of the CNT direction (using plasma or other methods). This advantage allows us to design electronics devices with complex arrangements of carbon nanotubes. Also lower temperatures, below 900 °C for thermal CVD and between 550-700 °C for PECVD, are needed during the process. Finally, as already explained, this solution can be homemade because of its lower cost compared to laser ablation and arc discharge. However, currently in 2013, we still have difficulties to fabricate carbon nanotubes with a perfect control of their diameters, length, defects-free in a large quantity.

In our PhD work, we will only focused on vertically aligned carbon nanotubes over the substrate. With CVD, the high CNT density ($> 1.10^{14}$ m^{-2}) maintains the CNTs vertically aligned by the Van der Waals whereas in a PECVD process, the plasma direction will affect the CNTs alignment. More details will be given on the respective sections. Today, this lack of CNT direction and structure controls is mostly due of the incomplete understanding of the carbon nanotubes growth mechanism. In this report, we will try to expose a review of the state of the art in CNTs growth with a brief explanation of the CNT growth mechanisms. Indeed, they play a major role for the final realization of the electronics structures/devices for high frequencies that will be presented in the next chapters.

First, we present the thermal CVD, the growth mechanisms and the pros and cons. Secondly, PECVD based on plasma will be presented.

A. Thermal chemical vapor deposition (TCVD)

a) Principle

The chemical vapor deposition method is working as follow: a catalyst layer (ranging between few nanometer to 50 nm) is deposited on a wafer surface at the locations where the carbon nanotube growth needs to occur. Usually, a thicker catalyst layer will return bigger CNT diameter with a lower CNT density. The catalyst is based on metal (Fe, Ni, Co, etc) and plays a major role for carbon atoms diffusion in the CNT growth, as it will be explained later in this part. Then, the wafer with the catalyst layer is loaded in a chamber (usually a quartz tube) with a controlled pressure. This chamber is also composed by a furnace and equipped with mass flow controllers in order to meter the feed gases (Figure 17).

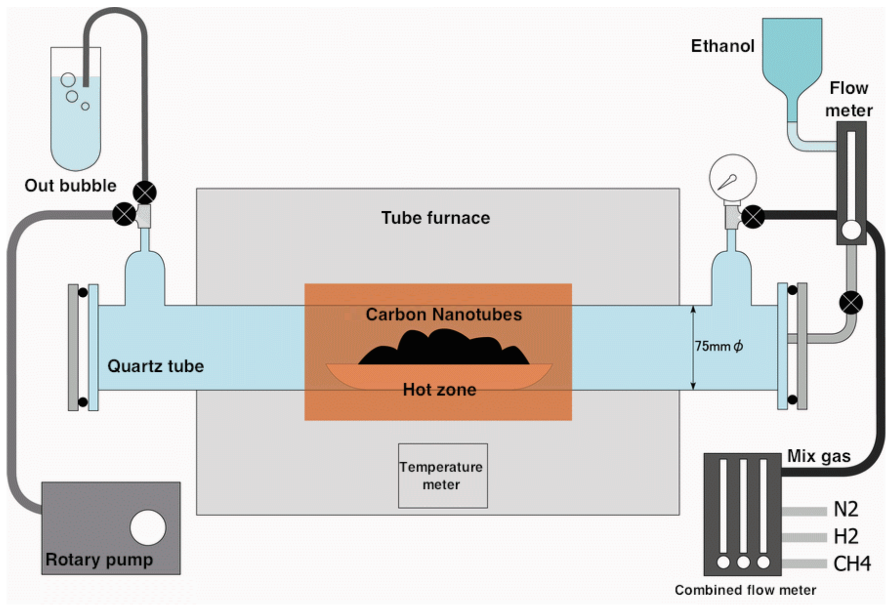

Figure 17: Chemical Vapor Deposition (CVD) process principle. The central tube, which is surrounded by a furnace, is the CNT growth location.

At the beginning of the process, the chamber is purged by argon while the furnace starts to heat the chamber up to 900 – 1000 °C. Once the temperature is reached and a stable atmosphere is obtained, a hydrocarbon gas containing carbon atoms (such as CH_4, C_2H_2, C_2H_4, etc) is sent at a controlled rate. The hydrocarbon vapor (gas) goes through the furnace tube for 15-60 min at a high temperature between 600 and 1200 °C. The high temperature will decompose the hydrocarbon (the precursor) and carbon atoms will be diffused on a metal catalyst disposed in the tube.

Briefly, the catalyst film located at the hottest part in the furnace/tube forms all along the surface small clusters or nanoparticles. These "hot" nanoparticles will help the decomposition into carbon and hydrogen of the hydrocarbon sent. The hydrogen will fly away from the process and be dissolved by the metal. Instead, the carbon atoms will get dissolved into the metal catalyst and once the metal nanoparticles will reached the solubility of the carbon because of the high temperature (and the lower melting point of catalyst at the scale of few nanometres), carbon atoms will crystallize into a hexagonal network following a cylinder shape that we will call carbon nanotube. The CNT growth occurs at this time until a saturation of the catalyst particles happens, the feeding gas is stopped or the temperature decreases in the chamber. The grown carbon nanotubes are then collected in a cooled system placed after the tube. The argon gas flowing through the tube will transport them outside the tube. If the hydrocarbon is under a liquid form, the liquid is first heated in a flask before being sent by an inert gas (such as argon) in the furnace tube where the CNT growth occurs. In the case of a solid hydrocarbon, the precursor is placed in the low temperature zone of the tube.

Thus, at the end of the process, the chamber is cooled below 300 °C in order to avoid a too important temperature contrast between the outdoor air and the chamber. Indeed, it could irreversibly damage the carbon nanotubes. Finally, the argon gas is sent again in order to purge the methane outside the chamber. Carbon nanotubes patterned on the wafer at the catalyst locations can be extracted from the chamber.

Finally, carbon nanotubes growth by CVD will be dependent of many parameters such as the catalyst preparation, temperature, pressure, gas flow rate, and process time. The details of CVD parameters are now presented on the next paragraphs.

b) Catalyst preparation [44]

The catalyst preparation and deposition are critical points to success the carbon nanotube growth. It has been shown that the deposited catalyst on the wafer needs to be in the form of particles/clusters instead of a uniform plan layer. Indeed, according to the catalyst particle size (diameter, roughness, material, melting point), the carbon nanotube diameter obtained and its type (SW or MW) will be modified. Hence, bigger catalyst clusters will grow bigger CNT diameter. The metals as Fe, Ni, Co and Mo are usually used as catalyst with different results obtained for each of them.

i. Choice of catalyst material

Thus, the most important with the catalyst is to obtain small particles/clusters at the nano-scale in order to enable the hydrocarbon decomposition with a lower temperature. The three main catalyst materials used by researchers for CVD process are Fe, Ni and Co. Indeed, two reasons explain this choice of material. First, experiences show that the carbon solubility is high in these materials at high temperature and secondly, the carbon diffusion rate is also important in them. Finally, their melting point is at a very high temperature (see Figure 18), allowing a large window of temperature for the CNT growth by CVD process. By looking at the same Figure 18, we understand now, according to the CNT diameter and the growth temperature (CVD or PECVD as we will see later), the choice of the compatible couple catalyst/hydrocarbon will be very important. Indeed, the catalyst particle diameter is intimately link to the CNT diameter; bigger cluster will grow larger CNT diameter and so on. Campbell's group has detailed this fact in their work using an iron catalyst model [45].

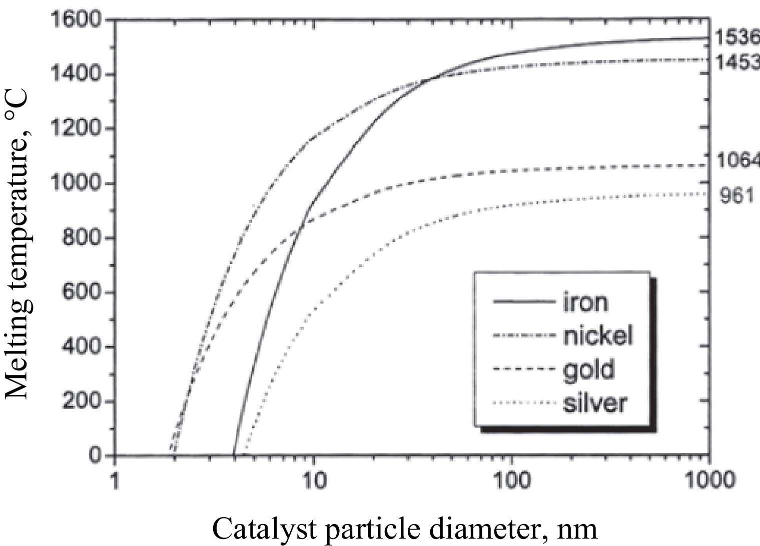

Figure 18: Melting points of several metallic particles (Fe, Ni, Au and Ag) in function of their diameter. Iron presents the higher melting point with particle diameter above 30 nm. Source: [46]

We can also denote that other materials can be used and have been used as catalyst with usually less efficiency. We can mention the use of metals such as Cu, Au, Ag, Pt and Pd. The work of Kumar's group [46, 47] has written a review explaining the new methods to grow CNTs by CVD with new catalyst material such as the ones mentioned above, with metal-free or even new CNT precursors such as polymers.

Finally, these catalyst materials can also be employed in arc discharge and laser ablation methods for CNT growth, proving a common mechanism between all processes. A mix between two catalysts can be also done. Indeed, where the Fe has a stronger effect of hydrocarbon decomposition, the use of Co results in a better network structured CNTs. Thus, a mix of Co and Fe catalysts allow producing a large number of CNTs with lower impurities.

ii. Catalyst deposition method – Ebeam process

For catalyst, solution-based preparation techniques are mostly used in thermal CVD and include several steps such as dissolution, stirring, precipitation, refluxing, separation, cooling, gel formation, reduction, drying/annealing/calcination etc. This could be a very long process and confining small pattern of catalyst on the substrate is challenging with this method. In contrast, a physical deposition of the catalyst film will be preferred to obtain small patterns. This deposition includes ebeam/electron gun evaporation, thermal evaporation, pulsed laser deposition and magnetron sputtering. In this work, we will uniquely choose the ebeam evaporation as the method to deposit catalyst film on substrate.

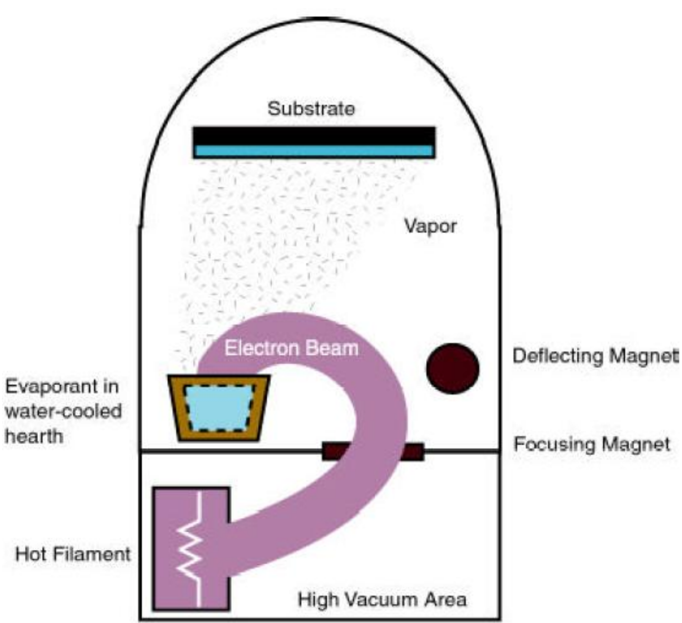

Figure 19: Ebeam principle for metal deposition on substrate.

Ebeam evaporation is a simple process to deposit metals on any surfaces and allows a good control of the layer thickness up to few nanometers. In a vacuum chamber (10^{-6} mbar), a tungsten filament is heated by electrical current, which creates an electron beam (Figure 19). Then, this electron beam is oriented and accelerated by a magnetic field to a crucible

containing metal. The metal heats and evaporates to the substrate, which is located from the backside at the top of the chamber. Thus, the metal is deposited uniformly on the surface. To control the deposition rate, we need to play with the electrical current sent to the filament. A bigger current will increase the rate and so on. For a better homogenous metal film, a low deposition rate will be preferred.

iii. Catalyst deposition method – Underlayer and pre-treatment

Since it appears that a smooth layer of catalyst doesn't grow carbon nanotubes, it is important to perform a surface pre-treatment in order to break the catalyst layer into small particles/clusters. So, for CVD growth, a pre-treatment with ammonia gas (NH_3) at a high temperature (about 800 °C) for a small amount of time (2 minutes) can be done in order to prepare the catalyst into clusters before the growth process starts. Another solution consists of adding an underlayer (such as SiO2, TiN, Al, Ir, ..) under the catalyst film in order to increase its roughness. It appeared that a more important roughness on the catalyst surface provides more active nucleation sites for the CNT growth as shown on Figure 20. Indeed, on the Figure 20(a), a smooth layer of catalyst is visible (measured with AFM) but only sparse CNTs have been grown with a very low CNT density. On (b) and (c), a more important roughness are visible on both samples, and CNT bundle have been achieved. Moreover, if we take a look on the catalyst clusters visible on (b) and (c), we can observe that smaller clusters on (b) than (c). A higher number of clusters are also visible on (b) on the same surface area than (c). In results and as we already explained previously, smaller diameter CNTs have been obtained on (b) with a higher CNT density. On (c), CNT diameters are larger and the density was reduced, only due to the catalyst layer configuration that was deposited before the growth. By using an ebeam process, we can have a coarse control on the catalyst cluster size. Indeed, it appeared the catalyst layer deposited by ebeam is linked with the catalyst cluster size that can be achieved. Thus, a thicker catalyst layer will return bigger catalyst clusters.

Along this work, different underlayers will be used also to prevent the matter diffusion between the different layers during the growth. We call this underlayer: the barrier layer. We will keep in mind that the barrier layer plays an important role in the CNT growth according to its roughness and its thickness.

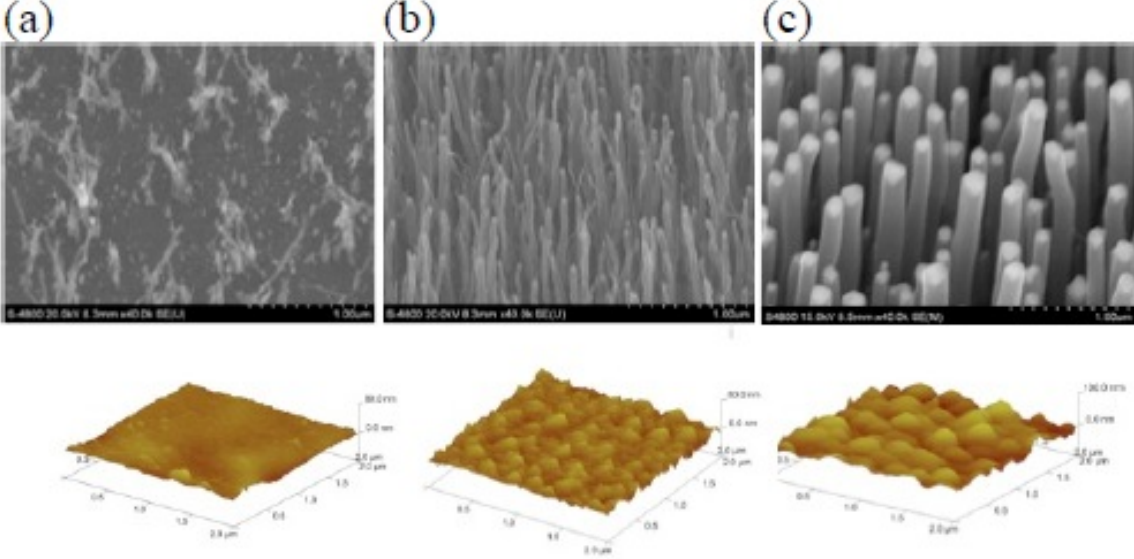

Figure 20: Effects of the catalyst layer roughness on the CNT growth by CVD. Source: [48]

Finally, the choice of the support is also an important issue. Indeed, the interaction between the substrate and the catalyst plays a major role. First, according to the type of growth wanted (bottom or tip growth), we will have to choose between a strong or weak link between the catalyst and the substrate (see next paragraph). Secondly, chemical bond formation must not exist between the catalyst and the substrate in order to do not inhibit the carbon nanotube growth. Finally, as already explained in this part, the substrate morphology will also affect the formation of clusters on it. In general, graphite, quartz, silicon, silicon carbide, silica, alumina, alumino-silicate (zeolite), etc are used as substrate support for catalyst. Moreover, substrate oxide (such as SiO_2) can be used as the support of the metal catalyst. We will see in this work that most of the time, we grow an oxide layer on the silicon substrate we are using as support for the CNT growth. Our experiences showed that this layer helps a lot in the carbon nanotube growth.

c) Bottom and Top CNT growth

i. Principle

We are able to yield two types of growth in CVD process (this is also applicant on the PECVD process): the bottom and the top growth. Indeed, these two names represent the two possible locations of the left catalyst particle at the end of the growth process. So, we will meet two cases: the catalyst will remain at the top of the carbon nanotube or the metal particle

will remain at the bottom of the CNT, stuck between the substrate and the nanotube (see Figure 21). The resulting growth obtained will directly depends on the strength of the catalyst-substrate interaction/interface. The reason is simple; if the interaction between the susbstrate and the metal is weak, the hydrocarbon will be disolved from the top of the catalyst particle and will precipitate out across the metal bottom. Thus, the catalyst nanoparticle will be pushed by the croissance of the carbon nanotube. As long as the temperature gradiant is keeped from the catalyst to the hydrocarbon, the CNT will keep growing. Only a saturation of carbon by the catalyst will stop the growth. This is called the "Tip-growth model".

In constrast, when the interaction between the substrate and the catalyst are strong, the same process of carbon precipitation across the catalyst will appear, but the crystalized carbon won't be able to push up the metal catalyst. Thus, the precipitation will happen from the top of the catalyst particle. The top of the CNT will appear in a hemispherical dome shape which is the most favorable closed-carbon network shape. This is called the "base-growth model".

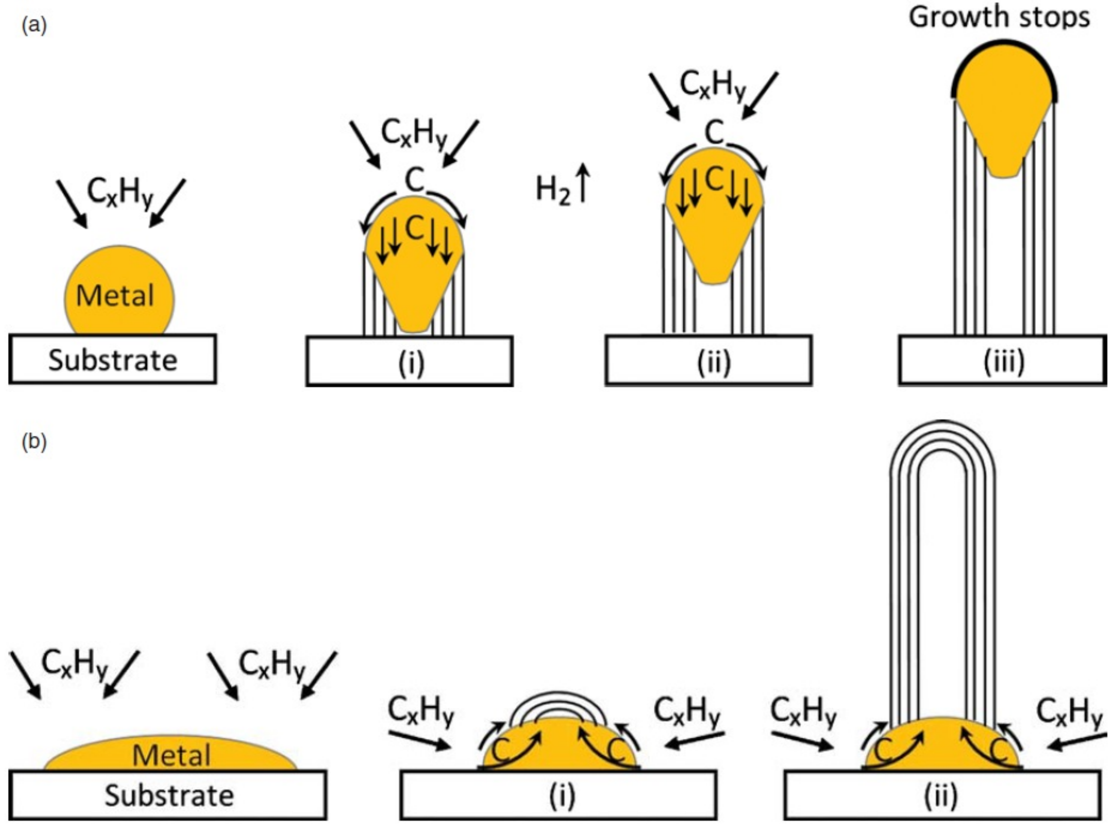

Figure 21: Top (a) and bottom (b) carbon nanotube growth mechanisms. The carbon atoms diffusion into the catalyst adopts a different path according to the type of CNT growth. Source: [46]

According to the growth type, the vertical standing of the carbon nanotube and the CNT length reachable will be affected. In our PhD work, only a top growth will be preferred, because of the higher CNT length that can be obtained. To remove the catalyst particles on top of the CNTs, an O_2 plasma etching can be realized. To choose between the growth of SWCNT or MWCNT, the catalyst particle size will play a major role. With few nanometers size, SWCNTs are formed whereas a catalyst particle size from 10 nanometers and above fabricate MWCNTs.

ii. CNT morphologies and effect on their structure

Three main morphologies of carbon nanotube exist [49]: bamboo type, straight-like type filled by the metal catalyst and catalyst-free (Figure 22). The last case needs a growth based on other methods than chemical vapor deposition (CVD) process such as arc discharge or laser ablation. These other methods won't be used for this PhD work and mostly for electronics because they are not adapted in a sense of growth temperature. According to the type of growth, flexibility of the CNT will be modified. As shown on the Figure 22(a), a bamboo type CNT is composed by intermediate layer of carbon atoms disposed in a hexagonal arrangement. Indeed, we can imagine that bamboo like CNT (Figure 22(a)) is more able to stay vertical than the straight kind of CNTs. However, we haven't found any studies comparing the flexibility of these two morphologies.

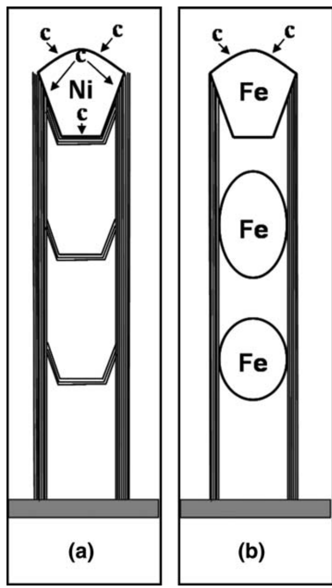

Figure 22: On left, bamboo type of CNT with intermediate layer of carbon nanotubes along the carbon nanotube. On right, straight-like CNT with particles of catalyst inside the CNT structure. Source: [49]

Another major point dealing with CNTs growth and the flexibility of the CNTs is the location of the catalyst particle at the end of the vertical growth of CNTs [50, 51]. As we have seen, we have two main growth morphologies: top growth and bottom growth. Several explanations have been given to show which growth return the more vertically CNT. Merkulov group said that an electrostatic force F creates a uniform tensile stress across the particle/CNT interface (Figure 23). With a bottom growth, it has been experimentally shown that with the increase of the length, the feeding catalyst particle is reduced and the carbon nanotube tends to bend. In the second case, with a top growth, the top catalyst particle assures the feeding of catalyst for carbon diffusion while the nanotube is growing and a more stable tube is obtained (also a lower grow rate).

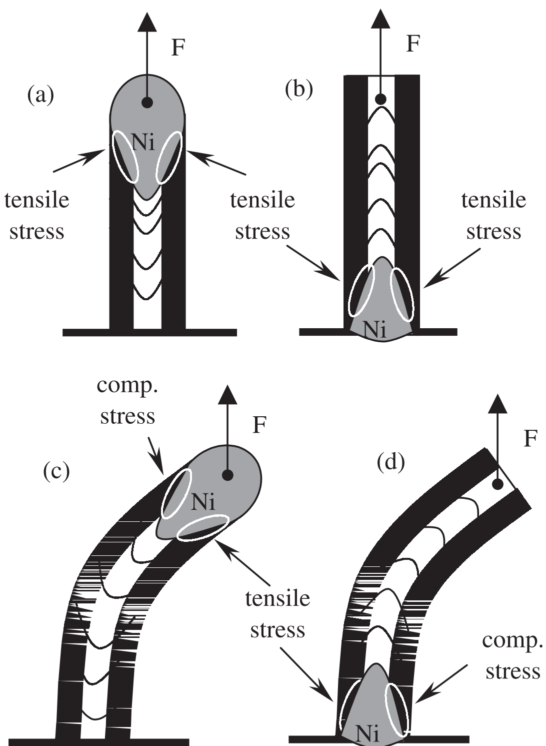

Figure 23: Bottom and top growth of carbon nanotube. Source: [15]

d) The choice of hydrocarbon (also called CNT precursors)

We can list the most used hydrocarbon precursors for the CNT growth by CVD with: methane, ethylene, acetylene, benzene, xylene, and carbon monoxide. According to the precursors, the temperature process will be modified. For example, with benzene, the decomposition of the hydrocarbon occurs at 1100 °C whereas a temperature about 700 °C is sufficient with acetylene. For these two hydrocarbons, the iron is used as catalyst. Indeed, the

reason of the differences in temperature comes from the strong link existing between certain catalysts with specific hydrocarbons. Consequently, a hydrocarbon will match with only a few catalysts. We already know that every catalyst material has a different melting point, that's why the process temperature will be different according to the couple hydrocarbon/catalyst. For our fabrication, we will target the lower process temperature, thus, acetylene becomes the natural choice.

Moreover, the molecular structure of the hydrocarbon will affect the final CNT structure. Some of them will create mostly hunched CNT instead of well uniform and structure carbon nanotubes. Thus, methane, ethylene, and acetylene will be preferred.

Finally, the works done on the CNT production by researchers with CVD show that between 600 and 900 °C, mostly MWCNTs are fabricated whereas above 900 °C and up to 1200 °C, we grow more SWCNTs. So, it becomes more difficult to grow SWCNTs than MWCNTs since there is less stable hydrocarbon at the very high temperature about 1000 °C. The detailed carbon nanotube growth mechanism will be explained on the next part.

e) Growth mechanisms and control [49]

As we discussed in the previous part, the key point in the CNT growth is the couple catalyst/hydrocarbon. Now, the question is: how and why?

At high temperature, a hydrocarbon (in the list presented previously) can easily break; we call it the Pyrolysis. The pyrolysis is a simple thermal decomposition of the hydrocarbons. The point is with a presence of a catalyst, the temperature where the hydrocarbon breaks can be decreased. We call it now the catalytic pyrolysis. This is exactly what occurs in a CVD process and we are trying to take advantage of this singularity in order to decrease the process temperature compared to laser ablation and arc discharge methods. So, the key in CVD process is to achieve a decomposition of the hydrocarbon at lower temperature thanks to the catalyst before the hydrocarbon decomposes itself by the thermal action only. This will happen with the right choice of CVD parameters and components.

First, the choice of catalyst: following the literature and what we explained previously, Fe and Ni has been the most common choice for many researchers because of their higher melting point (Figure 18). In this work, we will only use both of them for the CNT growth. The Fe is selected for CVD instead of Ni for PECVD.

Secondly, the process temperature needs to be controlled. Following the literature, no carbon nanotube growth happened below 500 °C with a CVD process. However, recently, a growth at 365 °C has been performed for on-chip CNT vias [52-55] and also some works at ambient temperature have performed the CNT growth with others method than CVD (PVD). From 500 to 600 °C, the growing rate has been found very low and only short length nanotubes (MWCNTs) have been obtained. The CNT growth starts to increase abruptly from 600 °C. The growth of clean CNTs with a very low number of metal impurities have been done up to 750 °C. Moreover, most of the time, at a low temperature below 600 °C, a base growth process happened with, as already explained in section "Bottom and Top CNT growth on page (41)", a lower CNT quality. Thus, for better CNT quality, we will prefer in this PhD work a CNT tip growth process. We can easily make the assumption that with a higher temperature, the catalyst clusters formation is better with more uniform particle size and carbon dispersion. Finally, once we reach a temperature higher than 750 °C during the growth process, it was observed that the CNT diameter increases drastically. Thus, from 750 °C process temperature, the catalyst clusters become bigger with the increase of the temperature. However, at 850 °C and above, the SWCNTs formation instead of MWCNTs starts because catalyst particles start to melt and create smaller clusters. To conclude on the process temperature for CNT growth, it was observed that the optimal temperatures for MWCNTs growth is about 650 °C whereas 900 °C for SWCNTs. Thus, a control of the CVD temperature allows obtaining one or the other kind of carbon nanotubes. Then, even if we won't go into deep details, the hydrocarbon flow and pressure are important parameters that need to be controlled for the CNT growth. Basically, a constant pressure will be maintained during the all process. The more stable is the flow, better is the CNT uniformity. Moreover, it is important to do not saturate with carbon the catalyst particles but in the same time feed these particles with enough carbon sources. Thus, an optimum needs to be found for an optimal carbon nanotube growth.

Finally, in order to be complete in the CNT growth mechanisms, we need to talk about the catalyst particles. It is still unclear if the catalyst particles stay whether in a solid or liquid form during the growth. With a liquid particle, volume diffusion happens whereas a surface diffusion occurs with a solid particle. However, some group already observed that the catalyst particle shape is changing during the CNT growth whereas other groups found a constant particle size and shape remained static during the growth. If we take a look on the Figure 18 showing the catalyst particle melting points, we can see the melting point decreasing

dramatically with the decrease of the particle size/diameter. Thus, the following assumption is done: as the temperature increases, bigger catalyst clusters are obtained in a solid state, which form MWCNTs in majority. The size of these clusters will increase with the increase of the temperature up to a specific temperature which will depends on the catalyst metal/material used and its melting point according to Figure 18. Thus, above this specific temperature, the catalyst particles will be on a liquid state and smaller clusters will be obtained. With smaller clusters, mostly SWCNTs will be fabricated. Finally, the carbon atoms diffuse on the outer surface of the metal particle (Figure 17 and Figure 24) to form the carbon nanotube structure.

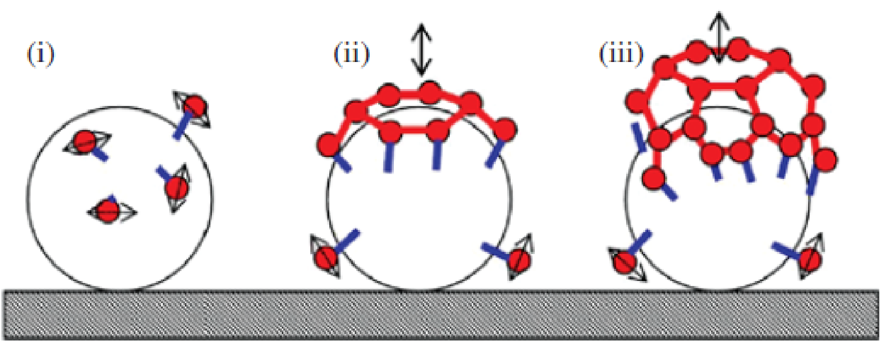

Figure 24: Representation of the surface diffusion of carbon atoms on a catalyst particle. On (i), the single carbon atoms diffuse on the surface in order to form the carbon nanotube network in a hexagonal arrangement (ii and iii). Source: [46]

f) Summary of CVD method to grow CNTs: Pros and Cons

- CVD allows a good control of CNTs parameter during the growth: the length, the diameter and the type (SWCNT or MWCNT) can be chosen by select the correct temperature/catalyst material/hydrocarbon mixture. A perfect uniformity among the all CNTs in a bundle is not yet achieved, but so far, this is the best process to control the CNTs parameters (diameter, length and uniformity). CNT chirality is not control during the CNT growth. Moreover, the number of shell into the MWCNT cannot be exactly predicted.
- All growth mechanisms are not yet fully understood and that's the reason why we don't know the effect of the use of one metal to another as catalyst on the CNTs properties. The exact role of the residual H_2, O_2 and H_2O is also not fully understood.
- Process temperature is still too high (above 500 °C) to be compatible for CMOS process. Some work already succeed to grow CNTs below a temperature of 400 °C but more investigations are necessary to obtain uniform and good quality CNTs.
- The CNTs fabricated by CVD process are known to have more impurities than the ones fabricated by arc discharge and laser ablation.
- CVD is the only process that allows growing carbon nanotubes on specific patterns. With this possibility, we are able to design more complex shape of carbon nanotube bundles for electronics devices, as it will be presented later in this work.

Carbon nanotubes have been fabricated in CINTRA/NTU using a thermal CVD with Fe catalyst (1-3 nm) coated on Al_2O_3 (barrier layer) and a silicon substrate (Figure 25). The process temperature was about 650 °C. As we can see on the Figure 25 taken by scanning electron microscope (SEM), CNTs are not perfectly aligned. However, a high CNT density was found at 1.10^{10} cm^{-2}. Table 4: summarizes the pros and cons of using laser ablation for the CNT growth in our applications.

Table 4: Summary of pros and cons of using thermal CVD method to grow CNTs.

	Pros	Cons
Process difficulty	+	-
Temperature process		-
CNT quality		-
CNT homogeneity and control	++	

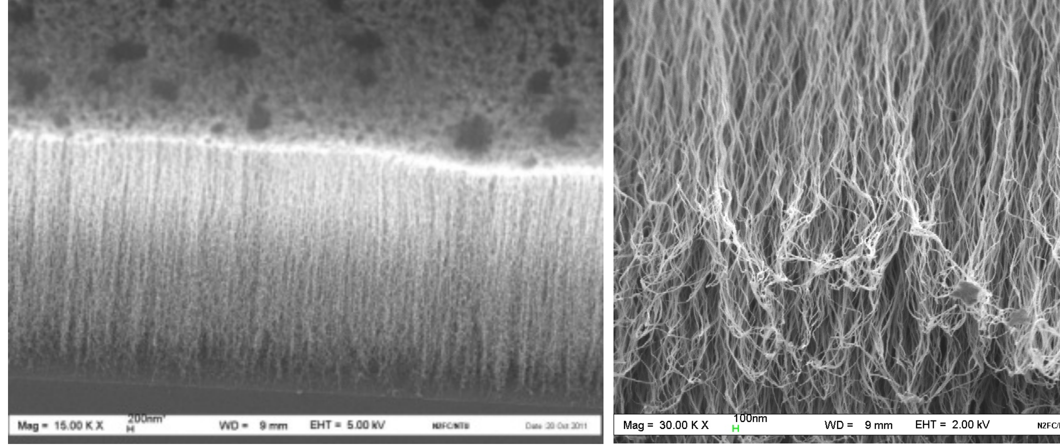

Figure 25: Bundle of MWCNTs grown by thermal CVD in CINTRA/Nanyang Technological University associated to the group of Prof Tay Beng Kang composed by Li Hong, Chow Wai Leong, Yap Chin Chong and Dunlin Tan.

B. Plasma enhanced chemical vapor deposition (PECVD)

We are now going to present the plasma enhanced chemical vapor deposition (PECVD) based on the CVD process explained in the previous part. Most of the carbon nanotube growth mechanisms remain the same with CVD. We will only present the small differences in the growth method and the results we are able to obtain. As we know, the control of CNT parameters is important during the growth such as the orientation, the diameter, etc in order to design complex forms for electronics devices. Thus, the advantage of using a PECVD instead a CVD is the possibility to obtain vertically aligned carbon nanotube

bundles. Indeed, even if we presented vertically aligned CNT bundle growth with thermal CVD, the reason of their alignments comes from the Van der Waals forces (VDW) due to their proximity/crowding. If the CNT density decreases in the bundle, the CNTs won't remain vertically aligned. By adding plasma in the correct direction during the CNT growth, PECVD is able and has been investigated for its ability to fabricate vertically aligned carbon nanotubes.

a) Principle

The PECVD setup is composed by a vacuum chamber with an anode and a cathode, which is also used as the substrate holder (Figure 26). A power supply (DC or AC current) generates plasma between the cathode and the anode. Temperature controllers placed outside the chamber control the holder temperature. Also mass flow controllers and pressure control allow selecting very precisely the gases flow rate sent into the chamber. Indeed, as presented with CVD, a fine control of each parameter is an important point to focus on in order to get the expected CNT growth and the best repeatability. At the beginning of the process, same as the CVD, the chamber is purged and vacuum (below 10^{-5} mbar) is realized in order to remove all impurities from outside. Then, same as CVD, hydrocarbon is sent into the chamber while the plasma is switched-on in order to grow CNTs on the catalyst cluster locations with a control of their directions according to the plasma orientation. The holder is heated at a temperature between 550 and 750 °C. Compared to a CVD process, the growth temperature process is lower. Indeed, the plasma is the reason of the lower temperature, because the plasma will pre-decompose the hydrocarbon in the chamber. More details will be given later in this section. The CNT growth occurs until the gases are stopped, the plasma is stopped or the temperature holder is cooled down. Finally, the chamber is purged again in order to remove all hydrocarbon particles remained in the chamber and the sample is unloaded once the chamber reaches a temperature close to the ambient temperature. Indeed, as a CVD process, a too important temperature contrast on CNTs may damage them.

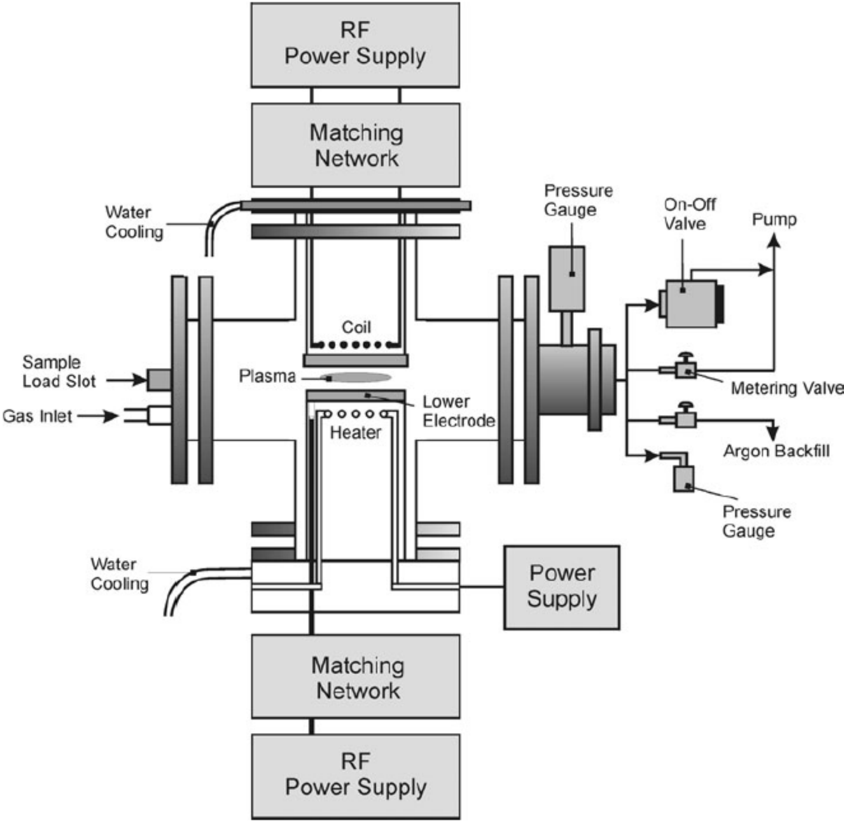

Figure 26: Schematic of the PECVD setup. Source: [15]

b) Catalyst preparation and selection

We only detail here the preparation of the catalyst with the more efficient materials to employ in order to obtain well-aligned bundles of carbon nanotubes. The objective of the catalyst film is to turn into small clusters at the beginning of the growth to permit a better carbon diffusion into them. Better is the size cluster uniformity; better would be the CNT parameters uniformity. In the case of PECVD, the materials used as catalyst include Fe, Ni, Co and Mo. A thin layer (below 20 nm) is deposited on the substrate by ebeam evaporation in this PhD work. In the case of using Ni as catalyst, a pre-treatment by NH_3 is necessary to etch the Ni layer in order to help the formation of small catalyst particles. In this work, only Ni catalyst will be used for the MWCNT growth by PECVD.

c) The choice of hydrocarbon

To perform a CNT growth based on PECVD, we also need to send a precursor gas composed by carbon atoms also called hydrocarbon. In the case of the PECVD, the gases used for the carbon nanotube growth include methane, ethylene and acetylene. The precursor

will be decomposed by the high temperature existing on the catalyst clusters and by the cold plasma. Therefore, hydrocarbons are usually diluted with argon, hydrogen or ammonia in order to avoid a substantial deposition of amorphous carbon. The precursor fraction rate needs to be correctly evaluated. A high fraction of hydrocarbon will saturate the catalyst particle and forming an excessive quantity of amorphous carbon. In contrast, a too low fraction of hydrocarbon will prematurely stop the carbon nanotube growth. In our PhD work, acetylene is used.

d) The plasma

Several solutions exist to generate plasma for the CNT growth by PECVD. Indeed, different kind of sources can be chosen: DC [15], AC/RF, hot filament, microwave, inductively coupled plasma reactors and RF with magnetic enhancement. Most of the time, DC or AC is selected to generate the plasma between the two electrodes. However, the choice of the source can impact the CNT growth. The plasma will break hydrocarbon molecules sent into the chamber into CH_x, C_2H_y and C_3H_z radicals and into stable molecules such as C_2H_2, C_2H_4 and C_3H_8, which are easier to dissolve into the catalyst particles.

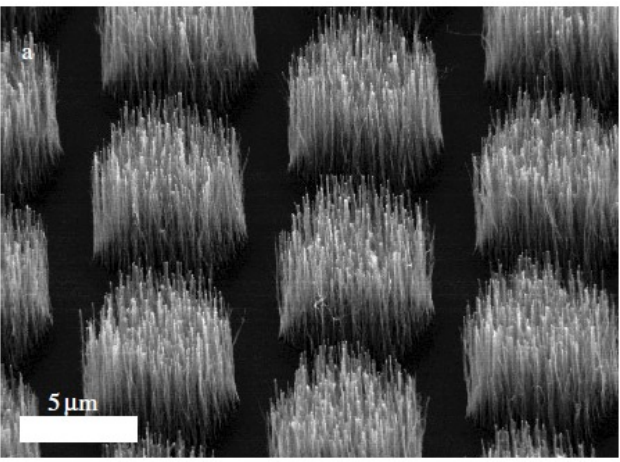

Figure 27: Bundle of carbon nanotubes grown by PECVD. The CNTs are vertically aligned in the direction of the plasma. Source: [15]

As we already explained, the plasma put into the CVD is used to obtain vertically aligned carbon nanotubes. Other groups such as Bower et al [56] performed CNTs growth with and without the plasma on the same process. What they observed show that without the plasma during the process (thermal CVD), only curly, hunched and randomly oriented carbon nanotubes were grown.

An increase of the plasma power will result in a bigger electron density. A bigger electron density will increase the precursor dissociation. Moreover, it appears that with a high power, most of the CNTs grown are MWCNFs. In contrast, when a low bias is applied on the substrate, mostly MWCNTs are obtained.

e) Summary of CVD method to grow CNTs: Pros and Cons

- The best advantages of using PECVD are the decrease of the process temperature compared to the CVD process and the result of vertically aligned carbon nanotubes standing above the substrate. Thus, lower CNT density can be obtained with still a good verticality and uniformity of CNTs into the bundle. This good arrangement and the lower process temperature bring us closer to a CMOS compatible process and to create even more complex electronics structures. That kind of structures will be presented and studied all along this work. However, such as in CVD, a lot of questions remains unanswered:
- So far, it is a big issue to grow SWCNTs bundle by PECVD. Since the PECVD helps the precursor dissociation, the process temperature needs to be decreased in order to avoid a pre-dissociation outside the catalyst particle.

Carbon nanotubes have been fabricated in our laboratory using a PECVD with Ni catalyst coated on a silicon substrate (Figure 28). As we can see on the Figure 27 and Figure 28 taken by scanning electron microscope (SEM), CNTs are well vertically aligned each other. A high of 20 µm is obtained and a good uniformity in CNT length and diameter is observed. However, a lower density than the CNT bundle obtained with TCVD (Figure 25) was achieved. On Figure 28, we observe a CNT density of 5-7.10^{8} cm^{-2}.

Table 5: Summary of pros and cons of using thermal PECVD method to grow CNTs.

	Pros	Cons
Process difficulty		-
Temperature process	+	
CNT quality		- -
CNT homogeneity and control	+++	

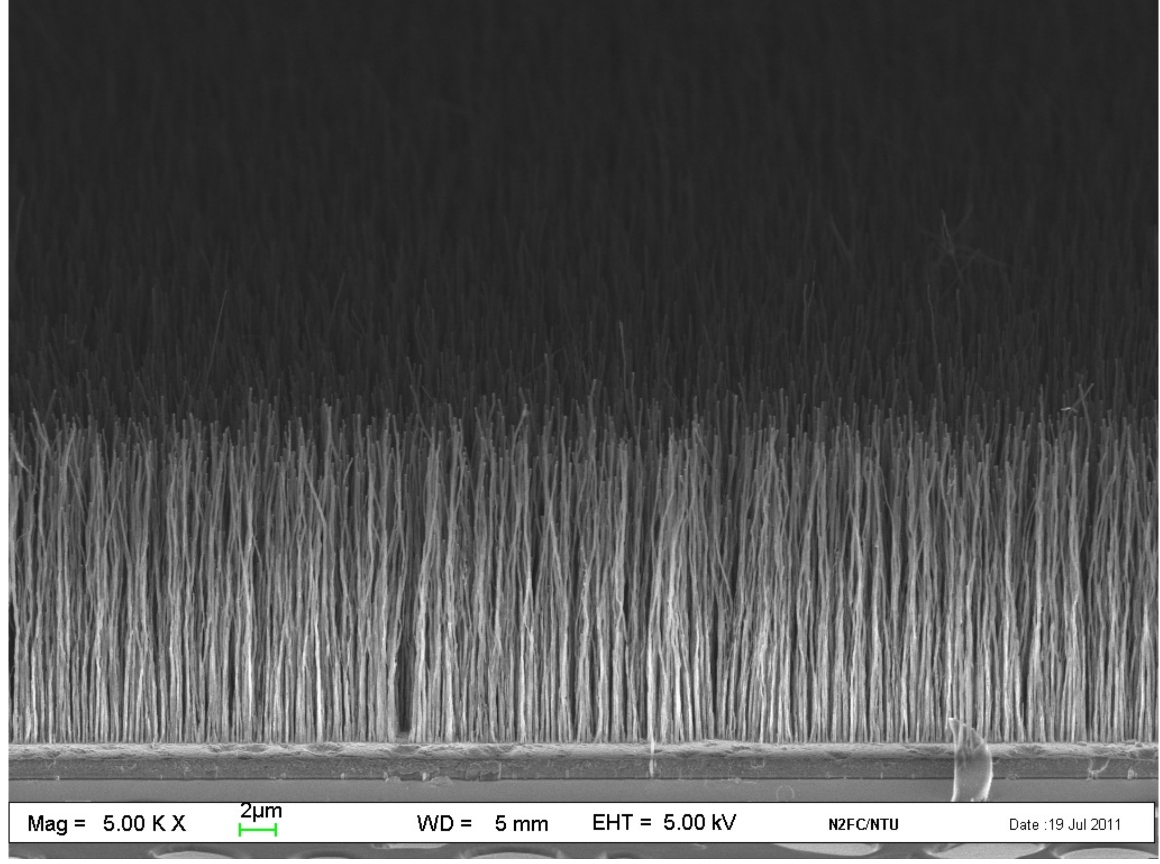

Figure 28: Vertically aligned MWCNT bundle fabricated by PECVD in CINTRA/Nanyang Technological University associated to the group of Prof Tay Beng Kang composed by Li Hong, Chow Wai Leong, Yap Chin Chong and Dunlin Tan.

4. Conclusion

The chemical vapor disposition (CVD) based methods are currently the most used processes by researchers to grow carbon nanotubes. There are three main reasons: low cost (can be homemade), high production and ease of scale-up. In CVD, a thermal decomposition of hydrocarbons in the presence of a metal catalyst represents the general process principle. If we compare the CVD method with arc discharge and laser ablation, CVD is a more economical technic at a lower temperature with ambient pressure. However, CVD process returns a lower CNT purity than arc discharge and laser ablation. Anyway, for a CNT structure as we want in this PhD work (vertically aligned carbon nanotubes that will be presented in the chapter II), CVD becomes the unique viable alternative. At last, CVD allows a good growth flexibility in terms of the CNT parameter control, the various substrates than can be used, the CNTs forms and their direction that can be obtained, the realization of pattern, etc. The Table 6 summarizes the pros and cons of all CNT growth methods we

discussed earlier and Table 7 shows the CNT growth capabilities in our group composed by Yap Chin Chong, Li Hong, Dunlin Tan and Chow Wei Leong and directed by Professor Tay Beng Kang in NTU.

Table 6: Carbon nanotubes growth methods summary: Pros and Cons

	Process difficulty	Temperature process	CNT quality	CNT homogeneity and control
Arc discharge	Easy and repeatable	3700 °C	CNT purity > 90 %	- Random diameter - Random length - No patterning possible - No CNT verticality
Laser ablation		1300 °C		
TCVD	Very sensitive parameters (temperature, pressure, time, gas, catalyst, etc)	700-900 °C	Good quality	- SWCNTs and MWCNTs - Very dense bundle - Long CNTs (up to mm) - CNT verticality by the VDW forces - Quite homogenous CNTs (length and diameter)
PECVD	Very sensitive parameters + the plasma	550-700 °C	Low quality	- Only MWCNTs - Less dense bundle - Short CNTs (up to 50 um) - Very good CNT verticality because of the plasma - Quite homogenous CNTs (length and diameter)

Table 7: CINTRA/NTU (with the group of Professor Tay Beng Kang) CNT growth capabilities

	SWCNTs	**MWCNTs**
Thermal CVD	- High CNTs quality - Dense CNT bundle (up to $1.10^{14\text{-}15}$ m^{-2}) - Long CNTs (up to mm with super-growth and up to 350 µm with normal growth) - Small patterns (5 µm)	- Acceptable CNTs quality - Lower CNT density (up to 1.10^{13} m^{-2}) - Long CNTs (up to 1.7 mm with super-growth and up to 350 µm with normal growth) - Big diameters (from 50 to 350 nm) - Small patterns (5 µm)
Plasma CVD	On going by other groups	- Low CNTs quality - Low CNT density (up to 1.10^{10} m^{-2}) - Short CNTs (up to 30 µm) - Big diameters (from 50 to 350 nm) - Small patterns (5 µm)

We have described the four main methods to grow CNTs for our electronics applications. In summary, only two of them (TCVD and PECVD) will be kept for our studies because of their growth of CNTs in bundle. In the next part of this chapter, we will explain how we model in high frequency a bundle of CNT, starting by the model of a SWCNT alone. Two main approaches will be described for CNT modeling: analytical and electromagnetic modeling.

III. Carbon nanotubes modeling

1. Microwave properties of CNTs versus DC

To understand the quantum mechanism existing in CNTs, we have to consider the electrons following the wave-particle duality, meaning an electron follows rules/behaviors of a particle of matters but can be also described by a wave. Indeed, especially in quantum-scale objects/material such as carbon nanotubes, electrons will be more described by waves properties than particle ones. The reason comes from the electron wavelength, an important parameter in the case of CNTs. This wavelength can be calculated with the following equation (8) [3, 57]:

$$\lambda\ (electron) = \frac{h}{p} \tag{8}$$

With h the Planck's constant and p the relativistic momentum of the electron. p is calculated according to the accelerating potential giving the electron velocity. Usually, electron wavelength in metals and SC, also called Broglie wavelength, ranges between 0.1 and 10 nm [3]. As explained in section "Single-wall carbon nanotube on page (17)" and "Multi-wall carbon nanotube on page (19)" CNTs diameter is between 1 to 10 nm (SWCNT) and 10 to 100 nm (MWCNT), which is around the scale of the electron wavelength described here. Thus, because of the nanoscale of CNTs, their physics in electronics (DC and RF) is different than a bulk material.

In DC, the physics behind CNTs is well understood as Burke explained in his review [3]. By applying the Landauer-Buttiker formalism to a 1-D system as carbon nanotubes, we obtain the fundamental ballistic conductance of the CNT (equation will be given on the modeling section). This resistance will be used all along the report as an important property of carbon nanotubes.

However, the AC properties of a carbon nanotube are not well understood yet. We still don't know if such as in DC, the impedance is based on the CNT conductance e^2/h. Moreover, according to the configuration of the CNT and the environment surrounding it (dielectric, ground plane, etc), the behavior will be modified. Hence, in this work, we will focus on one configuration, which is a carbon nanotube above a ground plane. In RF, we will generally

meet this case if we are working on passive components as the ones described in this report: interconnections, antennas, filter, etc.

2. Carbon nanotube modeling for high frequency electronics applications

This section is divided into two parts. The first part deals with the analytical model of carbon nanotube nanotubes in DC and RF. We will explain how from analytical model of CNT, we developed circuit model that can be integrated to classical software such as ADS. Such model will be helpful and efficient for CNT based RF component designs. The second part will explain how we managed to model CNT and bundle of CNTs in 3-D EM simulator software for high frequency applications. An equivalent 3D bulk material was considered in this case, for modeling bundle of CNTs in 3D EM simulation with shorter computing times and lesser CPU resources.

A. Analytical modeling of carbon nanotube for DC

In the first part, we will describe the DC modeling of SW and MW carbon nanotubes. In DC, we will model a carbon nanotube (SW and MW) only by an electrical resistance. More precisely, three resistances in series compose the total resistance: the contact resistance R_C, the quantum resistance R_Q and the distributed nanotube resistance R_{CNT}. Indeed, we can consider a CNT as a metal wire with a contact resistance at each extremities and a distributed resistance along the wire. However, an extra resistance R_Q will appear due to the quantization of the conduction in CNTs as we already explained in section “Electrical properties on page (25)”. More details will be given later in this part. Below, we are presented a carbon nanotube and its DC circuit schematic (Figure 29).

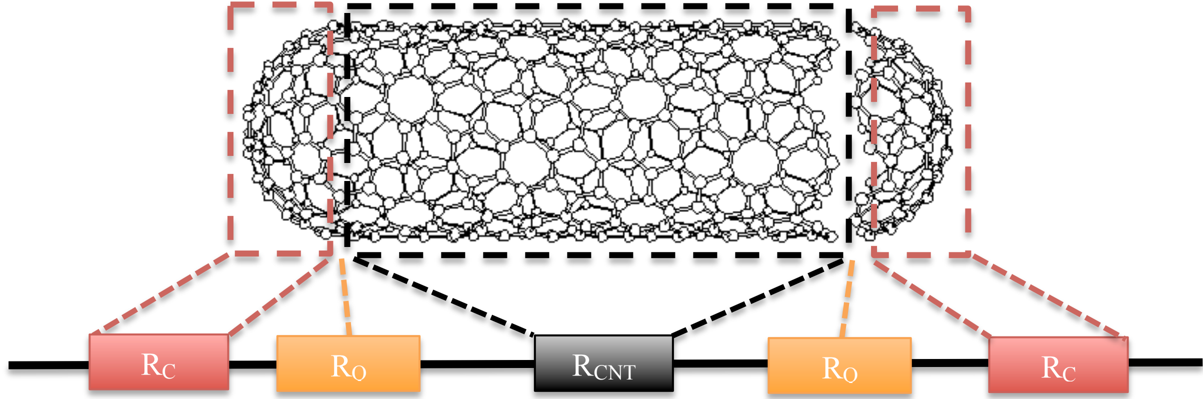

Figure 29: Schematic circuit of a carbon nanotube model in DC.

a) Contact resistance R_C

First, R_C is the contact resistance between the materials (metal, dielectric, polymer, etc) in contact with the carbon nanotube. In this work, most of the time, the contact will appear to be between a metal layer and a carbon nanotube. Many works have been done on that last case in order to determine the value of the contact resistance [58-63]. What we had observed from the other group works, but also from our own works and experiences (shown in the next part), was the contact resistance was strongly dependents to the contact surface and the diameter of the carbon nanotube (SW or MW). Generally, R_C values between 10 and 200 kΩ have been found in literature [34, 60, 64]. But it also appeared that CNT-metal contact reaches the MΩ on some cases.

The main reason of the high resistance between the metal and the CNTs is the weak distributed coupling existing between the two layers. Indeed, on many cases, this contact appears to be from the tips of CNTs and the material. As we can see on Figure 29, the surface in contact at the CNT extremity is small, and the electrons will need a large amount of energy to get access into a 1-D carbon structure such CNT from a 3-D bulk material such as metal. For example, a SWCNT with a diameter of 1 nm would approximately have a surface in contact equal to 3.14 nm^2. The consequence is the emergence of a high quantum resistance in carbon nanotubes (6.4 kΩ, calculated in the next paragraph), but also an important contact resistance R_C. The contact resistance in this configuration has been largely studied so far, and high values from 10 to 50 kΩ have been found when the CNT is grown directly on metal surfaces [63, 64]. In this paper, [65], R_C resistances range between 5 and 30 kΩ for SWCNTs alone and bundle of SWCNTs disposed in a gap between two metallic electrodes.

Mainly two parameters, the CNT diameter and the CNT contact length, lead the contact resistance (Figure 30). Obviously, more the diameter or the contact length will be important, lower is the contact between the metal and the CNT (the contact resistance is inversely proportional to the contact surface). A third parameter leading the contact resistance value can be the catalyst material and its thickness if the CNTs have been grown by CVD methods.

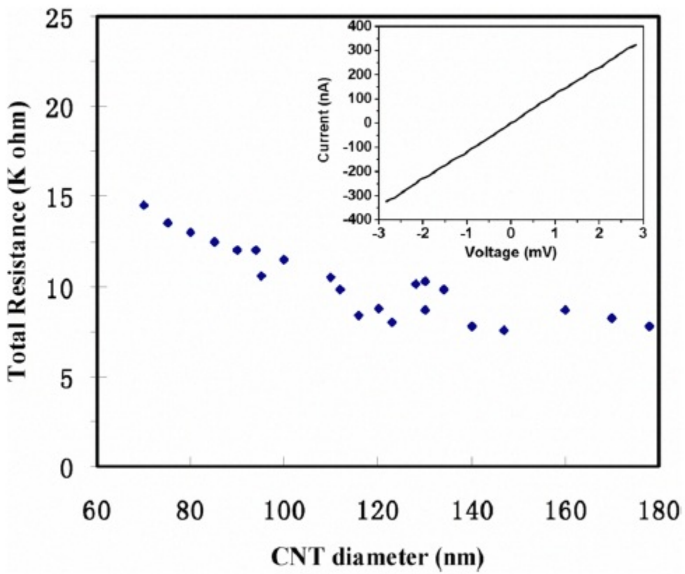

Figure 30: Contact resistance Rc in function of the CNT diameter. Source: [63, 66]

Finally, the choice of metal connected (such as copper, gold, etc of an electrode) to the CNTs is an important issue. Indeed, according to the metal electrical properties and its conductivity, contact between carbon nanotubes and metal will be modified [39].

In the next part, we will detail the quantum resistance properties existing in CNTs [14].

b) Quantum resistance R_Q

As we already explained in the section "Electrical properties on page (25)", the electron propagation is quantized in CNTs, meaning we have only a limited number of discrete conducting channels for the electron conduction. Thus, "quantum" effects appear, such as the quantum resistance, because each conducting channels are able to accept the entrance of one electron at the time. R_Q thus comes from this particular physics existing in

such 1-D structures such as the carbon nanotube. Indeed, as we already explained in the section “Electron transport: Ballistic conduction versus Diffusive on page (25)”, the electron adopts an anisotropic ballistic transport along the nanotubes. For ballistic transport, the Landauer formula gives the relation between the current I and the voltage V, and so the conductance of a quantum wire G_0=I/V=1/R_Q such as a carbon nanotube. As long as the length of the carbon nanotube is below the mean free path length (approximately 1 μm in SWCNTs, 25 μm in MWCNTs), we will have only a lumped quantum resistance existing at each contact of the carbon nanotube. Indeed, no additional scatterings than the ones presented in chapter 1 section “Mean free path in CNTs (MFP) on page (26)” will affect the electron propagation along the carbon nanotube. The R_Q equation (9) is:

$$R_Q = \frac{h}{N_{spin} \times N_{i-channel} \times e^2} = 6.45\ k\Omega \quad \text{in the case of SWCNT} \qquad (9)$$

with h the Planck’s constant; e the elementary electron charge; N_{spin} the number of electron spin for the CNT channel; $N_{i\text{-channel}}$ the number of channel in the selected shell (see section “Number of conducting channels in MWCNTs on page (21)”).

In a SWCNT, as already explained, we have only two spin channels and two additional channels of conduction. Thus, we can easily solve the equation (9) and find a value of R_Q=6.45 kΩ per SWCNTs. This value is quite high and explains why most of time, the CNTs are arranged in a bundle to be used for passive electronics components. Indeed, we have to consider the high CNT quantum resistance with the area occupied by a large number of CNTs. With a maximum SWCNT diameter of few nanometers (10 nm exactly), bundle of SWCNTs would have a resistivity much more smaller if we aggregate them in a bundle form to create an equivalent bulk material. As we can observe on the equation (9), the quantum resistance doesn’t depend on its geometry in contrast with bulk materials where the well-known electrical resistance formula $R=(\rho L/W^2)$ (see Figure 13) is applied (ρ the material resistivity, L the material length and W the material section). This CNT bundle resistance is the key where carbon nanotubes become interesting for low scale electronics components. Indeed, a bundle of CNTs is compatible with the nano/micro-scales and is able to outperform the metal electrical properties.

In the case of MWCNTs, as we already explained in section “Number of conducting channels in MWCNTs on page (21)”, we have calculated the number of conducting channel

for each MWCNT shell (equation (5)). Thus, to get the value of R_Q for a MWCNT, we have to sum up all the channels existing in it, we will obtain $N_{channels/MWCNT}$ (equation (10)). As a reminder, p was calculated with equation (3). Finally, we will be able to calculate the value of R_Q, regarding all the conducting channels existing in the MWCNT.

$$N_{channels/MWCNT} = \sum_{i=1}^{p} N_{i-channels/shell} \quad (10)$$

For example, a 10 nm diameter MWCNT has 8 shells. Hence, a rapid calculation (using equation 3, 4, 5, 10 and 11) will return a value for R_Q equal to 1.6 kΩ, which is below the quantum resistance of a SWCNT. In this work, we will prefer to use the MWCNT instead of the SWCNTs for their lower resistance and also because they are always metallic.

$$R_{Q-MWCNT} = \frac{h}{N_{spin} \times N_{channel/MWCNT} \times e^2} = \frac{h}{2 \times N_{channel/MWCNT} \times e^2} < 6.45\ k\Omega \quad (11)$$

c) Carbon nanotube resistance R_{CNT}

The last DC component composing the CNT resistance is the distributed resistance RCNT along the tube. This resistance only appears if the length of the CNTs is greater than its mean free path (approximately 1 µm in SWCNTs, 25 µm in MWCNTs as explained in section "Mean free path in CNTs (MFP) [20, 21] on page 26"). The electron losses its ballistic propagation properties and adopts a combination of ballistic/diffusive conduction. Thus, an additional resistance R_{CNT}, which depends of the tube length, must be considered. This resistance has been confirmed by measurements [67, 68]. The R_{CNT} equation ((12) and (13)) is defined as follow:

$$R_{CNT-SWCNT}(l > MFP) = R_Q \times \frac{l}{MFP} \quad (12)$$

$$R_{CNT-MWCNT}(l > MFP) = R_{Q-MWCNT} \times \frac{l}{MFP} \quad (13)$$

with l the CNT length and MFP the CNT mean free path. Typically, for a 20-µm-long SWCNT, using the equation (12), we find R_{CNT} = 129 kΩ. From the equation ((12) and (13)), we understand why the purity of the CNT structure can play an important role in the electrical transmission. A CNT with few defects will decrease the MFP and so increase its distributed resistance R_{CNT}.

As said in this PhD work, we considered MWCNT bundle. So, in the case of MWCNT bundle, to calculate the total resistance, we divide the total CNT resistance $R_{Bundle} = 2R_C + 2R_Q + R_{CNT}$ by the number of CNTs (n_{MWCNT}). That's suppose all CNTs are identical with the same electrical/structural properties.

$$R_{Bundle-MWCNT} = \frac{2R_C+2R_Q+R_{CNT-MWCNT}}{n_{MWCNT}} \quad (14)$$

B. Analytical modeling of carbon nanotube for RF

a) Modeling of a single-wall carbon nanotube (SWCNT)

In this part, we will present the carbon nanotube model for high frequency. Based on past works done by P.J. Burke [69] using Luttinger liquid theory as a model of the gigahertz electrical properties of carbon nanotubes, the carbon nanotube wave propagation in high frequency can be modeled by a single tube above a ground plane, equivalent to the metallic part of a microstrip line. Thus, a transmission line, derived from the Telegrapher's Equations based on Maxwell's equations, is used to model carbon nanotube wave propagation in high frequency. In this case, the circuit model describing the electrical behavior of the test structure is presented in Figure 31. This RLC circuit (representative of a transmission line model) is composed by 1 lumped component (R_Q presented previously) and 5 distributed components [11, 69, 70]:

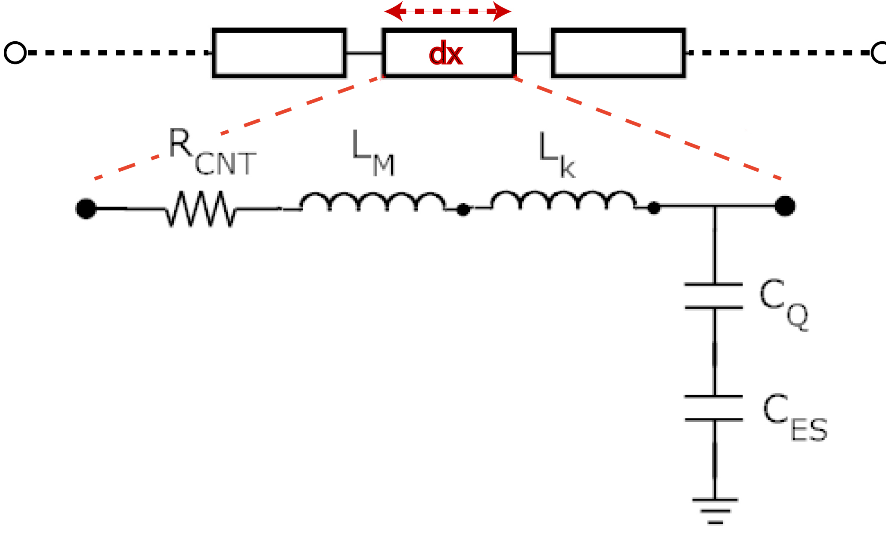

Figure 31: Transmission line model of a single-wall carbon nanotube in parallel above a ground plane. The model is composed by distributed RLC components.

The magnetic inductance L_M and the electrostatic capacitance C_{ES} can be found from the classical electromagnetic models. Indeed, from Maxwell's equations, we know that an alternative voltage/current will generate magnetic and electric fields along a conducting material. By calculating the EM field, we will be able to extract the distributed inductance and capacitance along the conductor. Since a carbon nanotube is a cylinder shape with a finite diameter, the value of its magnetic inductance and electrostatic capacitance can be determined by the equation (15) and (16) [71, 72]:

$$L_M = \frac{\mu_0 l}{2\pi} arcosh\left(\frac{d}{a}\right) = \frac{\mu_0 l}{2\pi} \ln\left(\frac{d}{a} + \sqrt{\frac{d^2}{a^2} - 1}\right) \tag{15}$$

$$C_{ES} = \frac{2\pi\varepsilon_0 l}{arcosh\left(\frac{d}{a}\right)} = \frac{2\pi\varepsilon_0 l}{ln\left(\frac{d}{a} + \sqrt{\frac{d^2}{a^2} - 1}\right)} \tag{16}$$

with a the CNT radius, d the distance between the CNT (d > a) and the ground plane, l the CNT length, ε_0 the vacuum permittivity and μ_0 the vacuum permeability. These two components depend mostly on the conductor geometry. The electrostatic capacitance C_{ES} will depends on the geometry of the CNT or the whole bundle of CNTs as we will confirm later.

Next to the magnetic inductance and electrostatic capacitance, we have the distributed CNT resistance R_{CNT} and the lumped "quantum" resistance R_Q. We already detailed the equations of these components on the DC model section. The equations of R_{CNT} and R_Q remain the same and can be used in our model for high frequency. Indeed, the physical resistance of the CNTs remains the same in RF since we still have the same number of conducting channels in CNTs in RF.

Finally, we end up the model by 2 unusual distributed components: the kinetic inductance L_k and the quantum capacitance C_Q [69, 73-76]. As we have already said, conduction in carbon nanotubes is quantized because CNT is a 1-D conductor structure with a limited number of conduction channels. The second consequence is the density of state is low in carbon nanotubes, and an electron needs a high level of energy in order to occupy a quantum energy state only available above the Fermi level. Thus, first, the quantum capacitance C_Q models the extra charge required for the electron to reach that energy level in carbon nanotube. The equation of the quantum capacitance for one channel of conduction is shown on (17) [69, 74]. In the presence of one SWCNT or a few numbers of CNTs, the

quantum capacitance C_Q becomes significant in the model. However, in a bundle of hundreds and more CNTs, C_Q will be negligible compared to the electrostatic capacitance C_{ES} that will directly depends on the bundle geometry (see equation (16)). Later in this part, we will study that difference with electromagnetic modeling.

$$C_{Q/channel} = \frac{1}{2}e^2 D(\mu) = \frac{2e^2}{\pi\hbar v_F} = \frac{4e^2}{hv_F} \approx 193\ aF/\mu m \quad (17)$$

with h the Planck's constant; e the elementary electron charge; v_F the Fermi's velocity (9.10^5 m/s) and D(μ) the density of states at the Fermi energy of metallic CNTs $D(\mu) = 4/\pi\hbar v_F$.

Secondly, following the same approach as the quantum capacitance for modeling the effect of the electron moving through a 1-D conductor, we need to add extra kinetic energy to reach the available quantum energy states. Thus, the kinetic inductance models this effect and the equation is shown below (18) [69, 74].

$$L_{K/channel} = \frac{h}{4e^2 v_F} = 8\ nH/\mu m \quad (18)$$

The same observations can be applied for the kinetic inductance. Since the kinetic inductance of a CNT directly depends on the number of conducting channel, hence the total kinetic inductance will goes down with the increase of the number of CNT in a bundle or the increase of shells in a MWCNT. For small CNTs diameter, the magnetic inductance will become negligible compared to the kinetic inductance.

Thus, the transmission line model presented here will be the base of all the carbon-nanotube based device models for high frequency that will be exposed later in this report.

b) Modeling of multi-wall carbon nanotube (MWCNT)

To model a MWCNT composed by a defined number of shell, two cases can exist:

First, only the outer shell is in contact with another material such as a metallic electrode for example. Van der Waals distance separates the inner MWCNT shells and low coupling can be considered. In this case, the MWCNT can be modeled in high frequency as a single transmission line with the corresponding calculated components according to the MWCNT outer shell dimensions (diameter and length). Inner shells (more resistive than the outer one) will affect the electric conduction. In the second case, we consider the coupling

between MWCNT shells not negligible. Thus, on the MWCNT circuit modeling, shells are connected at the MWCNT extremities and the MWCNT can be modeled by the schematic presented on Figure 32 [11].

As you can see on the Figure 32, the schematic is based on the transmission line schematic presented previously. Thus, each shell composing the MWCNT will be modeled by one transmission line. Because each shell has a different diameter, the value of each component will be different. Moreover, as we already seen, according to the diameter of the shell, the number of conducting channel varies. The number of conducting channel need to be calculated and takes into account in the schematic. Finally, three “coupling” effects (mutual inductance, coupling capacitance and tunneling resistance) between close shells exist and can be calculated by the equations (19), (20) and (21). We have to consider a capacitance C_S, a conductance G and a mutual inductance M_{shell} between two adjacent shells.

$$C_S = \frac{2\pi\varepsilon_0}{\ln\left(\frac{D_i}{D_i - 2\times space}\right)} \times l \qquad (19)$$

$$G = \frac{1}{\sigma\pi D_i \times l} \qquad (20)$$

$$M_{shell} = \frac{\mu_0}{2\pi}\left(ln\frac{4l}{D_{i+1}} - 1 + \frac{D_{i+1}+D_i}{\pi l}\right) \qquad (21)$$

with σ is the tunneling conductivity ranging between σ=0 and 0.3 $(\mu\Omega.cm^{-2})^{-1}$ [11], ε_0 the vacuum permittivity, μ_0 is the vacuum permeability, l is the CNT shell length, D_{i+1} and D_i are the diameters of the outer and inner shells, d is the distance between two adjacent shells (0.34 nm).

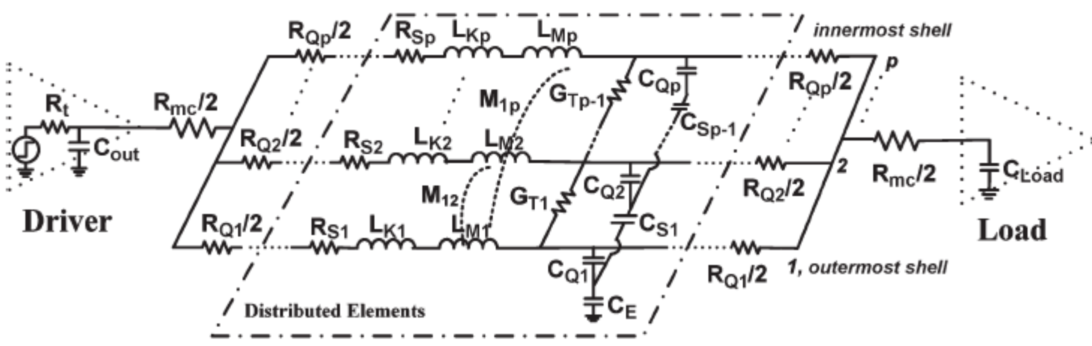

Figure 32: MWCNT circuit model based on RLC transmission line models. Additional coupling effects between MWCNT shells are considered. R_C=R_{mc} represents the contact resistance between the MWCNT and the material in contact. Source: [11]

c) Modeling of a bundle of CNTs

In this PhD work, most of the time, we will consider the carbon nanotubes in a bundle arrangement. In order to simplify the modeling of a bundle of SWCNTs or MWCNTs, we consider that all carbon nanotubes in the bundle have uniform length and diameter. In real case, this will never happen with the current fabrication technologies. However, as we have seen on the section "Chemical vapor deposition (CVD) on page (34)", a CVD and PECVD process returns a quasi-homogenous bundle of CNTs. As we can see on the SEM picture on Figure 33, the length and the spacing between carbon nanotubes can be considered uniform as first approximation and the error in simulation will be small enough to be considered acceptable.

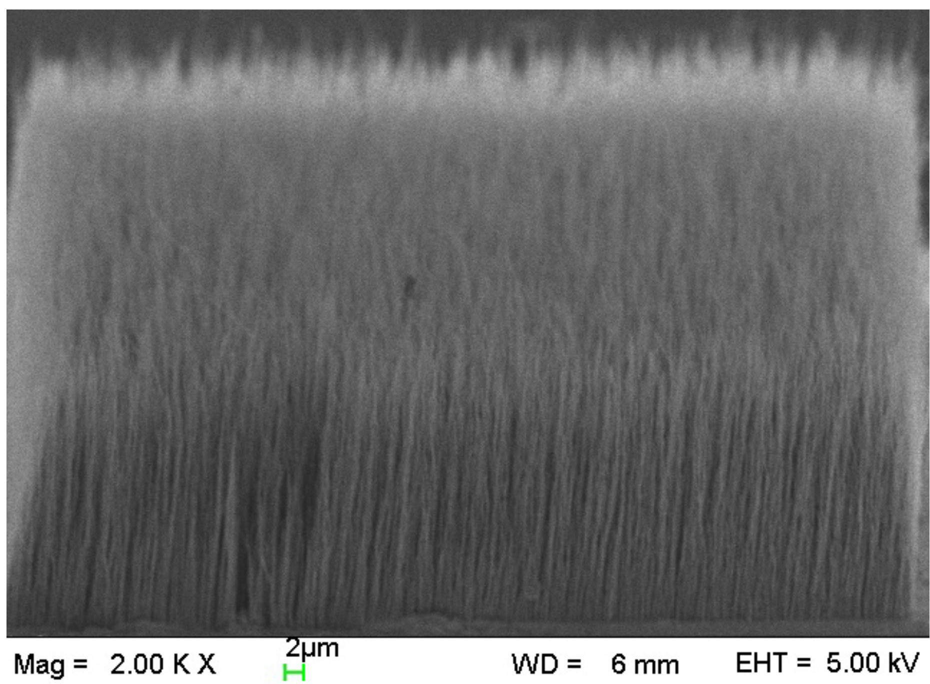

Figure 33: MWCNT bundle grown by PECVD process at CINTRA. CNTs appear to be quite uniform in term of length and diameter.

To calculate the value of each component, we meet two cases: for the components in parallels in the transmission line circuit such as the resistances and inductances, we divide their value by the number of CNTs. In contrast, components in parallels such as the capacitances, we multiply their value by the corresponding number of CNTs in the bundle (N_{CNT} or N_C). In the case of a bundle of SWCNT, $N_{i\text{-channel}}$ is two (because we have two conducting channels in SWCNTs). In the case of a bundle of MWCNTs, the total number of conducting channel for each MWCNT needs to be used, we so have $N_{i\text{-channel}}$=$N_{channel/MWCNT}$ (see equation 10). In this second case, the coupling effects between shells (mutual inductance,

tunneling resistance and coupling capacitance) are not considered in order to simplify the model. Indeed, it has been shown that the coupling effects between shells are negligible. [77-79]. This calculation is based on the equations from (9) to (18) presented previously.

$$R_{Q-bundle} = \frac{h}{2e^2} \times \frac{1}{N_{i-channel} \times N_{CNT}} \quad (22)$$

$$R_{CNT-bundle} = R_{Q-bundle} \times \frac{l}{MFP} = \frac{h}{2e^2} \times \frac{1}{N_{i-channel} \times N_{CNT}} \times \frac{l}{MFP} \quad (23)$$

$$L_{k-bundle} = \frac{h}{2v_F} \times l \times \frac{1}{N_{i-channel} \times N_{CNT}} \quad (24)$$

$$C_{Q-bundle} = \frac{2e^2}{hv_F} \times l \times N_{i-channel} \times N_{CNT} \ (or\ N_C\ within\ the\ bundle\ configuration) \quad (25)$$

$$C_{ES-bundle} = \frac{2\pi\varepsilon_0}{ln(\frac{d}{a}+\sqrt{\frac{d^2}{a^2}-1})} \times l \times N_C \quad (26)$$

To calculate the number of CNTs in a bundle, we use the following equation [80]:

$$N_{CNT} = n_F \times n_G \times (\frac{d_{bundle}}{d_{CNT}})^2 \quad (27)$$

n_F represents the filling factor of the original bundle shape and ranges between 0 and 1. For example, a circular shape bundle will have a fill factor n_F equal to 0.9 since the whole edge of the circle cannot fit with the edge of the carbon nanotubes. n_G represents the CNT density factor. To obtain n_G, we need to divide the space area occupied by a defined number of CNTs (using the surface of the CNTs) by the total area. n_G also ranges between 0 and 1. Finally, d_{bundle} is the bundle diameter and d_{CNT} the average carbon nanotube diameter in the bundle.

For example, a 10-µm circular bundle with 10 nm CNT diameter, a filling factor of n_f=0.9 and a density factor n_G=0.001 is composed by 900 CNTs. Thus, a 200-µm-bundle diameter with the same type of CNTs will be composed by 360000 CNTs.

Another example will be a 150-µm square bundle composed by 100 nm MWCNTs diameter. We found 6 CNTs in a square of 1 µm. We keep n_F=0.9 and we will obtain $n_G=(6x100e\text{-}9^2)/(1e\text{-}6)^2$ =0.06. Thus, we can estimate 121500 MWCNTs in the square bundle.

Among the total number of CNTs inside the bundle, we can also estimate the number of circumferential CNTs (named N_C) located at the edge of the bundle by the equations (28) for a circular bundle and (29) for a square one:

$$N_{C-circular} = \frac{\pi(d-d_{CNT})}{d_{CNT}} \quad (28)$$

$$N_{C-square} = \frac{4(c-d_{CNT})}{d_{CNT}} \quad (29)$$

with d the bundle diameter, c the side dimension of the square bundle and d_{CNT} the CNT diameter.

d) Application and determination of the CNT parameters by experiments (work with Chow Wai Leong)

With the PhD student Chow Wai Leong working under the professor Tay Beng Kang in NTU, we decided to fabricate a simple RF structure with bundle of double-wall CNTs (DWCNTs) and characterize it from DC up to 40 GHz. Chow Wai Leong had fabricated the entire structure presented in this part. The results obtained will be compared with other similar experiments and to our analytical model presented in the last paragraph. Data such as the contact resistance R_C and the CNT resistance R_{CNT} from the measurements will be extracted. Thus, we will be able to confirm the analytical model we derived previously to the measurements in high frequency. Regarding the RF structure, we have synthesized ultra-dense horizontally aligned carbon nanotubes (HACNTs) film and fabricated coplanar waveguide ground-signal-ground (CPW GSG) structures on the film to allow a systematic RF characterization in the gigahertz regime where the length and number of CNTs in each device can be predetermined. Our results have indicated that the CNTs are mainly resistive, making it an ideal candidate for interconnect application.

i. Fabrication of the structure and CNT growth

The process flow from the synthesis of ultra-dense HACNTs film to the fabrication of CPW GSG structures is illustrated in Figure 34. High resistivity silicon wafer (> 10 kΩ) coated with 655 nm thermal oxide was used as substrate. Standard lithography process was used to define windows for an array of lines, 5 µm wide and 1 cm long, for the deposition of 1 nm Fe catalyst and 10 nm Al_2O_3 barrier layer. The growth of vertically aligned CNTs lines

array was carried out using AIXTRON 2-inch Black Magic PECVD system at growth temperature of 625 °C with 150 sccm of C_2H_2 as carbon feedstock under low vacuum pressure of 10 mbar for 10 minutes. The CNTs lines array was then planarized by pouring isopropanol alcohol (IPA) over the samples at 90° angle, carefully withdrawing it from the liquid and dried by N_2 gun at room temperature and atmosphere pressure. A second lithography step was used to define regions where O_2 plasma (O_2 = 20 sccm, RF power = 30 W, time= 180 s) was used to etch off the unwanted CNTs, leaving behind well-defined CNTs films of various sizes. The last lithography step was used to define the metallization in the form of CPW GSG structures with electron beam deposition of 1 µm Au and 100 nm Ti.

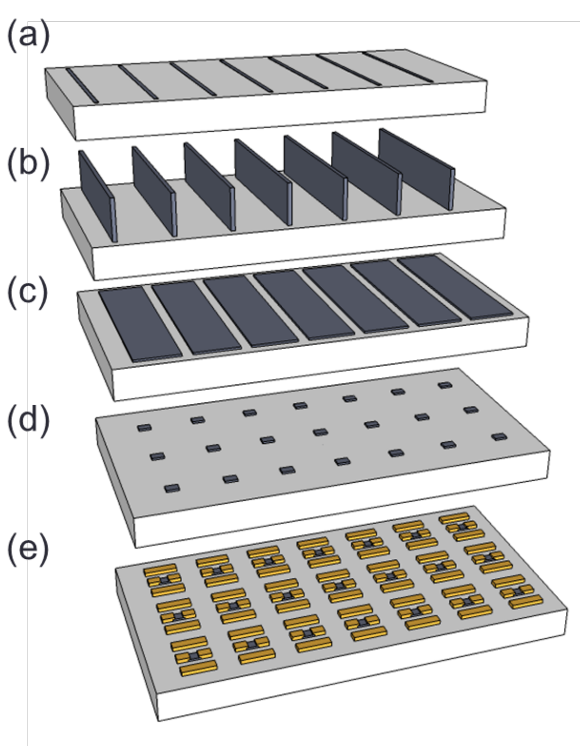

Figure 34: Schematic illustrating the process flow from the synthesis of CNTs to the fabricated CPW GSG structures. (a) Patterned deposition of catalyst and barrier layer line array. (b) Growth of VACNTs line array by TCVD process. (c) Realization of ultra-dense HACNTs film by planarization using IPA. (d) Patterning of ultra-dense HACNTs film by O_2 plasma etching. (e) Patterned metallization for final CPW GSG structures.

The carbon nanotubes Ultra-dense HACNTs films with different lengths (10, 20 and 50 µm) and widths (20, 50 and 70 µm) were hence well patterned and then contacted by metallization in the form of CPW GSG structure as shown in Figure 35. The length of HACNTs film can be referred to be the size of the signal electrode gap. Here, we used 10, 20 and 50 µm.

The samples were then observed by SEM (Figure 35) and characterize in DC and HF. For the HF measurement, vector network analyzer (VNA, Agilent HP 8510C) with 150-µm pitch Cascade Microtech Infinity probes were used. The samples were measured from 6 to 40 GHz at resolution of 0.2 GHz at room temperature without illumination. To ensure the accuracy of each measurement, a Thru-Reflect-Line (TRL) calibration process was done with maximum error of 0.1 dB.

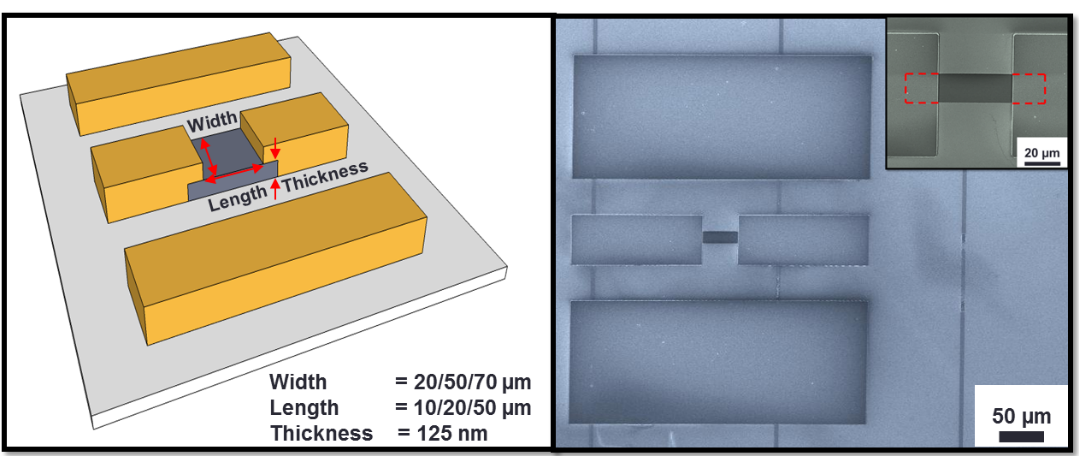

Figure 35: (a) Schematic of CPW GSG structure with 125 nm thick HACNTs film with variation in length and width. (b) Typical SEM image of CPW GSG structure with 20-µm HACNTs film width, inset shows that overlap between metal-to-CNTs is well defined.

ii. DC characterization and resistance extractions

The DC measurement has been used (Figure 36) to extract the value of the contact resistance R_C between the nanotube and the metal (gold here) and the distributed carbon nanotube resistance R_{CNT}. In this study, R_Q will be included in R_C. Indeed, even if the contact between the metal and the CNTs is optimized and become negligible (R_C=0), because the electron conduction is diffusive in metal and quantized in CNTs (as explained in section “Electrical properties on page (25)”), the quantum resistance will exist at the interfaces metal/CNT.

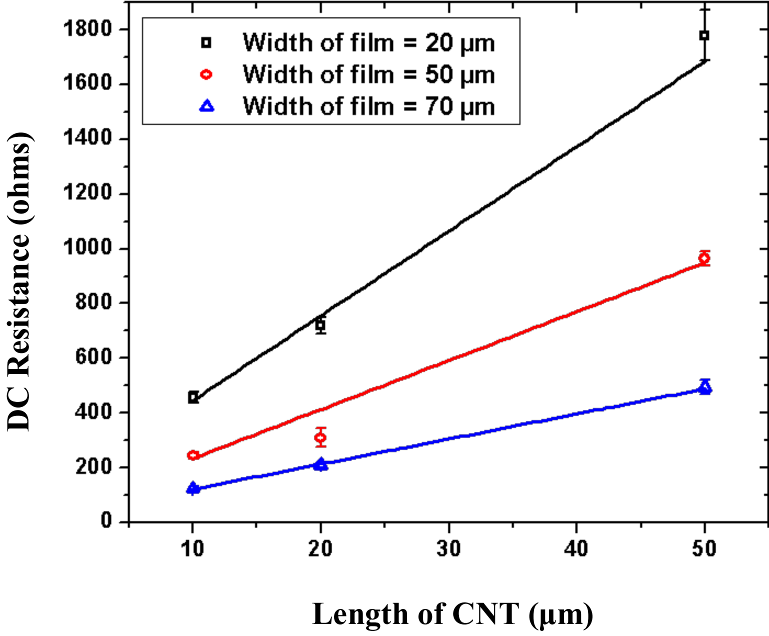

Figure 36: DC resistance vs. length of CNTs for three different widths of HACNTs film.

Three to ten devices of each specific structure were characterized and their average DC resistances with standard error bar are shown in Figure 36 above. As we can see, linear curves are obtained for the DC CNT resistance. That does allow us to extract for each sample the contact resistance R_C and the distributed CNT resistance R_{CNT}. Their DC resistances are as follow:

$$R_{DC} = R_C(total) + R_{CNT}(total)/\mu m \times L_{CNT} \tag{30}$$

$$R_{DC}(20\ \mu m\ width) = 136.7\ \Omega + (30.9\ \Omega)/\mu m\ \times L_{CNT} \tag{31}$$

$$R_{DC}(50\ \mu m\ width) = 50.7\ \Omega + (17.9\ \Omega)/\mu m\ \times L_{CNT} \tag{32}$$

$$R_{DC}(70\ \mu m\ width) = 29.8\ \Omega + (9.2\ \Omega)/\mu m\ \times L_{CNT} \tag{33}$$

The DC resistance consists of both the contact resistance between metal-to-HACNTs film and the resistance of the HACNTs film. The contact resistance varies from 29.8 Ω to 136.7 Ω and the HACNTs film resistance varies from 9.2 Ω/µm to 30.9 Ω/µm depending on the number of CNTs between the signal electrode gaps. By estimating the number of CNTs in the bundle and assuming only the first layer of the HACNTs film is being in contact with the electrodes, it is possible to extract the contact resistance and CNT resistance for individual CNT. By linearly fitting the data, the contact resistance was found to be 174.81 ± 25.47

kΩ/CNT. Similarly, the resistance of a single CNT was found to be 43.98 ± 4.75 kΩ/µm that is much higher than the theoretical value (about 3.2 kΩ/µm for a DWCNT with 4 conducting channels, see equation (11)). Without possible observation of the contact between the CNTs and the electrodes, the estimated number of CNTs in contact with the electrodes can vary. This variation might imply some error in the resistance calculation. Thus, a higher number of connected CNTs would return a lower CNT resistance. This can also be due to the impurities existing in the carbon nanotubes we have fabricated. Indeed, as we explained in the chapter I section "Mean free path in CNTs (MFP) on page (26)", the MFP depends on the level of defects in CNTs. Thus, with higher defects, we obtain a higher CNT resistance.

iii. High frequency measurements and analytical model extraction

The second step of this work is to develop a coherent model according to the measurements done. The objectives by making CNT models are to improve our knowledge about CNT behavior in high frequency domain. In this case, CNTs are horizontally aligned on a silicon substrate so simulations must take into account this structure configuration. The model developed in our PhD work is based on analytical simulation with Advanced Design System (ADS) software from Agilent. As the measurements, the simulations will be conducted between 1 to 40 GHz with a 0.1 GHz step.

Gold coplanar waveguides models already exist in ADS and can be used in our simulation by setting the correct dimensions (Figure 37). Then, a contact resistance R_C in parallel with a contact capacitance C_C model the contact between bundle of CNT and metal as shown in Figure 38. The coupling capacitance C_C represents the coupling existing between the CNTs, which are not in direct contact with the gold electrode. Indeed, as already explained in the fabrication part, the bundle of CNTs has been grown first, next the gold electrodes have been deposited. Thus, we can expect a non-as good contact as direct growth of CNTs on metal. As suggested in this similar work [81], a coupling capacitance C_C also exists at the interface between the carbon nanotubes and the gold electrodes. As presented in measurements part, the contact resistances R_C were calculated for each sample. We used these values as starting points for our simulations. Then, the software allows a fast tunneling of each component value in order to fit with measurements.

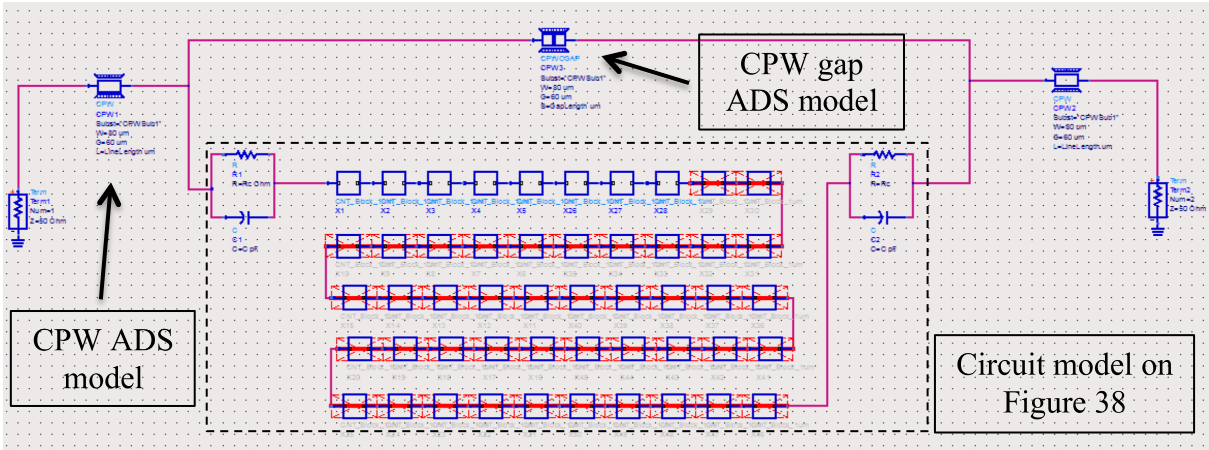

Figure 37: ADS schematic of the GSG structure presented in Figure 35 and composed by HACNTs. Each box models 1-µm length bundle of DWCNTs as detailed on Figure 38.

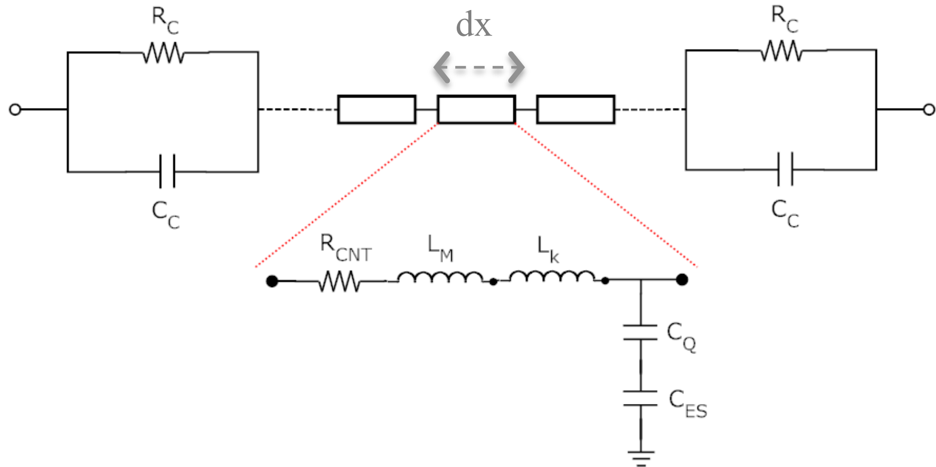

Figure 38: Circuit model of the bundle of CNT. A distributed RLC circuit with quantum components as the kinetic inductance L_k and the quantum capacitance C_Q compose this model. On both side, a contact resistance R_C in parallel with a contact capacitance C_C models the CNT/metal contacts.

The RLC circuit already presented in the previous part (see section "Modeling of a single-wall carbon nanotube (SWCNT) on page (62)" and Figure 31) is used to model carbon nanotube bundle. The contact resistance R_C and an average value of R_{CNT} were extracted from DC measurements previously (equations (31), (32) and (33)). These data are chosen as the starting point for our simulations and then will be tune in order to fit with measurements. All other components such as the magnetic inductance L_M, the electrostatic capacitance C_{ES}, the kinetic distributed inductance L_k and the quantum-distributed capacitance C_Q were already defined by the theoretical values (see equations (15), (16), (24) and (25)). The contact capacitance C_C has been optimized from its original value found in this similar work [81] in order to fit with the measurements. The magnetic inductance L_M is negligible compared to the

kinetic inductance L_k, because the ratio L_M / L_k is about 10^{-4} [69] in the case of a large amount of CNTs in the bundle (L_M was calculated using a distance d of 10 nm, see equation (15)). Finally, C_{ES} is the electromagnetic capacitance related to the capacitance effect between the nanotube and the ground lines. The capacitance C_{ES} was described by the equation (26). It is found that the number of CNT facing the ground plane is low, we found N_C = 100 using the equation (29) and c equal to the HACNT thickness (125 nm). Then, C_{ES} becomes insignificant compared to the quantum capacitance and can be neglected (see Table 8). The number of CNTs in the bundle divided each resistances and inductances while each capacitances were multiplied by this number assuming only the first layer of CNT film is being contacted by metallization. All other effects as phonon scattering and defects along the carbon nanotube are supposed negligible [82]. Moreover, coupling between CNTs is considered low because of the small surface facing other CNTs [75, 82].

Coplanar waveguides are modeled by using the existing models in Advanced Design System (ADS) of coplanar lines GSG and connected to the CNT bundle model presented above. Using the same ADS software, an analytical simulation of the entire device is conducted from 1 to 40 GHz and compare with the measurements. An additional coplanar GSG gap model is added in parallels to the CNT bundle model. No measured de-embedded CPWs have been used during the simulation because we consider the CPW losses quite low compared to the bundle of CNTs losses.

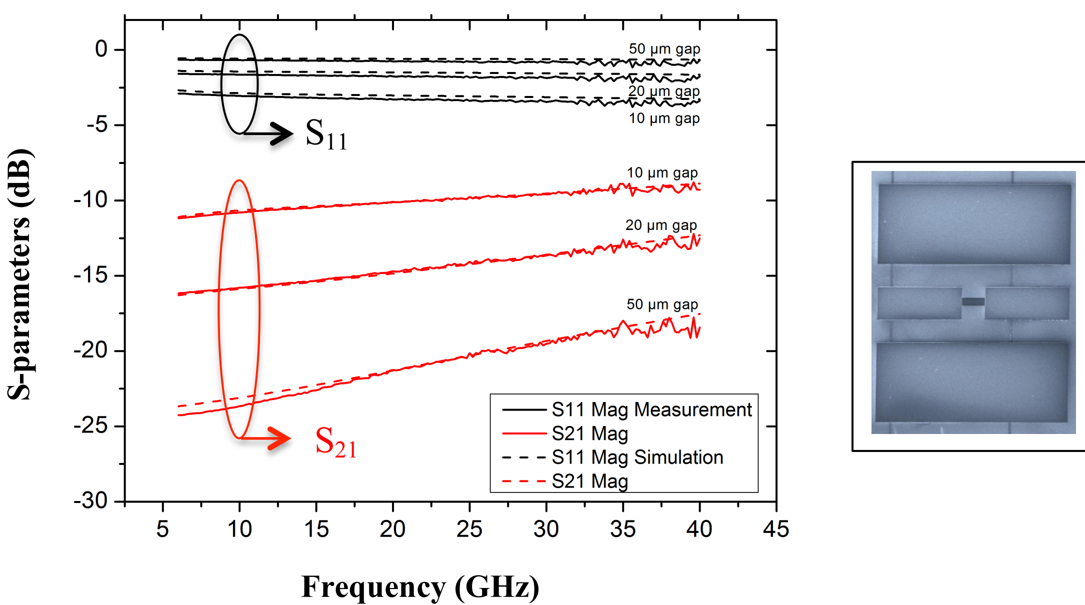

Figure 39: S parameters of HACNT structure (presented in Figure 35 and in the asset (top view)) for a 20-µm-width bundle of CNT. By increasing the gap between electrodes, S_{21} transmission is decreasing.

On Figure 39, S-parameters comparison of simulations with measurements is done for the 20-µm-width device after optimization of each circuit components. Values of each component are returned on the Table 8. S_{11} parameter represents the return loss at the device input while S_{21} is the high frequency insertion loss along the device. As we can see on Figure 39, simulations are consistent with measurements for all gaps. On the last row of this table, average values of each component for a random number of CNT (noted Y) are estimated. By using these values, we compare our results with a similar work done by Minghui Sun [81]. Results are reported on the Table 9 and show that again, our study is consistent with other work done before. Using MWCNTs (from 2 to 3-4 shells) than DWCNT in Minghui's works can make the small differences between the two works. By increasing the number of CNT in the bundle, the transmission is improved. However, with an important number of CNT, kinetic inductance becomes negligible and most of the device losses come from the CNT resistance itself. The quality of the CNT structure is an important point to focus in order to improve the CNT performance in high frequency.

In conclusion of this part, we have demonstrated that the circuit modeling of carbon nanotubes and CNT bundles are suitable for the high frequency applications we will develop on the next chapters. Using these analytic models, we can hence also easily extract some information regarding the CNT and CNT bundles behaviors (resistive, inductive or capacitive effect). However, all electromagnetic problems such as coupling between CNTs or coupling between CNTs and metal electrodes are not taken into account with such a circuit model. EM modeling or hybrid EM/analytical simulations would solve these issues, as we will see on the next parts.

Table 8 – Values of circuit components for each bundle of CNT width.

Width (µm)	**Estimated number of CNT**	**CNT resistance R_{CNT} (Ω/µm)**	**Magnetic inductance L_M (pH/µm)**	**Kinetic inductance L_k (pH/µm)**	**Quantum capacitance C_Q (µF/µm)**	**Electrostatic capacitance C_{ES} (fF/µm)**	**Contact resistance R_C (Ω)**	**Contact capacitance C_C (fF)**
20	1380	30.8	3.10^{-4}	1.45	107	5.10^{-4}	136.7	724.0
50	3450	13.3	$1.2.10^{-4}$	0.58	266		50.70	986.0
70	4830	8.57	$0.8.10^{-4}$	0.41	373		29.90	2029
Average value for Y CNT	Y	$\frac{43.6.10^3}{Y}$	$\frac{0.42}{Y}$	$\frac{2000}{Y}$	$0.077\times Y$	$5.10^{-6}\times Y$	$\frac{169.3\times10^3}{Y}$	$0.408\times Y$

Table 9 – Comparison of circuit components values obtained by our previous extracted values and Minghui gap's work. The device is a 20-µm gap coplanar waveguides working up to 40 GHz.

	Number of CNT	Contact resistance (Ω)	CNT resistance (kΩ with 20 µm gap)	Contact capacitance (fF)
Our work	332.5 ± 87	509 ± 181	2.62 ± 0.93	136 ± 36
Minghui Sun work		375	1.77	228

C. Electromagnetic (EM) modeling of carbon nanotube for RF

In this section, we will present the second part of our CNT modeling works. As we have studied earlier, we have developed an analytical model for CNTs (SW or MW) but also for bundle of CNTs. However, most of the time, the RF structures are modeled in 3-D with specialized software such as HFSS, Comsol or CST. In our case, only HFSS and the homemade EMXD software developed at Xlim will be employed using the finite element method to resolve 3-D electromagnetic problems. Thus, by using 3-D models of CNTs for RF, we can have a better integration of this carbon nanotube material in our devices, access to a better study or our problems and get more information on their behaviors in RF.

a) SWCNT modeling

In this part, we will present the carbon nanotube full electromagnetic model for high frequency. Based on G.W. Hanson's works [83], derived from the Boltzmann equation reduced to a 1-D system, an armchair SWCNT (always conductive) can be modeled by a tube with a radius 'a' and an infinitely thin wall provided with a surface conductivity given by the equation (34). It includes the quantum effects described previously, and can be applied from the GHz frequency range up to the beginning of THz range. The SWCNT surface impedance is a complex function with frequency dependence:

$$\sigma_{zz\ SWCNT}(\omega) \cong -j\frac{2e^2 v_F}{\pi^2 \hbar a(\omega - j\nu)} \tag{34}$$

With a the CNT radius, ħ the reduced Planck's constant ($1.06.10^{-34}$ $m^2.kg/s$), e the elementary charge, v_F the Fermi's velocity ($9.71.10^5$ m/s), $\nu = 1/\tau$ the plasmon relaxation time ($(3x10^{-12})^{-1}$ Hz) and w the pulsation.

This electrical conductivity can be applied only for radius below 3.4 nm. The electrical current propagates along the tube surface only in the CNT direction (here along the z axis). As it is shown in Figure 40, we consider a SWCNT with a finite radius a and a variable length L. The carbon nanotube is placed in parallel above a ground plane with a distance of h'. In these conditions, this test structure is considered as a transmission line structure.

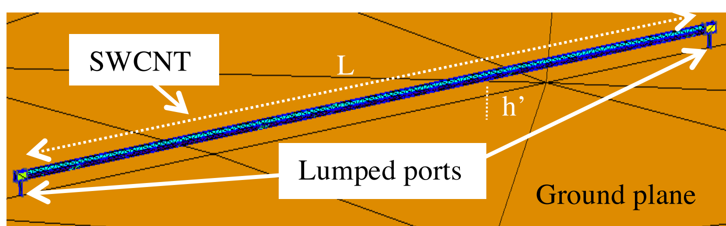

Figure 40: Carbon nanotube in a transmission line configuration. L is the CNT length and h' the distance between the SWCNT and the ground plane. The SWCNT is considered with a circular shape.

Electromagnetic simulations are done using the electromagnetic software EMXD developed by Mr Aubourg at XLIM or HFSS software by Ansoft. Both are based on the finite element method (FEM). The definition of the SWCNT surface impedance (equation (35)) was introduced in the software. The Maxwell's equations are solved in the frequency domain in order to define the S-parameters of the test structure. Besides, we consider lumped ports at the structure input/output. The characteristic impedance of the lumped ports is equal to 50 Ω in order to determine the resonances of the SWCNT and consequently improve the sensitivity on

the simulated S-parameters. These resonances will be able to confirm the behavior of SWCNTs in the hyper frequencies.

In EMXD and HFSS (v15 and above only), only complex impedance can be given instead of an electrical conductivity. This conductivity is applied on the CNT surface as an impedance boundary. Thus, a simple conversion can be done and give us the equation (35):

$$Z_{zz\ SWCNT}(\omega) = \frac{1}{\sigma_{zz\ SWCNT}(\omega)} = \frac{\pi^2 \hbar a}{2e^2 v_F}(\nu + j\omega) \quad (35)$$

Next, a thin comparison between circuit and EM models permits to highlight CNT interaction effects exciting around CNT environment. The two SWCNT lengths 10 and 20 µm are simulated. These circuit and EM models are in good agreement as shown in figure 40. The resonances which appear are λ/2 resonances due to the Fermi's velocity $v_F = (f \times L)/2 = 9.7 \times 10^5\ m/s$ with f the frequency and L the SWCNT length. These first tests permit to validate our EM/circuit models.

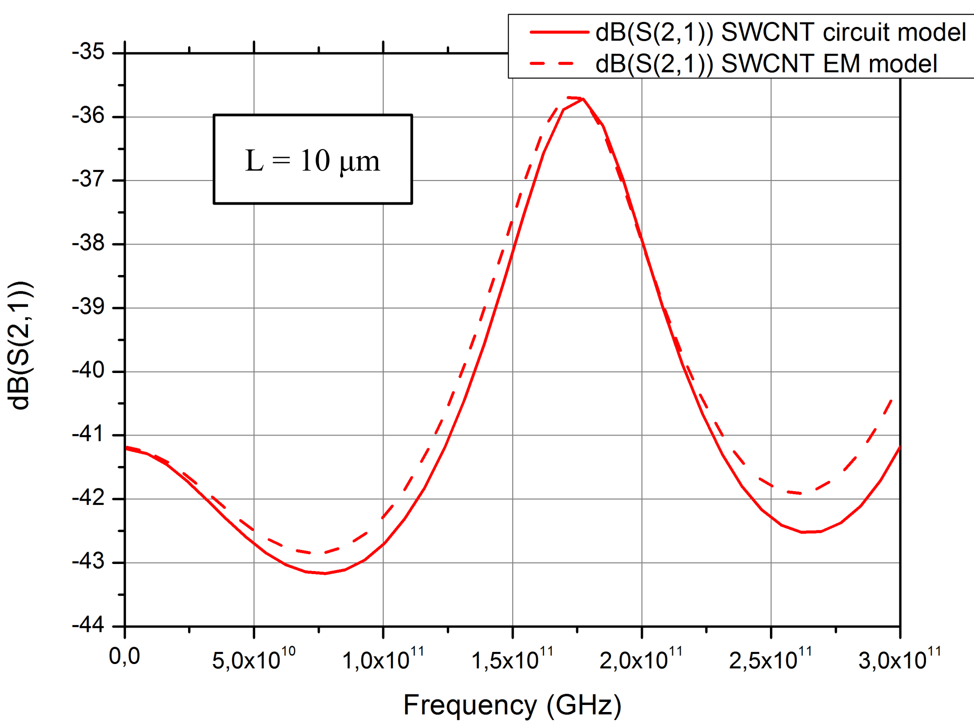

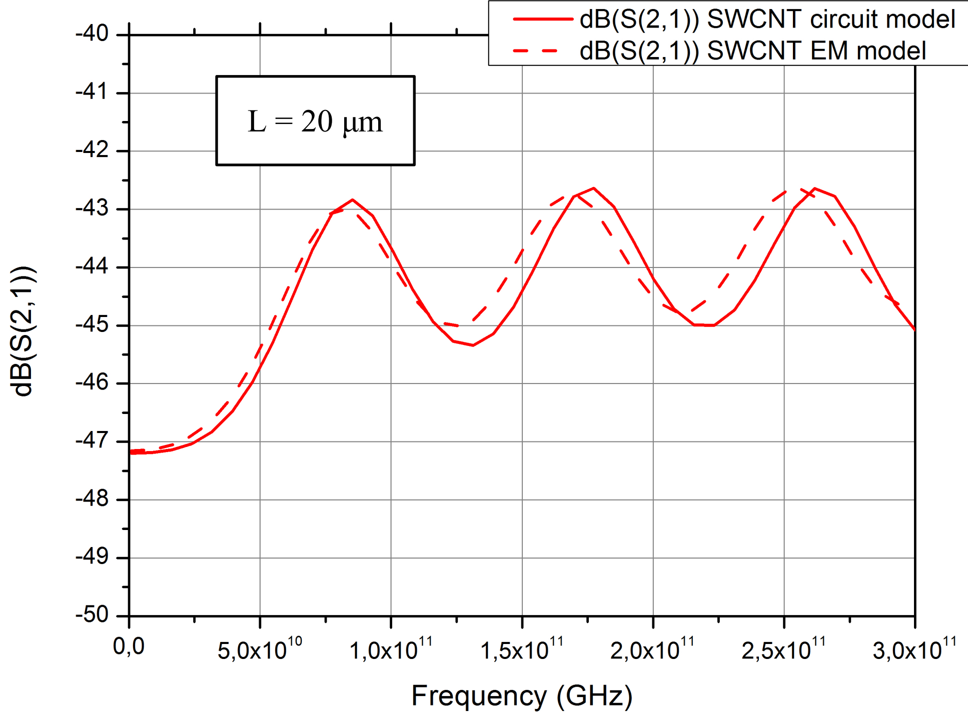

Figure 41: S-parameters of 10 and 20 µm length single-wall carbon nanotube in transmission line configuration.

b) MWCNT modeling

An electromagnetic (EM) simulation was also realized on MWCNTs. We applied the complex surface impedance (equation (35)) on each multi-wall shell and compared the EM results with the circuit model in a transmission line configuration. Our simulation used a 1-µm length DWCNT with an external radius of 2 nm. The circular shape of each shell was simplified by an equivalent square shape as shown on Figure 42.

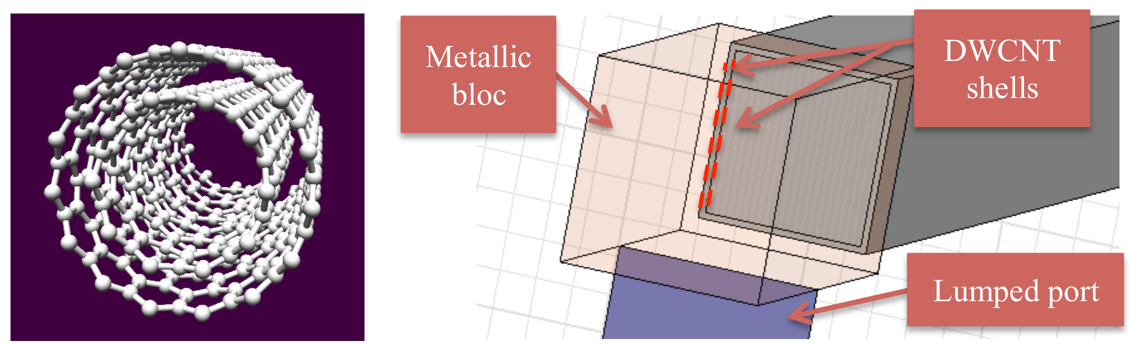

Figure 42: DWCNT design on HFSS. A metallic box links the two DWCNT shells at the extremities.

The results from circuit modeling weren't coherent with the EM simulation. We suppose that the EM simulation doesn't consider the tunneling effects existing between the shells (detailed on section "Modeling of multi-wall carbon nanotube (MWCNT) on page

(64)”). However, for a CNT bundle, it has been shown that tunneling effects in MWCNTs are not significant [11]. Indeed, the large number of CNTs placed in parallels decrease the importance of these effects. Moreover, MWCNT with a large number of shells would decrease also the importance of the crossed coupling effects. These effects were confirmed by EM modeling. However, it required large computer resource to consider an EM modeling of MWCNTs for our future applications.

c) Bundle of CNTs modeling

Most RF applications are using CNT bundles [3, 16]. That’s why in the second part of this work, we purpose to compare EM models of CNT bundles and then to use these models for optimizing CNT based RF applications. Additional schematic models of CNTs will be plotted for each configuration in order to help the comprehension of each effect. However, only EM simulations have been performed in this part.

i. Bundle of three SWCNTs

The first simulations are based on three SWCNTs in transmission line configuration above a ground plane. To get a better understanding of coupling between carbon nanotubes and reproduce main cases existing in bundle, three layouts are simulated. As shown in Figure 43, the first layout (L1) corresponds to three SWCNTs horizontally aligned above the ground plane. The second layout (L2) shows a triangle CNT arrangement. At last, the third layout (L3) is 3 SWCNTs vertically aligned with only one on them at 10 nm above the ground plane. EM simulations of these bundles were performed by finite element method from 1 to 300 GHz. Gap between SWCNTs varies between 1 and 10 nm and their length is equal to 10 µm. The distance between the ground plane and the SWCNTs is constant and kept at 10 nm for the CNT number 2. Each single-wall carbon nanotube has a diameter of 6 nm. They are all linked together at each extremity by a perfect conductor and excited by 50-Ω lumped ports.

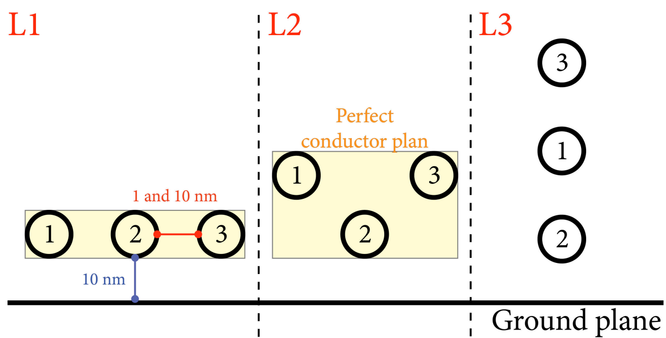

L1

1 2 3

10 nm

Ground plane

L2

1 3

2

10 nm

Ground plane

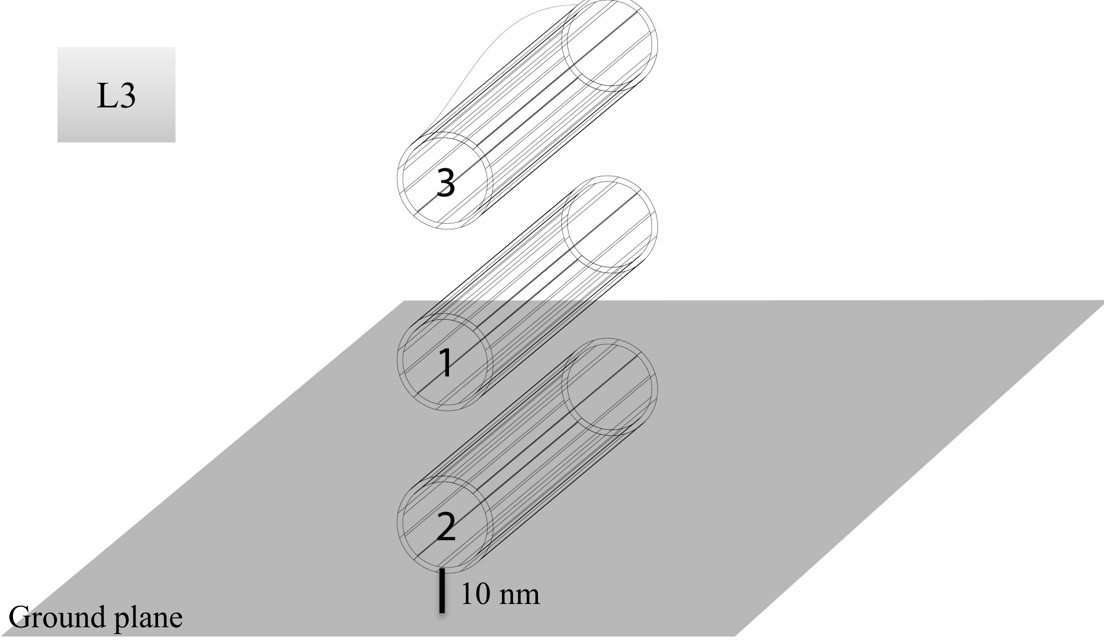

Figure 43: The three bundle configurations (in 2D on the first schematic and in 3D in the others) composed by 3 SWCNTs with a 10-µm length.

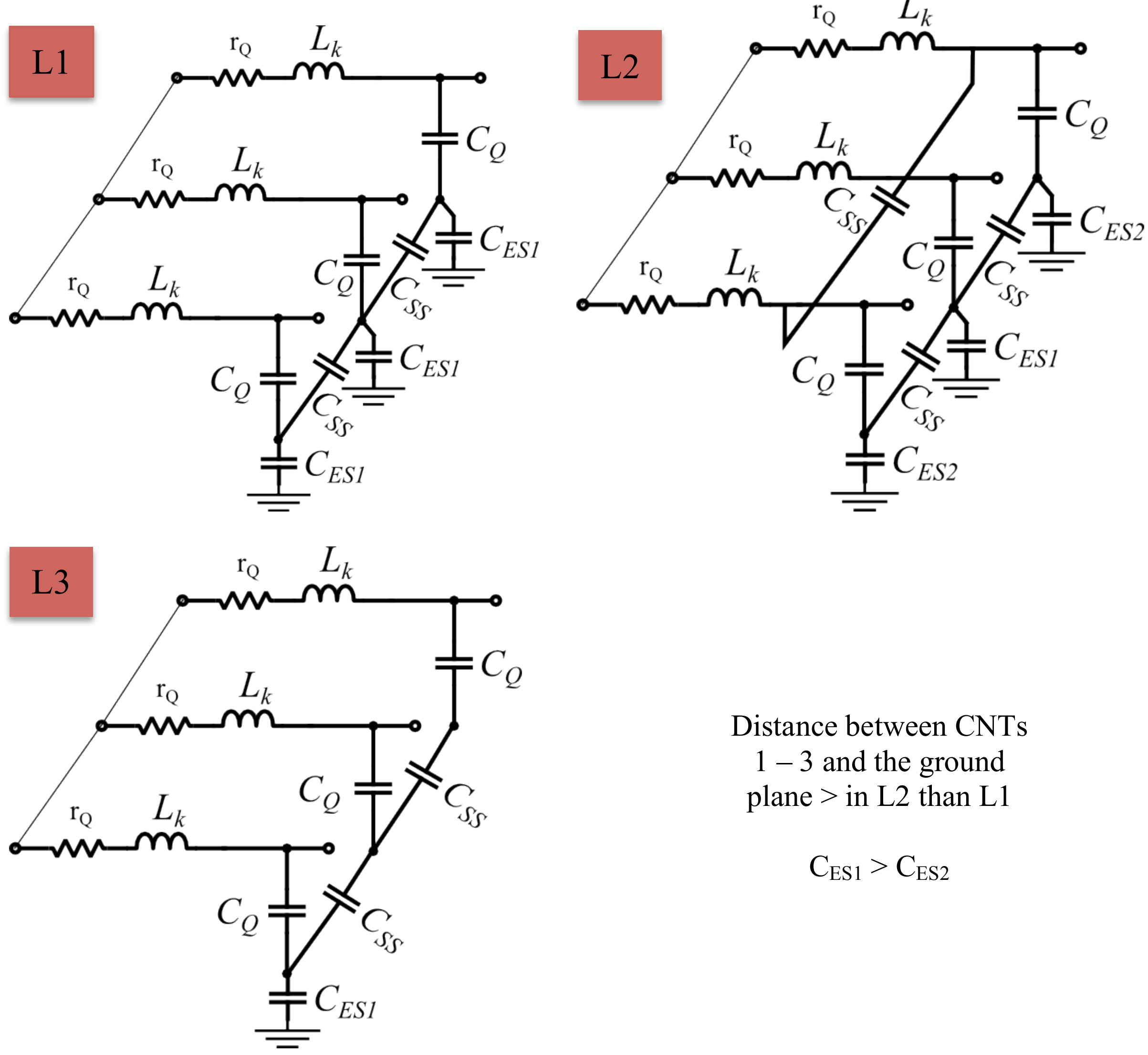

Figure 44: Circuit representations of the three configurations L1, L2 and L3. C_{SS} represents the coupling capacitance between carbon nanotubes. (No analytical modeling or simulation have been done for this study)

As shown in Figure 45, a significant difference is visible between the 3 layouts. In L3 (Figure 45-L3), no coupling effects are visible by changing the distance between the CNTs. Indeed, only an electrostatic capacitance C_{ES1} is present between the bottom CNT number 2 and the ground plane as the schematic approach shows (Figure 44-L3). This electrostatic capacitance is not modified by varied the CNT distance. In L1, as shown in Figure 45-L1, the resonance is shifted to the low frequency by a modification of the distance between the CNTs. With a circuit representation for L1 (Figure 44-L1), an electrostatic capacitance C_{ES1} exists between each carbon nanotubes and the ground plane. By changing the distance between the carbon nanotubes, a modification of these capacitances occurs. If we take a look on the second layout (L2) graph presented in Figure 45-L2, a smaller shift resonance is visible. Thus, in this intermediate case, by a circuit approach visible on Figure 44-L2, the electrostatic capacitances C_{ES1} and C_{ES2} are still existed for the 3 CNTs but their values are lower for two

of them (CNT 1 and 3) because of the higher distance from the ground plane. Thus, the shift is less important with L2 than L1 because the coupling effects between CNTs are reduced. For the first layout (L1), another distance of 20 nm between CNT is added in order to confirm the tendency. From this result visible in Figure 45-L1, a shift of the resonance to the low frequency is still visible, which confirms the previous results. From these studies, we demonstrated that the coupling between carbon nanotubes is always weak. That does confirm the references [75, 82]. We also confirmed that the electrostatic capacitance existing between CNTs and ground plane is modified if CNTs are placed as a bundle. This capacitance modification is directly linked to the distance from the CNTs to the ground plane and the distance between CNTs. Thus, we arrived at the conclusion that the value of the electrostatic capacitance depends on the all CNT bundle shape and the distance between the CNT bundle and the ground plane.

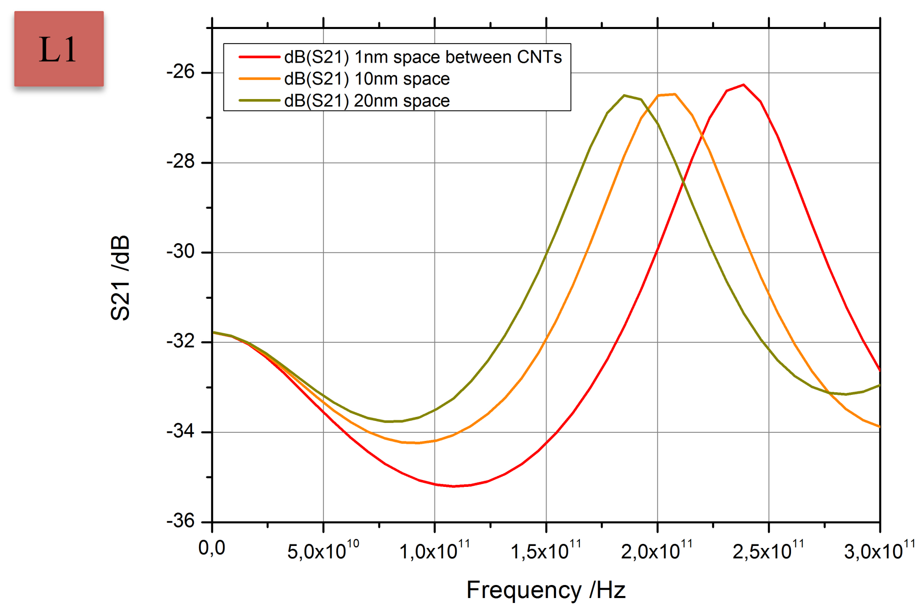

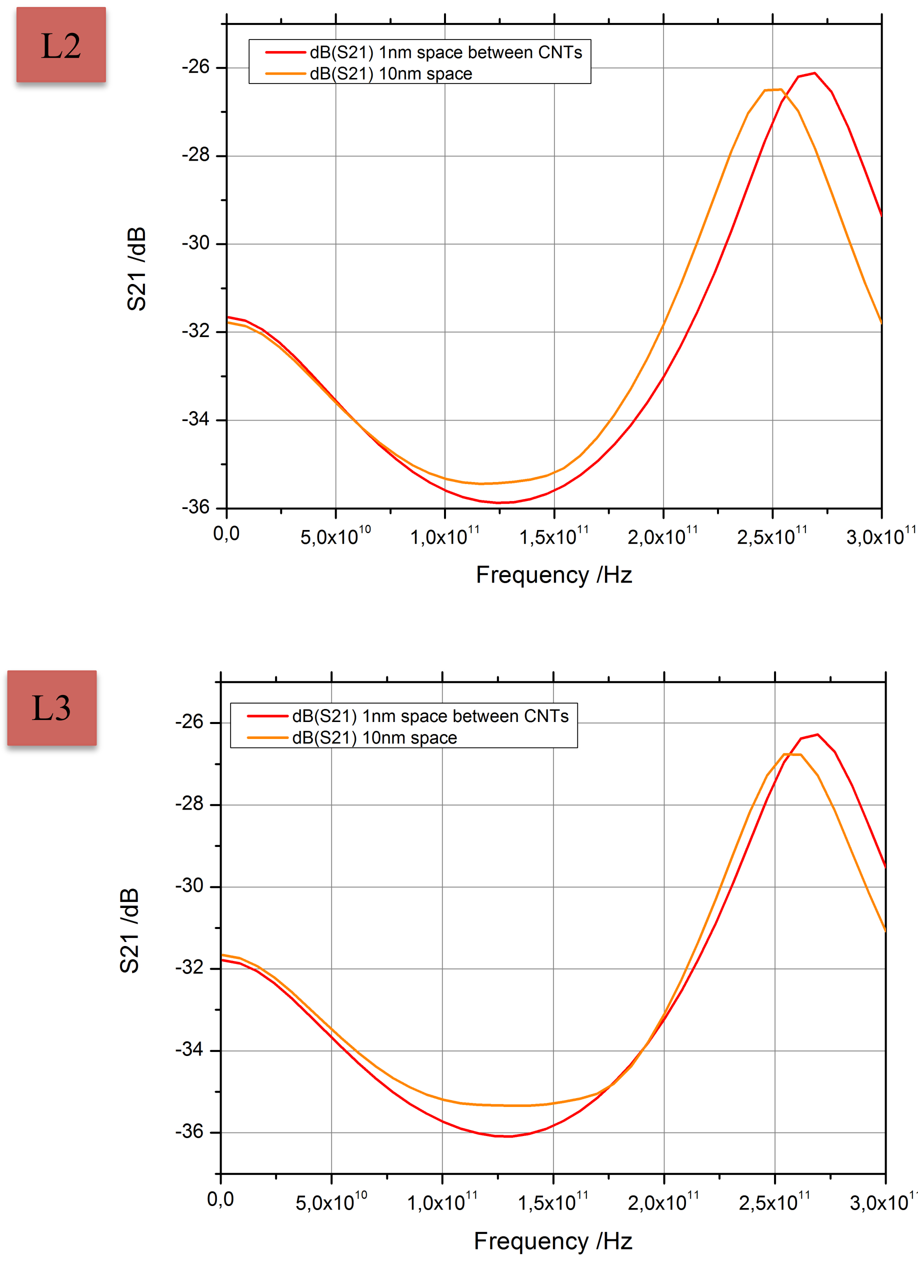

Figure 45: S_{21} parameters of 10 µm length single-wall carbon nanotube bundle in transmission line configuration and EM simulations with different distance between CNTs (1, 10 and 20 nm). S-parameters results for the 3 configurations L1, L2 and L3.

ii. Bundle of twenty-one SWCNTs

Another EM simulation of a bundle with twenty-one SWCNTs was performed by finite element method from 1 to 300 GHz. This additional simulation permits to verify the previous results with a bigger bundle composed by more than three CNTs. Gap between SWCNTs is 10 nm and their length is equal to 1 µm. The distance between the ground plane and the SWCNTs is 10 nm. Each single-wall carbon nanotube has a diameter of 6 nm. The SWCNT bundle is composed by three rows. Only the first row will have an electrostatic

capacitance C_{ES} (equation (16)) between the CNT and ground plane. Again, EM simulations were performed with EMXD software and analytical simulations with ADS software. 50-Ω impedance was kept. EM models were compared with SWCNT circuit models in a bundle configuration respectively with and without coupling capacitance between CNTs (Figure 46). The equation (36) of the coupling capacitance C_{SS} between CNTs is:

$$C_{SS} = \frac{\pi \varepsilon_0}{ln(\frac{d}{2a}+\sqrt{\frac{d^2}{4a^2}-1})} \times l \quad (36)$$

with a the CNT radius, d the distance between the CNTs, l the CNT length and ε_0 the vacuum permittivity.

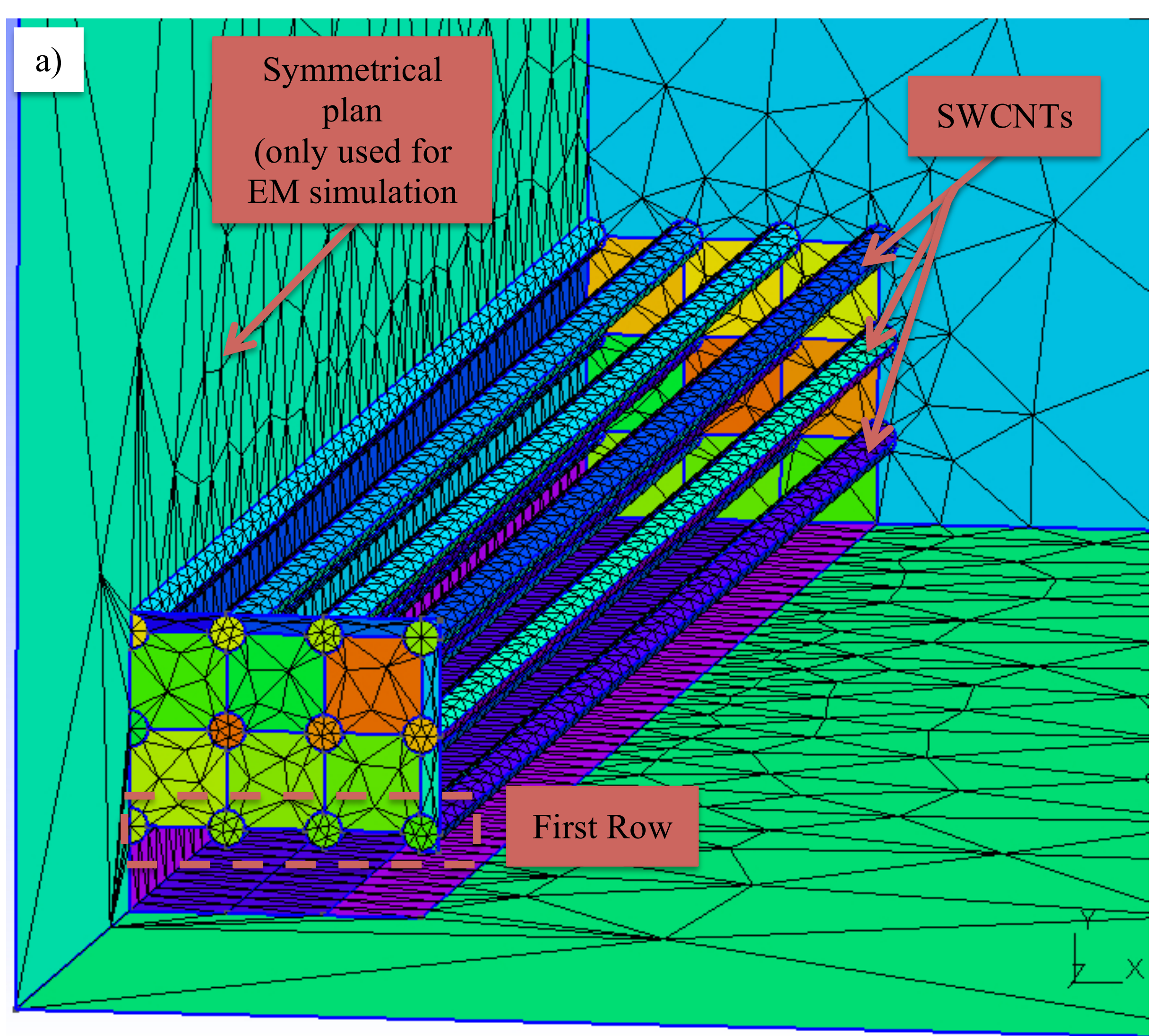

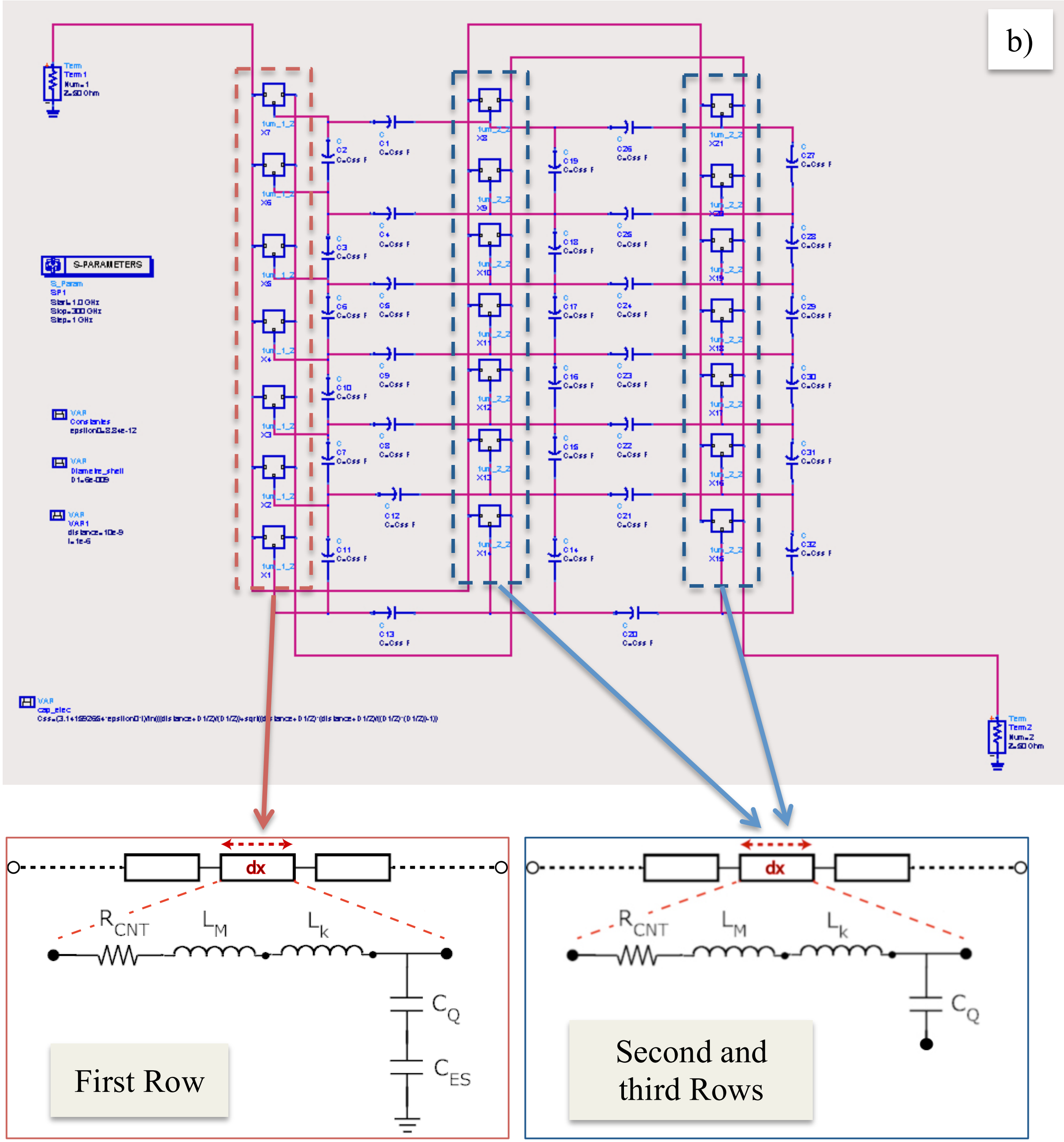

Figure 46: On a), transmission line model of the bundle composed by 21 SWCNTs. On b), equivalent circuit model of the SWCNT bundle with coupling capacitance between nanotubes; each box is a 1-µm single-wall carbon nanotube transmission line (see Figure 31) as represented in the assets below. Only the first row has an electrostatic capacitance C_{ES} between the CNT and the ground plane.

In both cases, all the models fit each other (Figure 47). Only a difference beyond 150 GHz can be observed, however, there is no impact for our applications. From these second studies, we demonstrated that the EM coupling between carbon nanotubes is still weak. That did confirm again the results obtained in the previous section. We also validated our both approaches (EM and analytical) by finding a good agreement in a quite complex case such as the bundle of 21 SWCNTs.

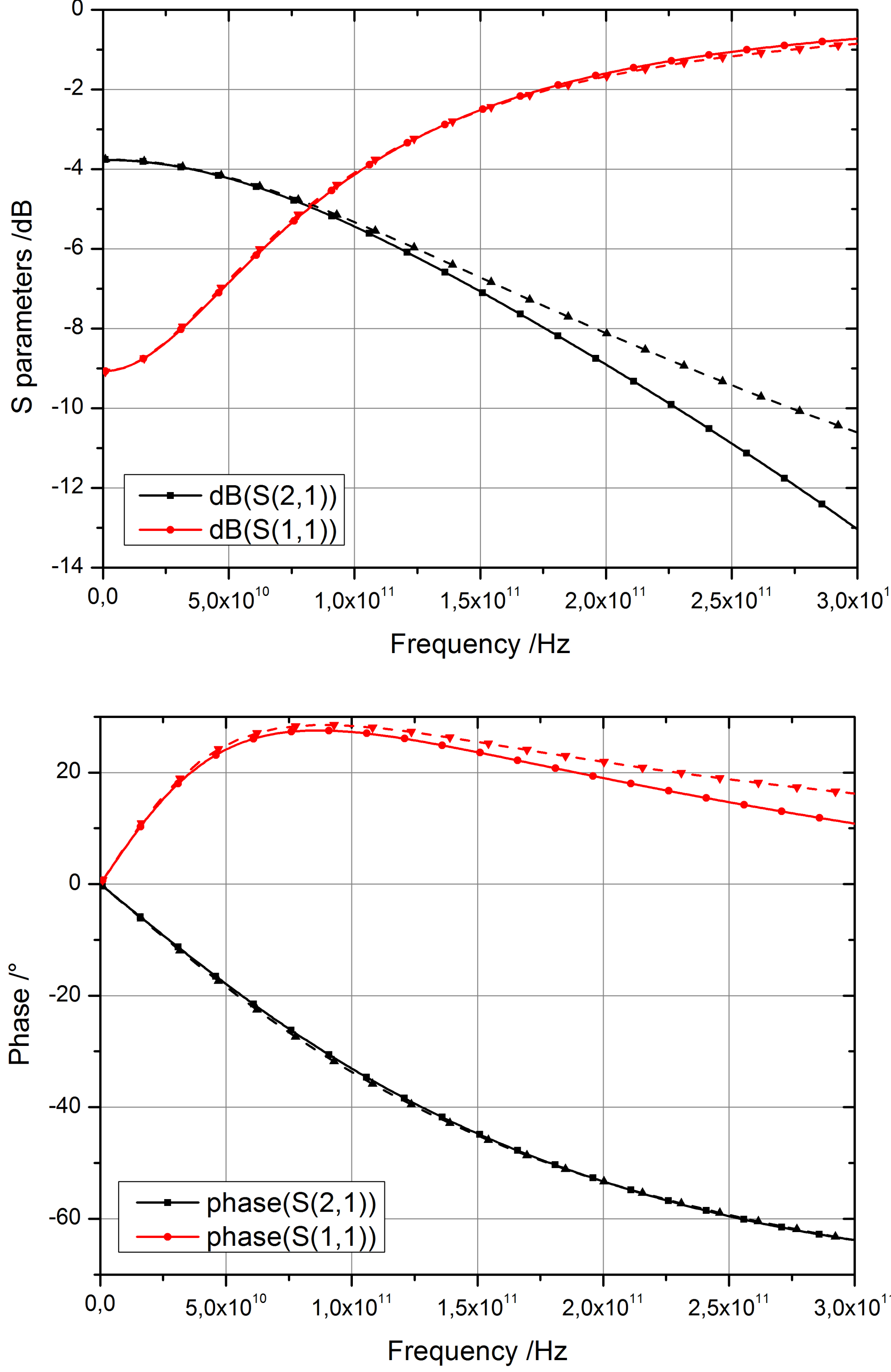

Figure 47: S parameters of 1 µm length bundle of single-wall carbon nanotube in transmission line configuration. Solid lines: Circuit model – Dash lines: EM model.

iii. Bundle of MWCNTs

Because we were not able to model in EM a MWCNT (see section "MWCNT modeling on page (79)"), we didn't manage to simulate a bundle of MWCNTs with EM

simulations. Indeed, the complex conductivity presented earlier (equation (34)) cannot be applied on CNTs with a radius bigger than 3.4 nm. Thus, MWCNTs cannot be modeled in EM using this equation.

Only an analytical approach will be able to solve the issue. To model a bundle MWCNTs, we simply use our MWCNT analytical model we presented earlier and we dispose them in a bundle configuration, as we did for the bundle of 21 SWCNTs. The EM coupling will remain low between MWCNTs (such as the SWCNTs) and so a simplification of the model can be done. Some example of MWCNTs bundle will be given in the second chapter on this manuscript.

iv. Bundle with an unlimited number of SWCNTs

In the previous part, we have showed that the coupling between carbon nanotubes remains low compared to the EM effects such as the electrostatic capacitance applied on the bundle itself. It becomes possible to create a full 3-D electromagnetic model representing a bundle of single-wall carbon nanotubes. To model in 3-D an electromagnetic problem such as a large amount of CNT vertically aligned above a ground plane, we face an issue of calculation time and power consumption. To solve this problem, a bulk SWCNT bundle model has been recently proposed [84]. In this PhD work, we will use the proposed model but we won't work on it. Indeed, considering the coupling effects between CNTs low, we are able to simplify the all bundle by only one entity, which divide the electrical conductivity of one SWCNT by the number of SWCNT existing in the specified area. Thus, using finite element method by HFSS software, a complex conductivity $\sigma_{CNTarray}$ (37) modeling a specific number of parallel CNTs aligned on a specific axis (x,y or z) is applied on a unique entity. This anisotropic complex conductivity is calculated according to equations (37) to (39) for CNTs aligned on z-axis (transverse conductivities σ_{Tx} and σ_{Ty} will be detailed later).

$$\sigma_{CNTarray(z)} = \begin{pmatrix} \sigma_{Tx} & 0 & 0 \\ 0 & \sigma_{Ty} & 0 \\ 0 & 0 & \sigma_{axial} \end{pmatrix} \tag{37}$$

$$\sigma_{axial} = \frac{8e^2 v_F}{h(v - jw)} \times D_{NT} \tag{38}$$

where w is the angular frequency, e = $1.602.10^{-19}$ C is the elementary charge, h = $6.626.10^{-34}$ m^2kg/s is the Plank constant, $v = T^{-1}$ is the relaxation frequency and v_F is the Fermi velocity in

CNTs [84]. D_{CNT} is the density of nanotube (number of nanotube per unit area). As we can see on the equation (2), the conductivity will depend on the dimensions of the CNT bundle and the bundle density. It is also important to say that the transverse conductivity σ_{Ti} is null if the bundle of CNT is embedded in a dielectric media with zero conductivity (σ_M=0) and the distance between CNTs is large enough according to equation (39), [84]:

$$\frac{\Delta r}{2a} < \sqrt{\frac{\pi}{\sqrt{3}}} \approx 1.35 \quad (39)$$

where a is the radius of the CNT and Δr = r + 2a is their spacing, center to center, while r is the shell-to-shell spacing. This last equation (39) also confirms our first observations with the 21-SWCNTs-bundle, which exhibit a much higher CNT density. Indeed, with a 6 nm diameter and a 10 nm spacing between carbon nanotubes, we obtain Δr/2a = 2.67. This result is still lower than the conduction shown on equation (39).

The main advantage of this method is the lower computing resources necessary to model a bundle of thousands (or more) SWCNTs. Indeed, even if a fine mesh into the entity is necessary, the distance between cells will be bigger than the distance between the carbon nanotubes. Indeed, by designing all the SWCNTs in the bundle, the mesh will have to follow the geometry of the bundle and CNTs, which will considerably increase the number of cell.

The inconvenient of this model is its several limitations: we can only model an homogeneous bundle of CNTs, meaning all carbon nanotubes have the same diameter and length; only single-wall are modeled; and CNTs need to be aligned.

In order to integrate the anisotropic complex conductivity in HFSS (for versions before V15), we need to transform the conductivity into a combination of a relative permittivity $\varepsilon_r = \frac{\varepsilon}{\varepsilon_0}$ and a loss tangent $\delta_\varepsilon = \frac{\varepsilon_r^{"}}{\varepsilon'_r}$. To proceed, we use the equation (40 to 43) shown below:

$$\varepsilon = \varepsilon' + j\varepsilon" = K\varepsilon_0 - j\frac{\sigma}{w} \quad (40)$$

$$\varepsilon = \left(K\varepsilon_0 - \frac{\sigma"}{w}\right) - j\frac{\sigma'}{w} \quad (41)$$

And therefore, $\varepsilon'_r = \frac{\varepsilon'}{\varepsilon_0} = K + \frac{\sigma"}{w\varepsilon_0}$ (42)

$$\tan\delta_{\varepsilon} = \frac{-\sigma'}{Kw\varepsilon_0 + \sigma''} \quad (43)$$

The model presented here will be used in the chapter III of this manuscript for the design of CNT monopoles.

D. Conclusion

In conclusion of this modeling part, we have partially validated our both approaches (analytical and electromagnetic) in order to be able to model SWCNTs, MWCNTs and bundle of CNTs. We also compared our two models and found quite good agreements, which gave us an important freedom in term of CNT modeling for various high frequency applications. As we will see on the next parts, these models have been used in several applications in order to have a better understanding of our CNT-based devices, but also these models permit us to develop innovative devices for RF. These innovative devices will be presented on the next parts and chapters.

We have presented the CNT modeling with several approaches. With this large panel of tools to model carbon nanotubes for high frequency, we will be able to design, model and extract some CNT parameters for the applications that will be presented on the next part and the next two chapters. Indeed, since the CNT discovery, a lot of works by researchers have been conducted in order to find and develop practical applications for CNTs. Some of these applications are directly link to the high frequency electronics, as we will present on the next part of this manuscript. They are all using different CNT properties that have been presented in the first part.

IV. High and low frequency applications based on carbon nanotubes (state of the art)

Since their discovery, carbon nanotubes have been widely used in many applications for high frequency electronics. However, researchers spent many years to learn how to control the CNT growth and improve their process in order to achieve more and more complex devices based on carbon nanotubes. In the second chapter, we will discuss about the use of CNTs as interconnections and in the third chapter, we will present an innovative wireless interconnection based on CNTs. On the next paragraph, we will present few applications using CNTs that have been developed recently. These applications can give an idea about how wild are the possibility to use CNTs as an electronics component with quite unique behavior and performance.

1. Transistor (low frequency) [85]

One of the applications the researchers have widely focused on is the field effect transistor based on carbon nanotubes (CNTFETs). By using the SC properties of carbon nanotubes, this material might be able to outperform silicon devices. The advantage of CNTs against silicon is their large capability to carry an important diameter-normalized current density. Their unique and excellent properties push them at the front of the scene. Indeed, new transistor will require a shorter channel length (below 10 nm) with constant or better performance than current bigger technologies (22, 14 nm). Moreover, it was found in 2003 that CNTFET are able to exhibit an ON current 20-30 times higher than Si MOSFETs [86, 87].

However, during the last years, most of the research has focused their work on the graphene and its properties for the development of FET transistors. Thus, recently, the carbon nanotubes are more and more abandoned for transistor applications and replaced by graphene material. These graphene FET transistor are showing promising results [88].

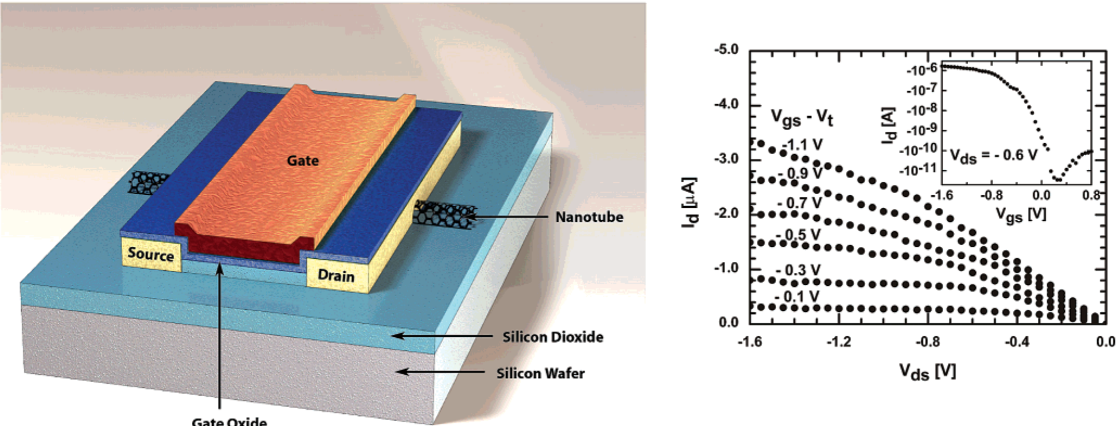

Figure 48: (Left) Schematic representation of a top-gated CNTFET. (Right) Room-temperature output electrical characteristics of a 300-nm-long, top-gated CNTFET. Source: [89]

2. Gas sensor [90, 91]

Another application, which has been largely developed by using carbon nanotube, is the gas sensors. The use of carbon nanotubes in these sensors permits to obtain more sensitive with a faster response and a good stability gas sensor (Figure 49). These sensors can be used in applications such as environmental monitoring and biomedicine. The carbon nanotube is indeed very sensitive to some various gases such as NO_2 and NH_3.

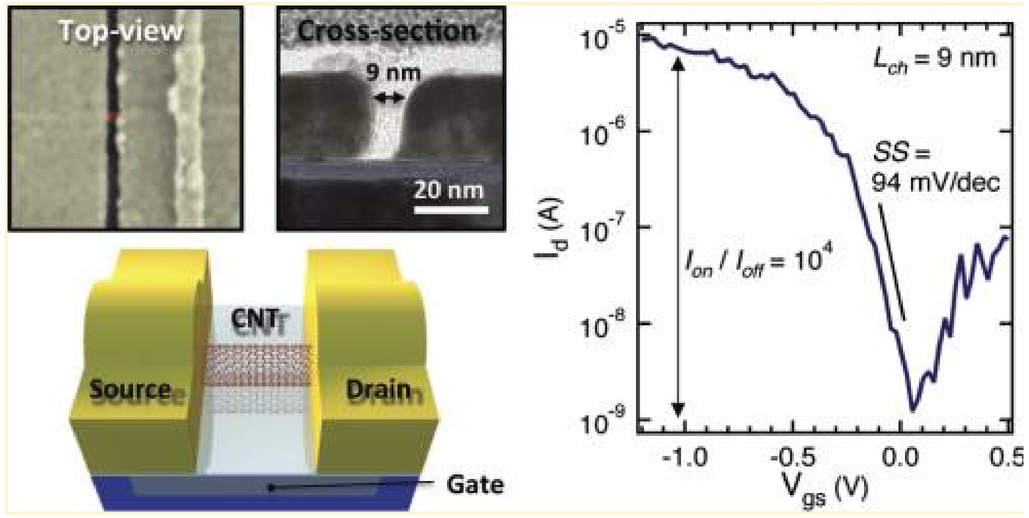

Figure 49: Sensing (gas) based on CNT FET transistor. Source: [90, 91]

3. Thermal management

Carbon nanotubes can be used also in thermal management. Indeed, because of their high thermal conductivity, they represent a good candidate to replace metal-based coolers. By

using a thick layer of carbon nanotubes, we can achieve a lighter cooler than copper-based one with better performance [92, 93].

4. Antennas

Most of the fabricated antenna based on carbon nanotubes so far focused on existing antenna designs and technologies based on metal. For example, they used a patch design and replaced the metal by CNT inks [94, 95]. In this other work also based on a patch antenna, they grown vertically aligned CNTs bundle on a flexible substrate and included it in a composite polymer in order to form the antenna [96]. The patch performances got a reasonable 5.8 dB gain at 2.3 GHz. None of them yielded a size reduction factor of the patch antennas due to CNTs. Finally, CNT-based antennas were fabricated by using the CNT mechanical vibration [97, 98]. Indeed, a single CNT was used for an antenna working in the 40-400 MHz range [97, 98].

5. Other applications

Because of the semi-conducting properties of the carbon nanotubes (see section “Semi-conducting properties on page (18)”), we can imagine to fabricate tunable filters and resonators working at high frequencies where some metal parts are replaced by coated or printed carbon nanotube layer. Thus, the resonant frequency can be shifted for instance optically and controlled by the light emitted on the device [99].

The group of Professor Manos Tentzeris [100] has also fabricated gas sensors, antennas and filters using inkjet printed carbon nanotubes on flexible paper substrate such as the work presented previously. The high CNT sensitivity to the gases, the light or even a EM wave makes them interesting to use for all these sensing applications and permit to get a low-cost solution.

Finally, a group worked on NEMS using MWCNTs as an electromechanical switch (see Figure 50) [40]. The advantage of using CNT-based switch is the low switching time (few nanoseconds) compared to more classical approaches because of the low CNTs mass. Moreover, a lower switch capacitance can be reached, and consequently decrease the switch response. However, most of the devices showed failures with high power tests. Thus, reliability of the CNT-based switches needs to be investigated.

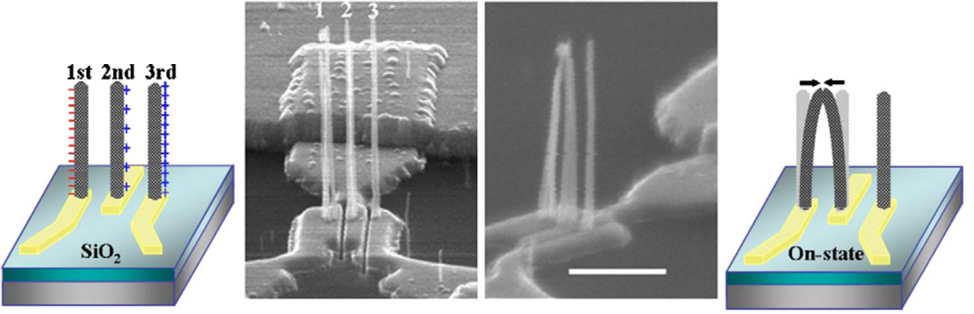

Figure 50: Electromechanical switch devices consisting of three MWCNTs. Source: [40]

6. Conclusion

In conclusion of this part and this first chapter, we have presented the CNT composition and its properties regarding electronics applications. Thus, CNTs have shown a large potential to be used in a large domain of applications, as we presented earlier. The fabrication of CNTs have been described and we have shown that a lot of work still need to be push on that part. Indeed, the control of CNT growth seems to be the weakness point of a larger use of CNTs on current electronics applications. However, research on CNT fabrication has improved a lot recently and as we will see later, quite complex structures using CNTs can be achieved. Moreover, a full CNT modeling have been presented in order to go further in the understanding and the design of complex devices as the ones that will be presented in the two next chapters. On the chapter II, we will present interconnections using bundle of CNTs for flip-chip technology.

Chapter II

I. Interconnections using carbon nanotubes

RF packaging in electronics combines all assembly technics to build with the best accuracy, repeatability and stability the RF systems. Combination of the active and passive devices forms the RF system. Interconnections will connect all blocks (sub systems, chips) together in order to mesh the entire system. Thus, interconnections play a major role in the functioning of the entire RF system. Interconnections need to bring the power and the signal with the lowest losses possible and the shortest delay reachable. With the increase of the frequency, they need to be more and more compact with a constant degree of performance. The Moore law predicts the transistor size will continue to linearly decrease in the future electronics chips. Hence, smaller interconnections on the first and second level will be necessary in future (Figure 51). Currently, metallic interconnections are used in conventional high frequency electronics up to the micro-scale. However, bulk materials such as metals have serious limitations at the nano-scale and even at a few micron scale (electromigration and grain scattering issues). Indeed, with a low current density and below 20 nm, metal behavior is not suitable for using as interconnections in terms of performance and mechanical, thermal constraints. As already detailed in section "Mean free path in CNTs (MFP) on page (26)", carbon nanotubes could be a perfect candidate for interconnections because of their long mean free path and their high current carrying capability. The focus of this PhD work will be to overcome these limitations by using the nano-material at the micro-scale.

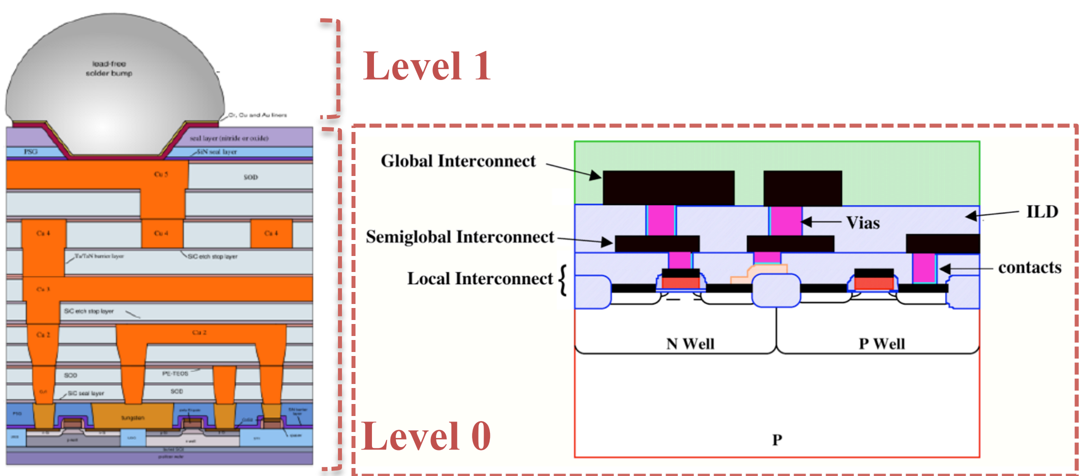

Figure 51: Level 1 and level 0 of interconnections. As we can see, level 1 connects the entire chip while the level 0 interconnections are smaller and only bond unique components together such as transistor.

Two main levels of interconnection exist in integrated circuits: the first and second (also called level zero) levels regarding to their size, their length and their purpose (Figure 51). The first level lists all "chip-to-chip packaging" interconnects such as the wire bonding, the flip chip or via hole. There are used to connect the chip to its package. There is the main interest of the work presented in this thesis. On the second hand, we have the back-end-of-line interconnection (BEOL), which lists all smaller interconnections than the first level. They are usually located into the integrated circuits themselves. A short presentation from literature works is conducted on that second level whereas an important focus will be given on the first level of interconnection and more precisely the flip-chip method to interconnect.

1. Level 0 of interconnection using CNTs [7, 101]

As we already said, interconnections serve to bring the signal and the power to the electronics components. Interconnections at level 0 are split into two categories because the interconnections to bring signal won't have the same technical requirements (size, material, etc) than the interconnections for power. Moreover, they are indexed in three categories according to their length: local interconnects for the smallest length, semi-global interconnects and global interconnects for the bigger length.

Mostly simulations have been performed on that interconnects in order to verify if the use of carbon nanotubes in interconnections is able to outperform the performance of the actual metallic interconnections. Most of the works (modeling and fabrication) so far with carbon nanotubes have been focused on the level 0.

A. Local interconnections using CNTs [102]

a) Local interconnects: properties and issues

Since the electronics is at the edge of the nano-scale, the smallest interconnects in integrated circuits that are the local interconnects will necessarily shrink their size in future. They will be indeed the most affected interconnect by the size reduction of the electronics circuits. This reduction will cause few problems such as the way to develop fabrication tools and equipments to manipulate nano-scale components (such as nano-scale lithography, etc) and electromigration issues (grain boundary scattering, surface scattering and high resistive diffusion barrier layer) appearing on bulk material at nano-scale.

The length of the local interconnects is short (between 500 and 1500 nm). However, once they are aggregated, their length becomes usually larger, that's the reason why today, 50 % of the interconnect power is dissipated in local interconnects. One of the main issue to solve with the local interconnects is the lateral capacitance existing in them. This high capacitance decreases interconnects performance by increasing the transmission signal delay. In the other hand, to carry the power in interconnects, the smallest resistance is necessary, which implies a thicker interconnect, also to avoid the electromigration effect. Thus, we will see how the carbon nanotubes bundles are able to solve these issues approaching the nano-scale.

b) Local interconnects: performance of CNTs (SW vs. MW)

Simulations showed that controlled diameter single-wall carbon nanotubes are able to lower the lateral capacitance by a factor of four and the power dissipation by two compared to a metallic local interconnect and thus improve the speed of the interconnect by 50 % [102]. Indeed, by controlling the number of carbon nanotubes in a given area, we are able to decrease the total lateral capacitance by decreasing the number of CNTs into the bundle. The SWCNT diameter can be also decreased (lower CNT surface) in order to still low down the lateral capacitance. In the second hand, to bring the power in local interconnects, because of an important quantum resistance existing in an individual carbon nanotube, it is necessary to keep a minimum of parallel CNTs. This will have the effect to decrease the total interconnect resistance. Thus, a trade-off between the capacitance and resistance needs to be investigated regarding the CNTs bundle density. At last, because of the too short length of the local interconnects (below the value of the CNT MFP), CNT resistance remains high compared to a copper wire for example and may not be suitable for this level of interconnects. Indeed, because of the length-independent quantum resistance effects existing in CNTs (up to the MFP length, see section "Mean free path in CNTs (MFP) on page (26)"), they will be more efficient with longer CNTs, at least as long as the MFP.

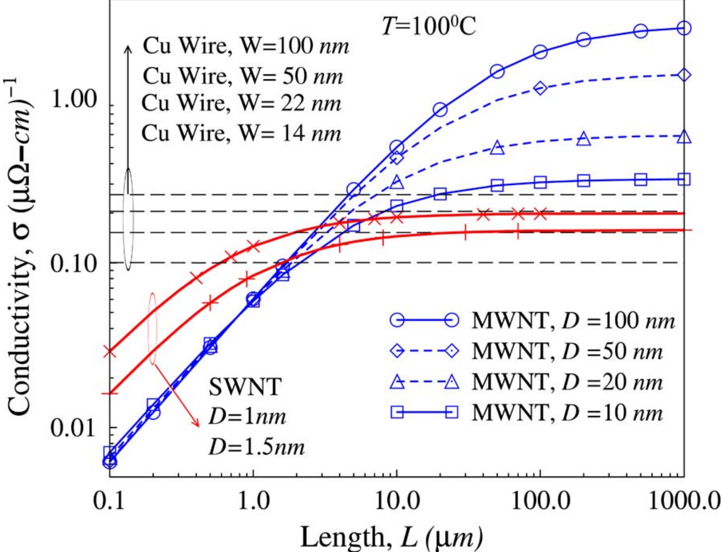

Figure 52: Interconnections electrical conductivity as function of the length. Copper and CNTs based interconnections are compared. W is the width of the interconnection made by copper and D is the diameter of CNTs. Sources: [2, 7]

The main challenge remains to align the carbon nanotubes with a controlled density, length and diameter. As already explained in section “Plasma enhanced chemical vapor deposition (PECVD) on page (48)”, PECVD growth method is able to solve these issues. Thus, as shown on Figure 52, MWCNTs will be preferred for power distribution because of their lower resistance whereas SWCNTs will be preferred for signal transmission because of the lower lateral capacitance. However, we have to stay careful about the proportion of SC-SWCNT existing in a bundle that can compromise the performance of the interconnection. The choice of MWCNT can guarantee a metallic behavior.

In conclusion, local interconnects made by carbon nanotube may not be the best choice of material. Indeed, their length-independent resistances decrease their interests and efficiency with short interconnection lengths lower than the CNT MFP.

B. Semi-global interconnections using CNTs

The length of the semi-global interconnects is logically located between the local and global interconnects: between few micro and hundreds of microns (Figure 53). They only represent a small proportion of interconnections length. Considering the state of these interconnects and following what we have discussed on the previous part, densely packed DWCNT-bundles will be preferred for this level of interconnection. Indeed, because the product R×C (R is the interconnect resistance and C is the interconnect capacitance)

determines the delay, an important number of carbon nanotubes with the lowest capacitance are necessary and so DWCNTs are the perfect candidate for. DWCNTs will be preferred to SWCNTs because of the higher proportions of metallic CNTs we are able to achieve with current fabrication process.

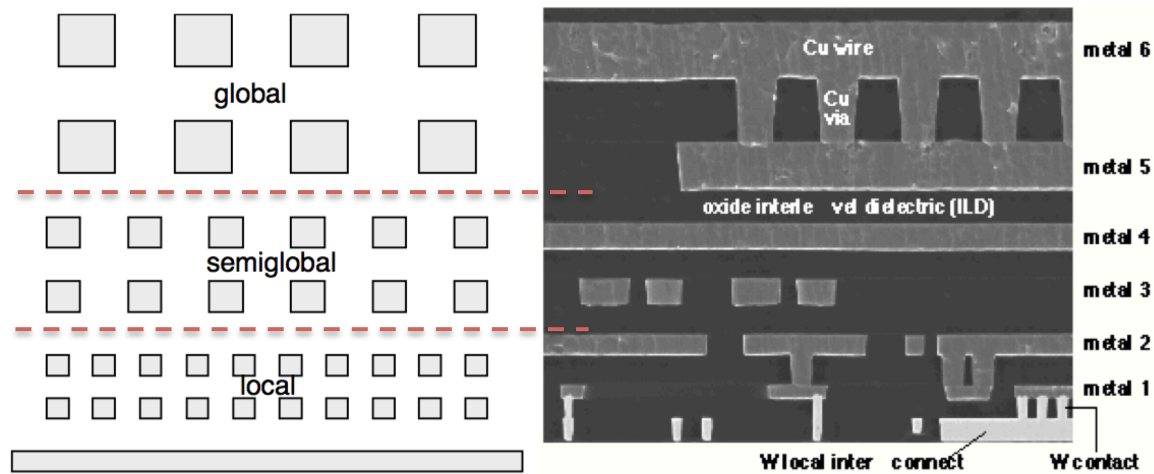

Figure 53: SEM images of each level of interconnections. Global interconnections are the biggest whereas local ones are the smallest.

C. Global interconnections using CNTs

Global interconnects are all interconnections with a length higher than few hundreds of microns (Figure 53. They are mostly made in Al and Copper. With these metal materials used for global interconnects, the resistance becomes proportional to the square root of the material resistivity (Figure 13). With carbon nanotubes bundles and the correct density of CNTs, we are able to decrease the width of the interconnections made by metal. However, a relatively large density of CNTs is necessary in order to reach a total interconnection resistance lower than a metal wire. If we use the SWCNTs instead of MWCNTs, a perfect control of the carbon nanotube chirality during the growth need to be done in order to get only metallic ones. An expected control of the CNTs chirality during the growth has so far not been achieved. At the global level, for the same reasons as the local interconnects level, capacitance in CNTs bundle can be easily lower than the metal interconnections especially because the interconnects width at this level is larger. Finally, the inductance in CNTs interconnections includes the kinetic and magnetic inductance effects. The kinetic inductance effect will be very low and can be neglected because of the large number of CNTs in parallels in the bundle. The magnetic inductance remains the same than the metal interconnection.

In conclusion, at the global level of interconnects, physical models showed bundle of large diameter (50 nm) MWCNTs could be used for power distribution because of their lower resistance whereas dense SWCNT bundles (with at least 40 % of metallic SWCNT) can outperform the of signal interconnects made by metal. The percentage of metallic versus semiconducting carbon nanotube is the major issue for the use of single-wall carbon nanotube in interconnects. A CNT density as high as 9.10^{15} /m^2 has been obtained [103].

D. Conclusion

In conclusion, carbon nanotubes (SW and MW) have pros and cons to be used for these three levels of interconnection. According to the dimensions of the interconnections (length, diameter, etc), carbon nanotubes bundles with the correct density and type of CNTs might be able to outperform the performance of metal interconnections. Finally, CNTs would be an optimal material for multilevel interconnect network by combining carbon based structures. However, the state of the art shows us that this type of interconnections made by carbon nanotubes still need an improvement on the CNTs growth control in order to be integrated in future devices. So far, several carbon nanotubes bundles have been successfully fabricated for IC applications (Figure 54). However, most of the time, it appeared that the CNT density into the bundle is too low to level the performance of metal interconnections.

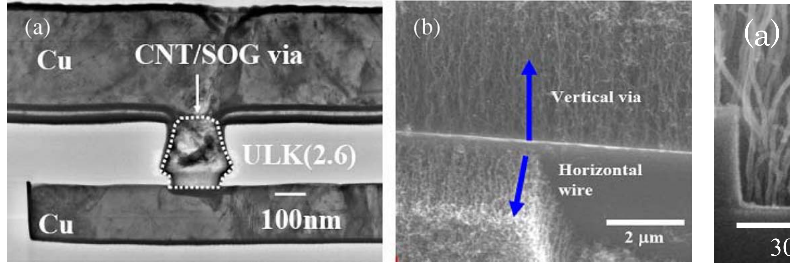

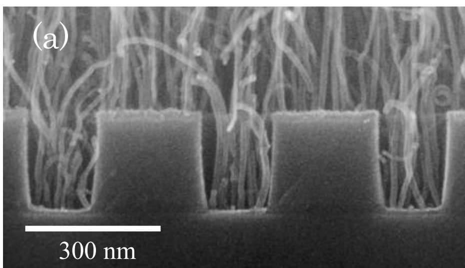

Figure 54: Three interconnection configurations using carbon nanotube materials. On left, we have CNTs embedded in metal bump. Next, we have a combination of horizontally and vertically aligned CNT bundle. On right, a 160 nm diameter CNT bundle in via is presented. Source: [104]

Thus, a densification process can be used. The densification consists of applying a solvent (such as IPA isopropyl alcohol or acetone) on the carbon nanotube bundle in order to help them to aggregate using the electrostatic and Van der Waals attractions. The CNTs become closer and a higher density of carbon nanotube is reached (Figure 55). So far, the best SWCNTs bundle density obtained is about 1.10^{16} /m^2 [105]. With this density, interconnections made by carbon nanotube are able to outperform the performance of metal

interconnects. However, advanced CNT growth techniques must be developed in order to use them in IC interconnects. Indeed, the quality, the chirality, the diameter, the length of the carbon nanotubes must be perfectly controlled during the growth with a high degree of uniformity. Moreover, since the CNT bundle needs a densification step, a larger bundle of CNT needs to be fabricated first. It causes many fabrication step issues that must be solved in the future.

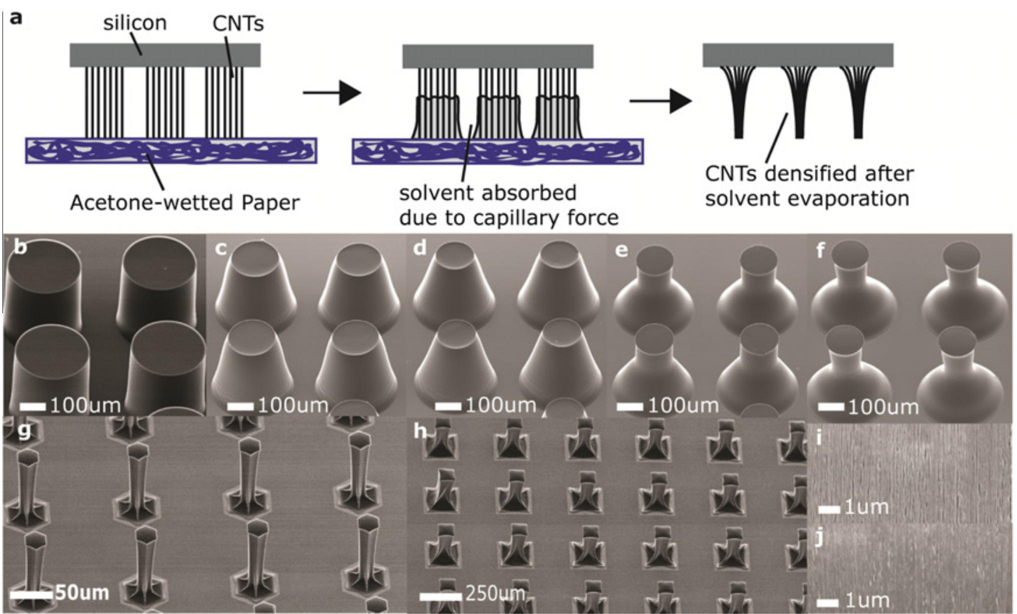

Figure 55: The densification process steps and principle is visible on the top asset. Others SEM images show the effect of the densification process on carbon nanotubes bundles according to their size. On the bottom images, we can also see the effect of the solvent with several depth of penetration into the carbon nanotube bundle. Source: [105]

2. Level 1 of interconnection using CNTs [2, 104-107]

Now, we present the connections from the chip to it package. They play a major role in the packaging because they have to deal with the powering, cooling and protecting electronics components in RF systems. Not surprisingly, the performance, the size, the cost and the reliability of the packaging and more precisely the interconnections will be strongly dependent on the material used and the method employed (wire bonding, flip-chip, via hole). As the local and global interconnections presented previously, because of the scale down of the transistor sizes in integrated circuits, further miniaturization will be necessary for interconnection.

A 3-D packaging will increase the level of integration in electronics and in this part, we focus on the used of wire bonding, via hole and flip chip technologies. These three methods to interconnect a chip to an IC have a high degree of integration, however, their uses involve some manufacturing process that deal with thermal and reliability issues. The shrink of the interconnect size will even more complicate the fabrication process. Thus, it becomes important to find new materials with unique and excellent properties compatible to the nano-scale. Carbon nanotubes might be a solution for off-chip interconnections that are used for signal and power transmission, same as the local and global interconnects. Moreover, because most of the time, they "feed" an entire chip, they are more exposed to thermal and mechanical constraints within the time. Again, the solution might come from the carbon nanotubes and their unique mechanical, electrical and thermal properties.

A. Wire bonding

The wire bonding has been the most used technology so far and the first way discovered to interconnect the integrated circuits. The wire is usually made by gold (can be made by Cu or Al as well) with a minimum diameter of 15 µm. We encounter two major problems with this type of interconnection. First, the integration is not maximal and optimized since the wire bonding is a wire with a length between 200 and 400 µm located around the chip. As shown on the Figure 56, the wires are surrounding the chip/IC, wasting an important precious space for other components. Secondly, the wire has a very low diameter (15 µm), which implies a high magnetic inductance. So, the use of the wire bonding technology might be an issue above 50 GHz because of this high magnetic inductance.

To use carbon nanotubes with this type of technology would be very challenging. Indeed, a perfect control on the CNT growth direction will be necessary in order to make a wire and long CNT bundle with very low diameter will be expected. All of these last points have not been fully controlled so far in fabrication. Thus, wire bonding may not appear as the optimum interconnection technology for the use of carbon nanotubes.

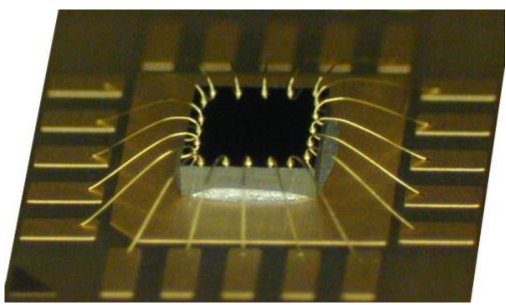

Figure 56: Wire bonding made by gold.

B. Hot-Via [63, 108, 109]

This second interconnection configuration called hot via is based on the flip-chip (FC) technology. Instead of flipping the chip in order to interconnect it from the topside, the backside is directly interconnected. Thus, a metallic bump links first the motherboard with the backside of the IC and a via is connected through the substrate to the IC (Figure 57). This technology keeps the advantages of allowing a glance on the IC and the possibility to realize a transition between coplanar accesses on the motherboard to a microstrip line on the chip. A schematic view of the hot via transition is presented on figure 33. For the bumps, metal materials are currently employed such as copper and gold. Thus, the size reduction of the chip will still affect them and the use of carbon nanotubes as the via hole transition could be an answer of the downscaling issues.

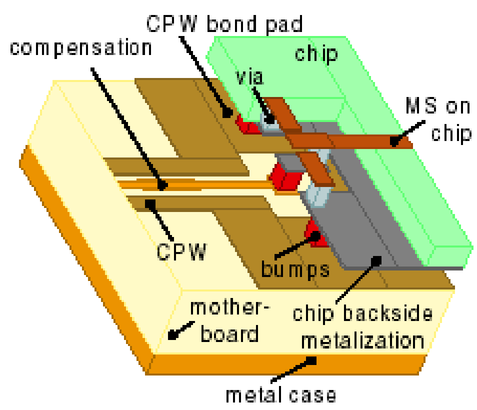

Figure 57: Schematic of a hot via interconnection

Many works have been done in order to integrate carbon nanotubes bundles into via or to directly grow these same bundles into the vias. However, a direct growth of carbon nanotubes into via has been obtained only with a very low via depth (Figure 58). This limitation can be explained by the hydrocarbon molecules that cannot reach the catalyst

particles deposited at the bottom of the hole. Another work from Jean Dijon's group [55] had successfully achieved a 1-μm via filled by CNTs grown by CVD process (Figure 60). A CNT density of 2.5.10^{12} /cm^2 was achieved. The top of the vias were polished and encapsulated in order to realize a 4-probe measurement. A resistance of 10 kΩ was obtained (Figure 60), which is still very high to think about integration in circuits. However, with 1000 vias in parallels, they obtained a reasonable resistance of 22 Ω. With deeper via hole, a transfer of the carbon nanotubes bundles was necessary or a post-deposition of polymer around the bundle was done. On the first case, we compromise and increase the contact resistance between the metal and the CNTs. On the second case, we still need the substrate support for the printed integrated circuit on the chip. In conclusion, as you can see on Figure 59, even if solutions have been given for via with CNT bundle, no experiments have been done so far on an entire hot via structure. However, the flip chip technology (presented on the next part) based on carbon nanotubes bundles might start to give some answer for this technology.

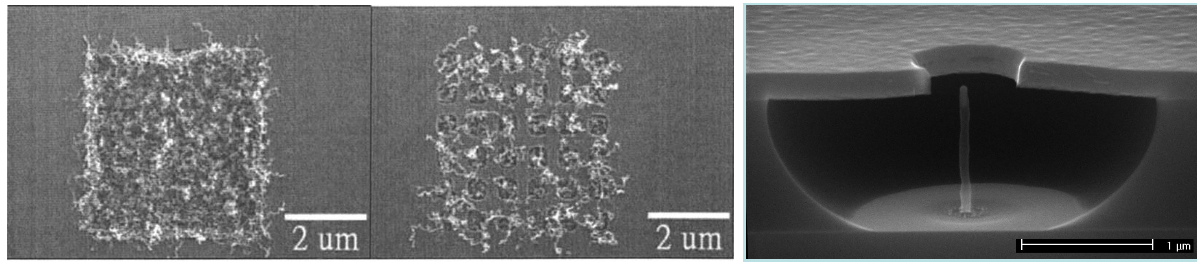

Figure 58: Growth of CNT bundles in vias. As we can see, the depth of the via is quite low (below 1 μm on the right SEM image) and CNTs growth is not really suitable for interconnect applications (images on the left). Source: [109]

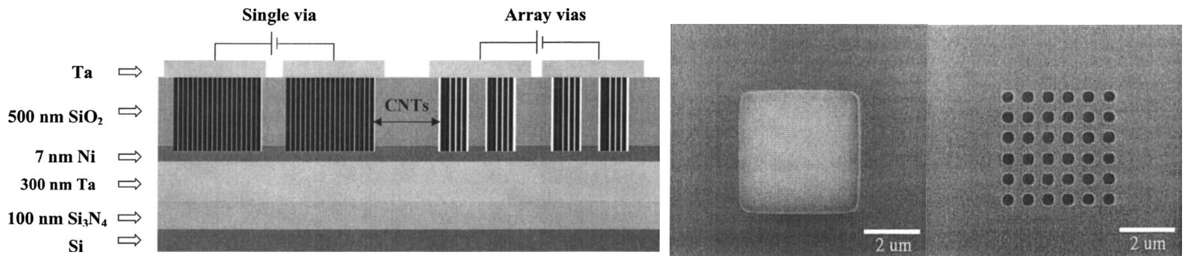

Figure 59: On left, cross sectional schematic of CNTs via. Ni is used as catalyst and only 500 nm high via is expected. On right, CNT growth in via. Source: [109]

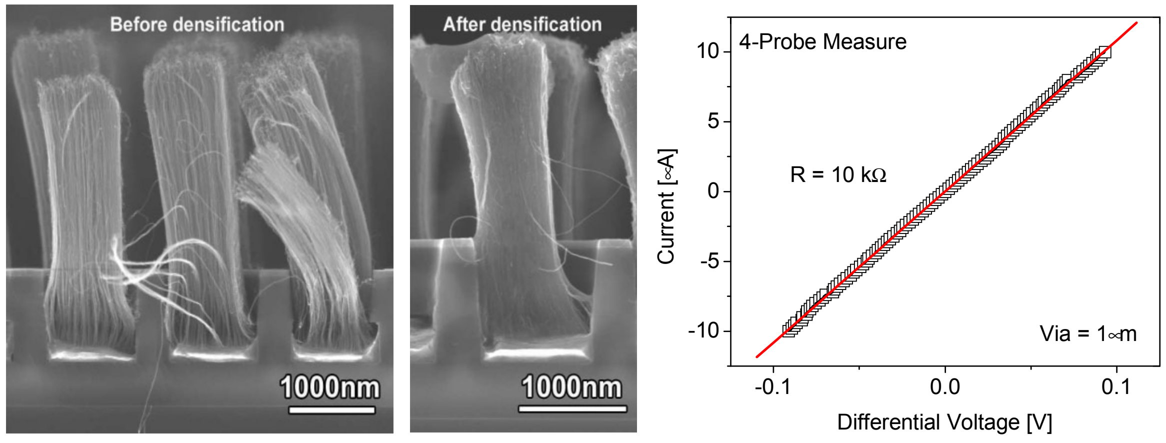

Figure 60: On the left SEM images, vias filled by CNT bundle before and after a densification process. On the right graph, a 4-probe measurements for 1 µm via filled by CNTs. A 10-kΩ resistance was found. Source: [55]

C. Flip-Chip

In recent years, many research focused on compact designs, 3D integration and high operation frequency in electronics. Flip-chip is one of the technologies offering lower insertion loss [110], compact packages [111] and low-cost fabrication [112], but such requirements are limited at higher frequency (higher than 100 GHz) because of the size limitation of the interconnection. As the name of the technology suggests, the flip-chip consists on flipping the chip/IC and connect the back face with the motherboard by metal bumps. In contrast with the hot via presented previously, the back face of the chip, where the integrated circuit is, is connected. No vias through the substrate are necessary and only a planar technology is sufficient to make the flip-chip compatible. This advantage of topology permits to avoid the issues of via growth with carbon nanotubes and so simplify the fabrication process steps. IMB introduced the first flip-chip interconnections in 1970. At this time, the flip-chip technology was named C4 (controlled Collapse Chip Connection). Today, flip-chip technology reached the industry and daily used in many electronics devices.

a) Flip-Chip fabrication process

There are four steps of fabrication. First, the wafer surface needs to be prepared for the bump solder: the wafer is cleaned and the existing layers are protected. Secondly, the metal bumps are fabricated by evaporation, electrolyze, inkjet or direct placement. Then, the bump is aligned with the substrate and the connection is done (with a high temperature). Finally, an underfill is inserted between the chip and the motherboard in order to fix and stabilize the whole structure. As we can see on the Figure 61, several metal layers compose the solder bump. Indeed, some of them are used for the bump adhesion and others as a barrier layer to

avoid the diffusion and increase the electrical conduction. The advantages of this technology are the strong mechanical connection between the two parts, the chip that is protected against its environment and a better thermal dissipation by the bumps.

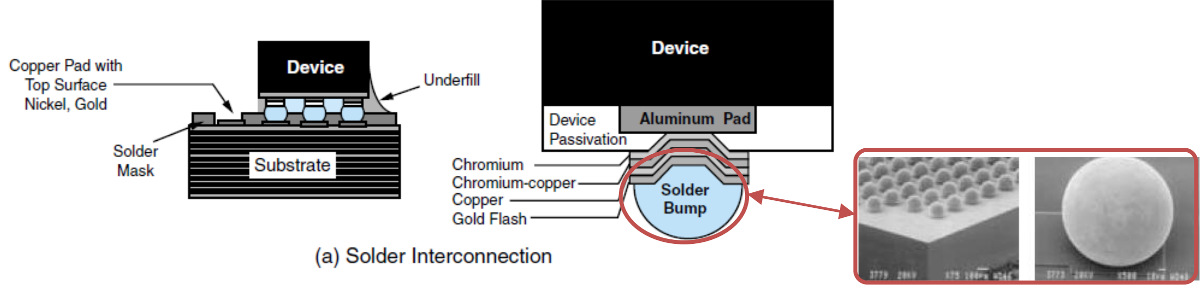

Figure 61: On left, a schematic of the current flip chip bumps made by metal. On right, a SEM image of these metal bumps. Source: [113]

b) Flip-Chip limitations

To meet the demands of compact size multifunctional designs at higher frequency, metal bumps have to be downscaled. However, the downscaled of metal bumps in the micro-scale regime is highly susceptible to electromigration issues, hence affecting adjacent devices or causes reliability issues [114] as already presented with local and global interconnections. The use of vertical carbon nanotube bundles as flip-chip bumps is an alternative approach for overcoming this problem and proposes interesting capabilities. Indeed, compared to gold, an ideal CNT is able to reach an electrical conductivity 3 times higher and mean free path up to 25 orders of magnitude larger [2]. Its large kinetic inductance and a negligible magnetic inductance [2] also allow CNT to have a negligible skin depth effect. Another advantage of using CNTs as interconnection is their high current carrying capacity (10^9 A/cm2) and their excellent thermal conductivity (3000 $W.m^{-1}.K^{-1}$) [115], potentially giving a better thermal management and power dissipation to a flip-chip structure. According to the International Technology Roadmap for Semiconductor, the forecasted requirement for flip chip bump pitches will be shrinking beyond 20 µm [116]. However, traditional solder bumps have difficulties downscaling beyond 30 µm pitch due to the high diffusive and softening nature of solder [117], electromigration and grain scattering issues [114]. CNTs are a suitable choice for future flip chip interconnect [2]. These advantages motivate the researchers and our group to evaluate the performance of CNT bump for interconnects usage in both DC and high frequency applications [2, 118]. Thus, a combination of both flip chip and CNT has the potential to make devices workable beyond 100 GHz with high performance. Indeed, in

literature for flip chip technology, we cannot find interconnections with a diameter lower than 20-25 μm [33, 119] working at higher frequency than 100 GHz.

c) Flip-Chip using CNTs (state of the art)

Many works on CNT bumps have been performed in recent years and Soga et al. had reported low DC resistance of 2.3 Ω for a 100 μm diameter bump [120]. But only a few works have presented a flip-chip-based technology. Flip-chip using CNT bundles as bumps for high power amplifier is presented here [33] by Iway's group (Figure 62). They showed high density (10^{11} cm^{-2}) CNT bundle as a bump for flip-chip technology. Au was plated on the surface of patterned metal and CNT bumps to allow a thermal assisted flip-chip bonding bumps. Then a temperature of 345 °C is necessary to fix the flip-chip. The bundle diameter is 10 μm and bundle resistance was found negligible because of the high number of CNT. As we can see on their work, flip-chip technology coupled with carbon nanotubes is able to exhibit a good heat-removal technology. Indeed, the thermal management in interconnects requires new material and new approaches at nano-scale. Carbon nanotubes-based flip-chip could be a very efficient method.

A flip chip interconnect was also presented by Hermann et al. using CNT pads on one side and metal contact pads on the other [118]. However, to realize a permanent mechanical contact, the bumps were filled with epoxy and heated to 200 °C to achieve 2.2 Ω bumps resistance. Hermann et al. demonstrated reliable electrical flip chip interconnect using CNT bumps working over 2000 temperature cycles [118]. In all the works above, the CNT bumps were grown using the chemical vapor deposition (CVD) approach. The mechanism for vertically alignment during thermal CVD approach is mainly achieved by the electrostatic and Van der Waals forces between CNTs, resulting in tubes that are not exactly 'aligned' [121] (Figure 25) The poor 'alignment' forms bends, reduces the mean free path and increases the resistance of CNT [122]. Plasma enhanced chemical vapor deposition (PECVD) is able to resolve this issue by introducing of electric-field to achieve alignment as well as lower growth temperature [115] as we already explained in the first chapter of this thesis.

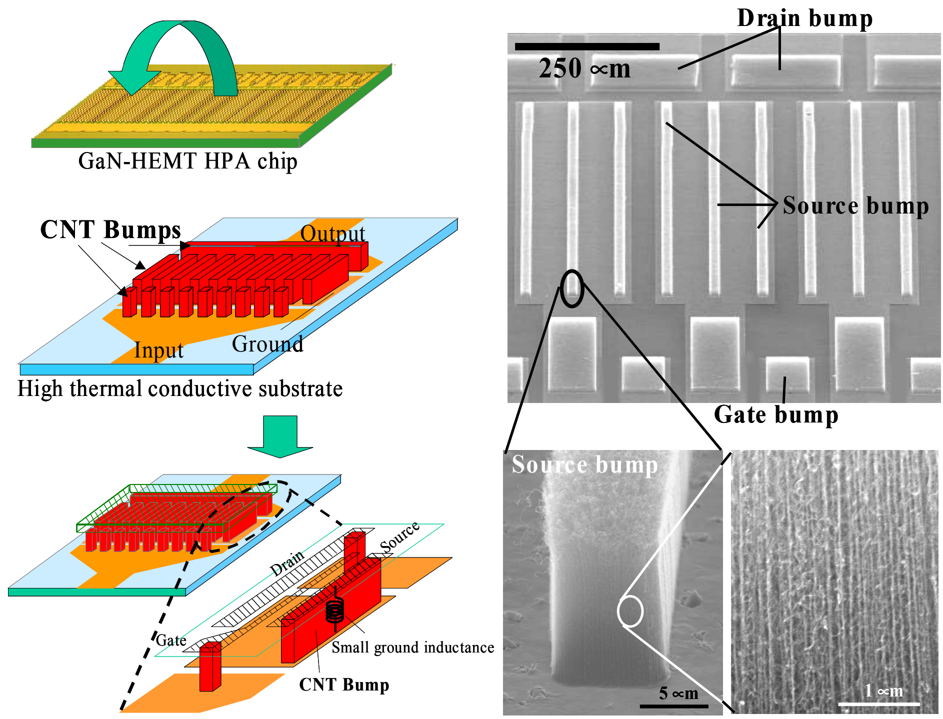

Figure 62: On left, concept of a flip chip using carbon nanotube interconnections for thermal management. On right, SEM images of the corresponding CNT bundles. A high CNT density is observed. Source: [33]

To summarize, a high aspect ratio (with CNT bundle diameter below 20 µm) is necessary to get good performance with the increase of frequency. High aspect ratio CNT bumps are reachable for better high frequency performance. Lower process temperature need to be reach and beyond the proof of flip chip concept by 3D interconnected CNTs, future devices with a better control of density and a higher density will be suitable to increase the number of CNT contact. Finally, another problem meet in nano-packaging concerns the solder. Indeed, mechanical and thermal constraints become too high at a very low scale to support an important lifetime. Thus, the idea of using a contact between carbon nanotubes, and the electrostatic and Van der Waals forces as the mechanical solder will be presented later in this PhD work.

II. Interconnections based on carbon nanotubes for flip-chip technology

In the flip chip scenario, the grown CNT bumps are usually pressed onto pre-patterned conductive adhesive [120] or solder materials [123] to form the connections as we have seen in the previous part. This approach requires heating up the structure to a minimum of 200˚C in order to re-flow the materials to obtain good contacts. Yung et al. demonstrated a large scale assembly process using vertically aligned CNT interconnection bundle showing that CNTs to CNTs adhere well to each other by van der Waals and forces and electrostatic interactions [124]. However, no work using CNT interconnection bump was reported for CNT bump pitch below 150 µm, which is a requirement for the future, flip-chip technology.

In this part, we demonstrate the CNT interconnection bump joining methodology for pitch smaller than 150 µm. The fabrication methodology is divided into 3 parts:

- Fabrication of the structure dedicated to RF application,
- Growth of CNT bumps on both sides of the substrate using PECVD approach,
- Alignment and 'insertion' of the CNT bumps into each other using a flip chip bonder machine.

A first flip-chip device working up to 40 GHz will be fabricated and characterized in order to set up and optimize the process and finally to demonstrate the feasibility of our innovative approach to interconnect CNTs. Working at 40 GHz is easier because of the bigger size of the device (RF lines and bumps). Moreover, we will discuss the technological aspects of developing the test structure, and will present the DC and RF behavior of small-scale CNT interconnection bumps. Finally, a modeling using electromagnetic (EM) and hybrid EM/analytic approaches will be conducted in order to extract CNT parameters. The contact resistance between two carbon nanotubes (MWCNTs) will be extracted and compare with the state of the art found in literature. In a second time, a flip-chip working up to 110 GHz will be presented following the same process flow presented previously. Smaller CNT bundle diameters will be achieved (20 µm).

In this work, a PhD student Ray Yap Chin Chong helped me all along to fabricate the device and grow CNTs. He assisted me during the growth, optimized the all process and

helped me to understand the several issues we encountered during the different steps. I managed the design and the mask, actively participate to the fabrication of the device and the CNT growth, realized the flip-chip bonding with Ray, and did the RF measurements and the modeling exploitations. We both taught each other how to use equipment and software in order to be independent for future studies.

1. Design and fabrication of a test structure with CNT bumps working up to 40 GHz

A. Problems to solve

In order to study the use of vertically aligned CNTs for RF interconnects applications, there are problems that need to be resolved. One of the issues is the requirement for low growth temperature to ensure reliability of underlying components. Indeed, high temperature process (higher than 400 °C) can be a problem for CMOS compatible applications [125]. However, other applications for high frequency without CMOS circuits allow temperature process higher than 350 °C. Lowering the growth temperature of CNT increased the defects, and decreased the degree of crystallinity of the CNT structure, which affects the electrical characteristics of CNT [126, 127]. Improving the quality of the CNT at low temperature is still under investigation, and the variation of metal resistance before and after CNT growth process will be taken into consideration. Moreover, low-temperature growth of CNTs has been already demonstrated [52-54], but the qualities of these CNTs were not consistent [128]. Also with the work of Dunlin Tan, a PhD student of CINTRA/NTU, using a radiative approach, in order to heat the catalyst cluster locations from the top instead from the bottom through the substrate, is one of the ideas currently investigated. This approach would replace the bottom heating used in PECVD that require a higher process temperature (600-700 °C). A temperature below 400 °C is expecting by using this innovating radiative approach. Encouraging preliminary results have been obtained.

Works on this topic is an active field of research currently and very encouraging results start to come out [93].

The second issue is the controllability of CNT growth density on Au as well as the understanding of interaction between different barrier layers and Au underlayers. Au inhibits CNT growth, and thus a study for suitable barrier layers is required between the catalyst and Au metallization [129]. CNT growth has been reported to be influenced by different types of barrier layers: Titanium (Ti), titanium nitride (TiN), and chromium (Cr) were reported to support CNT growth, while aluminum (Al), Ni–Cr alloy, Cu, and Au inhibit growth [129-131]. The reason for using different barrier layers depends on the needs of applications; TiN is claimed to be the best barrier layer on Cu, whereas Ti and Cr are common barrier layers used to improve the adhesion of Au on Si and in the under-bump metallization for bumps [131, 132]. In this first part, we demonstrate the growth of CNTs using the PECVD technique on Au metallization supported on three different conductive barrier layers (Ti, TiN, and Cr). This study focuses on the worst-case scenario to determine the performance of the underlying Au after being stressed at 800 °C temperature in the presence of reactive gases such as ammonia (NH_3) and acetylene (C_2H_2). In the next section, we report the influence of different barrier layers to grow CNTs on Au metallization.

a) Experimental details

The test structure consists of 50-Ω coplanar waveguide (CPW) with a length of 0.7 mm for the signal (center) and 1.2 mm for the ground (Figure 63). The line and bump patterns were obtained using photolithography techniques, as we will detail on the next part. First, 700 nm of thermal oxide was grown at 1200°C on high-resistivity Si wafers (> 10 kΩ.cm). The high-resistivity wafer is necessary for the microwave applications. Next, 10 nm Ti was used as an adhesion promoter followed by depositing 1-µm thick Au metallization lines. These two layers were deposited using an ebeam process. Using the lift-off approach, 50-µm diameter bumps were formed followed by 50 nm barrier layer and 20 nm nickel (Ni) catalyst deposition. All metal depositions were carried out using the e-beam evaporation technique at room temperature and TiN was sputtered deposited at 75 °C. The final CNT growth process was performed at 8 mbar inside a PECVD chamber. The growth process includes pretreatment of the Ni catalyst in NH_3 environment for 2 min at 800 °C. The growth was carried out for duration of 15 min using C_2H_2 as the carbon feedstock gas at 4:1 ratio. The cathode voltage was biased at -707 V providing a DC plasma power of 100 W. Ex-situ characterizations were carried out using the LEO 1550 Gemini scanning electron microscope (SEM) for a CNT structure at different stages, and 532 Renishaw Visible Raman for Raman

analysis. The RF measurements were done using a probe station connected to an Agilent HP 8510C network analyzer. The test environment was calibrated using short-open-load-thru scheme in order to remove the losses from the setup (cables, connectors, VNA, etc) and S-parameters were extracted for the range of 1–20 GHz with a step of 0.1 GHz.

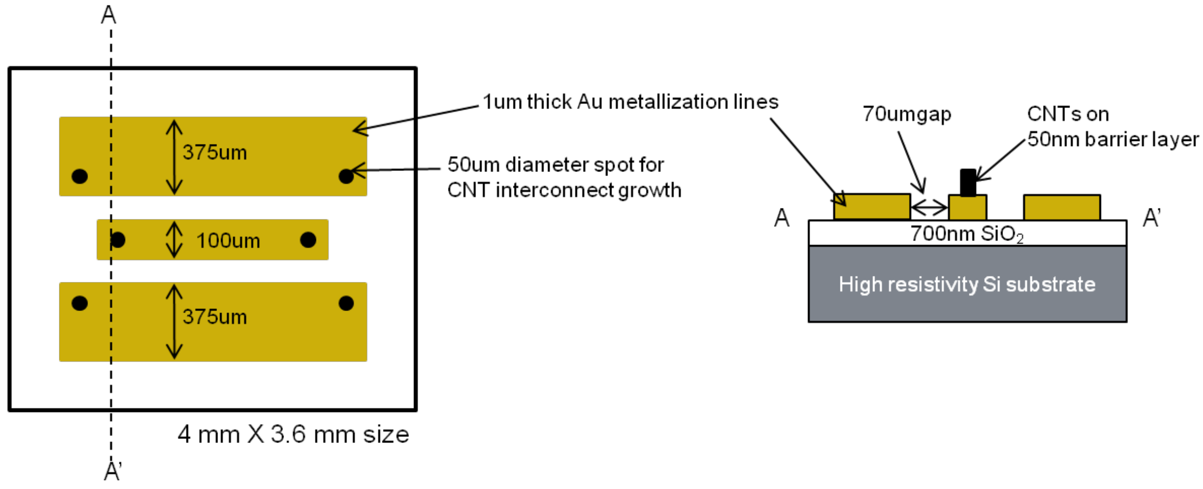

Figure 63: Schematic of coplanar waveguides (CPW) test structure used (not drawn to scale). Left shows the top view of the CPW with a length of 0.7 mm for signal and 1.2 mm for ground. The dark circles indicate the locations of the CNT interconnects. Right shows the cross-section view indicating different layers of the test structure. Note that the 50 nm barrier layer is not shown in this figure.

b) Results and discussion

i. Influence of the PECVD process on the Au metallization and the RF performance

The influence of the CNT growth parameters on the Au metallization lines was observed at various stages of the growth process as shown in Figure 64. Figure 64(a) shows the morphology of the deposited Au metallization, which is smooth with no cracks under the observation of SEM. As a reminder, the Au was deposited with e-beam equipment with a process temperature always below 70 °C. Figure 64(b) shows the morphology of Au metallization after subjected to high-temperature processing at 800 °C in ambient NH_3 resulting in the formation of crack lines. Finally, Figure 64(c) shows the surface roughening of the Au metallization after exposure to C_2H_2 feedstock gas and plasma treatment. The Au have agglomerated and formed a hill-like structure. De Los Santos et al. [133] suggested that the top layer of the Au melted and Au atoms diffused and nucleated at new sites. The addition of plasma at 800 °C raised the surface energy and likely induced the melting of the top layers of Au.

Using a two-point probe technique, the resistance of the Au coplanar strips lines registered an initial resistance of 2.03 and 7.73 Ω after the PECVD process. Increase in resistance is likely the result of film cracking and the formation of eutectic composition at the Au interface during annealing at 800 °C [134]. Thus, from the SEM micrographs and two-point probe testing, it was shown that the Au lines have degraded and suffered as a result of the CNT growth process.

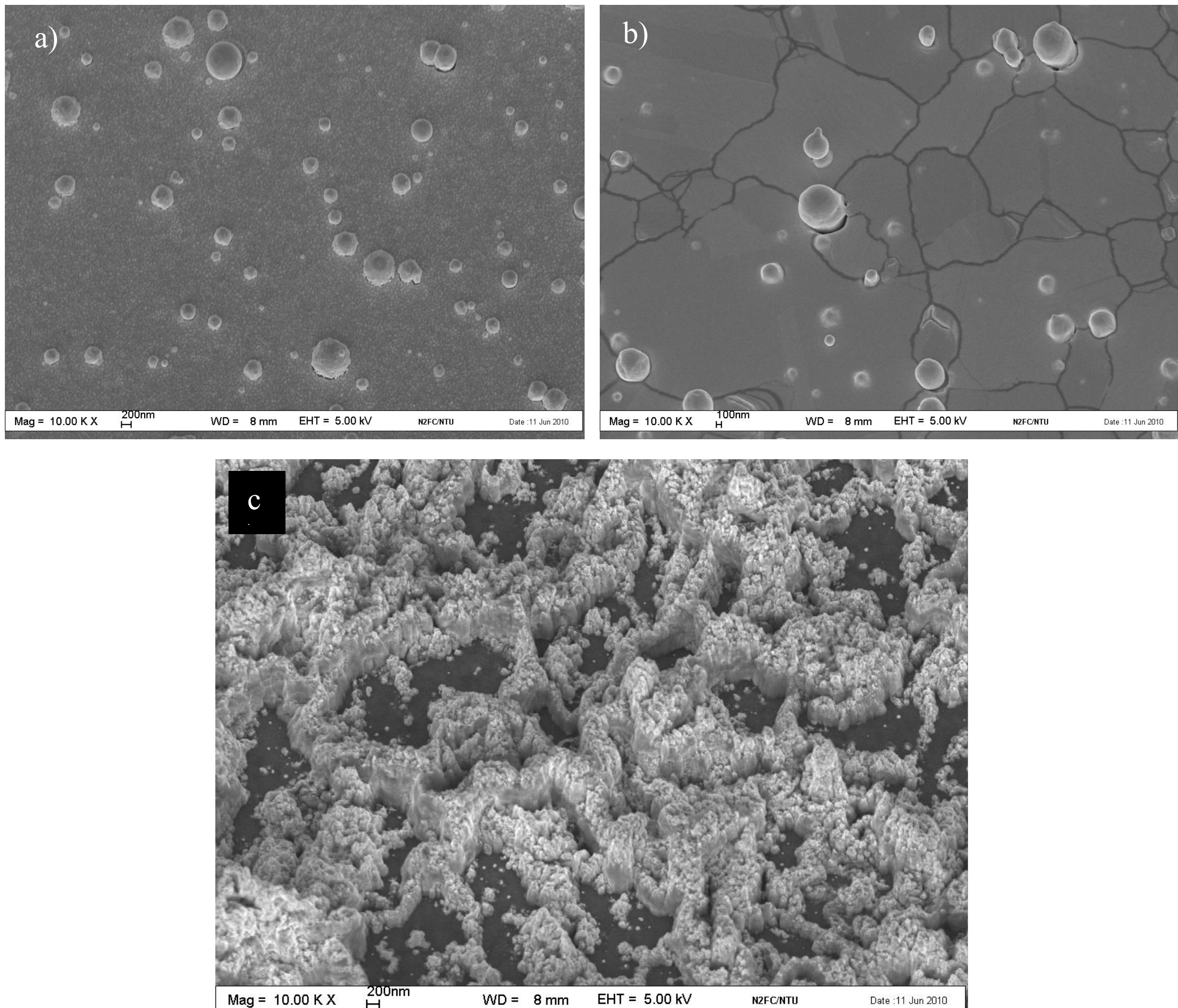

Figure 64: SEM micrographs of the Au metallization at different stages of CNT growth. (a) Au-deposited film was smooth with no crack-lines. The circular islands were formed during the deposition of Au metallization by e-beam evaporation process. (b) After annealing for 2 min at 800 °C in ambient NH_3 and crack-lines were observed. (c) After subjecting to C_2H_2 and plasma treatment for 15 min in a PECVD chamber, the Au film formed a hill-like morphology.

Despite the structural degradation of the Au coplanar lines, the S-parameter measurements shown in Figure 65 present promising results. To eliminate errors due to physical differences between test structures during the fabrication processes, the same

coplanar structures (A and B) were used at every stage of measurements. Figure 65(a) and Figure 65(c) show the return loss parameter (S_{11}) and insertion loss parameter (S_{21}) of test structure A, respectively, whereas Figure 65(b) and Figure 65(d) refer to measurements from test structure B. Each individual graph includes measurements at three different stages, namely (i) the As-deposited film, (ii) after 2 min annealing in ambient NH_3, and (iii) after 15 min of CNT growth. The results show that the cracks formed on the Au metallization after annealing caused the S-parameters measurements to worsen as compared to the As-deposited coplanar lines in Figure 65. Insertion losses (S_{21}) decrease by 1.5-2 dB and a degradation equal to 5 dB is visible on the S_{11} reflection parameter. However, the line performances were still correct between 1 and 20 GHz. Interestingly, the same test structures show improvement as compared to the annealed case after being subjected to the plasma effect. After plasma treatment, the S_{11} reflection parameter had improved and behaved like the Au-deposited lines (highest peak at -17 dB for structure A and -19 dB for structure B). Moreover, the S_{21} transmission parameter of the coplanar line was also improved by an average of 1.87 dB for structure A and 1.32 dB for structure B as compared to the annealed lines. The observed results have two possible explanations:

- Reports have shown that plasma had been used to improve silicon nitride properties or used to clean the Au surface from particles [135, 136]. In our case, plasma could help to improve the quality of the line by cleaning off native oxide or amorphous carbon.

- Plasma increased the surface energy of the Au lines leading to surface change at the Au metallization and form new agglomerated structure, which presents new channels to carry the signal. Most importantly, these results demonstrate that PECVD-grown CNT could be integrated on Au metallization for RF applications up to 20 GHz.

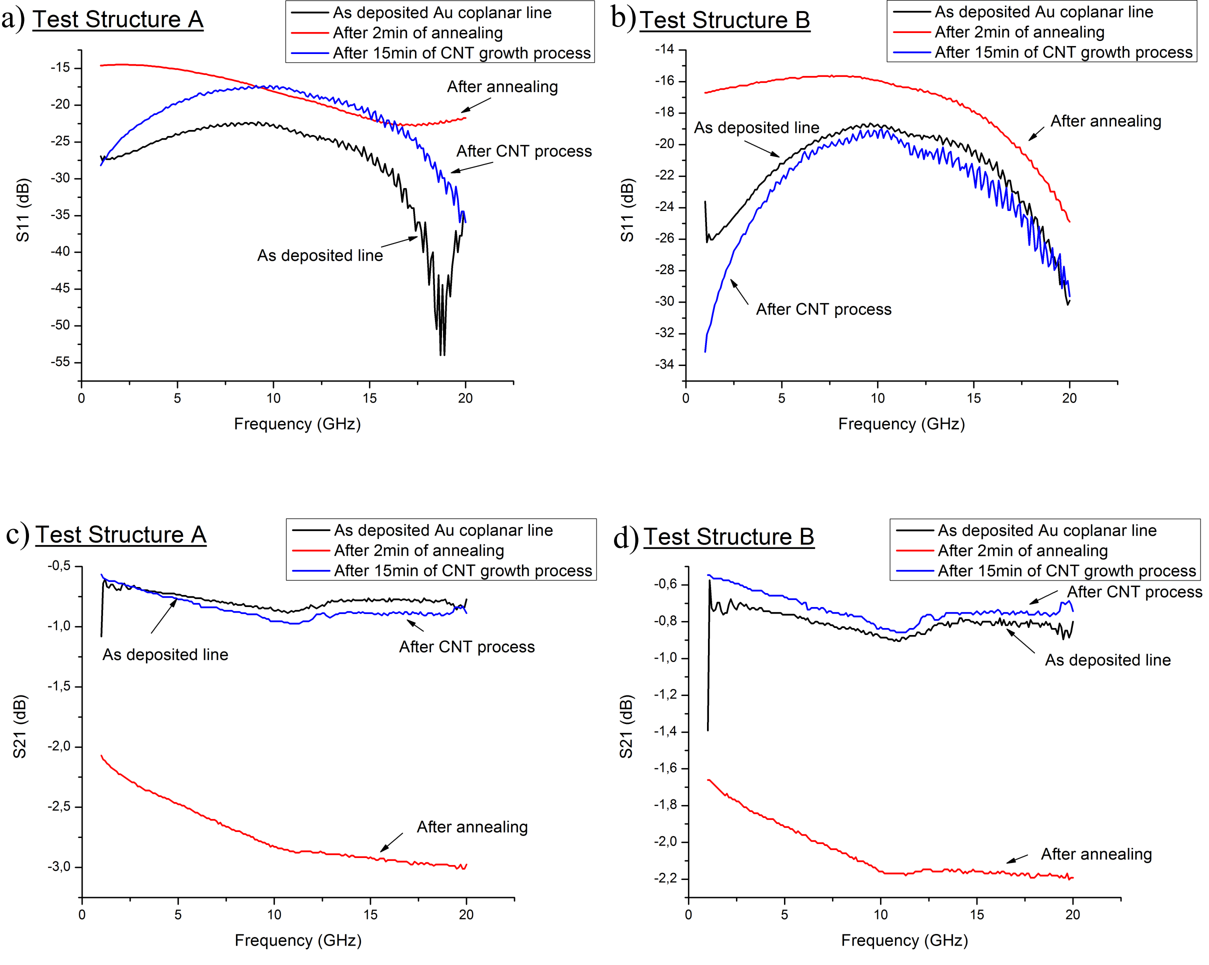

Figure 65: S-parameters of the two test structures A and B: (a) return loss of structure A, (b) return loss of structure B, (c) insertion loss of structure A, and (d) insertion loss of structure B. Note that the peaks at 1 GHz in each S-parameter results above are due to the calibration process for the probe station. The calibration shows no successful results at this frequency.

ii. Influence of the barrier layer on the CNT growth

Figure 66 shows a portion of the test structure observed under SEM and Figure 67 shows the growth of CNT on different barrier layers. As seen in Figure 67(a), the CNTs grown on 50 nm TiN were thinner and denser, whereas the CNTs on 50 nm Ti (Figure 67(b)) and 50 nm Cr (Figure 67(c)) were similar in terms of diameter and density. Residual carbon was more apparent in the CNTs grown on the Cr barrier layer. There was no significant growth of CNTs using 20 nm Ni on Au without the use of a barrier layer (Figure 67(d)). There are reports of nanoscale Au particles acting as a weak catalyst for SWCNTs growth and growth of aligned CNTs using aerosol-assisted CVD [137-140]. However, no CNT growth was observed in our study in the absence of a barrier layer.

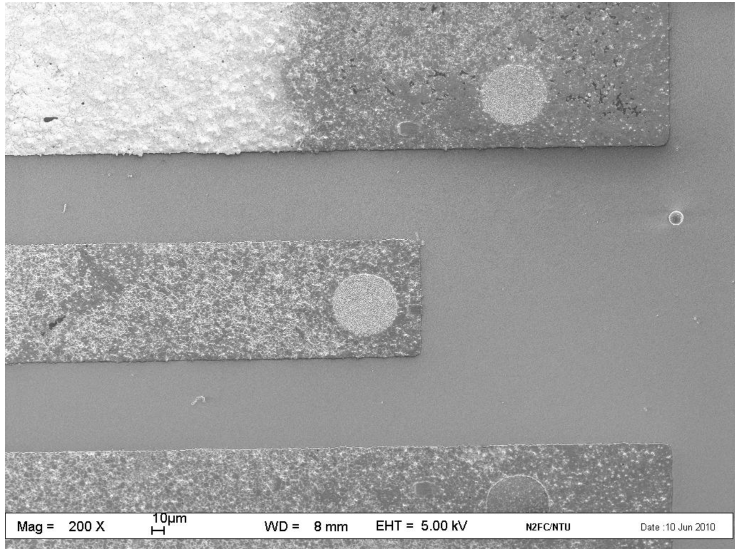

Figure 66: SEM image of the test structure with three Au lines on a silicon oxide surface. The catalyst used for CNT growth is patterned in the circular bumps. The roughness on the Au lines is the result of agglomeration during the PECVD growth process.

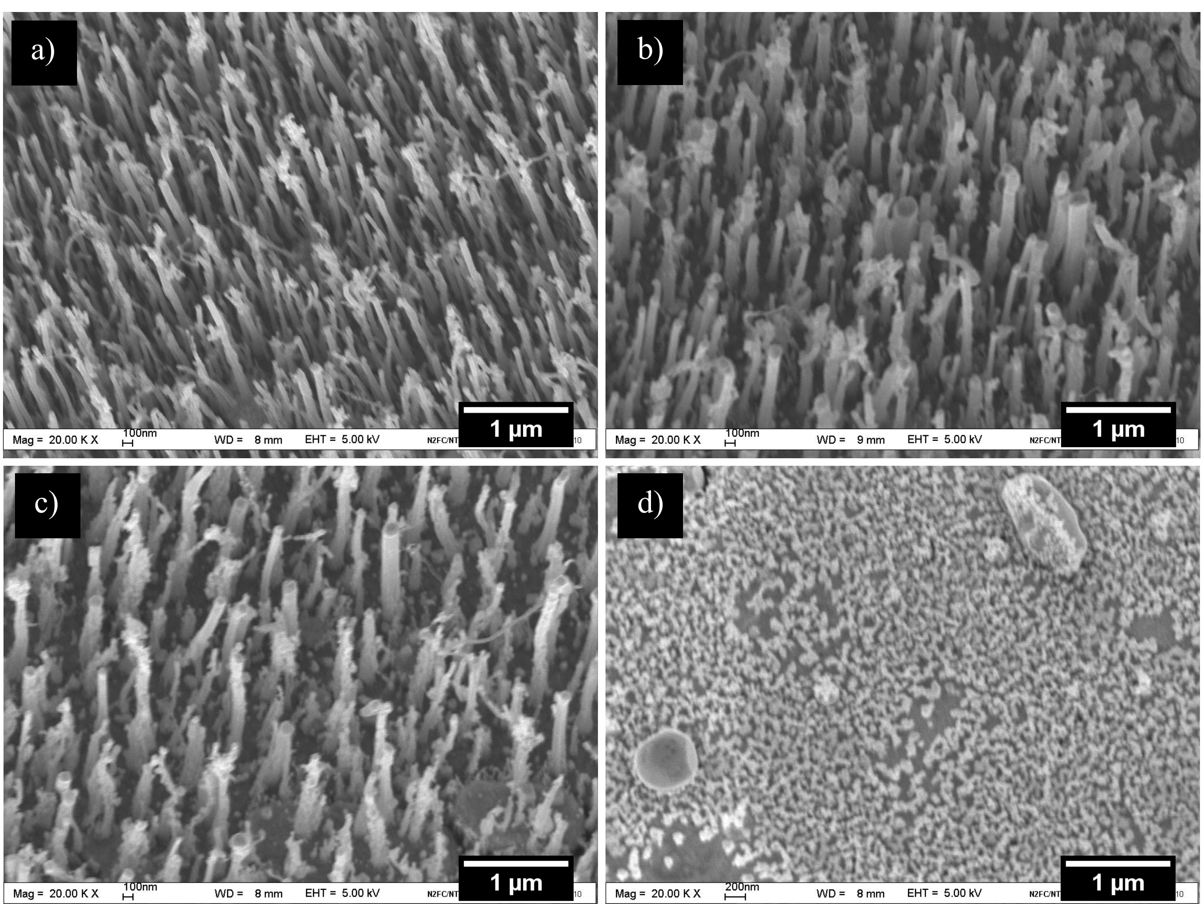

Figure 67: SEM micrographs of CNTs grown using PECVD approach using different barrier layers on underlying Au metallization: (a) TiN, (b) Ti, (c) Cr, and (d) on the Au surface.

iii. Influence of the barrier layer on the CNT quality

Characterization of the ID/IG parameter on the quality of the CNT growth was conducted using Raman spectroscopy as shown in Figure 68. The Raman spectrums have two peaks, which usually fall in the range of 1370–1400 and 1580–1600 cm^{-1}. The former peak is usually known as the D peak, which suggests the presence of defects, whereas the latter is known as the G peak, which indicates the presence of crystalline graphite. By analyzing the Raman spectrum, the type of CNTs present and their structural quality can be identified [130, 141]. Obtaining I_D/I_G as close to zero is usually desired, but CNT produced using PECVD have higher I_D/I_G due to the plasma-induced defects [142] as explained in chapter I.

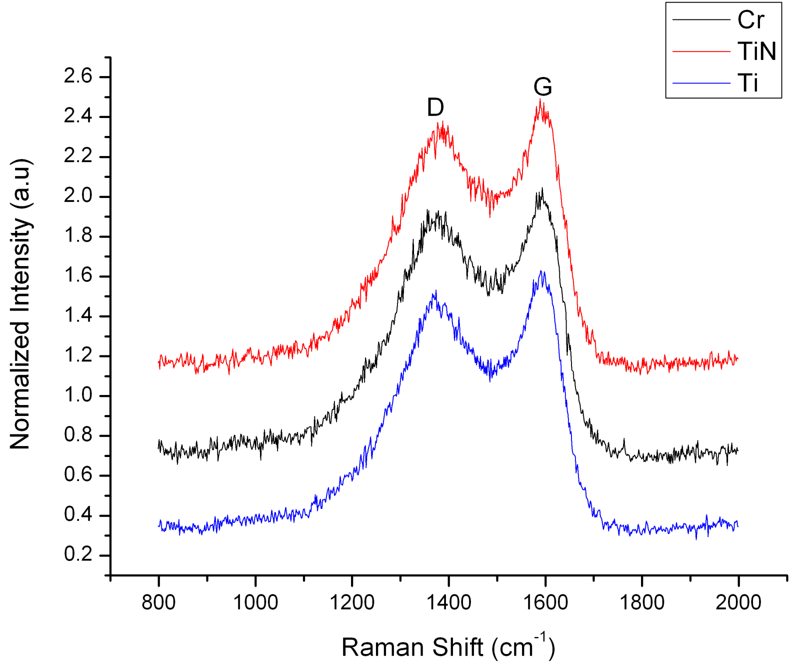

Figure 68: Raman spectrum of the CNT grown on different barrier layers normalized to their G maximum intensity.

Table 10 shows that the CNTs on Ti present the lowest ID/IG data, which correspond to the aligned CNTs images shown in Figure 67(b). An important level of defect on the MWCNT structures appears with values of ID/IG higher than 1. Good quality MWCNTs can show an ID/IG value of 0.6. Even though Sun et al. [142] reported that the quality of CNTs were independent of the Ni thickness and the underlying metal, we believe that the kind of underlying metal used could affect the quality of CNTs growth. Current investigations also show that Ti and TiN were more suitable for the CNTs barrier layer, because they formed silicide phases instead of carbide phases at high temperatures [143]. The formation of

carbides will deplete the carbon source available, degrading the CNTs growth. Therefore, the CNTs on Ti and TiN barrier layers appeared to be more graphitized and have less defects than the CNT grown on Cr. Based on the current study, we proposed to use either TiN or Ti for future barrier layers on Au to grow CNTs.

Table 10: Positions of D and G peaks, calculated I_D/I_G of Raman spectra of CNTs grown on different barrier layer.

Types of barrier layer	**Position of D peak (cm^{-1})**	**Position of G peak (cm^{-1})**	**I_D/I_G**
TiN	1387.7	1589.3	1.225
Ti	1385.5	1588.8	1.192
Cr	1385.4	1588.1	1.248

iv. Conclusion

In this part, we demonstrated that Ti and TiN were the best barrier layers to use to achieve well-aligned bundle of CNTs by PECVD process. We also showed that the PECVD process doesn't affect the RF properties of our gold structures, which is a very important point for the rest of our works. Indeed, we can now imagine fabricating more complex CNT bundle patterns directly on RF devices without affecting the performance. More details on this part can be found in the Yap Chin Chong's thesis report. Current works in CINTRA/NTU are also trying to improve the CNT fabrication process by PECVD in order to get better CNT quality and a better control of the bundle patterns. The Table 11 summarizes the process we defined in the previous part.

Table 11: Process flow summary of the device fabrication including CNT growth.

Process flow:	
CPW gold line fabrication	- High resistivity silicon substrate (400 µm) - Deposition of 700 nm thermal oxide - 10 nm of Ti for a better Au adhesion - 1 µm of Au deposited by ebeam
Catalyst deposition	- 50 nm barrier layer (Ti of TiN) - 15 to 25 nm of Ni catalyst
CNT growth by PECVD	- Chamber pressure of 8 mbar - NH_3 pretreatment for 2 min a 800 °C - CNT growth for 15 min with a C_2H_2 carbon with a ratio of 4:1 (C_2H_2: NH3) - Plasma power at 100 W

B. Flip-chip structure under test

a) Design and fabrication of the flip-chip test structure based on CNT bumps

i. Design of the device

Based on flip chip technology principle presented in the first part, we decided to use CNT bundle to replace conventional metal bumps. Thus, we designed a very simple flip-chip structure composed by 50-Ω coplanar waveguides (CPWs) uniquely in order to verify the feasibility and high frequency transmission along the all device and the CNT bumps. An entire modeling (EM and hybrid EM/analytical) of the device will be done including CNTs interconnection in order to extract some CNT properties such as the contact resistance between CNTs. Matching parts have been added in order to allow us to dispose the probes with the right pitch (150 µm up to 40 GHz) on the three bundle-size configurations we have developed (Figure 69). Indeed, to demonstrate the feasibility of using PECVD approach to achieve fine pitch CNT bumps, three different sets of test structures comprising of (Structure 1) 170 µm by 150 µm, (Structure 2) 120 µm by 100 µm and (Structure 3) 70 µm by 50 µm CNT bumps size were designed (Figure 69 and Figure 76). We also reduce the size of the signal line in regard with the top part of the flip-chip to compensate for the parasitic capacitance we have between the two parts. All other dimensions are given on the Figure 69.

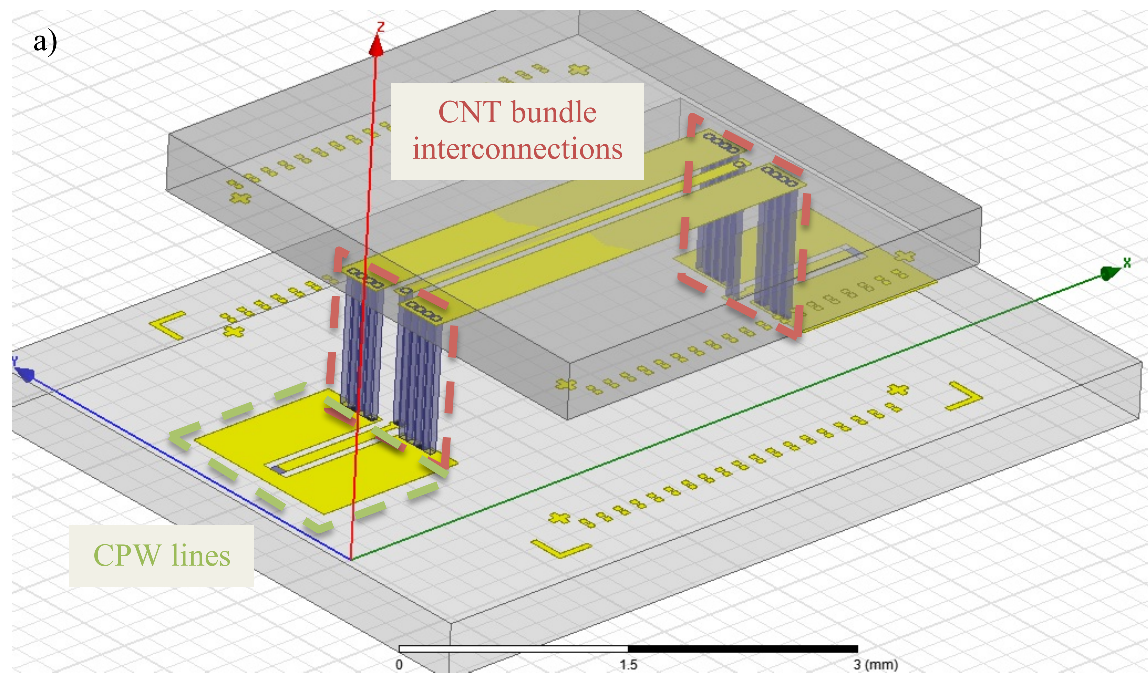

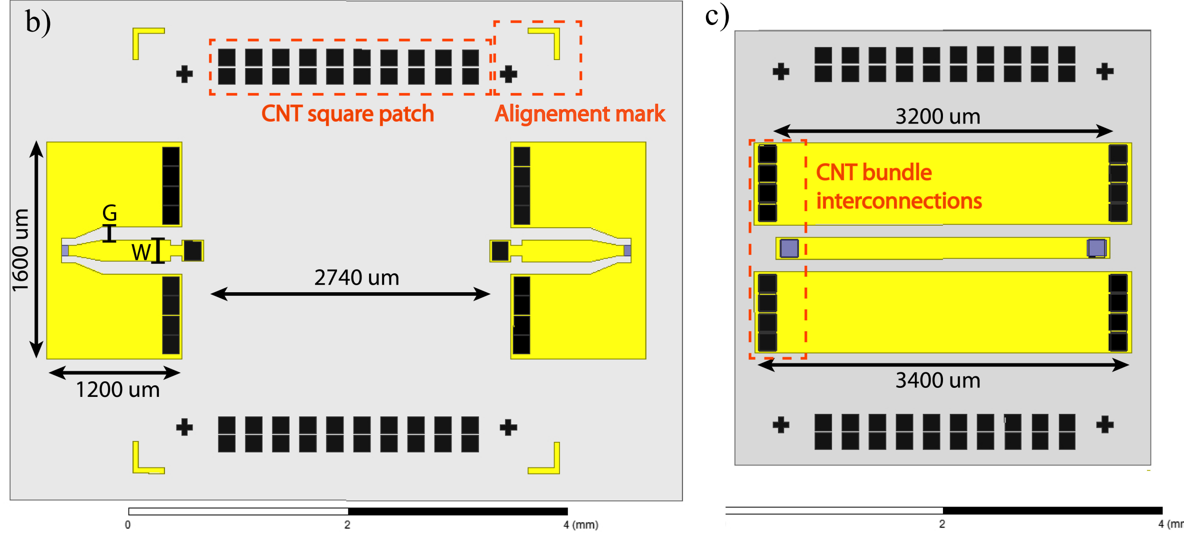

d)

Structure	1 (170 µm by 150 µm)	2 (120 µm by 100 µm)	3 (70 µm by 50 µm)
W /µm	200	150	100
G /µm	115	87	61
Number of CNT bundle	58	74	94

Figure 69: shows the schematic of the flip chip structure been fabricated to test for both DC and RF functionality. (a) the final flip chip after the chip is flipped and combine with the carrier, (b) carrier design which comprises of an ‘open’ coplanar line structure, (c) chip design which comprises of coplanar line, (d) shows the variation of the size of 3 flip chip test structure.

In order to compensate for the alignment accuracy of +/- 10 µm of the bonder machine, the CNT bumps on the metallization lines were deliberately fabricated to be a rectangle. For example, the size of one bump on the carrier is 120 µm by 100 µm, while that on the die is 100 µm by 120 µm. This enlarged bump area helped to decrease the occurrence of open-circuitry and reduced connection resistance due to misalignment [144]. In order to improve the mechanical support between CNT to metal contacts, non-conducting adhesive (NCA) are usually employed [118]. In contrast, we introduced rows of dummy CNT bumps positioned at the sides of the chip and die to increase the densities of CNT bumps. The dummy bumps provided additional mechanical support to hold the weight and leveled the attached die.

This first study will be conducted from DC to 40 GHz regarding to the RF characterization equipment available in the laboratory. The flip chip test structure used in this experiment consisted of a carrier and a die structure as shown in Figure 69. The dimension of the carrier is ~ 6 mm by 5 mm while the die is 4 mm by 4 mm. The choice of barrier layer to grow CNTs on Au metallization and the detailed fabrication details were described on the previous paragraph. Briefly, e-beam evaporation was use to deposit Ti (10 nm)/Au (1 µm) to serve as the metallization layer while a second layer of TiN (50 nm) barrier layer and Ni (15nm metal catalyst for CNT growth) were deposited onto the predefined patterns above the Au metallization using a lift-off technique (Figure 71).

ii. Photolithography process

The photolithography process serves to “print” planar patterns on a substrate. The process uses a mask and a photo resist. The principle is quite simple: after deposition on the all substrate, the photo resist is illuminated locally in order to change the properties of the material. After illumination, the photo resist is removed (positive type) or kept (negative type) and only the desired patterned region remaining. Transparent and opaque areas compose the mask made by glass or plastic in order to localize the illumination of the photo resist (Figure 70). Photolithography consists on 5 steps:

- The wafer is cleaned with isopropyl alcohol (IPA) and acetone in order to remove all impurities that can affect the patterns. The wafer is dried using an air gun and a heater at 110 °C for at least 10 minutes. The wafer surface needs to be polish to facilitate the process.

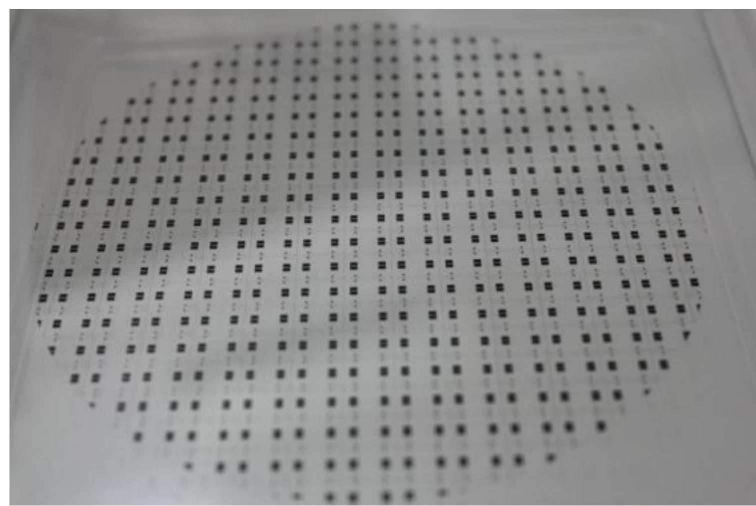

Figure 70: Picture of the plastic mask with carrier line patterns presented in the first paragraph.

- The wafer is disposed on a spin coater and the photo resist is applied on the whole surface. According to the photo resist used, the correct rotation speed and time needs to be set. This information can be easily found on the photo resist datasheet. Ideally, at least twice the thickness of the expected material deposited thickness need to be applied. For example, in our case, we expect a 1 µm-gold metallization, thus, we need to deposit at least 2 µm of photo resist. With the photo resist we are using (ref az5214e), we need 2000 rotations per minute for 30 s.

- Immediately after the spin coating, the wafer needs to be placed on a heater at 110 °C for 30-60s. Again, the time depends on the photo resist used. This step serves to reduce the solvent in the photo resist.

- A first UV exposition is done using the mask aligner equipment. Light exposition lasts for 2.3s and the wafer is heated at 110 °C in a furnace for 8 minutes. Then, a second light exposition without the mask is realized during 23s. This second exposition is used to reverse the photo resist properties from positive type to negative.

- Finally, the patterns are developed using an AZ developer solution diluted in 2/3 of water. The duration of this step is crucial for the success of the patterning. A too long time will over-etch the photo resist while a too short time will under-etch the resist. A sample needs to be used first in order to find the correct time. At the end, ebeam process can be done and acetone will be employed in order to remove the remained photo resist after metal depositions.

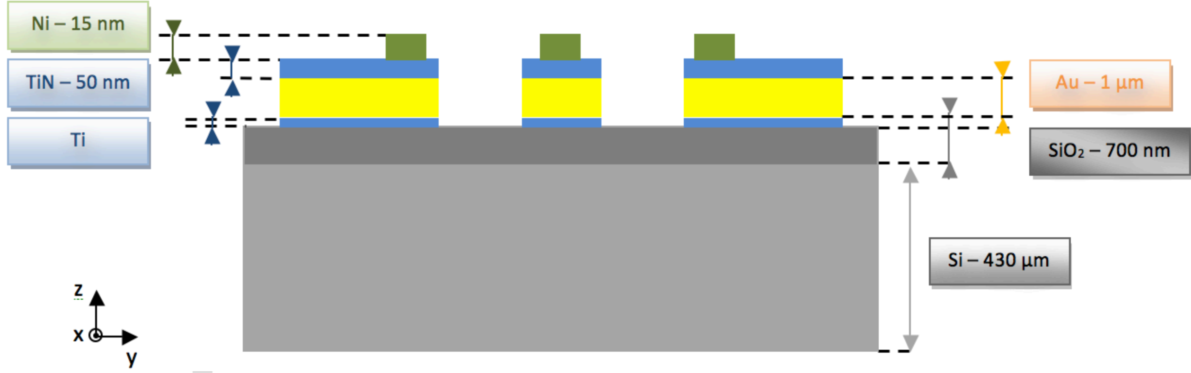

Figure 71: Side view of the deposited layers after two consecutive photolithography followed by ebeam processes. Gold is 1 µm in order to avoid skin depth losses at high frequency. Ti or TiN are used as a barrier layer and Ni as the catalyst for the CNT growth by PECVD.

iii. CNT bundle growth by PECVD

The wafers were dice to their specified dimensions, cleaned in de-ionized water before transferring to a PECVD chamber to perform the CNT growth. The CNT growth was conducted at 750 °C with a plasma power of 85 Watts for 30 min (Figure 72 and Figure 73). The growth pressure was at 6 mbars with a gas ratio of gas of 1:5 (C_2H_2: NH_3). From the literature point of view, there have been reports that using NH_3 during growth results in N-doped of CNT. The NH_3 function is necessary to act as an etchant source and possibly N-dopants according to varies group [145, 146]. CNT bumps height of ~ 20 µm was obtained as shown in Figure 73. Each of these CNT bumps comprised of multi-wall CNT (MWCNT) with an average diameter about 100 nm.

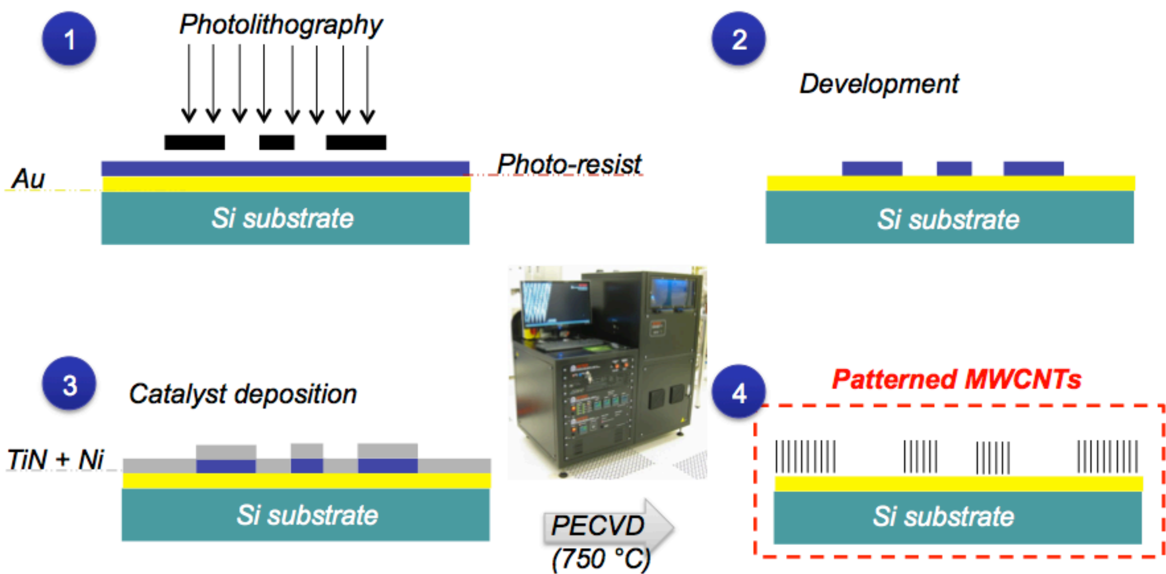

Figure 72: Photolithography, ebeam and PECVD steps to deposit pattern of catalyst material before CNT growth by PECVD. (1) shows the UV illumination of the photo resist using a shadow mask. (2) shows the development of the photo resist in order to remove non-wanted patterns. (3) is the deposition of the barrier layer and catalyst on the all sample by ebeam. Finally, in 4, CNTs are grown by PECVD and all the photo resist is removed in order to keep only the remaining bundle of CNTs.

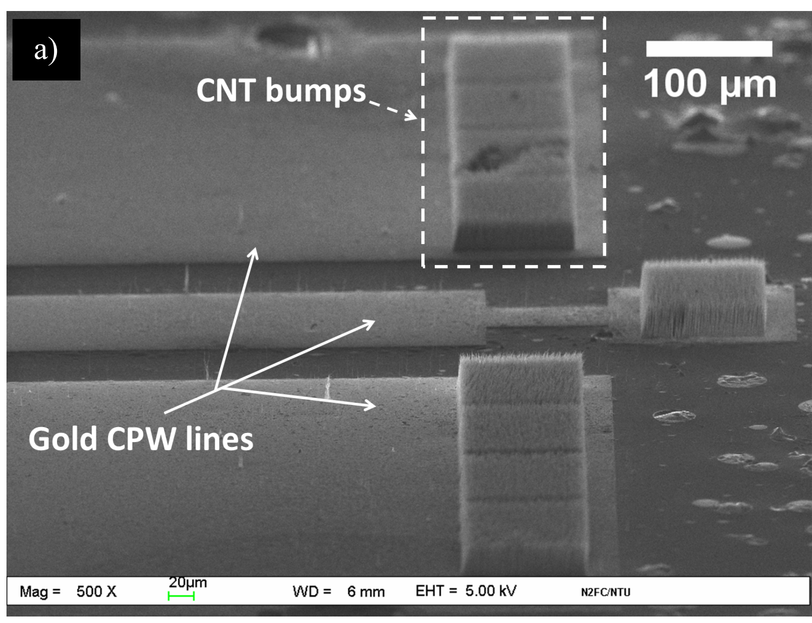

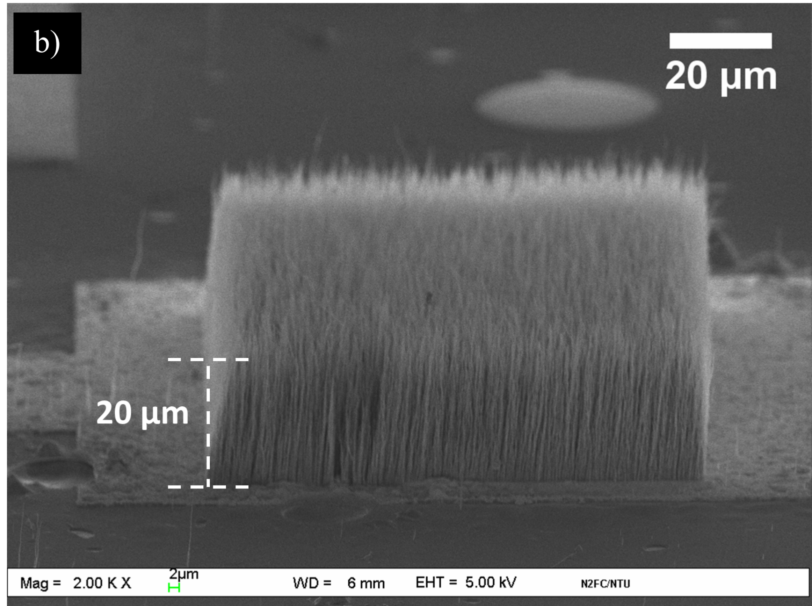

Figure 73: On (a), the low magnification view of the CNT bumps formed on the Au metal lines. On (b), SEM image of a CNT bump grown using PECVD approach. The grown CNTs were vertically aligned and their length was approximately 20 µm.

iv. Flip-chip bonding

Subsequently, a Panasonic flip chip bonder machine was use to perform the die alignment and attachment. The top part of the flip chip was flipped at 180° above the bottom part and a downward force was applied (Figure 74). A load setting from 0.5 to 3 kg with a bonding time of 30 sec was used as the bonding parameter.

The bonding load of 0.5 kg was sufficient to cause the CNT from the bottom carrier to 'insert' and touch the top die. The load of 0.5 kg which is equivalent to 4.5 N or 3.125 kg/cm^2 is much lower than those applied in previous reported flip chip experiments [33, 118, 120]. However, the load of 1.5 kg was found to provide the optimum electrical properties. Indeed, a higher electrical resistance was obtained when a low load (0.5 kg) was applied on it [147]. We believed that the CNTs start to be compressed when a larger load was used (greater than 1.5 kg), just like in the work of Soga [120]. Indeed, with a load of 3 kg, we obtained the higher rate of successful devices but all the time, the achieved resistances were higher than the one measured with an applied load of 1.5 kg. We believed the compression increased the depth of penetration and the chances of CNTs contact with each other (Figure 75). Once the bonding process is completed and the load removed, CNTs returned to its original vertical configuration. No bonding temperature was used in our experiment. Finally, we noticed that the mechanical adhesion between the two parts was good enough to carry and measure in

DC/RF our structures, but too weak to perform a stress test of the device. Thus, an improvement of the mechanical adhesion between the two flip-chip parts needs to be investigated.

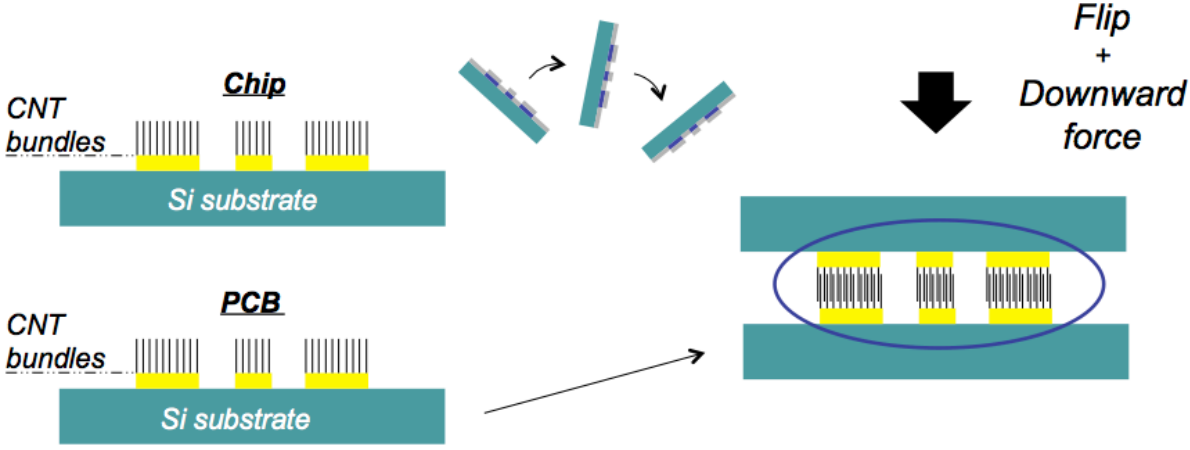

Figure 74: Principle of the flip-chip using interconnected bundle of carbon nanotubes. Top part (chip or die) is rotated at 180° above the bottom part (PCB or carrier) and a downward force is applied on it. CNTs will stick together by the electrostatic and Van der Waals forces.

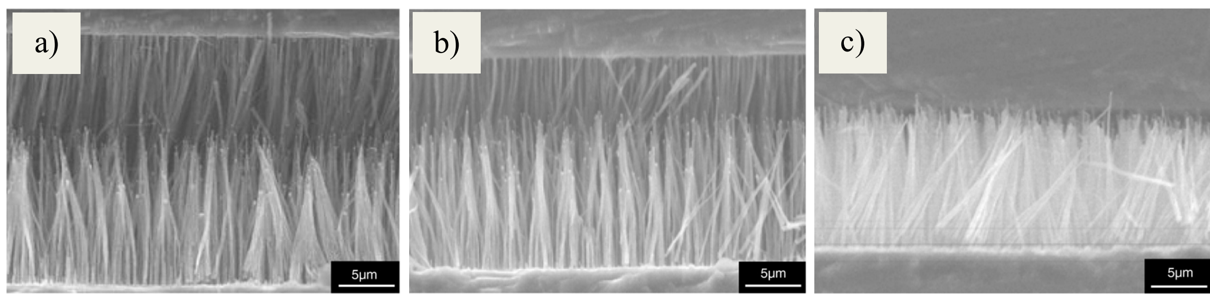

Figure 75: Interconnection length regarding the force applied: no load (a), 0.03 g (b) and 3 kg (c). At 3 kg, the interconnection length is maximal. Source: [124]

b) Results and discussion

i. Fabrication results

To demonstrate the feasibility of using PECVD approaches to achieve fine pitch CNT bumps, the three different sets of test structures (Figure 76) were fabricated. The SEM images in Figure 76 show the CNT bumps grown using the PECVD approach allows pitch sizes down to 80 µm (70 µm bump size + 10 µm distance between two bumps) with our experiment. Homogenous CNT bumps height can also be observed throughout the carrier and die (Dummy and CNT bumps on electrodes). Larger catalyst pattern geometry would result in

longer CNT length due to the differences in partial pressure of carbon feedstock gas [148]. However, the effect of catalyst pattern geometry was not significant in this experiment, and the height of all CNT bumps was assumed to be 20 µm regardless the bumps dimensions.

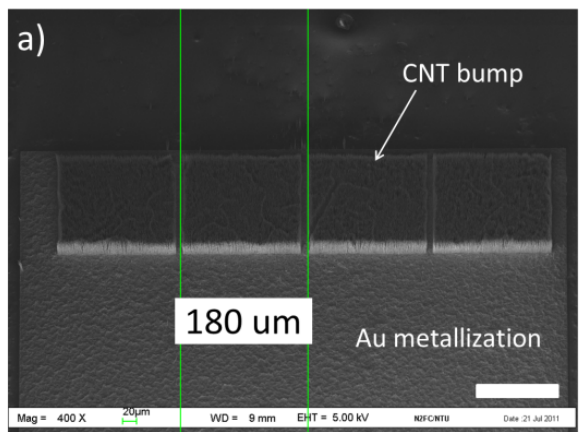

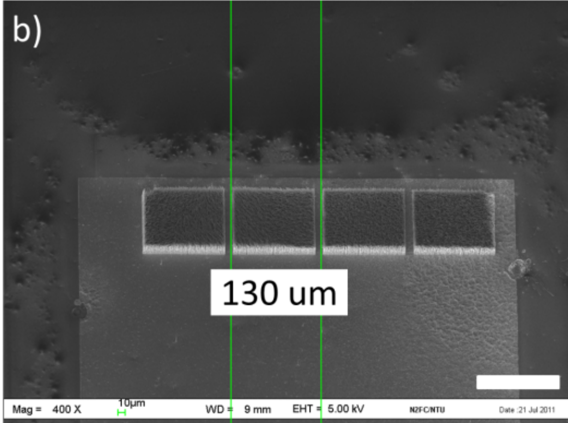

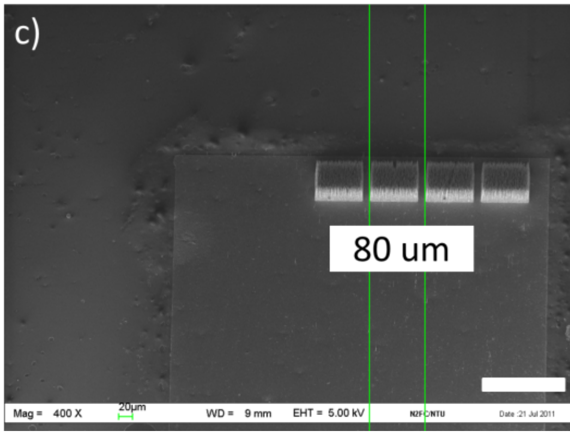

Figure 76: illustrates the CNT bumps on Au electrode with 3 different pitches. The smallest pitch designed is 80 µm in this work. The dimension of each CNT bump in (a) Structure 1 is 170 µm by 150 µm, (b) Structure 2 is 120 µm by 100 µm, and (c) Structure 3 is 70 µm by 50 µm. The scale bar at the bottom right of each image represents 100 µm.

Thus, for the first time, CNT interconnection bump joining methodology for fine pitch bump has been achieved, as shown on Figure 77 and Figure 78. In Figure 78a, the flip chip test structure was observed at an angle of 75° under the SEM. The assembled final structure, as shown in Figure 78b,c and d, is separated by an average distance of 20 – 25 µm as observed in the SEM micrograph. It is also observed that, some carbon nanotubes are able to reach the opposite part and be in contact with it, creating alternative paths to the CNT-CNT interconnections. A combination of both contacts could improve the device performance. Due to the equipment limitations, microphotographs of the CNT bumps during the bonding and release process could not be performed to demonstrate the mechanical flexibility of CNT bump as observed by Soga et al. [120]. However, based on the SEM images in Figure 78c-f,

the vertical alignment of CNT bump can still be observed, which is likely due to the mechanical flexibility of CNT bumps.

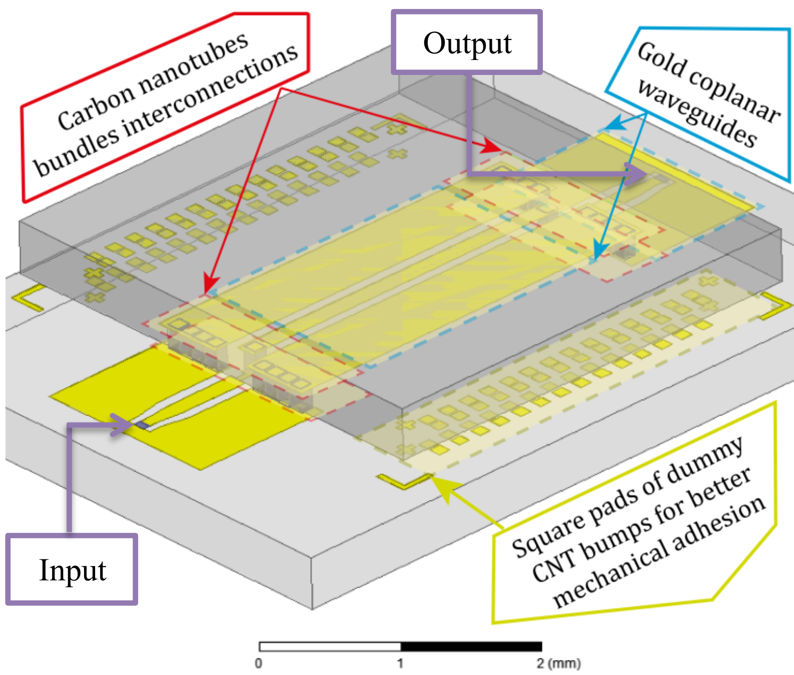

Figure 77: Schematic view of the assembled final flip-chip device.

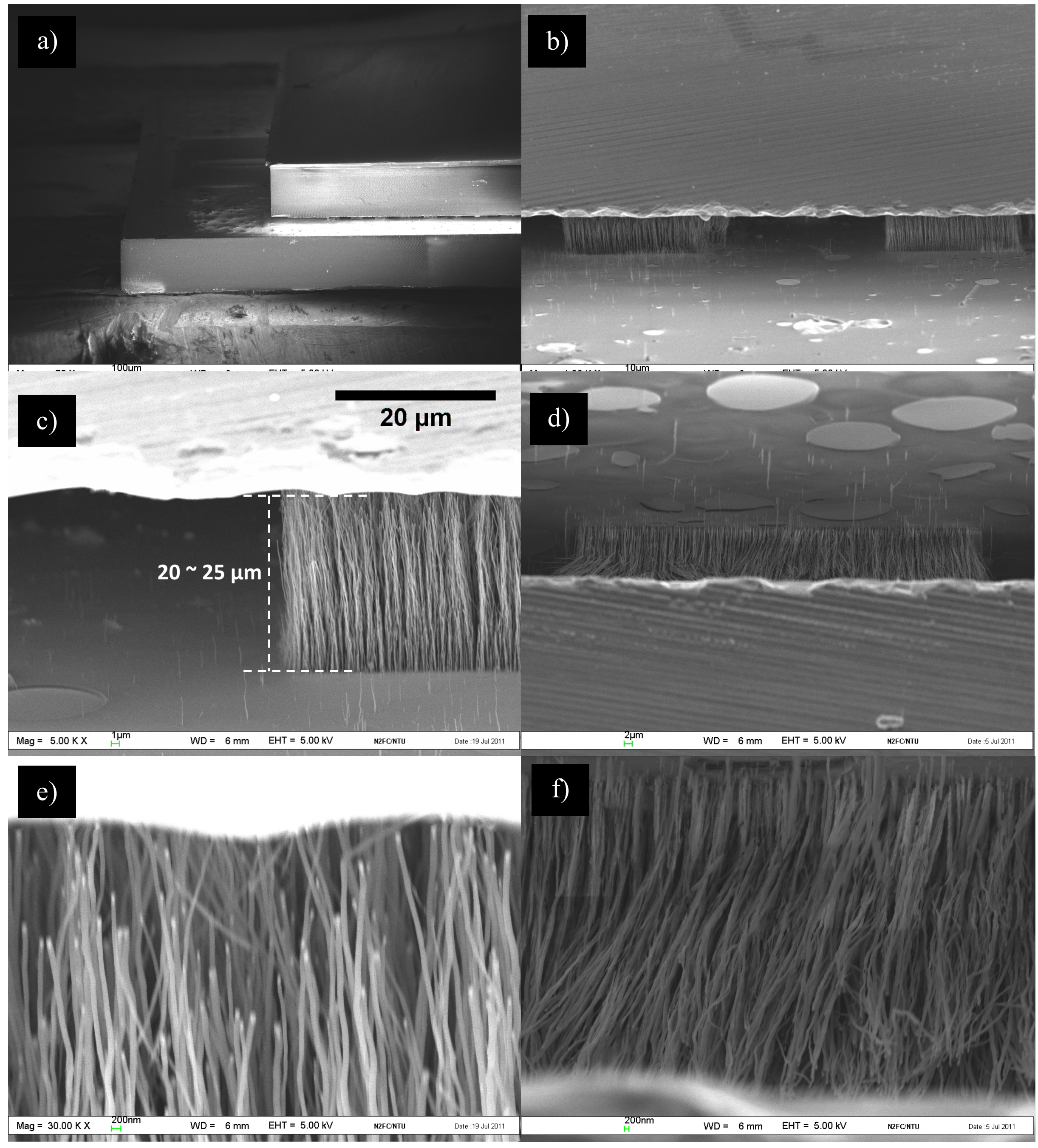

Figure 78: SEM images of the CNT interconnection bumps demonstrated using a flip chip concept (a-f). The dimensions of CNT bumps were 100 µm by 100 µm for all images. (a) Die attached to carrier at a tilted angle of 75˚, (b) magnified view of 2 CNT interconnection bumps, (c-d) show the distance separating the two parts of the flip-chip, (e) CNTs from bottom carrier were observed to be touching the die substrate indicative of the connections made and (f) shows the CNTs touching each others.

In this experiment, structures 1 (170x150 µm bump size) and 2 (120x100 µm bump size) were tilted to 75° in the SEM to observe the gap between test structures. This is remarkable as no bonding temperature or adhesive were used during this bonding process to mechanical bond the die to carrier. However, for the structure 3, the die tended to slide off its carrier during movement of the SEM stage. The dummy bumps in structure 1 and 2 were

effective to hold the weight of the die (16.5 mg), but not in structure 3. Assuming perfect alignment, the area occupied by a total of 74 CNT bumps on structure 2 is 0.74 mm^2 out of 16 mm^2 (die area). On the other hand, the area occupied by CNT bumps in structure 3 is 0.185 mm^2 out of 16 mm^2. This is logical because the dummy bumps in structure 3 were smaller as compared to those in structure 1 and 2. Based on structure 3, future designs using CNT interconnection bump will require more than 1.2% coverage of CNT bumps area to die area for sufficient mechanical support. This is to ensure that the bonding forces present within the CNT interconnection bumps are greater than the die weight to ensure mechanical stability. A study based on total energy and molecular dynamics calculation molecular on CNT to CNT joining methodology shows that the type of bonding between CNT to CNT is very strong, and force larger than of 3 nN will be required to disengage the joining structure [149]. Yung et al. suggested the van der Waals forces between CNT to be the bonding mechanism when CNT were 'inserted' into each other [124]. In this work, only the dimensions of bumps (area) were varied, the influence of densities and diameter of CNT within a bump may also be an important consideration to CNT bonding mechanisms as we will see later with work on modeling.

The attached die was subsequently removed from the carrier using a tweezers to observe the effect of the CNT bumps after bonding. The carrier and die were then loaded into the SEM chamber with the same orientation to observe the CNT bumps conditions that were in contact with each other, as shown in Figure 79. A portion of the CNT bump appeared to be smeared as seen from Figure 79a, but a high percentage of CNT bump retained their original structure. This is similar to Yung et al. observations for large scale CNT to CNT interconnects structure, which demonstrated that the bonding process is re-workable [124].

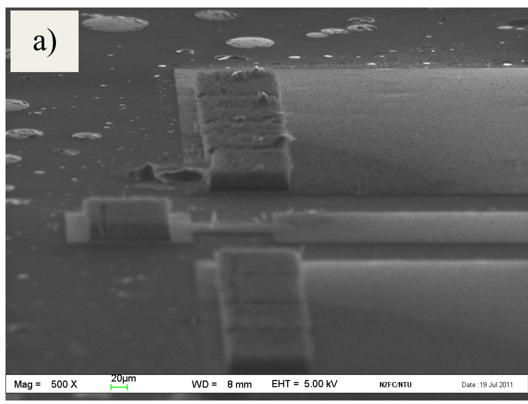

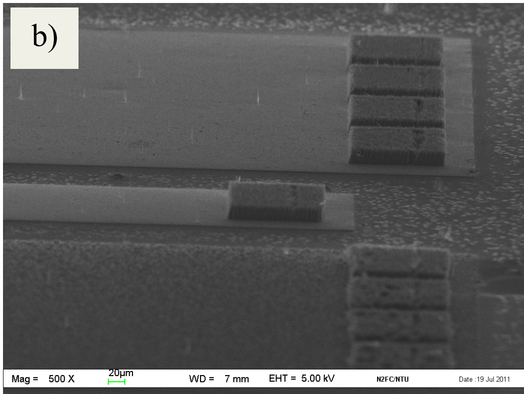

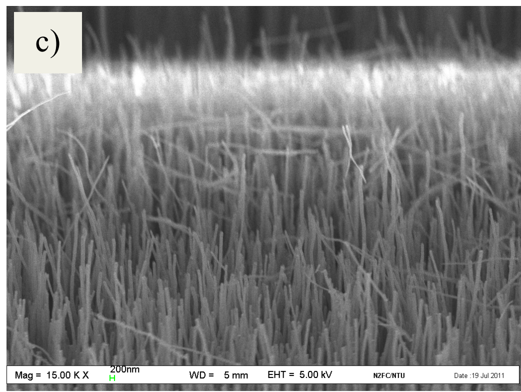

Figure 79: SEM images of the CNT bumps morphology after top die removal. (a) CNT bumps on the carrier, (b) CNT bumps on the chip joined to the carrier bump in (a) and (c) a magnified view of the bump. The remaining vertical alignments of the CNTs show the mechanical flexibility of CNTs.

ii. DC measurements

Once the carrier and die are mechanically linked by CNT bundles with electrostatic and Van der Waals forces, an I-V measurement is carried out using a two-point probe measurement. The measurements are performed between the input and output of the carrier lines (see Figure 77). Ground to ground and signal-to-signal resistances are extracted. We decided to show in this report the three lowest resistances we have achieved. An ohmic contact has been achieved with all our samples while the topology of the flip-chip devices remained the same. In these 3 samples, the lowest resistance is obtained by the device a (Figure 80) with a 12.5 Ω total resistance (measured from the input to the ouput of the flip-chip signal line). For other structures, a total electrical resistance between 100 Ω (device b) and 500 Ω (device c) are obtained as shown in Figure 80. Most of the time, the resistance obtained was too high (several kΩ) to believe we have a suitable interconnection between the two parts.

All devices a, b and c are fabricated undergone the same conditions and at the same time. However, all samples are not on the same location on the substrate holder, which can create small discrepancies on the CNT growth in term of length and alignment. Moreover, because of the non-perfect CNT uniformity on the bundle in term of inter-tube distance between CNTs and because of the low CNT density, the number of CNTs available for interconnection is different from the number of interconnects made during the bonding. Finally, as we already said, the flip chip bonder has a tolerance of ± 10 microns: for a 150 × 150 µm bump (structure 1), a 1 µm shift during the flip chip process represents a shift of 150 µm^2 bump square (calculated by 1 µm shift multiplied by 150 µm square bump size), which is about 1000 CNT candidates that won't be interconnected (we had an estimated number of

CNTs of 135 000 for a bump surface of 150x150 μm^2 and a CNT density of 6 CNTs.μm^{-2}). This tolerance can create a shift in results we obtained, leading to the random aspect of the interconnection result. Thus, this DC resistance shift could have been caused by a low-density bundle, and/or misalignment between carrier and die during the flip chip bonding process (± 10 µm tolerance), which resulted in a random number of CNTs linked in each sample. However, a higher CNT density will reduce the distance between CNTs and so increase the number of CNTs interconnected and finally improve the repeatability. As reported previously, an average MWCNT diameter of 100 nm had been observed using a scanning electron microscope. The average distance between CNT to neighboring CNT was also measured to be between 200-500 nm. Thus, inter CNT spacing within the bundle is large (about 500 nm) compared to the carbon nanotube diameter (100 nm) resulting in weak Van der Waals force interaction and huge tunneling resistance.

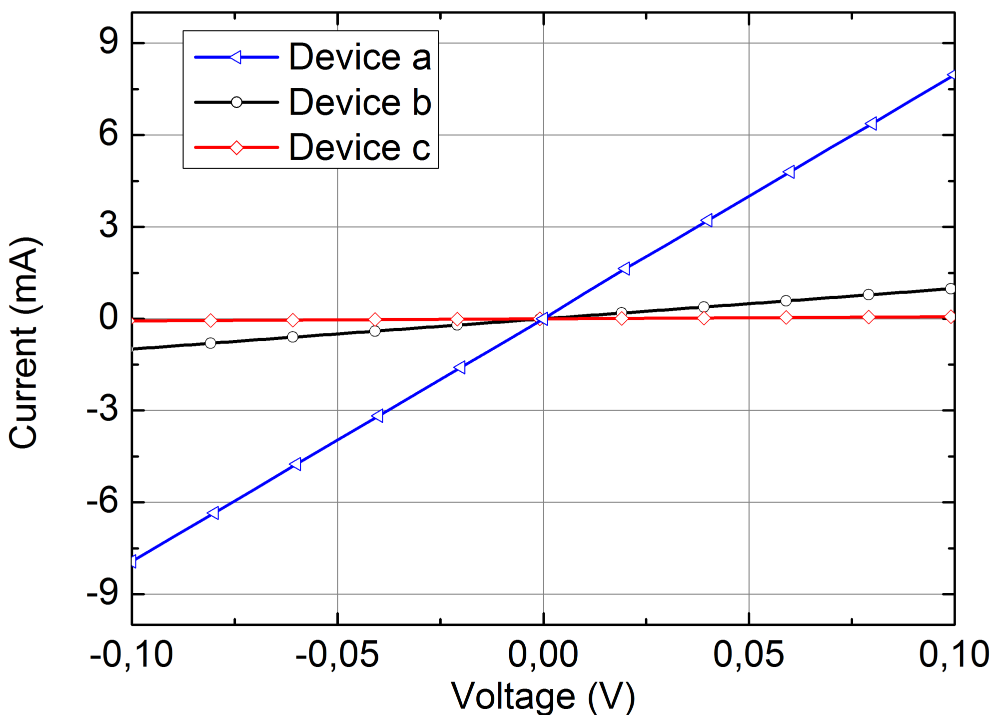

Figure 80: I-V measurements from the input to the output signal line for 3 samples. On blue curve (device *a*), a resistance of 12.5 Ω was extracted. Other devices returned a resistance between 98 Ω (device *b*) and 500 Ω (device *c*).

$R_{CNT-CNT}$ (the contact resistance between two carbon nanotube) is affected by the chirality of the CNT, the interface area, the gap between the CNTs and the interface imperfections [150, 151]. It is now a common knowledge that the properties of the CNT within the CNT bump cannot be the identical and that the CNT varies in terms of diameters

and chirality. However, the work functions for CNT are identical as they share the same graphene band structure. For MWCNT, majority of the current only pass through the outermost layer of MWCNT, and a metallic behavior is expected [152]. Even if the MWCNT is metallic, the bandgap of a semi-conducting MWCNT shell can be estimated by $E_g = \frac{(2\gamma b)}{D}$ (explained in chapter I, section "Semi-conducting properties on page (18)", equation (2)), which approximate a bandgap of 9 meV for CNT diameter of 100 nm [126]. In this case, the Fermi level of the CNT in contact with another CNT will align within the bandgap of the semi-conducting CNT. The resulting band structures have negligible schottky barrier height due to the small bandgap. Thus the metal to CNT and CNT to CNT interfaces are similar to metal-to-metal junctions. The major transport mechanism for electron transport is then through tunneling across air gap resulting in an ohmic and linear I-V behavior observed in Figure 80 and [151].

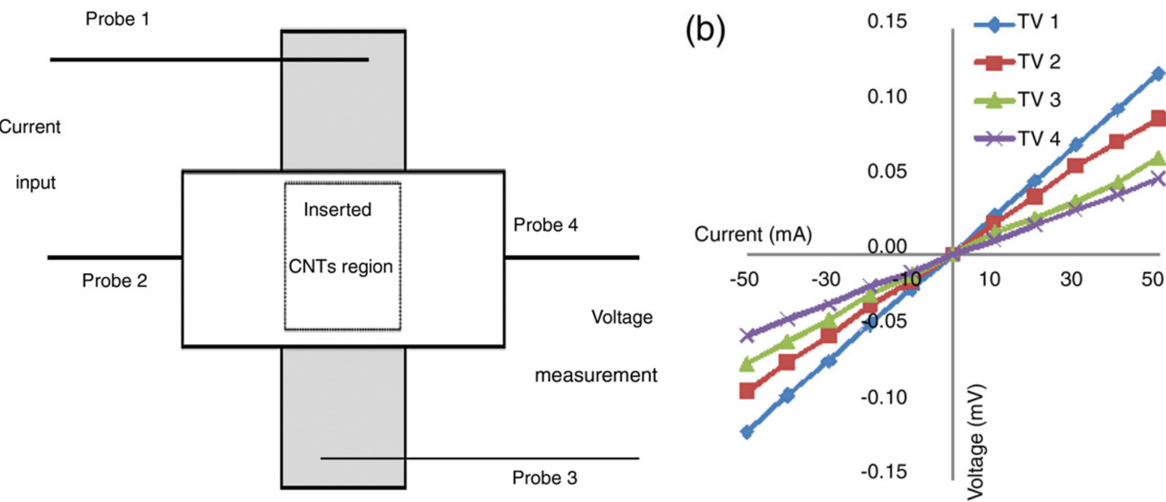

Figure 81: On (a), schematic of the four-point-probe measurement set-up. On (b), the corresponding DC measurements fro 4 penetrations forces (0.00003, 1, 2 and 3 kg respectively corresponding to a penetration length of 3.6, 7.3, 11.1 and 15 um). Source: [124]

From the literature, typical resistance between individual metallic CNT to metallic CNT separated by van der Waals distance of 0.34 nm is 200 kΩ [144]. In our work, the gap may be much larger than 0.34 nm, resulting in huge tunneling resistance through the air gap and absorbents [153]. Nevertheless, the results obtained from other experiments involving CNT to CNT contacts displayed positive results and outlook for use as alternatives to solve the high contact resistance between CNT tip to metal [64, 124]. Contact resistances of 16 and 45 kΩ between two carbon nanotubes were found in [64]. On [124], a resistance of 1 mΩ, when a 3 kg load was applied, was found using a similar flip-chip approach using CNT

bundles as interconnections (Figure 81). Thus, all these observations can be used to improve our process and the performance of our future devices. We are already satisfied by the current performance of our device, which proves the feasibility of our innovative way to interconnect CNTs using flip-chip technology.

iii. Repeatability of the flip-chip contact

To verify the CNT interconnection bundle resistances as well the concept of re-workable capabilities of the joining methodology, the die of test structure 1 was removed, and bonded to the same carrier again to measure the I-V characteristics. Using two-point probe, the DC measurement was performed across the input and output nodes (2 CNT interconnection bumps) as described in Figure 77. I-V measurements in Figure 82 displayed similar DC behavior, which seemed to demonstrate the concept of re-workable process. The slight deviation of “attempt 2” could be caused by the differences in die placement due to the limited alignment accuracy of the bonding machine. The current increased almost linearly with the voltage applied, indicating ohmic contact have been achieved between CNT and metallization [154]. The small variation in the resistance linearity can be due to the higher electrostatic forces existing between CNTs with a higher applied voltage. The line of “attempt 1” was fitted linearly to obtain a slope of 4.20 x 10^{-4} A/V. This indicates that a CNT interconnection bundle resistance of 1190 Ω was achieved. This resistance value is still too high to think about a plug/unplug system. However, we have a first proof of the re-connectivity of our devices. Further investigations need to be realized.

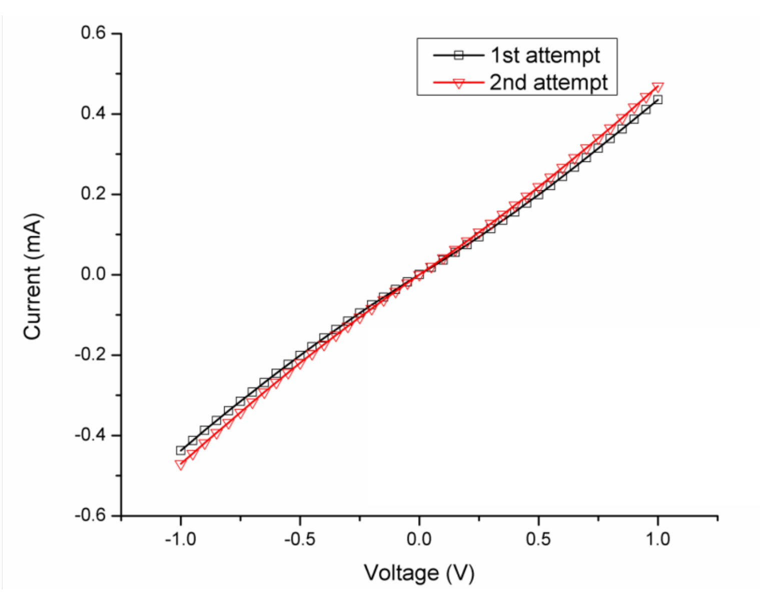

Figure 82: Two-point probe DC measurement across two interconnection bumps measured across the input and output of the carrier substrate. The CNT bumps dimension were 150 µm by 150 µm.

iv. High frequency measurements

Several high frequency measurements from 1 to 40 GHz are also performed on the flip-chip structures. Measurements are run with a vector network analyzer (VNA) Agilent HP8510C and 150-µm pitch Cascade Microtech Infinity probes. A Thru- Reflect-Line (TRL) calibration process is done before each measurement with a maximum error bar equal to 0.1 dB. TRL is a calibration process done before a high frequency measurement by a VNA. This calibration process consists of replacing the device under test by a thru line, a short circuit and finally a load circuit at 50 Ω. After this calibration, the losses caused by the equipment (cables, probes,..) will be omitted.

As explained in the previous part, the DC resistance varies between devices (*a*, *b* and *c*) resulting in difference in signal transmission between input and output accesses. However, a S_{21} parameter between -1 and -4 dB for samples *a* (structure 1: 170x150 µm bump size) and *b* (structure 1: 170x150 µm bump size) on all the bandwidth (1-40 GHz) is noticed (Figure 83). As shown on Figure 83 and Figure 84, device *a* exhibits a S_{21} parameters of -1.21 and -3.69 dB along the flip chip structure operated from 1 to 40 GHz. For the first time, this later gives the proof of high frequency transmission in the flip-chip device composed by carbon nanotube bundles. The return loss (S_{11}) stayed below -13 dB for the same device a. The small variations above 30 GHz are due to the calibration process, which returns a measurement error between 0.1 and 0.2 dB on some frequency points.

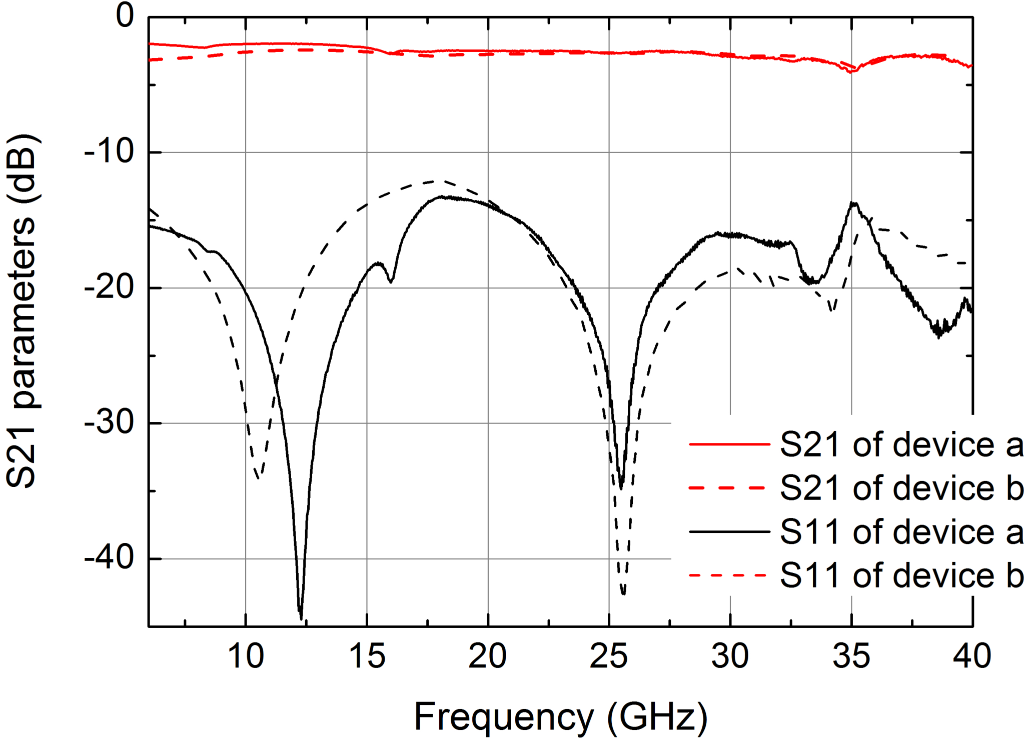

Figure 83: S-parameters measurements of the flip chip device *a* (solid lines) and device *b* (dash lines) between carrier input and output.

Comparing devices a and b, both samples were carried out in one process, meaning the CNT density was the same for both devices. However, device a shows a lower DC resistance (Figure 80) and the HF transmission increased by 1 dB below 20 GHz (Figure 84). At higher frequency (above 20 GHz), we believe the capacitance effect between gold lines on carrier and die parts overlap the 1 dB difference between device *a* and *b*. The S-parameters of the device *c* with lower performance (S_{21} between -12.5 and -5 dB and S_{11} below -7 dB) are presented on the Figure 85. Misalignment and the low carbon nanotube density in the bundle during the bonding process can result in more, or less CNT being interconnected and affect the DC resistance and HF transmission. For a better transmission, the carbon nanotube density should be evaluated in order to obtain better CNT contact and to compensate for the existing misalignment during the flip chip bonding. At the experimental stage, we consider that the proof of concept of HF CNTs based flip-chip is demonstrated. As mentioned, these results show encouraging performances.

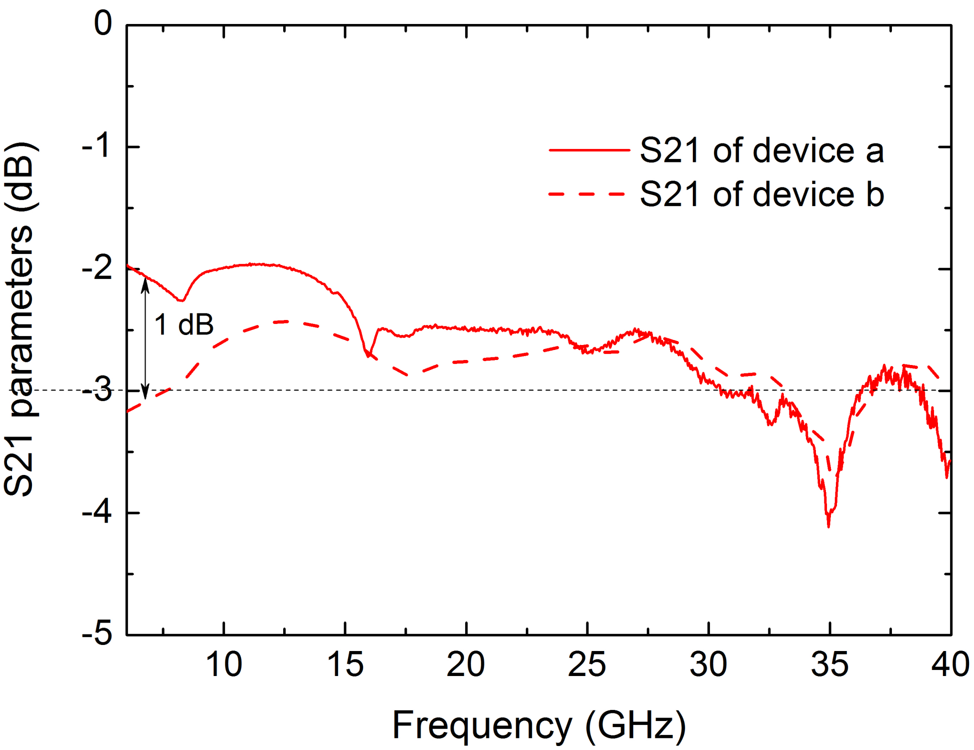

Figure 84: S_{21} parameters of device a and b between 6 and 40 GHz. HF transmission is increased by 1 dB at low frequency between device *b* and *a*.

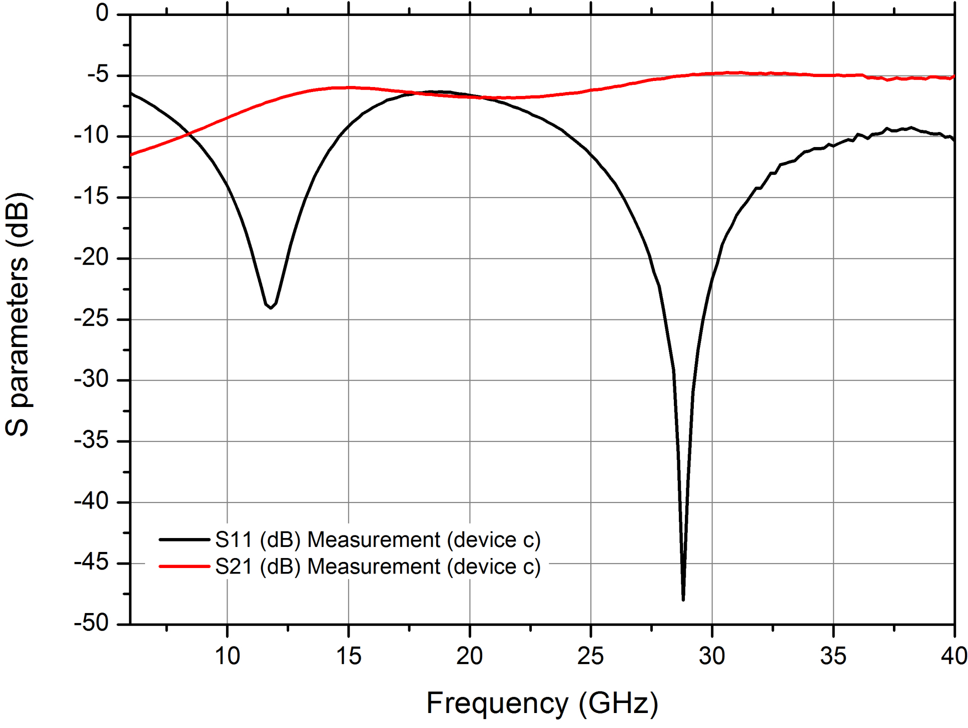

Figure 85: S-parameters measurements of the flip chip device *c* between carrier input and output.

We also measure up to 40 GHz the S-parameters of CPW lines on the top part of the flip chip before and after the PECVD process. The length of the CPW top line is 3.2 mm. As we can see on Figure 86, insertion losses before and after the CNT growth process remain near -1 dB while the return losses remain below -20 dB.

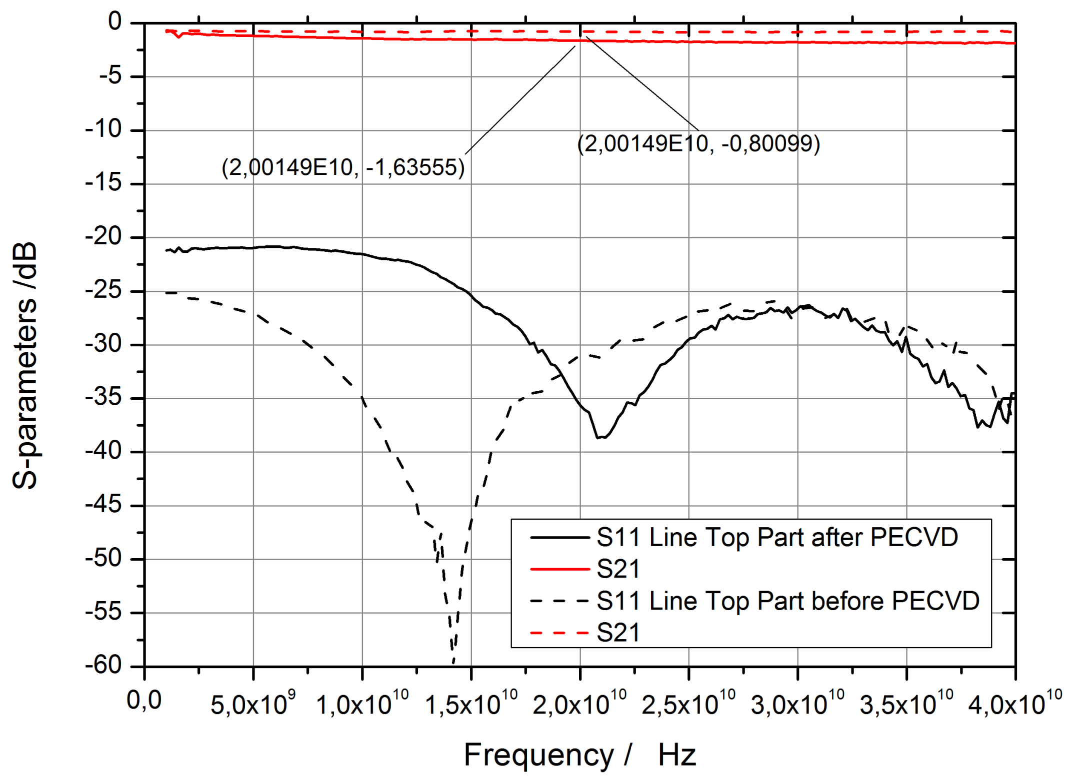

Figure 86: S-parameters measurements of the CPW transmission lines placed on the die before and after PECVD process.

The Figure 88 gives in details S_{11} and S_{21} parameters of the lines compared to our flip-chip performance. After PECVD, the line insertion loss was -1.6 dB at 20 GHz with 0.1 dB max calibration error. The insertion loss of the flip chip structure was -2.5 dB at the same frequency point (20 GHz). Then, for a total length of 5 mm from the input to the output of the flip-chip device, which represents losses of -2.5 dB (-1.6 dB for a length of 3.2 mm), we can also deduce that the insertion losses from the CNT interconnections are negligible in high frequency.

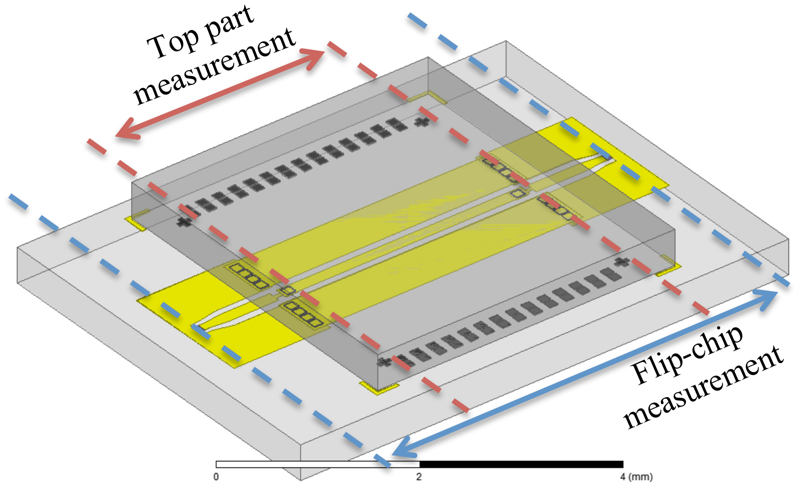

Figure 87: Top side view of the flip-chip device with the top scale.

Thus, we can make several observations. First, the PECVD process has increased by 0.5 dB the losses of the lines, which is in agreement with structure A on the test done in section "Results and discussion on page (113)" (see Figure 65). Secondly, the negligible losses in RF due to the CNT bumps need to be understood with caution. Indeed, if we take a look on the DC measurements (Figure 80), we obtained two different values of resistance for the device *a* and *b* whereas their RF measurements are quite similar (Figure 83). Thus, the increase of the resistance for device *b* can only be due to the CNT bumps since the gold lines were fabricated following the same process (1 µm of gold deposited by ebeam process). But if the RF S-parameters remain the same for device *a* and *b*, it means we can have some capacitance coupling overlapping the transmission from the CNT bumps. Also, a resistance of 12.5 Ω for device *a* it too high to attribute it on the 1-µm-gold layer itself. Therefore, the measurement in Figure 86 cannot ensure we have a negligible resistance of CNT bundles. However, we can surely consider the losses from the CNT bundles are low. Finally, these results show a very encouraging low resistance using carbon nanotube as flip chip interconnection.

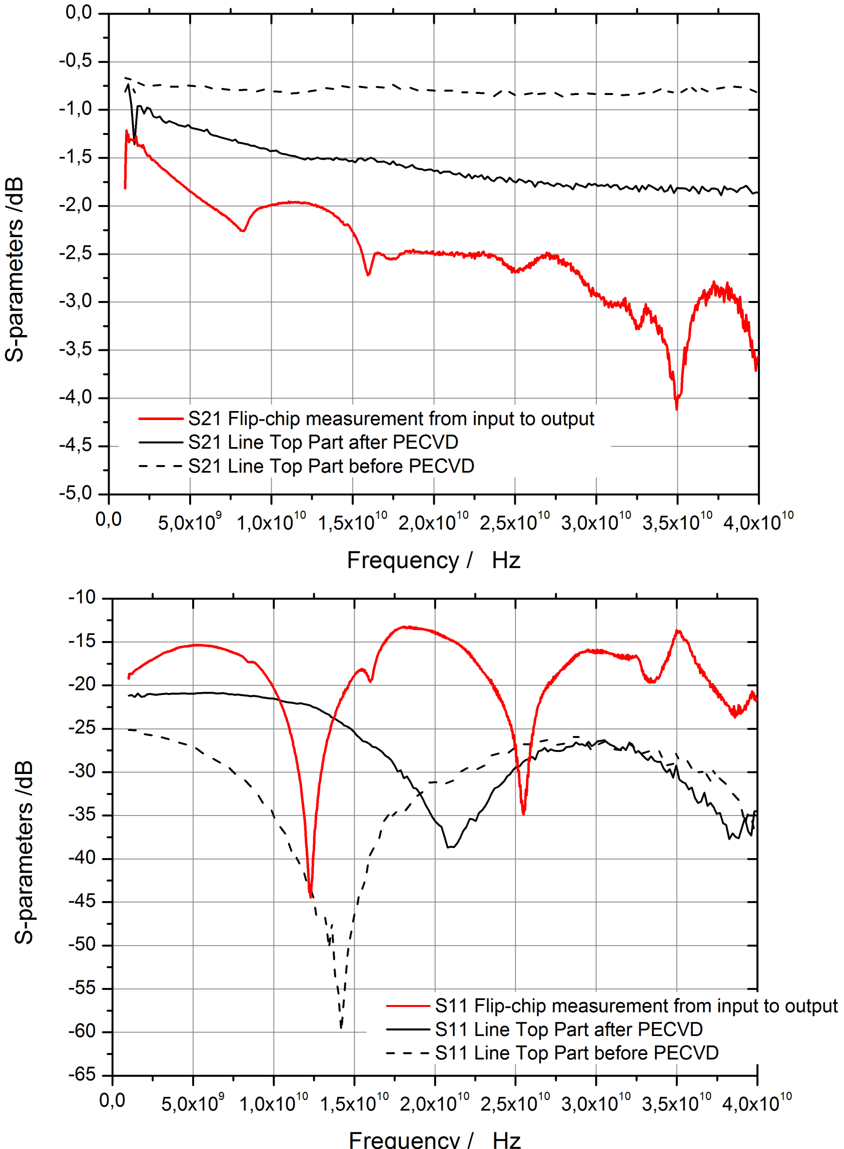

Figure 88: S_{21} and S_{11} parameters measurements of the CPW transmission lines placed on the die before and after PECVD process (black lines) and the flip-chip measurements from the input to the output (see Figure 87).

v. Discussion: pros & cons compared

Even if, experimental results are very encouraging, they present low performance compared to classical approach with classical metal bumps. In other work [119], performance of a classical Au based flip chip device using coplanar stripline is evaluated up to 100 GHz. S-parameters measurements return a transmission of about -0.5 dB up to 90 GHz and return loss of about -20 dB. Interconnections made by gold have a diameter of 35 µm and a height of 22 µm. Optimizing the line shape and adding a high-impedance line, which is not the case in our work, compensated the overall capacitance between the carrier and the die parts. Then, a work by Wei-Cheng Wu [155] presents a novel vertical coaxial transition for flip chip

interconnects working up to 40 GHz. With a 70 µm gold bumps diameter, this flip chip exhibits the return loss below -25 dB and the insertion loss within -0.4 dB from DC to 40 GHz. Very recent work [111] exposes a flip-chip working up to 50 GHz with transmission about -1.5 dB and return loss greater than -18 dB. Bumps diameter is 50 µm and they are also made by gold.

To summarize, we have demonstrated the first measurement of a flip-chip technology based on interconnected bundle of CNTs from DC to 40 GHz. An innovative way to interconnect CNTs similar to Velcro principle was used with successfully mechanical and electrical adhesions. No underfill or heat is necessary to interconnect the CNT bundles, which decreases the number of process steps and the cost of the device. The bumps size was 170x150 µm and only composed by 100-nm-diameter MWCNTs. This first measurement gives encouraging performance for using CNTs to replace metal bumps in flip-chip technology. Moreover, a bonding repeatability was observed in DC, which opens the door of a new type of device: CNT interconnected bumps can be flipped several times and it becomes possible to replace a defective component or to verify components in a complex environment. However, the performances are still lower than metal bumps at this frequency range. Future devices with a better control of density and a higher density will be suitable to increase the number of CNT-CNT contact. A densification of the CNT bundle after bonding can also be a solution to increase the CNT density and so decrease the distance between CNTs. We can imagine changing the CNT bundle geometry in order to increase the surface in contact between the two flip-chip parts. A better optimization of the access lines would also increase the performance of the device. CNT growth temperature needs also to be reduced in future, even if many works on this topic are in progress as we detailed in section "Problems to solve on page (111)". A temperature lower than 350 °C is being to be reach soon and will allow us to perform a fully CMOS compatible flip-chip device based on CNT interconnections. Finally, we need to carry on mechanical and temperature stress tests in order to verify the resistance of our device in an aggressive environment.

2. Modeling and model extraction of the flip-chip structure

In order to understand physical phenomena involving in the flip-chip interconnect and to extract a model, HF simulations are done. In this part, we will introduce a model of the CNT bumps we measured in the previous part with our flip-chip device. This model will

permit to extract an unknown CNT property: the contact resistance $R_{CNT-CNT}$ between two CNTs. Then, this resistance will be added to the analytical CNT model we presented in the first chapter in order to model the entire flip-chip structure using a hybrid EM/analytical approach. Later, such model will be used to perform parametric study and electrical optimizations. From this simulation, we will do a parametric study of our flip-chip by modifying the number of CNTs, their composition, their resistance, and other CNT parameters. We will discuss on the interest of using CNTs for flip-chip technology.

A. Full EM modeling of the flip-chip structure

In the previous part (see sections "DC measurements on page (132)" and "High frequency measurements on page (136)"), we obtained the best flip-chip performance with the device *a*. Indeed, the lowest DC resistance (12.5 Ω) and the highest S_{21} transmission (-2.5 dB at 20 GHz) were obtained. In this case, because of the low DC resistance, we considered that the measured DC resistance must be attribute to the CNT bumps. This is confirmed by measuring the resistance of the gold lines (R_{Au}), because we obtained only few ohms. In all cases, we are proposing here a modeling methodology of our flip-chip structure based on CNT bumps. This methodology can be employ for any measured flip-chip and gold lines resistances. In device *b*, we had a higher DC resistance (90 Ω) and almost the same S_{21} transmission, thus capacitance couplings must play a more important role in device *b* than device *a*. Thus, we decided to model the device *a* by a full EM model in order to extract the contact resistance between two CNTs $R_{CNT-CNT}$.

The flip-chip structure was analyzed using Ansoft HFSS software. The software is based on a 3D finite elements method and permits to solve Maxwell equations in frequency domain. Gold lines resistance (R_{Au}) was neglected, as it was less than a few ohms as reported in this paper [156] and in our DC measurements. As we already explained, in device *a*, we can consider the device mostly resistive since we showed the coupling and inductive effects are low. Thus, considering a full electromagnetic simulation, CNTs bumps are considered as equivalent bulk blocks with an equivalent electrical conductivity applied on them and fixed in order to fit with measurements. This electrical conductivity is equivalent to a real electrical resistance.

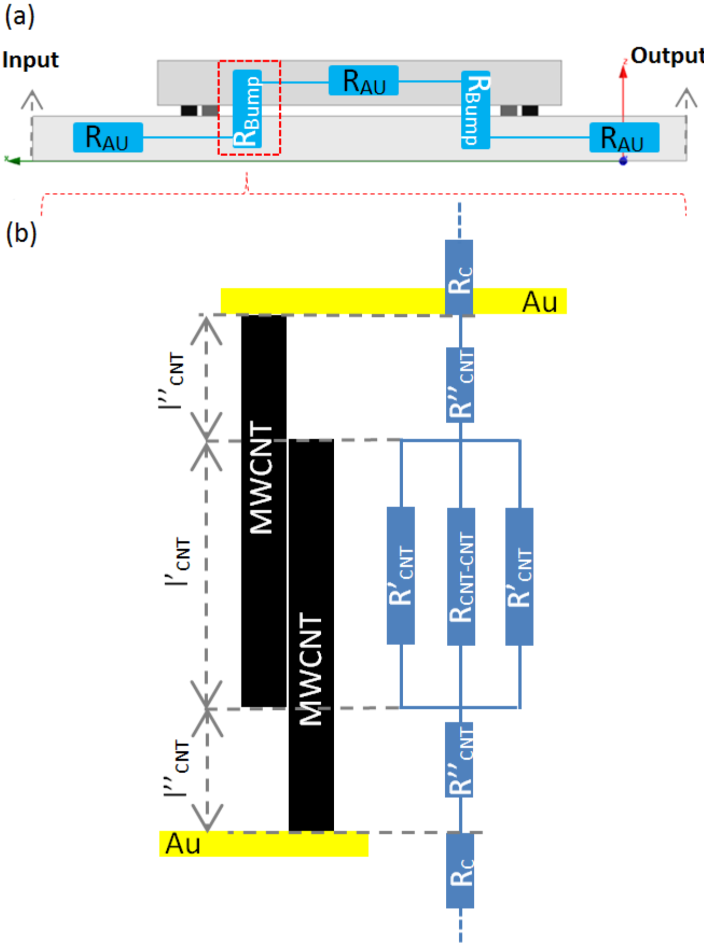

Figure 89: On (a), side view of the flip chip structure and the corresponding equivalent electrical circuit with a breakdown of the bump resistances. On (b), details on Rbump corresponding of the all bump resistance for two interconnected MWCNTs according to (a) schematic.

In our simulations, gold conductivity is $\sigma_{Au} = 4.1\times10^7$ S/m and silicon loss tangent is $\delta_{T-Si} = 0.002$. Based on this calculation, we inferred the total resistance of flip-chip device from the input to the output as described on Figure 89(a). The total measured DC resistance can be assimilated by $2R_{Bump}$ in series with R_{Bump} the DC resistance of one CNT bump including CNT/metal contact resistances (RC). On Figure 89(b), the details on R_{bump}, corresponding of the all bump resistance for two interconnected MWCNTs according to (a) schematic, are given: R′ resistance represents the linked CNT parts whereas R” resistance represents the non-linked part. R_C is the contact resistance between metal and CNT and finally $R_{CNT-CNT}$ is the contact resistance between two CNTs. In this case, capacitance between CNTs is supposed to be negligible because of the small surface in contact. For device *a*, DC resistance is 12.5 Ω for two bumps in series (Figure 80), which represents a 6.25 Ω resistance for one bump (R_{Bump}). Using the following equation (44), the equivalent bulk electrical conductivity of σ = 142 S.m−1 was extracted.

$$\sigma = \frac{1}{R_{Bump}} \cdot \frac{l}{A} \quad (44)$$

where l is the bump length (20 µm) and A is the bump area (150 × 150 µm^2). We are modeling the structure 1 (see Figure 77). As shown in the Figure 90 and Figure 91, a good fit is reached between experimental and simulation parts, which confirmed that the main cause of losses in the flip-chip device was due to the CNTs bumps resistances with negligible capacitances coupling between CNTs. That is in agreement with the study described in [84] and the studies we have done in our modeling part (chapter I section “Application and determination of the CNT parameters by experiments (work with Chow Wai Leong) on page (68)”).

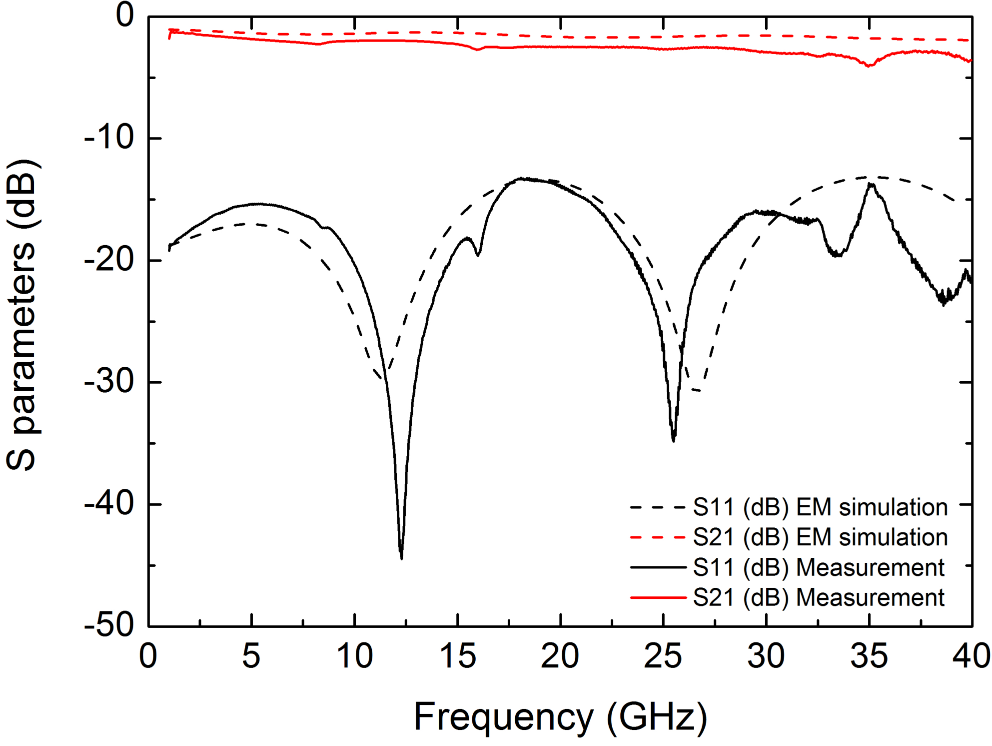

Figure 90: S-parameters measurements (solid lines) of the flip chip device a between carrier input and output of structure 1 (Figure 77) and EM simulations (dash lines) corresponding to the same structure with CNT bumps replaced by a material with a 142 S/m electrical conductivity.

Also, as already explained in the same section “Bundle with an unlimited number of SWCNTs on page (88)”, it was demonstrated that the transverse conductivity σ_T in a bundle of CNT is significant only if:

$$\frac{\Delta r}{2a} < \sqrt{\frac{\pi}{\sqrt{3}}} \approx 1.35 \quad (45)$$

where a is the radius of the CNT and $\Delta r = r + 2a$ is their spacing, center to center, while r is the shell-to-shell spacing. To use equation (45), embedding matrix media must be perfectly dielectric with an electrical conductivity equal to zero. In this case, the air surrounds CNTs into the bundle; the average distance between CNTs is estimated to be equal to 233 nm from a density of 6 CNT/μm^2. Average MWCNTs radius is 50 nm. By using equation (45), we obtain $\Delta r/2a = 3.33 > 1.35$, which shows that the transverse coupling between CNTs is small. The same equation (45) can be used now to calculate the maximum CNT density where the couplings between CNTs will become significant in order to achieve smaller losses. We obtain this new equation (46) from $\Delta r/2a = 1.35$, which give us the maximum CNT distance δr_{max} where transverse conductivity becomes significant:

$$\delta r_{max} \approx 0.7a \tag{46}$$

With a CNT radius of 50 nm, the distance between CNTs must be lower to 35 nm to get significant coupling. Thus, a density at least four times bigger must be reached. However, it was shown in [157] and in our modeling sections that, if the capacitance effect is stronger than CNT coupling, the coupling between CNTs will remain low even if the distance between CNTs is small. So, even if the CNT density is increased by respecting a CNT distance lower than 35 nm, we cannot predict if the coupling effects will become significant compared to the electrostatic capacitance existing between the outer part of the signal bundle and the outer part of the ground bundle. So, CNT resistance could be considered as the main contributing factors to the losses in transmission in this interconnect system. Hence, one solution is to increase the number of CNT, by increase the CNT density for example. High dense CNT bundles can be achieved by thermal CVD process. However, a higher density won't make the bundles able to interconnect. A trade-off between density and number of CNTs need to be made.

Based on an electromagnetic simulation using HFSS software, we place 20-μm high gold bumps (distance observed between the two flip-chip parts, see Figure 78) with a conductivity of $\sigma_{Au} = 4.1\times10^7$ S/m and with the same dimensions than our CNT bundles (150 × 150 μm^2 square size). S_{21} parameters from -0.04 to -0.75 dB are obtained at 1 and 40 GHz (Figure 91). The same simulation is now done using different CNT density for interconnections. With a density found at 6 CNT/μm^2, we considered a total number of MWCNT measured (N_{MWCNT}) in each bump to be equal to 1.35×10^5 (150 × 150 μm^2 square size). Another way to estimate the number of CNTs in the bundle is to use the equation (27) presented in section "Modeling of a bundle of CNTs on page (66)". With equation (27), we

find N_{MWCNT}=121500 MWCNTs, which confirms our first approximation. Using the equation (44) and with the same bump dimensions, we run EM simulations with respectively 142, 200, 300 and 1000 S/m bulk electrical conductivity applied on bumps, which represent respectively 1.35, 1.9, 2.9 and 9.5×10^5 CNTs in the bundle. As shown on Figure 91, with the biggest CNT density (9.5×10^5 CNTs), performance in transmission with gold bumps is almost reached. Thus, simulations show that by increasing by 7 times the CNT density, CNT bumps should be able to reach performance of metal bumps up to 40 GHz.

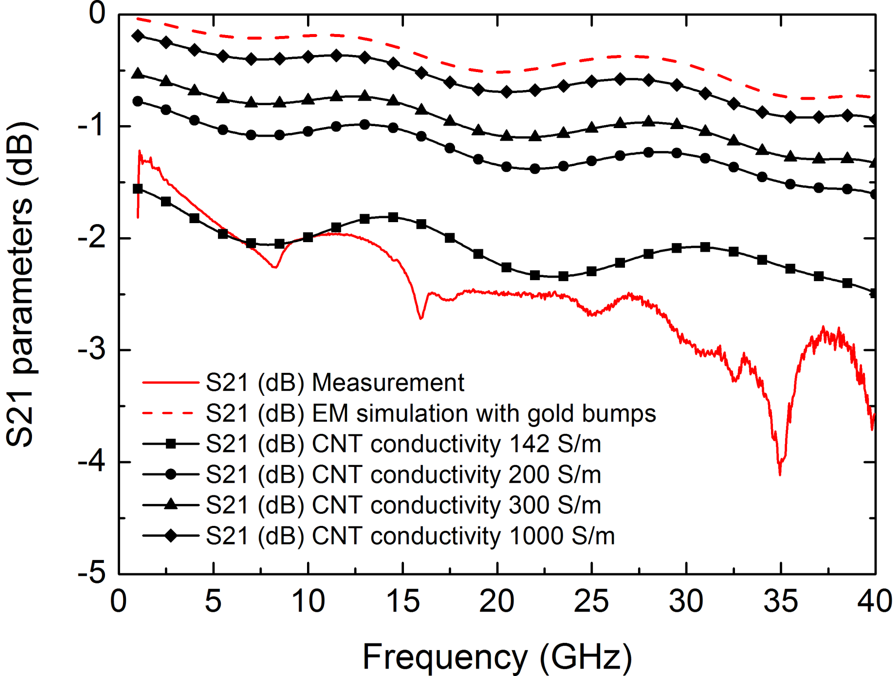

Figure 91: S_{21} parameters of device a between 1 and 40 GHz (solid line). EM simulation (dash line) corresponding to the same structure with gold bump (150 × 150 µm bump size and 25 µm high). EM simulations (lines and symbols) corresponding to the same structure with CNT bumps replaced by a material with respectively a 142, 200, 300 and 1000 S/m electrical conductivity.

B. Contact resistance $R_{CNT-CNT}$ between two CNTs extraction by full EM modeling

The DC schematic of the 6.25 Ω (R_{Bump}) can be represented by the Figure 92, which is a combination of the total carbon nanotube distributed resistance along one bump (R′ (47) and R''_{CNT} (48)), the total contact resistance ($2R_C$) between CNTs and the metal and the total contact resistance between carbon nanotubes ($R_{CNT-CNT}$) in the flip chip device. On the same Figure 92, l'_{CNT} represents the linked CNT length whereas l''_{CNT} represents the non-linked part.

$$R'_{CNT} = r_{CNT}\times l'_{CNT} \tag{47}$$

$$R''_{CNT} = r_{CNT} \times l''_{CNT} \quad (48)$$

r_{CNT} is the carbon nanotube distributed resistance representing the losses along the carbon nanotubes. r_{CNT} is the result of the distributed resistance of two interconnected MWCNTs $r_{CNT(1\ connection)}$ divided by the number of MWCNT (N_{MWCNT}) in parallel in the bump. As shown in Figure 78, CNT forests present a vertically low-density network not perfectly aligned, where carbon nanotubes were interconnected only at distinct points. In this case, the length l'_{CNT} become negligible to l''_{CNT} and the equivalent resistance becomes (49):

$$R_{bump} = 2R''_{CNT} + R_{CNT-CNT} + 2R_C = r_{CNT} \times (2l''_{CNT}) + R_{CNT-CNT} + 2R_C \quad (49)$$

Moreover, we can assimilate $2l''_{CNT}$ as the distance between the carrier and die which corresponds to 20 µm (Figure 78). In previous studies, MWCNTs have shown a resistivity of 20 kΩ/µm [34] grown by CVD at 850 °C and 29 ± 9 kΩ/µm [64] also grown by CVD but with a lower temperature (640 °C). As the PECVD process temperature in our studies occurred at 750 °C, assuming a linear relationship, the resistivity for two MWCNTs interconnected ($r_{CNT(1\ connection)}$) was taken to be 25 kΩ/µm. As explained previously, we considered a total number of MWCNT measured (N_{MWCNT}) in each bump to be equal to 1.35×10^5.

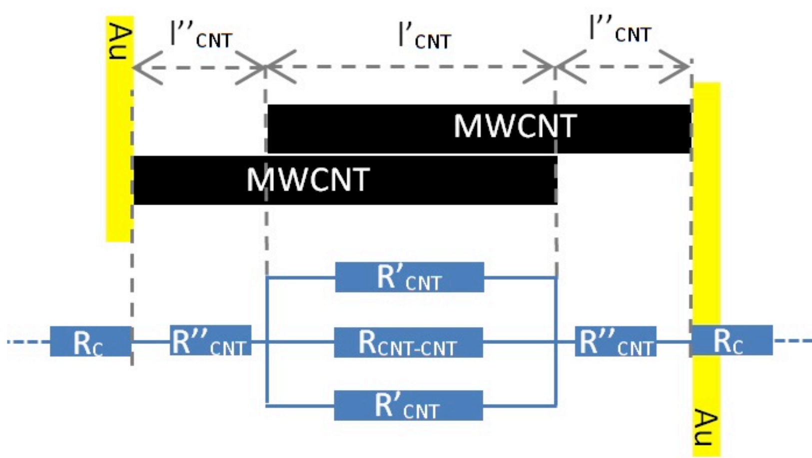

Figure 92: Details on R_{bump} corresponding of the all bump resistance for two interconnected MWCNTs according to Figure 89(a) schematic.

With the number of MWCNT linked (N_{MWCNT}) and the total bump resistance (R_{Bump}), the total resistance of two MWCNTs interconnected ($R_{Bump(1\ connection)}$) is extracted according to equations ((49) and (50)). On the other hand, we are able to estimate the contact resistance between two MWCNTs ($R_{CNT-CNT(1\ connection)}$) following the equation (51):

$$R_{bump(1\,connection)} = R_{bump} \times N_{MWCNT} \quad (50)$$

$$R_{bump(1\,connection)} = 2R''_{CNT(1\,connection)} + R_{CNT-CNT(1\,connection)} + 2R_{C(1\,connection)} \quad (51)$$

A total resistance $R_{Bump(1\ connection)}$ of 844kΩ is obtained, representing the total resistance for two interconnected MWCNTs. The metal/CNT contact resistance for one CNT $R_{C(1\ connection)}$ is known to be low, about 10 kΩ when carbon nanotubes were grown by PECVD [63, 64]. Considering $R''_{CNT(1\ connection)} = R''_{CNT}\ N_{MWCNT}$ is equal to the resistivity $r_{CNT(1\ connection)}$ multiplied by l''_{CNT} and according to the DC schematic (Figure 92), $R''_{CNT(1\ connection)}$ was found at 250kΩ.

$$R_{CNT-CNT(1\,connection)} = R_{bump(1\,connection)} - 2R''_{CNT(1\,connection)} - 2R_{C(1\,connection)} \quad (52)$$

$$R_{CNT-CNT(1\,connection)} = 6.25 \times N_{MWCNT} - 2 \times 250.10^3 - 2 \times 10.10^3 \quad (53)$$

$$\mathbf{R_{CNT-CNT(1\,connection)} = 324\ k\Omega} \quad (54)$$

Finally, by using the equations (51-54), the contact resistance between two MWCNTs $R_{CNT-CNT(1\ connection)}$ is equal to **324 kΩ**. This value is quite high but as we already discussed previously, also important contact resistance of 200 kΩ between nanotubes was found in the work of other group [150]. The surface contact between carbon nanotubes was also small and comparable as a distinct point. The nanotube-nanotube contact resistance is the main issue to decrease for optimizing the electrical behavior of CNT based bumps. The quality of the MWCNT bundles had been determined using Raman spectroscopy. By comparing the D peak and the G peak, a typical value of I_D/I_G = 0.9 to 1.2 is observed. We tried to correlate the quality of our CNT bundles with electrical measurements, but the effect of the quality of CNT bundles on electrical performance is insignificant and negligible as the contact resistance was still relatively large. From our point of view, the quality of CNT bundles will further improve the electrical conductivity, but the contact resistance issue must be first solved.

C. Hybrid EM/analytical modeling of the flip-chip structure

The flip-chip structure is now studied applying a hybrid approach based on 3-D electromagnetic (EM)/circuit modeling between 1 and 40 GHz. The advantage of this study is to be more accurate with a better control of the model parameters such as the analytical model of the CNT bundles. Indeed, the CNT circuit modeling allows us to tune easily several CNT

parameters: CNT diameter, CNT length, bundle CNT density and CNT components that will be described later. An optimization of the flip-chip performance becomes possible as well. All the structure, except the CNT bumps is considered by 3D EM simulations in order to define a generalized matrix [SG]. [SG] is defined between Input/Output ports (port1 & port2) and internal lumped accesses (3 to 6) for connecting circuit models of CNTs bumps (Figure 93 and Figure 94). EM simulations are performed by software Ansoft HFSS. On Figure 93, printed circuit board is visible on left and die part is shown on right. Black pads represent the CNT bundle locations. Red pad correspond to the lumped port for electromagnetic simulations and S-parameters matrix extraction. On Figure 94, [SG] represents the matrix extracted from EM simulation of the flip-chip structure. 'RLC transmission line' box correspond to the CNT bundle model that will be presented on the next paragraph. $R_{CNT-CNT}$ is the contact resistance between interconnected carbon nanotubes. We will use the value of $R_{CNT-CNT}$ = 344 kΩ found in the previous part.

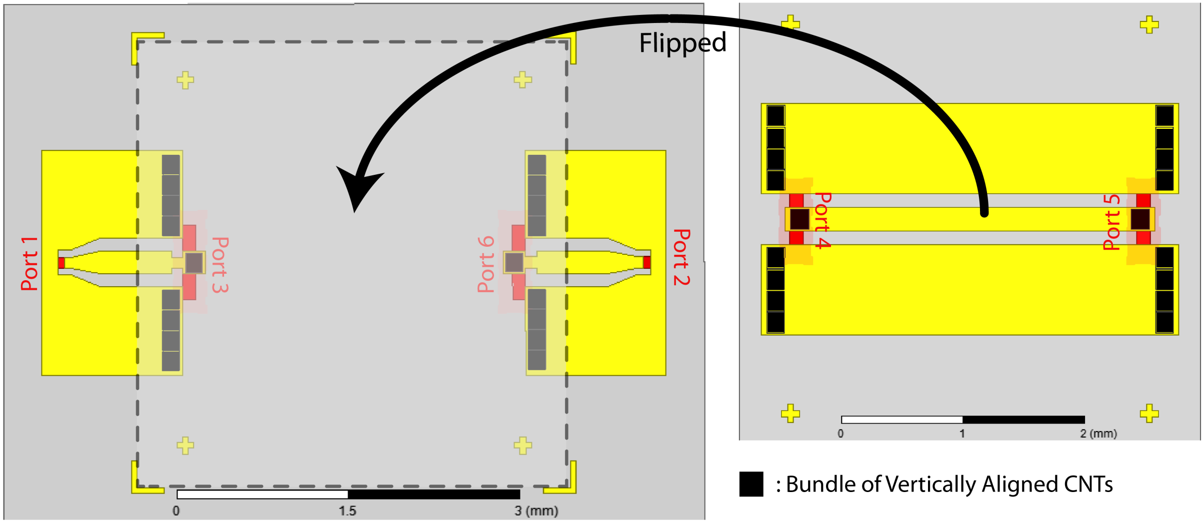

Figure 93: Top view of the schematic of the flip chip structure.

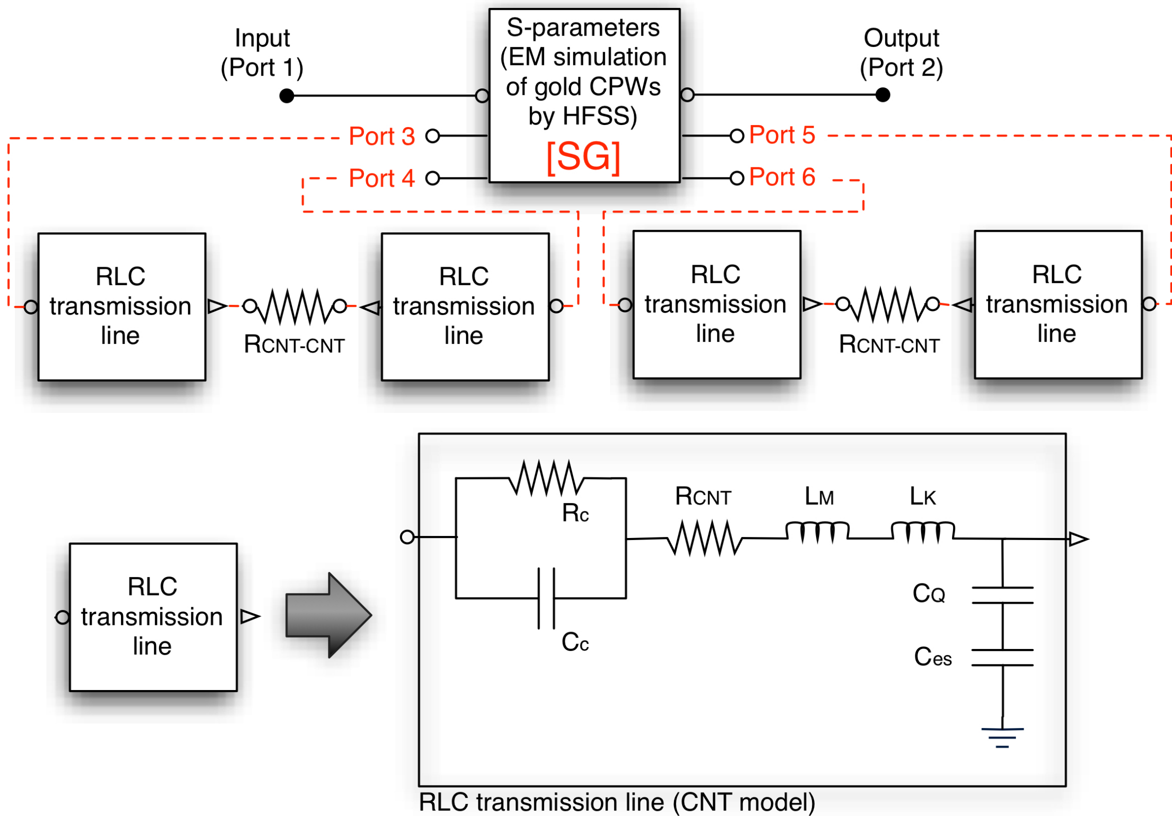

Figure 94: Diagram of the hybrid flip chip structure model.

The circuit model based on an RLC transmission line describing the electrical behavior of the CNT structure is presented in Figure 94 and was presented in the first chapter (sections "Modeling of a single-wall carbon nanotube (SWCNT) on page (62) and "Application and determination of the CNT parameters by experiments (work with Chow Wai Leong) on page (68)"). Also on Figure 94, the CNT circuit models are inserted between the lumped accesses (Ports 3-4 and Ports 5-6) of the flip chip matrix [SG]. The RLC transmission line is composed by lumped and distributed components as we described in the first chapter and in this reference [69]. Briefly, the contact capacitance C_C and the contact resistance R_C model the contact between the CNTs and the metal and values are found according to this other work [81]. All components values are visible on the Table 12. A quantum distributed resistance derived from $R_{CNT-bundle} = \frac{h}{2e^2} \times \frac{1}{N_{i-channel} \times N_{CNT}} \times \frac{l}{MFP}$ (equation (23)) represents losses along the carbon nanotube (h: Planck's constant; e: elementary charge; l: CNT length and MFP the mean free path). However, in our model presented on Figure 94, and following the same explanations than in our previous full electromagnetic model (see section "Contact resistance $R_{CNT\text{-}CNT}$ between two CNTs extraction by full EM modeling on page (147)"), a

quantum resistance of $R_{CNT} = r_{CNT(1\ connection)} = 20\ k\Omega/\mu m$ is used because of experimental work [34] showing a higher resistance in CNTs than the one predicted. The two other distributed components for nanowire effects are added: a kinetic inductance $L_k = L_{k-bundle} = \frac{h}{2v_F} \times l \times \frac{1}{N_{i-channel} \times N_{CNT}}$ (equation (24)) and a quantum capacitance $C_Q = C_{Q-bundle} = \frac{2e^2}{hv_F} \times l \times N_{i-channel} \times N_C$ (v_F=9.7×10^5 m/s: Fermi's velocity). According to equations (5) and (10), there are 74 shells and 374 conducting channels in a 100-nm-MWCNT diameter, so we have $N_{i\text{-}channel}$=374 in our model. The magnetic inductance L_M is considered negligible compared to the very high kinetic inductance L_k in nanowires [69] as we already shown in chapter I, section "Application and determination of the CNT parameters by experiments (work with Chow Wai Leong) on page (68)". Electrostatic capacitance C_{ES} represents the coupling effect between the ground plane and the CNT. Both C_{ES} and C_Q are calculated with the number of CNTs in the outer bundle layer (N_C, equation (29)). Because N_C=3000 is low and the distance between the signal bump and the ground bump (163 µm) compared to the MWCNT diameter (100 nm), C_{ES} and C_Q can be neglected. In order to model a bundle of CNTs, we also consider the coupling between CNTs weak because of the large distance between them (about 200-500 nm) as already defined in section "Full EM modeling of the flip-chip structure on page (143)". Then, the RLC CNT models are placed in parallels according to the estimated number of CNTs N_{MWCNT}= 1.35×10^5 in the bundle as defined in the previous part.

Table 12: CNT bundle components values.

N_{MWCNT}	R_C	C_C	R_{CNT}	L_K	$R_{CNT\text{-}CNT}$
1	10 kΩ	4.1. 10^{-6} aF	20 kΩ/µm	0.86 nH	324 kΩ
1.35×10^5	74 mΩ	55 pF	0.15 kΩ/µm	6.34 fH	2.4 Ω

As shown on Figure 95, a good agreement is found between simulations and measurements. Actually, we can observe an even better agreement in Figure 95 with the hybrid EM/analytical model than in Figure 90 with the full EM model. Indeed, the hybrid model is more detailed than the full EM one because we have directly access to all CNTs components such as the contact resistance and capacitance, the CNT resistances and inductance. As we will see in the next part, this hybrid model is easily tunable and allows us to exploit different configuration of CNT bundle. The number of CNT placed in parallel in the bundle can compensate for this high contact resistance. The measured CNT bundle resistance

is found at 6.25 Ω with 135 000 estimated interconnected CNTs. All component values can be found on the Table 12.

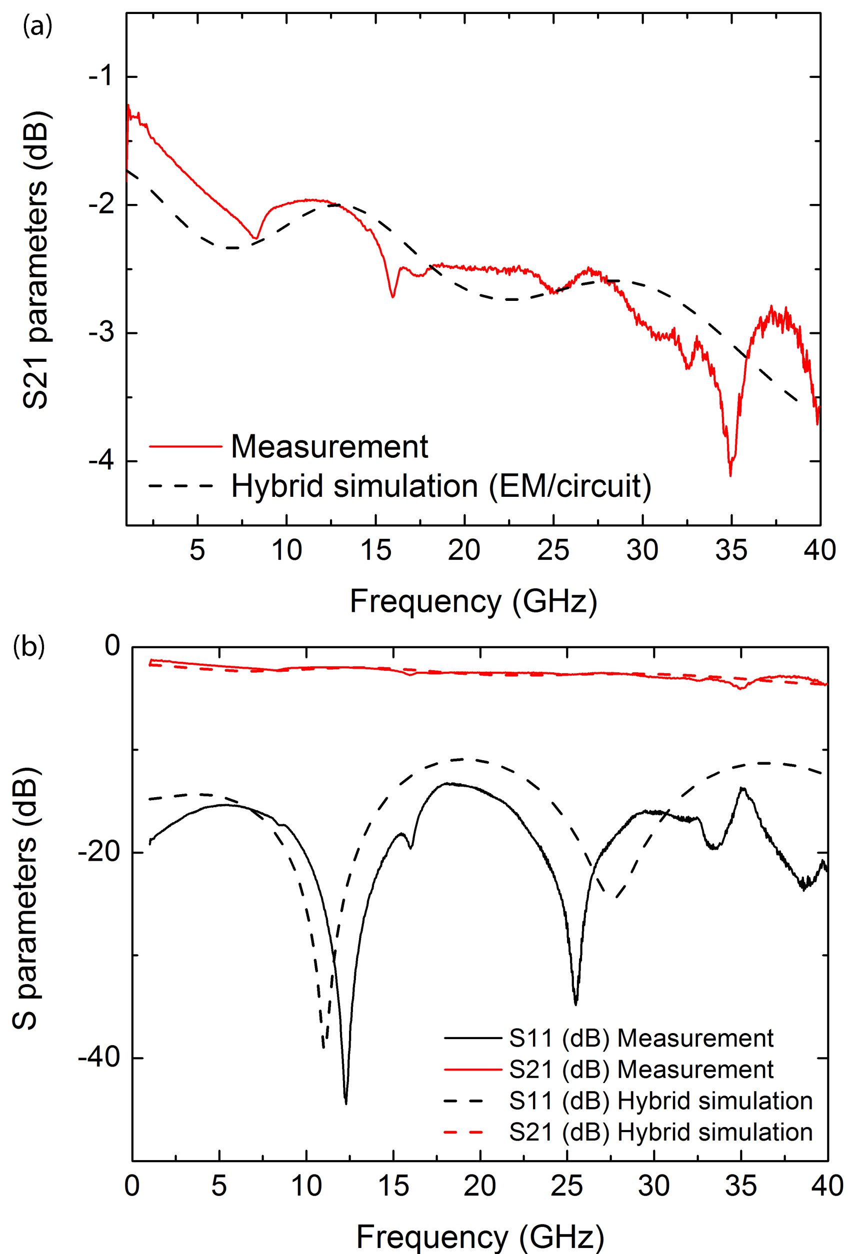

Figure 95: S-parameters of the flip chip structure measured between Port 1 and Port 2. Solid lines correspond to the measurements while dash lines show the hybrid EM/circuit simulation results.

D. Parametric study of the flip-chip using the hybrid EM/analytical model

In this part, we will proceed to a parametric study of our flip-chip structure using the analytical MWCNTs-bundle model we presented earlier. To proceed, we keep our EM simulation of the flip-chip structure without the bumps. The Figure 97 shows the results of this EM simulation where the ports (3 & 4) are directly linked to ports (5 & 6) and ports (7 &

8) are directly linked to ports (9 & 10) (Figure 96). Again, ports 1 and 2 respectively represent the input and the output of the flip-chip device. Thus, the best results we can expect to obtain with insertion loss S_{21} and return loss S_{11} for our flip-chip structure are those presented in Figure 96. As you can observe, insertion losses S_{21} from -0.045 to -2.3 dB has been obtained from 2 to 40 GHz. It is interesting to highlight that these results are consistent with the measurements of the CPW lines alone done previously (Figure 88). Indeed, losses from -1 dB to -2 dB had been achieved. Again, we show that the measured resistance of 12.5 Ω is mainly due to the CNT bundles.

Different CNT bundle parameters will be tune in order to execute our parametric studies. Since we have shown that our CNT bump act mostly like a resistance, we will focus on these components. First, we will modify the contact resistance between CNTs $R_{CNT\text{-}CNT}$; secondly we will change the distributed CNT resistance R_{CNT} and finally we will tune the CNT density. The CNT length cannot be modified since we would need to perform a new full EM simulation of the flip-chip structure for each distance between the two parts according to the new CNT length.

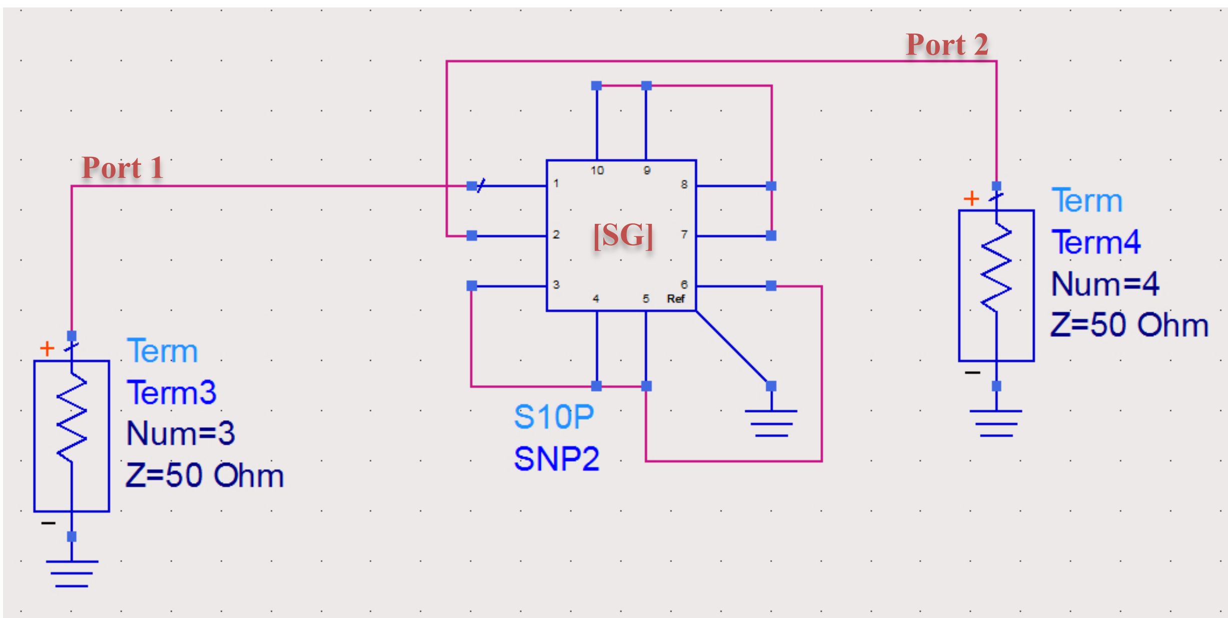

Figure 96: Schematic of the full-EM flip-chip simulation without bumps.

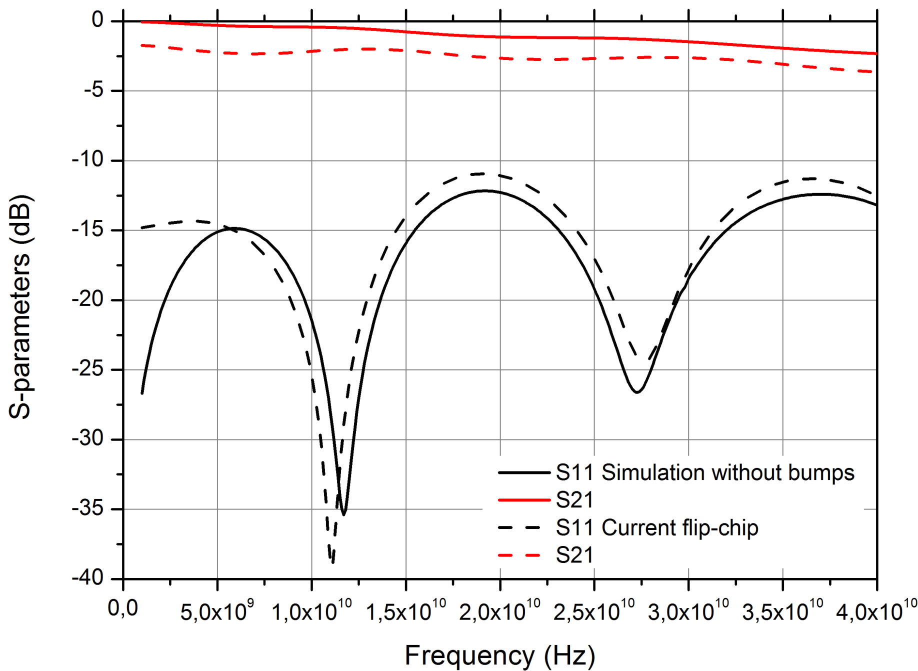

Figure 97: S-parameters of the full-EM simulation of the flip-chip structure without bumps according to the schematic in Figure 96.

i. Parametric study on the CNT resistance R_{CNT}

In this first parametric study, we modify the value of the CNT resistance R_{CNT}. With the flip-chip presented previously, we had R_{CNT} = 20 kΩ/µm, and as we already explained, this value is quite high compared the theoretical one equation (13)). However, the CNT resistance of our MWCNTs is lower than DWCNTs (43 kΩ/µm) we measured section "High frequency measurements and analytical model extraction on page (72)" (see Table 8). As we explained in chapter I, working with MWCNTs can be more interesting because of their lower resistance.

We decided to try two values of CNT resistance: 0 and 10 kΩ/µm. We can imagine reaching 10 kΩ/µm by improving our CNT fabrication process and hence decrease the number of impurities in our CNTs. With 0 kΩ/µm, we reach the theoretical resistance value of a perfectly structured MWCNTs. Indeed, as we explained in the chapter I, section "General properties of CNTs on page (28)", a MWCNT can have a mean free path equal to 20-25 µm, which is approximately the length of our MWCNTs in our flip-chip device (Figure 73). Thus, if we are below the MFP length of the MWCNT, no scattering will occur during the electron propagation, we have a ballistic transport of the electron. So, the 0 kΩ/µm represents the ideal case we could expect to achieve with a perfect control of the CNT fabrication process.

As we can observe on Figure 98, we don't improve so much the insertion loss S_{21} by dividing by two the CNT resistance (black dash curve). Thus, only an increase of 0.5 dB is visible in low frequency (1 GHz) and an increase of 0.25 dB at high frequency (40 GHz). Moreover, as we can see on the Figure 98 on the blue dash curve, even with no CNT resistance, we only increase our S_{21} by 1 dB at 1 GHz and by 0.5 dB at 40 GHz.

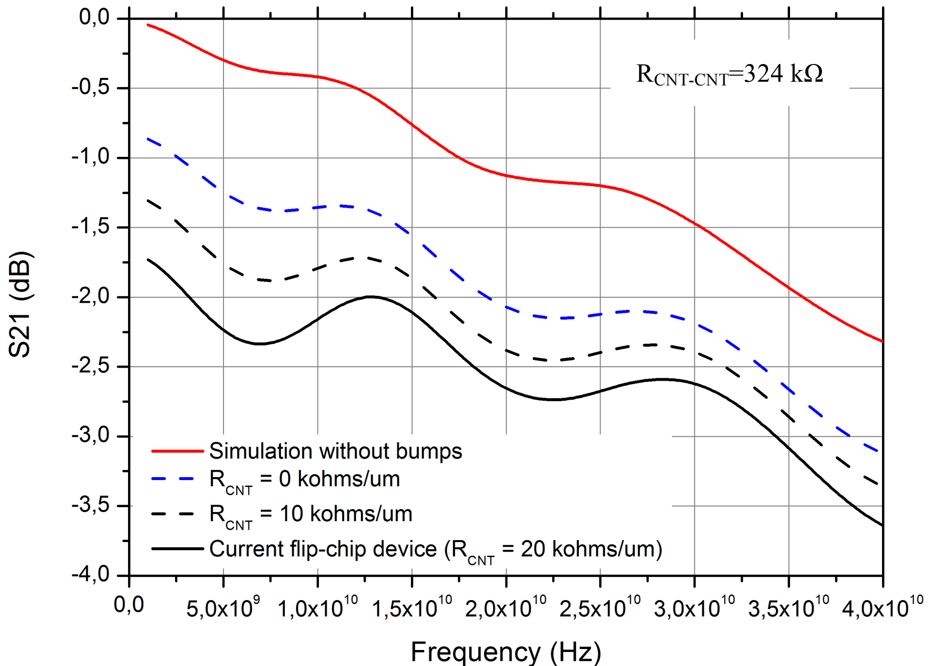

Figure 98: S_{21} parameter of the hybrid EM/analytical flip-chip simulation with a parametric study on the CNT resistance R_{CNT}.

In conclusion, by improving our CNT fabrication process and so decrease the CNT resistance, we show that we are able to improve the performance of our flip-chip. However, we can also observe that the CNT resistance is not the main loss of our device and we will see on the two next parts how the other components also affect the RF performance.

ii. Parametric study on the CNT contact resistance $R_{CNT-CNT}$

In this second parametric study, we modify the contact resistance between carbon nanotubes $R_{CNT-CNT}$ from its current value of 324 kΩ to 0 kΩ. As we can observe on the Figure 99 showing the insertion loss of the flip-chip with the different values of $R_{CNT-CNT}$, by dividing by 3 times $R_{CNT-CNT}$ (black dash curve), we only improved the S_{21} by 0.5 dB at low frequency (1 GHz) and by 0.25 dB at higher frequency (40 GHz). With $R_{CNT-CNT}$ = 10 kΩ, we improve S_{21} by 0.75 dB on all the bandwidth (purple dash curve). Thus, we observed that

decreasing the contact resistance between CNTs alone is not sufficient for improving more than 0.5 dB the S_{21} transmission.

Finally, we decided to model a case where we don't have any contact resistance between CNTs but also no distributed CNT resistance, which should be possible with perfectly structured MWCNTs without impurities and a MFP near 25 µm as we explained in the previous part. In that case and as we can see on the Figure 99 (blue dash curve), we almost reached the level of performance of the flip-chip without CNT bumps. Indeed, the S_{21} insertion loss was increase by 1.25 dB at low frequency (1 GHz) and by 1 dB at higher frequency (40 GHz).

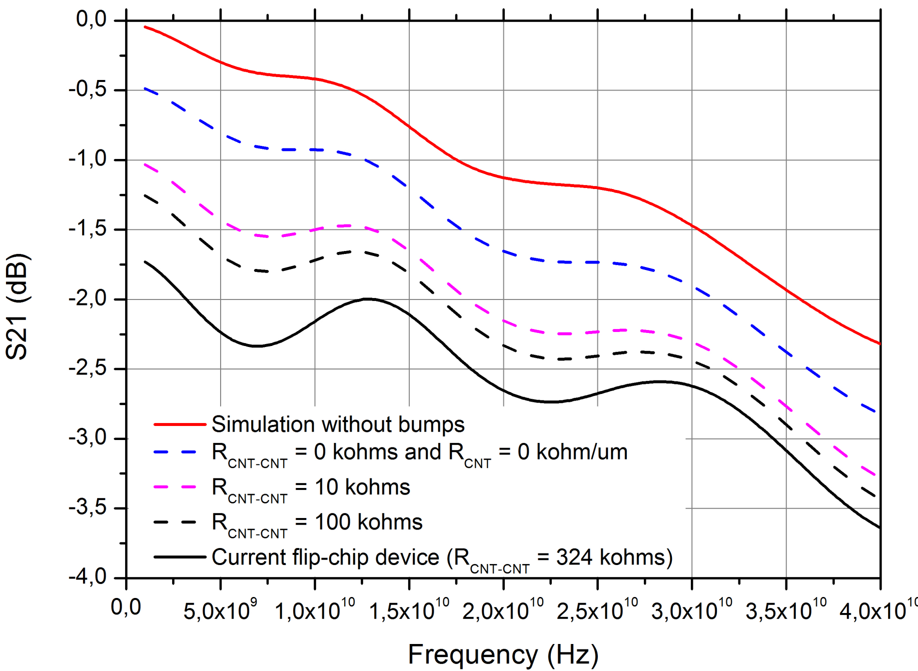

Figure 99: S_{21} parameter of the hybrid EM/analytical flip-chip simulation with a parametric study on the CNT contact resistance $R_{CNT-CNT}$.

In conclusion, an important work needs to be done on the CNT qualities by improving the fabrication process. As we already explained in the section "Growth mechanisms and control on page (45)", an increase of the process temperature would decrease the number of impurities in CNTs. Then, instead of decreasing the contact resistance between CNTs, we can imagine to increase the number of contact and hence achieve a level of performance near the red curve on Figure 99. By working on the both aspects (fabrication process and CNT contact density), we can imagine to reach a very good level of performance for our flip-chip based on CNT interconnections with a S_{21} parameter from -0.5 dB at 1 GHz to -2.5 dB at 40 GHz.

iii. Parametric study on the CNT density (N_{MWCNT})

Finally, we modify the CNT density (NMWCNT) in the bundle from $0.3.10^6$ CNTs to 1.10^6 CNTs. As you can observe on the Figure 100, by multiplying by two only the CNT density (black dash curve), we already improve our S_{21} parameter by 1 dB at 1 GHz and 0.5 dB at 40 GHz. Indeed, as we already explained and observed in the two previous parts, we need to improve the contact resistance between CNTs in the same time than the CNT resistance. Thus, by increase the CNT density, we are working on the two parameters on the same time: we decrease the total resistance by increasing the number of contact and we decrease the total CNT resistance by decreasing the number of CNTs in the bundle.

And the two others curves confirm this observation (purple and blue dash curves) and show an important increase of the S_{21} parameter with the increase of the CNT density. With a CNT density of 1.10^6 CNTs (blue dash curve), we achieve insertion loss from 0.25 dB at 1 GHz to -2.5 dB at 40 GHz, which is very close to the optimal results we could obtain visible on the red curve.

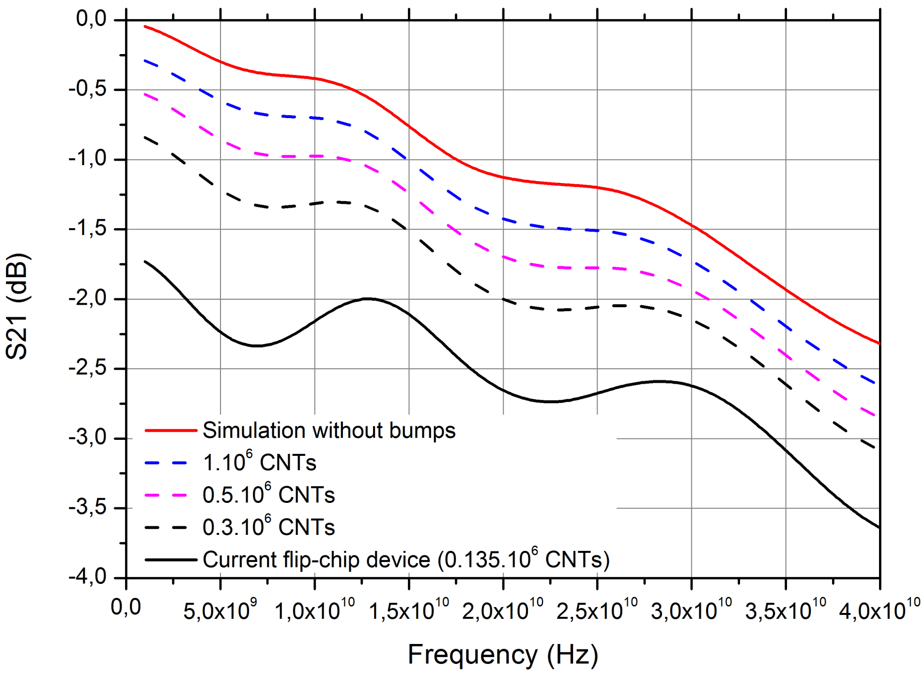

Figure 100: S_{21} parameter of the hybrid EM/analytical flip-chip simulation with a parametric study on the CNT density.

In conclusion, focusing on the CNT density might be the best choice to improve the performance of our flip-chip. As we already explained in the chapter I, section "Catalyst

preparation on page (37)", we can improve the CNT density by modifying the catalyst layer thickness with PECVD process. However, decreasing the process temperature will increase the degree of impurities in CNTs, hence, this is not compatible with improving the flip-chip performance. Thus, with a number of CNTs of 1.10^6 CNTs or above, which represents a density of 44 CNT/μm^2, we could reach higher flip-chip performance using CNT interconnections.

3. Remarks and observations on the flip-chip working up to 40 GHz

On the previous parts, we successfully demonstrated the feasibility of a flip-chip composed by carbon nanotube bundles interconnected from DC to 40 GHz with bumps size as low as 150-µm squares size. As we already explained on the previous part, the objective of replacing current metal-based bumps by CNTs is to reach higher frequency with lower bump size. However, from this first study, we faced several issues. We can denote two major issues we encountered: the too low performance in transmission compared to a metal bump (because of the too high CNT bundle resistance) and the weak mechanical adhesion between the two parts.

A. CNT bundle resistance issue

Regarding the first point, we need to decrease the total CNT bundle resistance. And as we have shown in the previous part, the best way to increase the performance of our flip-chip device is to increase the CNT density. Indeed, by increasing the CNT density, we will be able to interconnect more CNTs and consequently decrease the resistance of the interconnection. In the flip chip device presented on the previous part, the measured CNT bundle resistance is found at 6.25 Ω with 135 000 estimated interconnected CNTs. Thus, we performed analytical calculations in order to verify the effect of an increase of the CNT density on the bundle resistance and inductance. The objective is to show that at higher frequency with lower bump size, CNTs become a good candidate to realize interconnections for our flip-chip technology.

As shown on Figure 101(b), if the CNT density (N_{MWCNT}) is increased by seven, bundle resistance will decrease below 1 Ω and will become negligible. We finally found a good agreement between this calculation and our previous simulation (Figure 91). Indeed, with our full-EM simulation (Figure 91), we needed $N_{MWCNT}=1.10^6$ CNTs in order to reach the performance of the gold bumps. We also confirm that the losses of our CNT

interconnections are mainly due to the CNT resistances. With a CNT density at least 40 times bigger, CNT bundle resistance will approach the performance of a gold bump (red line on Figure 101(b)). Gold bump resistance and inductance are calculated from equations (55) and (56) (see appendix):

$$L_{Bump} = \frac{\mu_0 h}{2\pi} \times ln(\frac{s}{r}) \quad (55)$$

$$R_{Bump} = \frac{2h}{\sigma_{Au}\pi r^2} \quad (56)$$

with h is the bump length, r is the bump radius, s is the spacing between two bumps, σ_{Au} = 4.1×10^7 S/m is the gold electrical conductivity and μ_0 is the vacuum permeability [158]. Moreover, with the increase of frequency, bump radius needs to be reduced in order to match impedance. Above 100 GHz, a bump radius below 10 µm is needed [112] and as shown on Figure 101, below this 10-µm-bump radius, gold bump inductance and resistance increase very fast and grain scattering and electromigration effects can appear [114]. Then, up to a radius of 25 µm, CNT bundle inductance (with 100 MWCNTs with a diameter of 100 nm) is always below the gold bump inductance (Figure 101(a)). Thus, with a higher CNT density, a 10-µm-bundle radius is able to outperform the performance of metal bumps. As presented in this work [33], a 10-µm-diameter bundle was fabricated with a high CNT density (10^{11} cm^{-2}) and a negligible resistance was found. This experimental result confirms our predictions and shows that this new way to interconnect devices by flip-chip technology using CNT bundles is able to reach performance of metal bumps below 100 GHz and outperform metal-based bumps above 100 GHz without any electromigration issue. Thus, the next objective of this work will be to prove the feasibility of a flip chip with bump size, made by CNT bundle, below 20 µm and working up to 100 GHz.

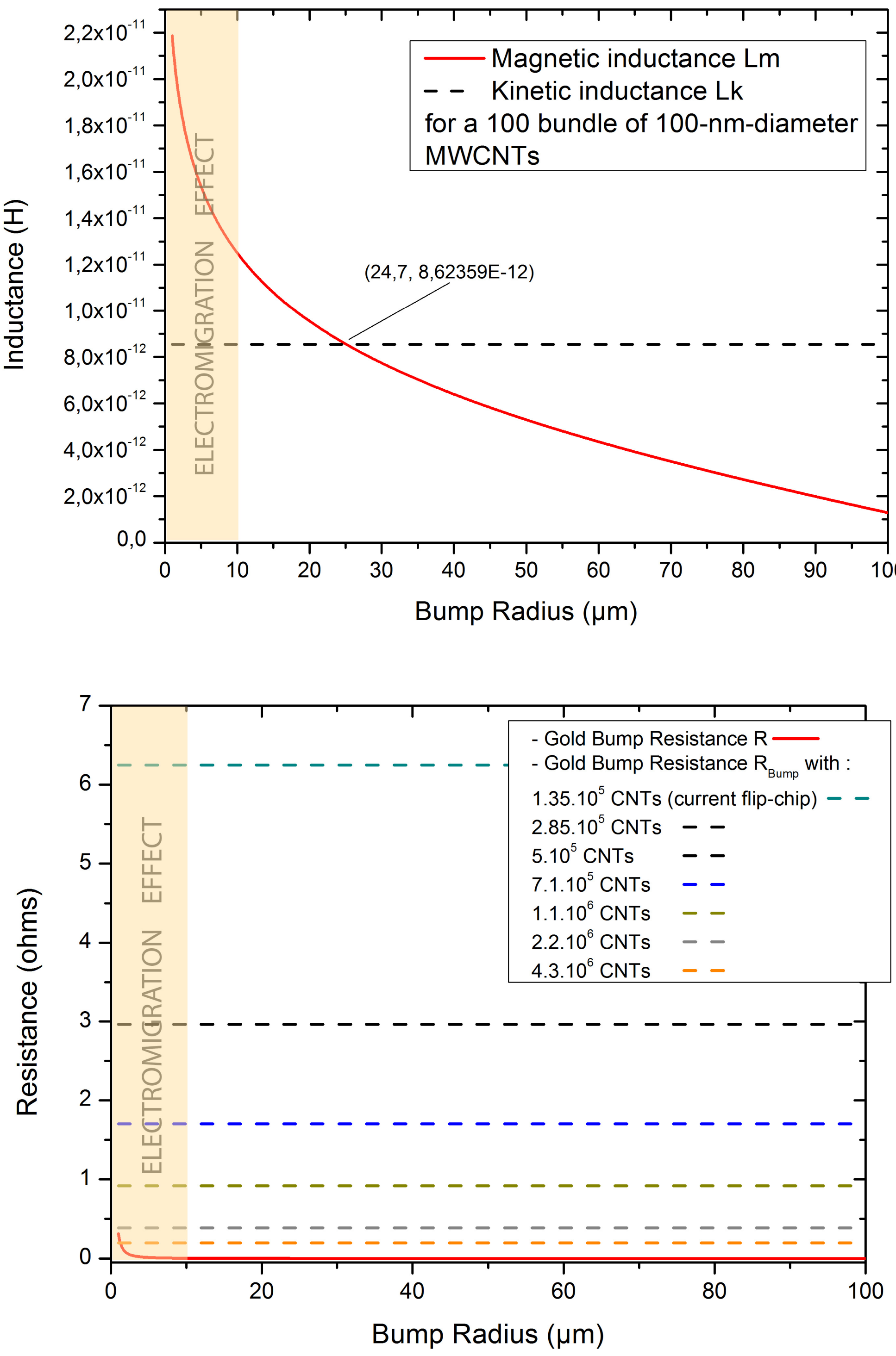

Figure 101: On (a), total inductance of a gold bump and a CNT bundle according to the bump radius. On (b), total resistance of a gold bump and a CNT bundle according to the bump radius. In gold bumps, electromigration effects appear with a radius below 10 µm.

B. Mechanical bond issue [159, 160]

The second issue we have faced with our first flip-chip device is the weak mechanical interaction between the two parts of the flip-chip. Indeed, even if we observed some stability,

it was impossible to place upside down the device for long or even shake it. It appeared that the mechanical strength between the two CNT bundles (one on the substrate carrier, the other on the chip) was too low to be able to sustain the top part of the flip chip over the bottom part.

Logically, the main reason of this issue is the lack of connection between the carbon nanotubes, which must compensate for the top part weight of the flip-chip. We can imagine solving this issue by increasing the number of interconnected carbon nanotubes. A higher number of bonded carbon nanotubes will increase the total electrostatic and Van der Waals forces between them. To verify the number of interconnection necessary in order to get a high enough mechanical bond, we decided to calculate the electrostatic and Van der Waals forces between the total number of carbon nanotubes interconnected each other.

In the case of the flip chip, we first measured the mass of the top part. We used an electronic balance and found a mass of 16.5 mg for the top part and 31.0 mg for the bottom part. We then calculate the weight of the top part and plot it on the graph shown on Figure 103. The dash orange curve represents the weight of the top flip-chip part.

In the second step, we estimate the number of interconnected CNTs in the flip chip structure presented previously. We estimated a number of 135 000 CNTs (N_{MWCNT}) bonded per interconnection. As you can count on the Figure 102, we have 58 bundles (N_{Bundle}) in the case of the 150 µm bump size configuration. Hence, we can easily estimate the total number of CNT linked each other in the entire flip chip structure. We suppose we have the equal number of interconnections between the two bumps. We call this number $N_{Connection} = N_{MWCNT}.N_{Bundle} = 7.68.10^6$ interconnections.

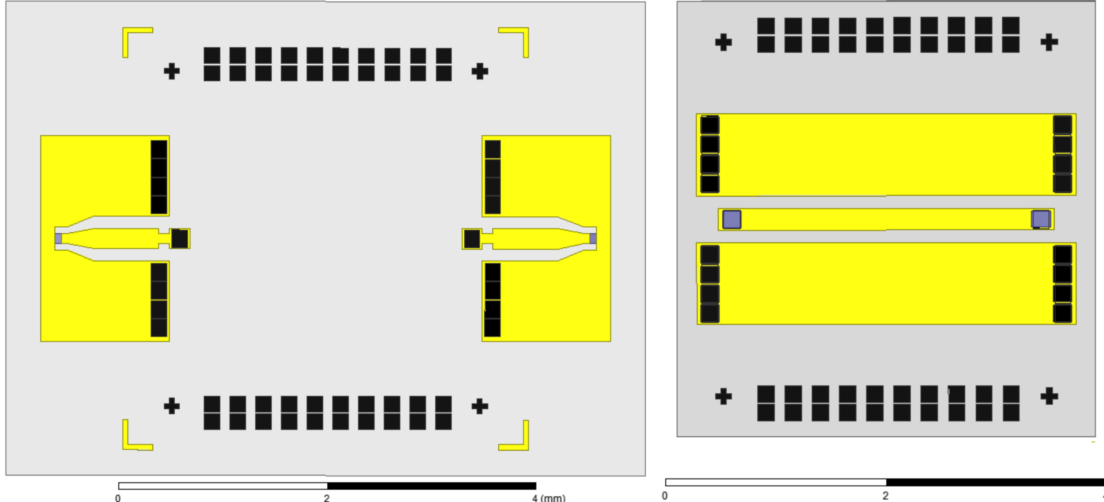

Figure 102: Top view of the 150-µm-bump size (structure 1) flip-chip device composed by the PCB (left asset) and the chip (right asset). In this structure, we can observe a total number of 58 bundles of CNTs.

In the third step, we want to calculate the Van der Waals force between two carbon nanotubes. For that, we use the Lennard-Jones potential [161] which gives the attractive and repulsive potentials between single atoms according to their distance (see equation (57)).

$$\phi_{ij} = -\frac{C_6}{r_{ij}^6} \tag{57}$$

with r_{ij} the distance between the atoms and C_6 the constant characterizing the interactions between the two atoms regarding to the material.

In the case of carbon atoms, we get C_6 = 15.2 eV A^6 [162]. From the potential phi, we are able to derivate the attractive force between two carbon nanotubes, as we can see on equation (58).

$$q_{VDW} = \frac{d\left(\frac{E_{VDW}}{L}\right)}{dr} = \sum_{R=R_{int}}^{R_{ext}} \sum_{R=R_{init}}^{(n-1)\times d+r_{init}} -\left(C_6\sigma^2\pi^2 R\sqrt{r(r+2R)}\times(8r^4+32r^3R+72r^2R^2+80rR^3+35R^4)\right)\times(2r^5(r+2R)^5)^{-1} \tag{58}$$

with σ= 38 nm^{-2} is the graphite surface density, L is the nanotube length, R is the nanotube radius and r is the distance between two carbon nanotubes.

The equation was originally derivate to determine the VDW forces of a carbon nanotube over a graphene sheet. However, in our case, we are using MWCNTs with a large

diameter (about 100 nm), which can be locally assimilated as a graphene sheet. We plot the VDW force as function of the distance between the two carbon nanotubes, as we can see on the Figure 103 on the blue dot curve with random number of interconnected CNTs. We consider the distance between CNTs and the CNT radius are constant for each bundle.

The last step is to calculate the electrostatic force between carbon nanotubes. A simple capacitance approach is used to solve the problem [163]. Indeed, from the well-known formula of a capacitance between two wires (equation (59)), we are able to derivate the electrostatic force from the electrostatic energy per unit length $\frac{E_{elec}}{L} = \frac{CV^2}{2}$ (equation (60)).

$$C(r) = \frac{\pi\varepsilon_0}{log\left[1+\frac{r}{R}+\sqrt{\left(\frac{r}{R}+1\right)^2-1}\right]} \tag{59}$$

$$q_{elec} = \frac{d\left(\frac{E_{elec}}{L}\right)}{dr} = \frac{\pi\varepsilon_0 V^2}{R\sqrt{\frac{r(r+2R)}{R^2}}\times log^2\left[1+\frac{r}{R}+\sqrt{\frac{r(r+2R)}{R^2}}\right]} \tag{60}$$

with V the applied voltage. In our case, we apply a low voltage (about 0.1 V) for the flip-chip characterization under a VNA up to 40 GHz. Thus, same than VDW force, we plot the electrostatic force as function of the distance between two CNTs (Figure 103, blue dash curve) with, again, a sample with a random number of interconnected CNTs.

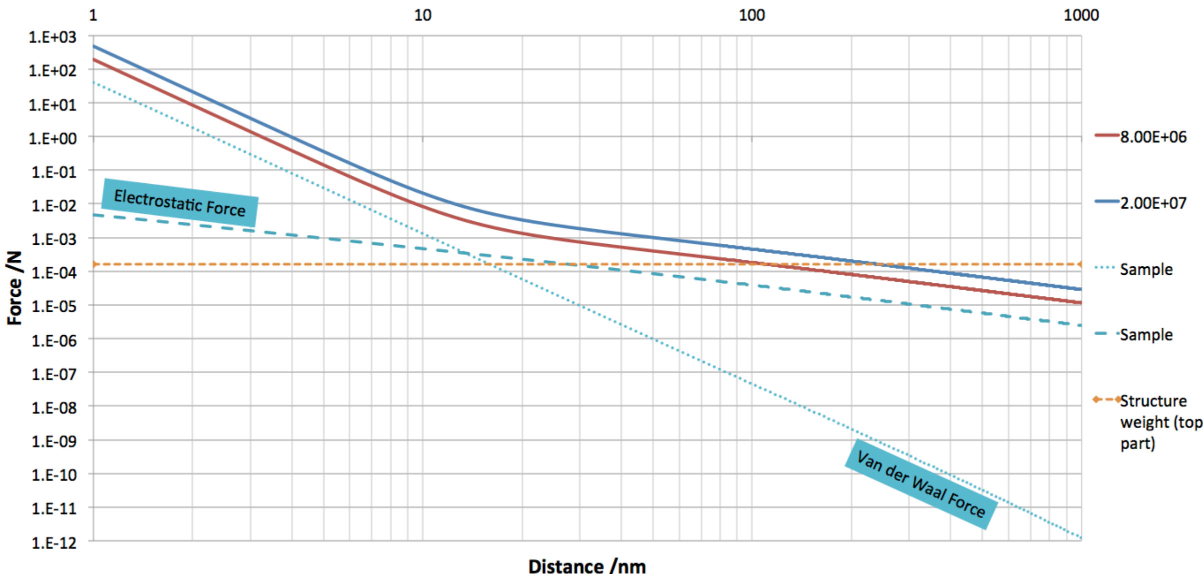

Figure 103: Electrostatic and Van der Waals forces of a given number of CNTs as function as the distance between two carbon nanotubes.

As we can observe on the same figure, VDW forces are stronger for short distance than electrostatic forces. However, at higher distance between CNTs, electrostatic forces become more significant. The red curve is the addition of the two blue dash curves.

With our flip-chip presented in the previous parts and as explained, we have an estimated distance between CNTs between 200-500 nm with a total of 8.10^6 interconnected CNTs for the all structure. Thus, by looking at the Figure 103, we observe that the distance between CNTs is too large to compensate for the weight of the top part of the flip chip. It can explain why our results are not always repeatable and why the mechanical adhesion between the two flip-chip parts is weak. If we take a look on the intersection between the red curve and the orange dash curve on the Figure 103, a distance below 80 nm between CNTs is necessary. However, by doubling the number of interconnected CNTs, we are able to shift the distance necessary to almost 200 nm (blue curve on Figure 103). Thus, in conclusion of this study, we must increase the CNT density in our flip chip structure in order to increase the number of interconnected CNTs, but also to decrease the distance between them. On the next part, we will see how we managed to follow these objectives.

4. Conclusion

The feasibility to use PECVD approach to achieve CNT bumps pitch smaller than 150 µm has been studied. The introduction of TiN barrier layer between Ni catalyst and Au metallization allows an efficient growth of CNT bumps directly on Au while maintaining good electrical connections between CNT and Au electrodes. The successful growth of CNT on Au metallization opens up opportunities to evaluate the performance of vertically aligned CNT bundles in very high frequency domain. By increasing the densities of CNT bumps, the first demonstration of CNT to CNT joining methodology with bump pitch smaller than 150 µm had been successful. The preferred densities of CNT bumps (area) to the die area must be higher than 1.2% to achieve sufficient mechanical support. The proof of concept of innovative RF CNTs bump flip-chip was also presented. A test structure has been built and tested. For the first time, very encouraging CNTs based flip-chip measurements have been obtained from DC up 40 GHz. In addition to the experimental work, a theoretical study based on 3D EM simulation and hybrid EM/analytical approach have been done. Electrical parameters of the CNTs bumps were extracted for better understanding. Finally a pros and cons discussion of the relevance of the CNTs bumps has been proposed.

We conclude that even if our process and the current electrical performances have to be improved, many advantages can be carried on such as, the high aspect ratio, the possibility to flip several times, the lack of underfill, etc. Suggestions to improve the process and electrical performances have been proposed. On the next part, we will present our current theoretical and experimental studies at operating frequency higher than 100 GHz using the same flip-chip technology.

5. Design and fabrication of a test structure with CNT bumps working up to 110 GHz

At higher frequency (above 100 GHz), CNTs bumps should outperform metal bumps due to their excellent electrical conductivity and low magnetic inductance [2] as explained in the chapter I. Based on CNT interconnection models up to 100 GHz, MWCNTs and SWCNTs return better performance than metal interconnect at frequencies above 100 GHz because of a lower resistance [7]. Moreover, best performance were obtained in global level of interconnects including chip-to-packaging interconnect applications. A work was done by Iwai's group [33] showing high density (10^{11} cm^{-2}) CNT bundle as a bump for flip-chip technology. Au was plated on the surface of patterned metal and CNT bumps to allow a thermal assisted flip-chip bonding bumps. Then a temperature of 345 °C is necessary to fix the flip-chip. The bundle diameter is 10 µm and bundle resistance was found negligible because of the high number of CNTs. In literature for flip chip technology, we cannot find interconnections with a diameter lower than 20 − 25 µm [33, 119]. At 100 GHz and above, larger diameter metal bump can be fabricated [164, 165] in order to get a good transmission performance using flip-chip technology. However, as explained previously, metal resistance increases with frequency and becomes larger than the CNT resistance, which is staying constant with the increase of frequency [7]. Above 100 GHz, smaller bump (below 20 µm) with low resistance can be made with high-density CNT bundles as we will in the next part with modeling [33]. The density needed will depend on the flip-chip working frequency and the CNT quality.

From the previous study, we decided to build a similar flip-chip structure working up to 110 GHz with smaller CNT bundle size (20x20 µm bump size). As explained in the previous part, we encountered an issue of a weak mechanical bond between the two parts. So, for this updated flip-chip structure with smaller bump sizes, which makes the mechanical

bond even weaker, it becomes our priority to overcome this issue. As we will show later, we tried to maximize the number of interconnected CNTs in order to optimize and increase the mechanical strength between the two parts of the flip-chip. Several options will be proposed to connect the flip-chip.

A. Design of the updated flip-chip

Based on the same idea than our first flip-chip, we designed three types of flip-chip with different impedance matching parts and several bundle sizes. On the Figure 104, we have a preview of the mask composed by all the flip-chip declinations (15) that will be available for this new structure. Several strategies have been defined. On the next parts, FC0 will represent the previous flip-chip design we presented above working up to 40 GHz. FC1 and FC2 will represent the two updated flip-chip structures with respectively a 20-µm-bump size and a 100-µm-bump size. FC3 won't be presented here.

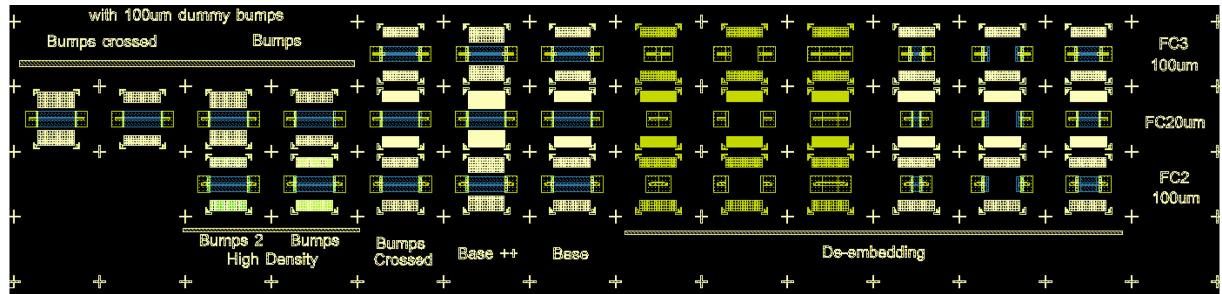

Figure 104: An overview of all patterns existing on the mask and representing the different new flip-chip configurations that they will be presented later. References are on the right and the size of the CNT bundles below the reference.

i. Flip-chip with 20-µm-bump size: FC1

- Design:

The first design is using a 20x20-µm-bundle size as we can see on the Figure 105. Again, the structure is using 50-ohms coplanar waveguides from input to output. The matching parts visible on the Figure 105 permit to compensate for the parasitic capacitance we have between the two parts of the flip-chip. Thus, by reducing the signal line width, we create an inductive effect. All dimensions are given on the Figure 105.

As we can see on the Figure 105, we have also decreased the size of the two parts, especially the size of the top part, which was shrinking by 2.9 times compared to the "40 GHz

version" of the flip-chip (FC0). We were able to decrease the size of the structure because of the higher frequency (about 100 GHz), which makes the line widths smaller. Thus, we obtain a lighter top part, so we expect that the mechanical strength necessary between the two parts will be lower.

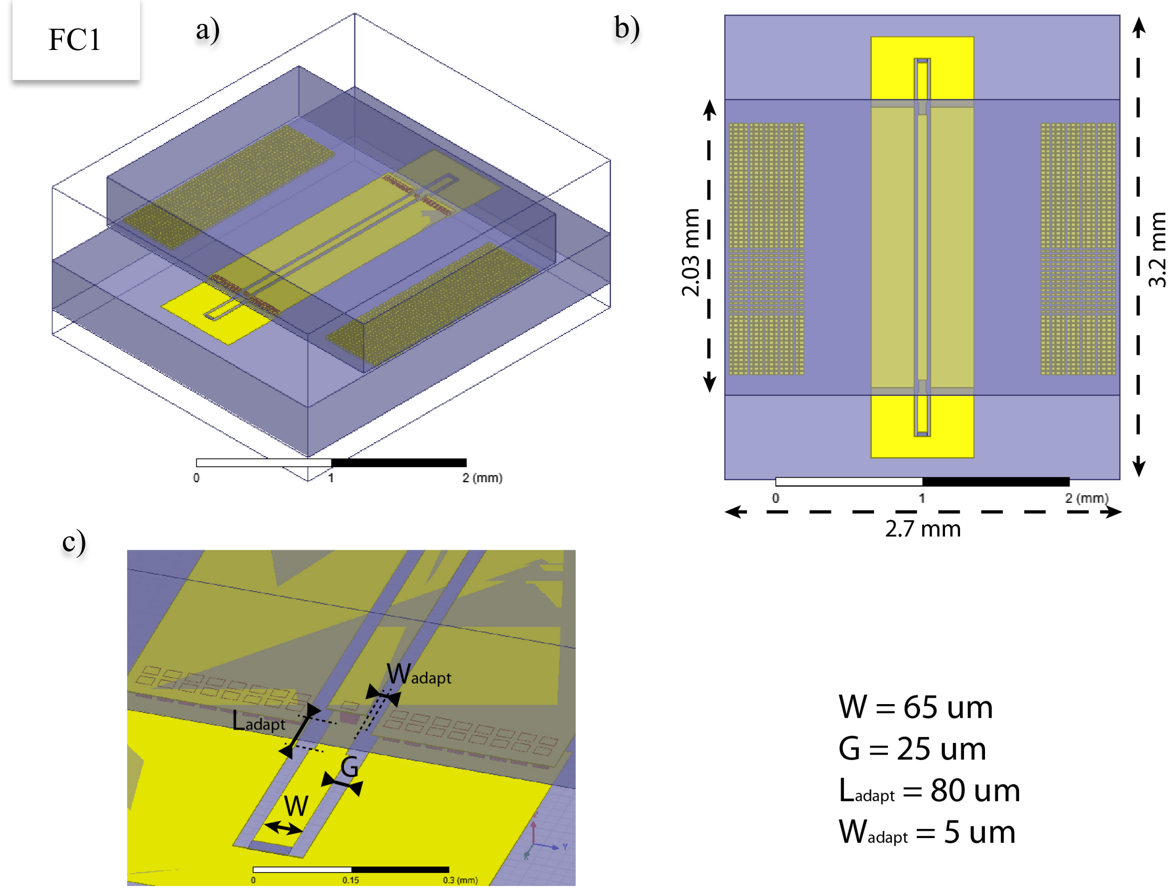

Figure 105: Side view (a), top view (b) and zoom in on the interconnections (c) of the first new flip-chip configuration (FC1).

The advantage of having smaller line size is that we can also gain some space to add more extra dummy bundles of CNTs, necessary for the mechanical strength. Last time, for the 150-µm-bump size flip-chip version (FC0 - structure 1), we had $N_{Bundle} = 58$ bundles of CNTs. Thus, we can easily compare (Table 13) the number of CNTs interconnected and also the surface in contact for the previous flip-chip FC0 and the new one FC1 (the estimated number of interconnected CNTs for the new structure is calculated in function of the previous results we obtained):

Table 13: Comparison of the two flip-chip configurations FC0 and FC1.

Flip-chip configuration	**Total CNT surface in contact (Bundle surface x N_{Bundle})**	**Total number of interconnected CNTs ($N_{connection}$ x N_{Bundle})**
FC0 (up to 40 GHz)	150 µm x150 µm x 58 = 130.10^{-8} m^2	$1.35.10^5$ x 58 = $7.8.10^6$
FC1 (up to 110 GHz)	20 µm x20 µm x 1806 = 72.10^{-8} m^2	2400 x 1806 = $4.3.10^6$

As we can observe from these calculations, we have a surface in contact twice smaller with the new configuration and so we have also twice less number of interconnected CNTs. However, with this new design, the die is three times smaller than the previous one. Thus, the mass of the die is expected to be also three times lower. Based on our previous studies on the mechanical forces between the two parts (see Figure 103), we have $4.3.10^6$ number of interconnected CNTs and a structure weight equal to 5.10^{-5} N, and as shown on the Figure 106, a distance between CNTs about 200 nm would be able to maintain the top part over the bottom part of the flip chip. These results are encouraging since a maximum distance of 80 nm was necessary with our previous flip-chip device.

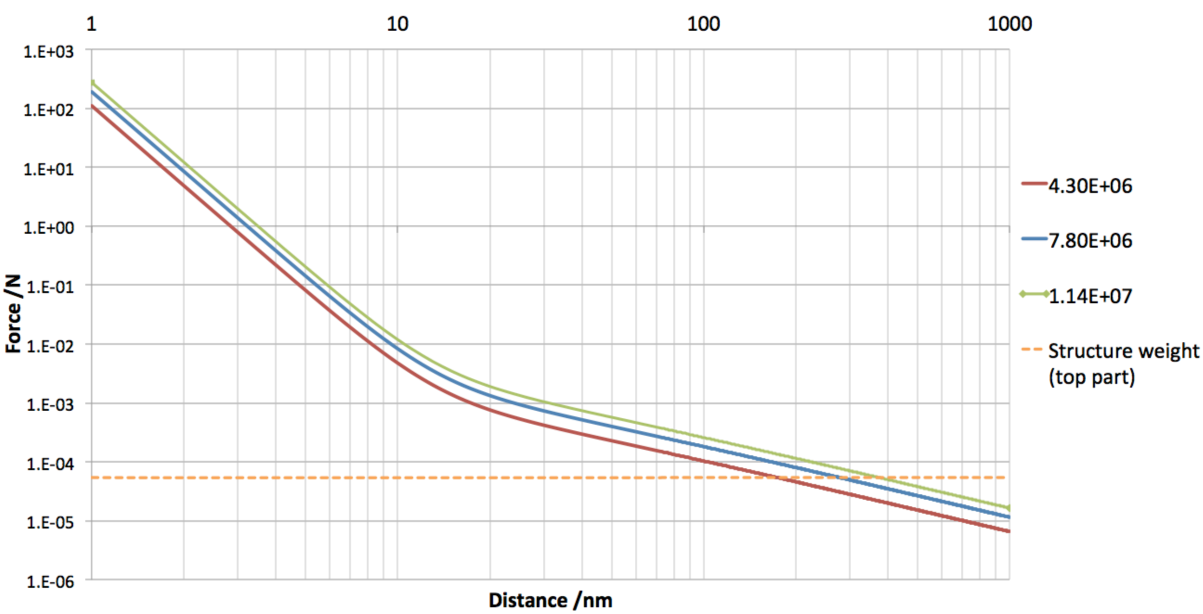

Figure 106: Electrostatic and Van der Waals forces of a given number of CNTs as function as the distance between them (the carbon nanotubes). On solid curves, we have the addition of these two forces. The dash orange curve represents the weight of the top flip-chip with the new configuration (FC1 and FC2).

- RF simulations:

Then, we model and simulate the all structure by using gold material and the hybrid CNT model we presented previously for the bumps. We used the exact same setup than the one presented in Figure 94. All CNTs parameters are indicated on the Table 14. Hence, we were able to optimize the insertion and return losses along the flip-chip. We performed EM simulations between 80 and 120 GHz using HFSS software and finite element methods. Hybrid simulations were done using ADS software from Agilent. As you can see on the Figure 107, the insertion loss remains between -1 and -2 dB and the return loss always below - 18 dB with the full-EM simulation using gold bumps (red and black curves).

Table 14: CNT bundle components values.

N_{MWCNT}	R_C	C_C	R_{CNT}	L_K	$R_{CNT-CNT}$
1	10 kΩ	4.1. 10^{-6} aF	20 kΩ/µm	0.86 nH	324 kΩ
2400	4 Ω	0.98 pF	8.3 kΩ/µm	358 fH	135 Ω

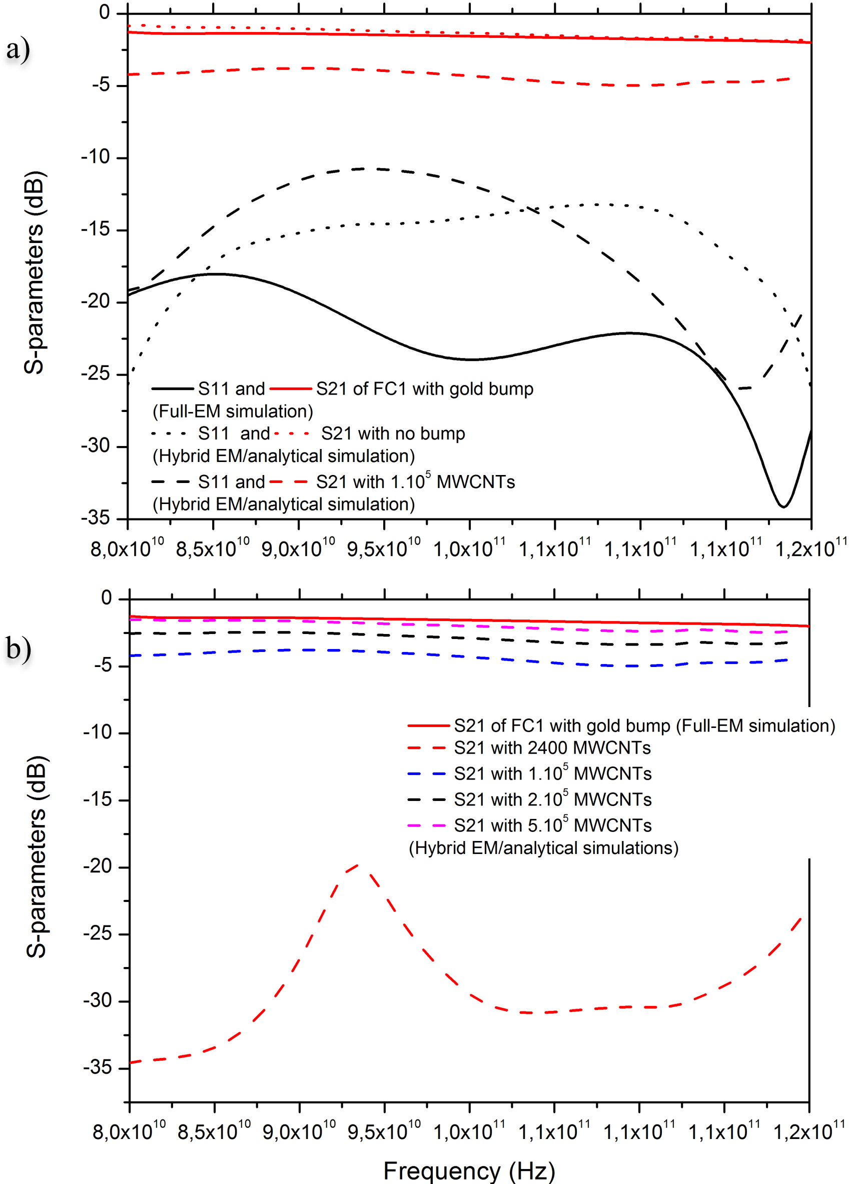

Figure 107: On (a), simulated S-parameters from 80 to 120 GHz of the first new flip-chip configuration (FC1) and a comparison with the hybrid EM/analytical simulations for 0 MWCNTs and 100000 MWCNTs per bumps. On (b), corresponding S_{21} parameters with several densities of MWCNTs (from 2400 to 500000 MWCNTs).

From the parametric study of the device FC1 using the hybrid simulation (Figure 107), we observe that 2400 MWCNTs is not enough to have acceptable RF performance (red dash curve in (b)). Thus, for FC1, we must increase the density of CNTs in the bundles in order to achieve a good RF transmission from 80 to 120 GHz. As we can observe on Figure 107, with $N_{MWCNT}=1.10^5$ (red and black dash curves in (a) and blue dash curve in (b)), we have already enough CNTs to achieve insertion loss higher than -4 dB and return loss below -10 dB. By increase the number of CNTs to $N_{MWCNT}=5.10^5$ (purple dash curve in (b)), we can even reach the same performance we obtained with the gold bumps (full-EM simulation). This represents

a CNT density of 1250 CNT.μm^{-2}, which is a realistic density (see Table 7). In conclusion, an increase of the CNT density is essential for the device FC1 in order to achieve a correct level of performance in high frequency.

- Improvement of the mechanical adhesion:

Moreover, on the mask, we have defined several strategies in order to increase the chance to get good mechanical strength between the two parts. As you can see on appendix 1, we have our “base” structure, which is also the one presented on Figure 105. We have also the “bump crossed” structure (appendix 1), with bundles of CNTs larger than longer on the bottom part and the opposite on the top part, in order to compensate for the tolerance error of the bonding machine. With the “bump crossed” structure, we keep the same number of interconnected CNTs than the “base” one. And finally, we have the “base ++”, which is the same structure than the “base” one with twice more dummies bundle of CNTs on each side. Thus, we estimate the number of interconnected CNTs for the “base ++” FC1 device (Table 15).

Table 15: Comparison of the two flip-chip configurations FC1 “base” and FC1 “base ++”.

Flip-chip configuration	**Total CNT surface in contact (Bundle surface x N_{Bundle})**	**Total number of interconnected CNTs ($N_{connection}$ x N_{Bundle})**
FC1 (up to 110 GHz)	20 µm x20 µm x 1806 = 72.10^{-8} m^2	2400 x 1806 = $4.3.10^6$
FC1 (base ++) (up to 110 GHz)	20 µm x20 µm x 2850 = 114.10^{-8} m^2	2400 x 2850 = 7.10^6

With this number of interconnected CNTs (7.10^6 MWCNTs), we still increase the minimum distance between CNTs we need in order to insure a high enough mechanical strength between the two parts. Now, a maximum distance of 300 nm is needed for the CNTs to sustain the top part of the flip-chip.

Next, we propose the same “base” design by replacing the 20-µm dummy CNT bundles (located on the sides) with 100-µm-bundle size (appendix 2). Thus, we decrease the chance of error from the bonder equipment tolerance.

Finally, same as the previous flip-chip design, we add some de-embedding structures for the bottom and the top part (Figure 108). However, these structures weren’t presented in

the first part because of the difficulties we encountered to success the interconnections with our first flip-chip. We have the thru, line and reflect. Thru is realized by connecting the input with the output parts without a line in between. Line is realized by adding a quarter-wavelength line. Reflect is realized by adding a short. A high frequency measurement of these structures will allow us to extract the CNT bundles S-parameters.

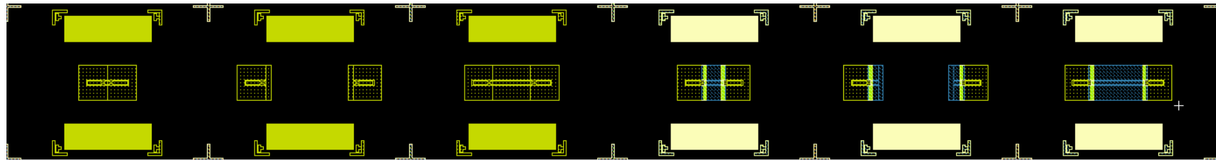

Figure 108: De-embedding parts of the flip chip devices composed by six structures: Thru (input and output connected), reflect (short) and line (quarter wavelength lines) disposed respectively before and after the interconnections.

ii. Flip-chip with 100-µm-bump size: FC2

- Design:

This time, in order to insure the workability of our flip-chip up to 110 GHz, we designed a flip-chip with 100-µm bundles, the same size than our previous studies. Thus, we avoid the complication to have smaller bundle size and will only focus with this structure on the measurement and feasibility of these interconnected CNTs at very high frequency. Again, some matching parts have been added in order to compensate for the capacitance effect between the two parts of the flip-chip. These marching parts have been optimized with the full-EM simulation using gold bumps. We present the FC2 structure and dimensions on the Figure 109 and we can see the FC2 S-parameters from full-EM simulations with gold bumps on Figure 110.

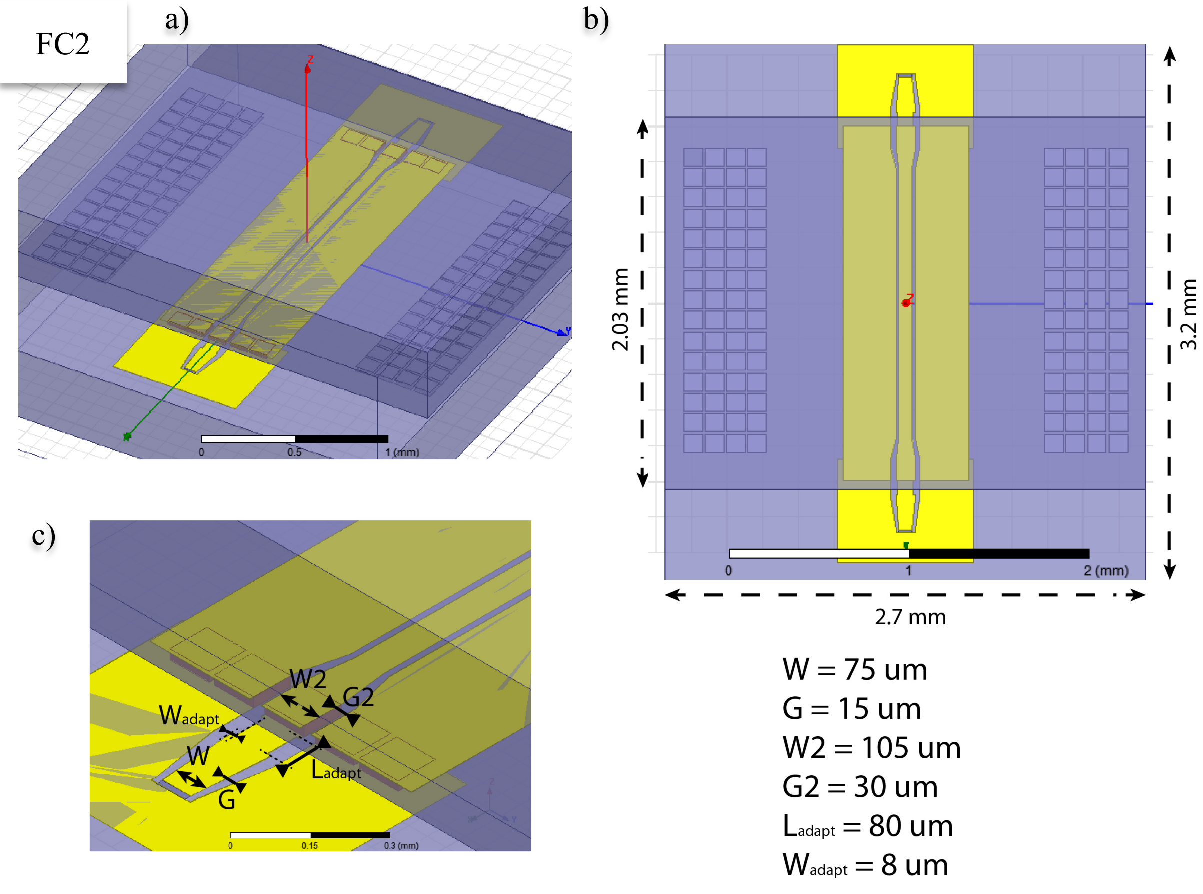

Figure 109: Side view (a), top view (b) and zoom in o the interconnections (c) of the first new flip-chip configuration (FC2).

Even if we have bigger size of CNT bundles with FC2 (100-µm-bundle size) than FC1 (20-µm-bundle size), we also tried to increase the number of interconnected CNTs. Using the same calculation than the previous paragraph, we calculate the total surface in contact and estimated number of interconnected CNTs (Table 16). Again, we compare with the previous flip-chip FC0 working up to 40 GHz.

Table 16: Comparison of the two flip-chip configurations FC0 and FC2.

Flip-chip configuration	**Total CNT surface in contact (Bundle surface x N_{Bundle})**	**Total number of interconnected CNTs ($N_{connection}$ x N_{Bundle})**
FC0 (up to 40 GHz)	150 µm x150 µm x 58 = 130.10^{-8} m^2	$1.35.10^5$ x 58 = $7.8.10^6$
FC2 (up to 110 GHz)	100 µm x100 µm x 130 = 130.10^{-8} m^2	60000 x 130 = $7.8.10^6$

With FC2, we have preserved the same estimated number of CNTs that will be interconnected, and if we take a look on the Figure 106, with the same CNT density than

before, meaning also the same spacing between CNTs (between 200 and 500 nm), we will almost be able to maintain a good enough mechanical strength between the two parts. However, to achieve this result, it will be important to success a quite accurate alignment during the bonding in order to have the maximum estimated number of interconnected CNTs (N_{MWCNTs} = 60000 per bundle). This can be the next issue since the new flip-chip structure is three times smaller than the previous one.

- RF simulations:

From the full-EM simulation using gold bumps (Figure 110) the insertion loss was calculated to be between -1.6 and -3 dB from 80 to 120 GHz and the return loss always below -12 dB. As we observe, lower performance is obtained with this FC2 structure, because of the additional matching parts we have to add. Indeed, because of the bigger size of the CNT bundle (100 µm), and the higher frequency (100 GHz), the width of the 50-ohms signal coplanar waveguide is not compatible with the size of the bundles. Thus, the width of the CPW signal part needs to be about 65 µm, which is almost two times smaller than the bundle size. As we can see on the Figure 109, we enlarged the bottom and top lines at the bundle locations in order to be able to grow our 100-µm-side bundle of CNTs.

We also performed hybrid EM/analytical simulations using the same configuration than the previous part. The value of each component in the analytical model is indicated on the Table 17 and the simulation results from 80 to 120 GHz are presented on Figure 110. Thus, we performed a hybrid simulation with several CNT densities from 6.10^4 to 1.10^6.

Table 17: CNT bundle components values.

N_{MWCNT}	R_C	C_C	R_{CNT}	L_K	$R_{CNT-CNT}$
1	10 kΩ	$4.1.\ 10^{-6}$ aF	20 kΩ/µm	0.86 nH	324 kΩ
60000	166 mΩ	24.6 pF	0.33 kΩ/µm	14.3 fH	5.4 Ω

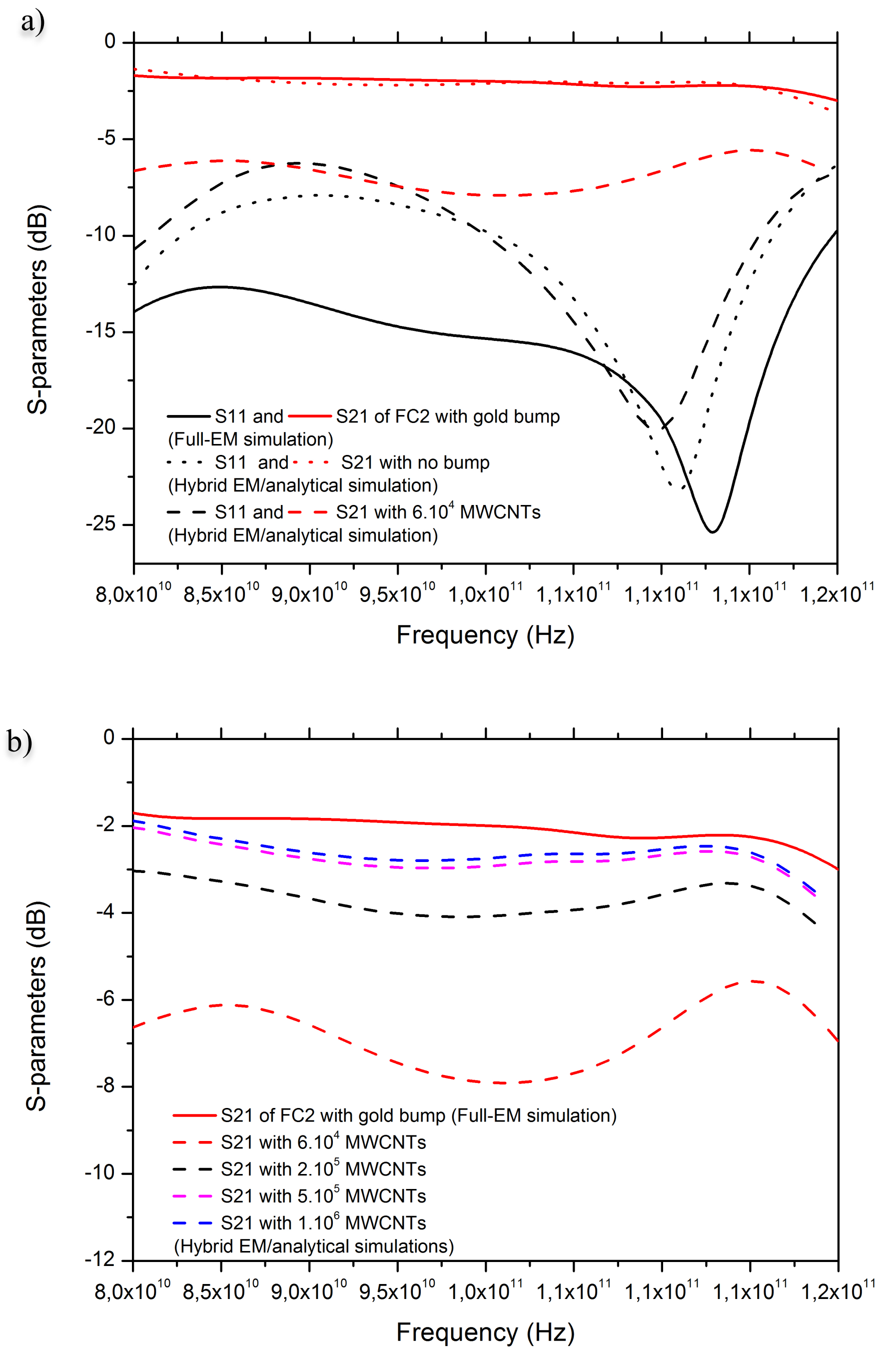

Figure 110: On (a), simulated S-parameters from 80 to 120 GHz of the second new flip-chip configuration (FC2) and a comparison with the hybrid EM/analytical simulations for 0 MWCNTs and 60000 MWCNTs per bumps. On (b), corresponding S_{21} parameters with several densities of MWCNTs (from 60000 to 1000000 MWCNTs).

As we can observe on the Figure 110(black and red dash curves on (a) and red dash curve on (b)), the number of interconnected CNTs (N_{MWCNT}s = 6.10^4 CNTs) is too small to get correct RF performance. Indeed, we obtain a S_{21} parameter between -6 and -8 dB and return loss always below -6.5 dB. However, by increase the CNT to N_{MWCNTs} = 2.10^5 (black dash curve on (b)), we reach a S_{21} parameter of -3 dB. We only increase the CNT density by three times and improved a lot the RF performance of FC2. If we still increase the number of

interconnected CNTs to $N_{MWCNTs} = 1.10^6$ CNTs (blue dash curve on (b)), again, we almost reach the performance of the flip-chip with the gold bumps. In conclusion, we really need to focus on an increase of the CNT density in order to improve the performance of our new flip-chip devices FC1 and FC2 working up to 110 GHz. Several solutions exist in order to increase the CNT density as we already explained in the chapter I, section “Chemical vapor deposition (CVD) on page (34)”.

- Improvement of the mechanical adhesion:

Based on the same principle than FC1, we did a “base ++” version of the FC2 flip-chip and also a “bumps crossed” version (appendix 3). With the “bump crossed” version, we decrease our chance to obtain a misalignment between the two parts during the bonding. With the “base ++” version, we will still increase the mechanical strength between the two parts of the flip-chip. If we calculate again the surface in contact and number of interconnected CNTs, we obtain (Table 18):

Table 18: Comparison of the two flip-chip configurations FC2 “base” and FC2 “base ++”.

Flip-chip configuration	**Total CNT surface in contact (Bundle surface x N_{Bundle})**	**Total number of interconnected CNTs ($N_{connection}$ x N_{Bundle})**
FC2 (up to 40 GHz)	100 µm x100 µm x 130 = 130.10^{-8} m^2	60000 x 130 = $7.8.10^6$
FC2 (base ++) (up to 110 GHz)	100 µm x100 µm x 190 = 190.10^{-8} m^2	60000 x 190 = $11.4.10^6$

With $11.4.10^6$-interconnected CNTs, we have decreased the minimum distance necessary to 400 nm, which is compatible with the current distance we have between the CNTs (about 200-500 nm).

Finally, again, de-embedding parts have been designed in order to eliminate the losses from the lines and extract the S-parameters of the interconnections made by CNT bundle only (Figure 111).

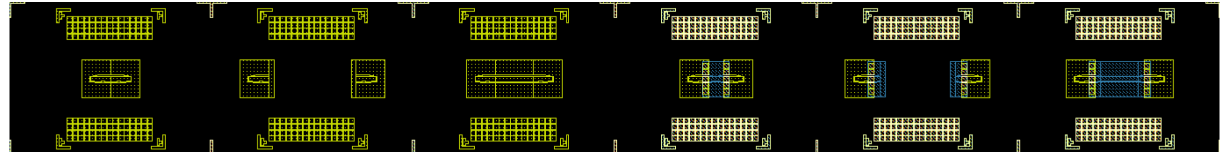

Figure 111: De-embedding parts of the flip chip devices composed by six structures: Thru (input and output connected), reflect (short) and line (quarter wavelength lines) disposed respectively before and after the interconnections. A high frequency measurement of these structures will allow us to extract the CNT bundles S-parameters.

- Improvement of the number of interconnection:

From the previous part, we arrived at the conclusion that we need to increase the CNT density. Thus, one of the easiest ways to increase the CNT density is to use the thermal CVD process instead of the plasma CVD to grow bundle of CNTs. Indeed, by thermal CVD, as we already explained in the first chapter, we are able to grow higher CNT bundle density. With a higher number of carbon nanotubes in the bundle, the spacing between them will be reduced (few decade of nanometers) and so the Van der Waals and electrostatic interactions will be stronger. However, during our experiments, we tried to flip-chip two bundles of CNTs grown by thermal CVD and we were not able to succeed the interconnection between them because of the two high CNT density. Indeed, the two bundles were shocking each other without any possibility to create a mechanical bond as shown on Figure 112.

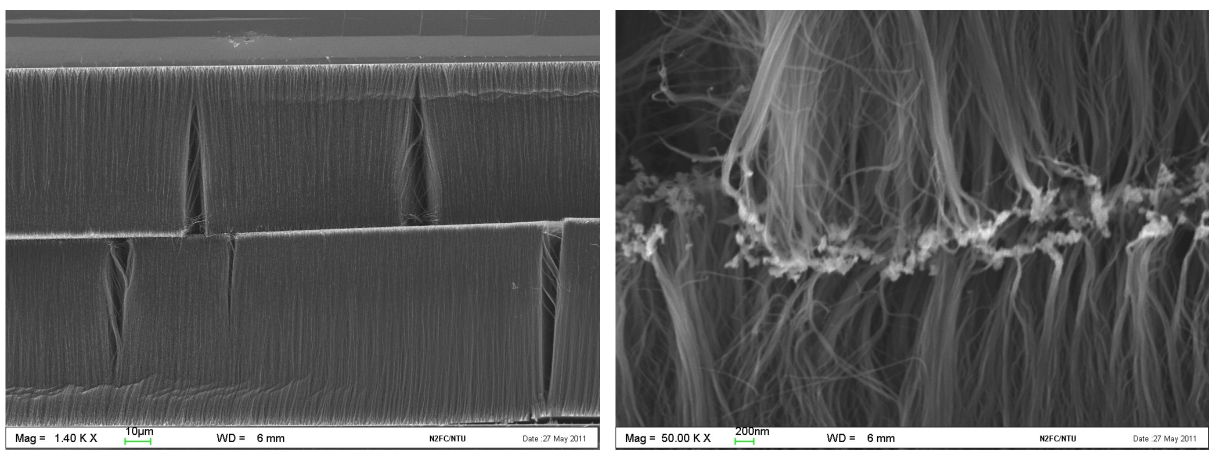

Figure 112: High-density CNT bundle interconnected.

Thus, to solve this issue, we changed the shape of the flip-chip bundles in order to allow an interconnection and a strong enough mechanical bond. As you can see on the Figure 113, we designed two bundle shapes: a square and a cross. In both cases, the CNT bundles from the top will be different than the CNT bundle from the bottom part. Both confirgurations

will be composed by verticaly aligned CNTs grown by thermal CVD with a very high CNT density (about 1.10^{14} m^{-2}).

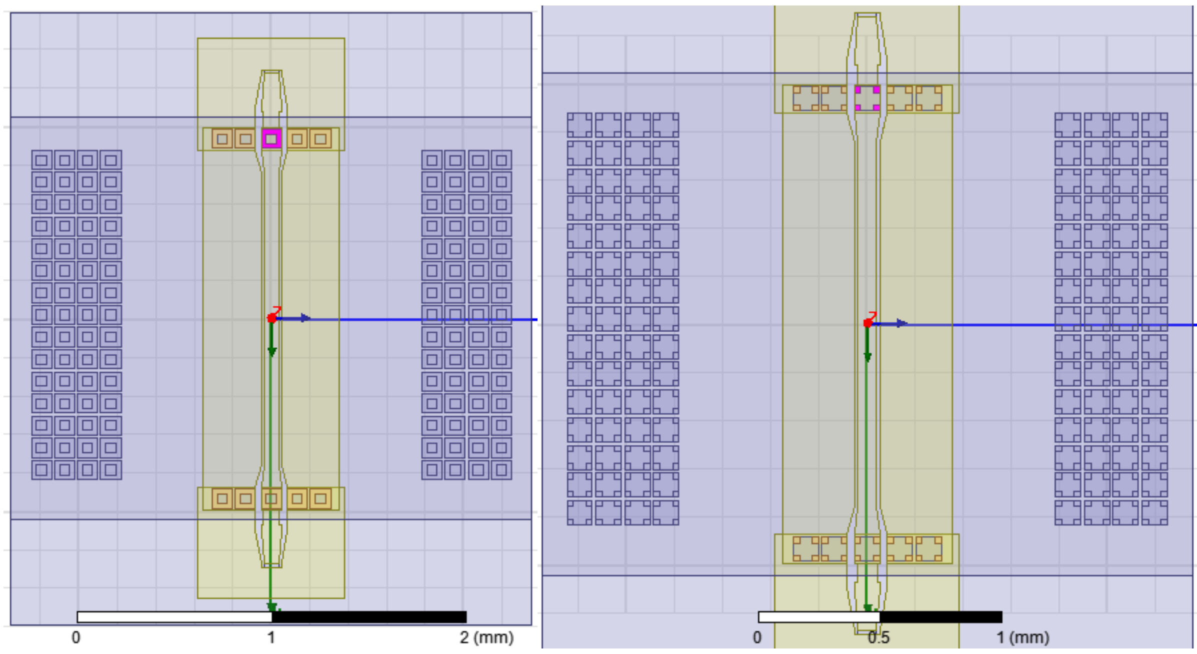

Figure 113: Top views of the flip-chips composed by high density bundles of CNTs. Square shapes are on the left figure and cross shapes are on the right figure.

For example, the big squares are grown on the bottom part while the small squares are grown on the top parts. Thus, the big squares will surround the small squares once the CNTs are interconnected. And the carbon nanotubes placed on the outer faces of the small squares and the CNTs on the the inner faces of the big squares will touch each others and create the mechanical and electrical bond between the two parts (as shown on Figure 114). The red square is grown on the bottom part and the blue square is grown on the top part. Vertically aligned CNTs (grown by thermal CVD) compose the two bundles. With a dimension of 80x80 μm^2 (blue square) and a CNT density of 1.10^{14} m^{-2}, we can have 16.10^6 interconnected SWCNTs (diameter of 2 nm) in the ideal case.

Figure 114: Schematic of the high density interconnected bundles of CNTs following the square shape.

In the second case, we grow the cross on the top part of the flip-chip whereas the four pillars are grown on the bottom part. Hence, base on the same principle, the outer faces of the cross will interconnect with the faces of the four CNT pillars bundle surrounding the cross (as shown on the Figure 115. Vertically aligned CNTs (grown by thermal CVD) compose the two bundles. With a dimension of 20 µm (red double arrow) and a CNT density of 1.10^{14} m^{-2}, we can have 12.10^{6} interconnected SWCNTs (diameter of 2 nm) in the ideal case.

Figure 115: Schematic of the high density interconnected bundles of CNTs following the cross shape.

The red cross is grown on the top part and the blue squares are grown on the bottom part. Vertically aligned CNTs compose the two bundles. With these two last cases, we are however losing the Velcro-type of interconnected bundles of CNTs.

B. Fabrication of the devices

Based on the same recipe than the one presented for our first flip-chip device, we fabricate the devices presented in the previous part. Fabrication and measurements (DC/RF) are still under progress and hopefully will be presented during the PhD defense.

C. Conclusion

In conclusion of the second chapter, we have demonstrated the feasibility of a flip-chip using interconnected carbon nanotubes up to 40 GHz. DC and RF results showed very encouraging results with a S_{21} parameter about -2.5 dB and a return loss always below -13dB. Repeatability in measurements has been shown and re-workability of the CNT interconnections has been demonstrated in DC. Finally, a full modeling of the device by EM approach and hybrid EM/analytical approach. Both approaches show a perfect agreement with the measurements and allowed us to extract the contact resistance value between two carbon nanotubes in high frequency. We showed the contact resistance between two CNTs is high (about 300 kΩ) and CNT bundle needs to be increased in order to get enough CNT contact.

The number of interconnected CNT needs to be increased also in order to improve the mechanical adhesion between the two flip-chip parts. Thus, new-flip designs working up to 110 GHz have been proposed with CNT bundle shapes and sizes have been optimized. Hybrid simulations demonstrated that the high frequency transmission could be as good as metal-based flip-chip with a high enough CNT density. Fabrication of these new flip-chip structures is under progress. In the next chapter, we will see how we can avoid the important contact resistance existing between CNTs and metal or CNTs by replacing the ohmic contact by wireless interconnections. These wireless interconnections will use CNT monopoles.

Chapter III

I. Wireless interconnections based on carbon nanotubes

In this chapter, we will present a novel approach to interconnect chip-to-chip electronics components but also the nano-materials, such as the carbon nanotubes, with the nano and micro-electronics worlds. We will try to extract the quantum properties of the CNTs in order to highlight their interests for wireless interconnections. A simple process will be set up to easily develop such wireless interconnect using bundle of CNTs. Both applications will be necessary in future devices since with the shrinking geometry of the current electronics devices (as we presented in the chapter II), interconnects become an important cause of loss [166]. Indeed, as we have observed with the flip-chip in the previous chapter, we faced a resistance issue once we wanted to contact a carbon nanotube with a metal layer or two carbon nanotubes. Because of the too high CNT resistance, a bundle of CNT needed to be grown and important CNT length needed to be in contact with the metal layer in order to decrease the total resistance. We also met an important impedance mismatch between carbon nanotube bundles and high frequency electronics.

Some groups tried to work on 3-D integrated circuit in order to reduce the length of the interconnections [167]. This alternative approach is viable but such interconnections are facing more complex fabrication process. Thus, to avoid all the contact resistance existing and the complex fabrication processes and by using the unique CNT properties, we will try to create wireless interconnection with unique behavior and property.

We will start our studies with the works that have been done on antennas using CNTs in order to use these antennas as wireless interconnections. Next, we will present interconnections that we have developed based on a monopole principle from 40 GHz to 300 GHz. Simulated transmission tests will be presented with simulation studies and fabrication of the wireless interconnections will be done.

1. Wireless interconnections based on carbon nanotubes

Carbon nanotubes have been mostly used as interconnections, transistors or sensors as we have shown in the first two chapters (sections “High and low frequency applications based on carbon nanotubes (state of the art) on page (91)” and “Interconnections using carbon nanotubes on page (96)”). However, some groups have worked on antennas based on carbon

nanotubes. The carbon nanotubes are a natural choice for making miniaturized antennas because of their nano-scale and their high electrical conductivity (see section "Electrical properties on page (25)"). These antennas based on CNTs are still a small active field of research since it is quite difficult to control the CNT bundle growth to achieve complex shapes and also a very homogenous bundle of CNTs in terms of CNT length and diameter. This last point is crucial for the antenna applications where the resonance frequency can be easily affected by the material properties. In the state of the art, we can find three main interests of using the carbon nanotubes as antenna.

A. Wireless on-chip interconnects based on CNTs for optical range

First, because it is easier to grow short length CNTs ranging between few nm to several micron and carbon nanotubes become compatible with the terahertz range (THz) and optical domain. Works on THz domain is still recent and new sources in THz frequencies are currently an active field of research. Simulation works [168-170] showed the geometrical resonances of the CNT antennas slow down the surface plasmon and, in consequence, shift the frequency resonance to the THz range. Thus, THz antennas made by carbon nanotubes might be a good option, also for creating a new way to interconnect devices in the THz range. A vertically aligned CNTs bundle (grown by PECVD) has been already used for an antenna working at the THz range and some work on the nanotube polarization has been done as seen on Figure 116 [171].

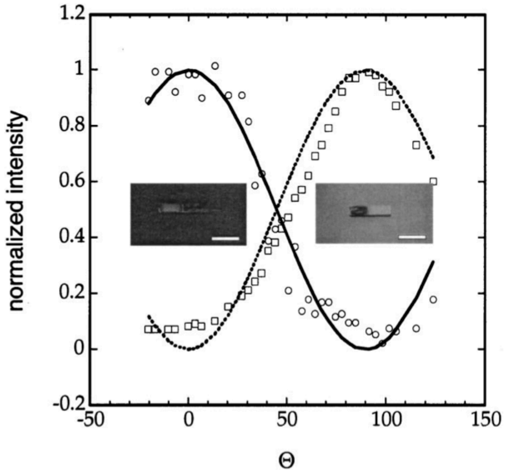

Figure 116: Polarization effect. Reflected, normalized light intensity vs polarization angle Θ for the sample shown in the insets. Circles represent the light intensity from the random array of nanotubes, and squares from the metallic film. Left inset: sample viewed with the polarization plane parallel to nanotubes (p-polarization), Θ=0. Right inset: sample viewed through polarizer with the polarization plane perpendicular to nanotubes (s-polarization), Θ=90°. Scale bars, 1 cm. Source: [171]

Secondly, some recent research has shown that carbon nanotubes have interesting optical emission and absorption properties [172]. These CNT properties can be used to realize antenna like behavior in CNTs and hence create an on-chip solution working at the optical frequencies. Indeed, using the optical range to transmit a signal would allow a higher data rate and a higher efficiency in term of loss. A higher frequency would also reduce the interference between components. An interband transition is used in CNTs, similar to the mechanism in optoelectronic devices [173]. Figure 117 presents a device using a carbon nanotube as an antenna working at the optical range. In this design, the nanotube acts as a modulator and an antenna for the transmitter (top figure) and a demodulator and antenna in the receiver (bottom figure). Thus, by applying a constant voltage on the SWCNT connected between two metal electrodes, light can be generated. The light wavelength (or the antenna working frequency) will be determined by the nanotube band gap, and so by the nanotube chirality (see section "Chirality vector on page (15)"). In the transmitter, the nanotube acts as a photo detector and will generate a voltage signal with the incoming light, which will do an electron-hole pair generation. However, the fabrication of such device remains a challenge since SWCNTs with exact same properties (length, diameter and chirality) need to be fabricated for both the transmitter and the receiver. Using CNTs as transparent electrodes in solar cells can be a potential application.

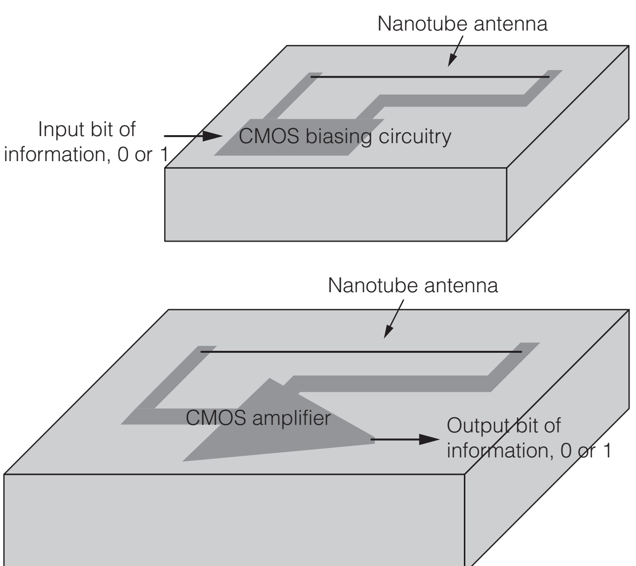

Figure 117: Schematic representation of a transmitter (top figure) and a receiver (bottom figure) using a nanotube antenna. Source: [172, 174]

B. Wireless chip-to-chip interconnects based on CNTs for high frequency range

In a second time, as we already presented in the first chapter (section "Electron transport: Ballistic conduction versus Diffusive on page (25)"), carbon nanotubes don't act as a usual bulk material because of their quantum behavior. Thus, an antenna made by carbon nanotubes would have very different radiation frequency than a metal-based one. Indeed, with the help of carbon nanotube models, it has been shown that the size of an antenna can be reduced using the "quantum" effects in carbon nanotubes such as the kinetic inductance (Figure 118) [83, 175, 176]. This behavior is quite different than the interband mechanisms presented in the previous part. At a given working frequency, a size reduction of an antenna made by CNTs becomes possible. Not only in THz range, Hanson [177] works showed that above a critical frequency of 53 GHz, a dipole antenna would be able to resonate. Indeed, below this frequency, the CNT length necessary will be too important and resistive damping along the tube will inhibit the resonance effect of the tube. In contrast, higher is the resonance frequency; shorter is the antenna and finally higher is the antenna size reduction. The major issue with these antennas is the high resistance of the CNT. The quantum resistance mismatches with the typical 50-ohms high frequency characteristic impedance, which obliges us to use carbon nanotube in a bundle arrangement in order to reduce this impedance. In addition, as already explained in section "Modeling of a bundle of CNTs on page (66)" by having more CNTs in a bundle, we reduce the total quantum effects of the antennas. Thus, a trade-off needs to be done between the size reduction effect and the performance of the antenna.

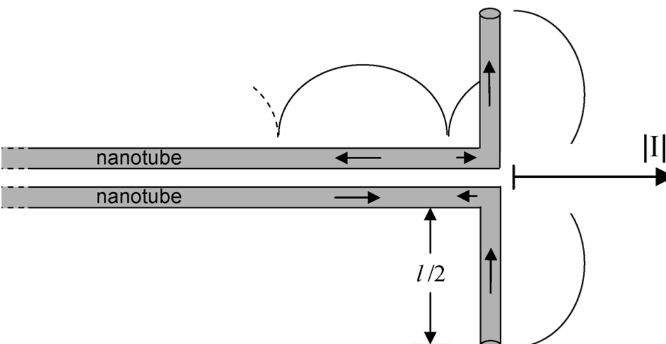

Figure 118: Dipole antenna concepts using carbon nanotube materials from Burke's works. Source: [176]

Finally, antenna modeling has shown a not satisfying efficiency radiation [83, 84, 175, 176, 178] and these monopole and dipole antennas with a size reduction effects haven't been

fabricated or measured so far because of the very high fabrication constraints/expectations: good control of the bundle size and the CNT density, good CNT quality (low impurity with high homogenous CNTs) and very high aspect ratio bundles (few hundreds microns tall with few microns diameter). Electromagnetic (EM) sensing applications would be a suitable application for CNT-based antenna at lower frequency with visible size reduction effects.

In this thesis, we will focus on that second point: the size reduction of a CNT-monopole-based wireless interconnection compared to a metal-based one.

C. Wireless interconnects: their applications

Finally, wireless interconnections presented previously using a carbon nanotube antenna from GHz to optical ranges would be an interesting option to connect the nano-electronics devices with the macro-electronics world. Indeed, today, most of the nano-components are connected using electrodes based on lithography fabrication process [176] and so far has returned a high ohmic contact resistance because of the mismatch in term of scale and resistance. As shown on Figure 119, a potential solution would be to fabricate a device composed by several single CNT antennas with different lengths. Each CNT length will correspond to one frequency resonance. Thus, an integrated nano-system, where several CNT antenna lengths would be grafted (as the proposed architecture on Figure 119), will be able to communicate with micro-electronics devices on a large band of frequency.

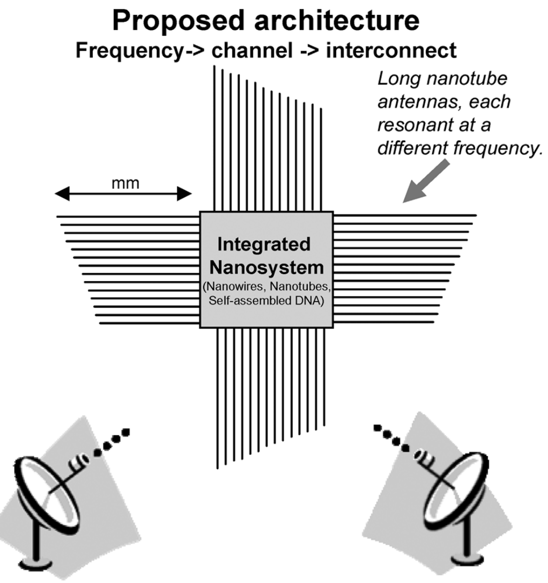

Figure 119: Potential solution to connect the micro-electronics word with the nano-electronics one using wireless interconnections. These wireless interconnections can be done with carbon nanotube antennas. Source: [176]

A second application would be to develop chip-to-chip interconnections. Currently, some wireless interconnections have been proposed in order to replace the traditional metal interconnections with too important losses due to the downscaling of dimensions in electronics [174]. Thus, the idea is to integrate an antenna on chip. Some other works studied such wireless interconnection using dipole antenna made by metal up to 90 GHz [179]. But so far, no works have been realized on wireless chip-to-chip interconnections using CNTs.

Thus, in this work, we will focus on this idea to make chip-to-chip wireless interconnections using CNTs with innovative properties.

2. CNTs-based-wireless interconnection for chip-to-chip communication

Based on the chip-to-chip wireless principle presented previously, in this part, we will present the simulation designs we have developed. These interconnections will be based on the monopole antenna principle and will be working at several frequencies within a range of 40 - 300 GHz. Two main configurations will be introduced with very different ways to fabricate them. Mostly works on simulation has been done in order to experiment and highlight the possibilities of using carbon nanotubes for wireless interconnections.

A. Principle

a) Definition of a monopole antenna

By definition, a monopole antenna is a quarter wavelength vertical metallic wire standing above a ground plane (Figure 120). The monopole length L determines the frequency resonance according to the equation $L = \lambda/4 = v/4f$ with λ the wavelength, v the propagation velocity which is c the celerity of light (3.10^8 m/s) with bulk material (such as metals) and f the working frequency, whereas the radius determines the antenna characteristic impedance.

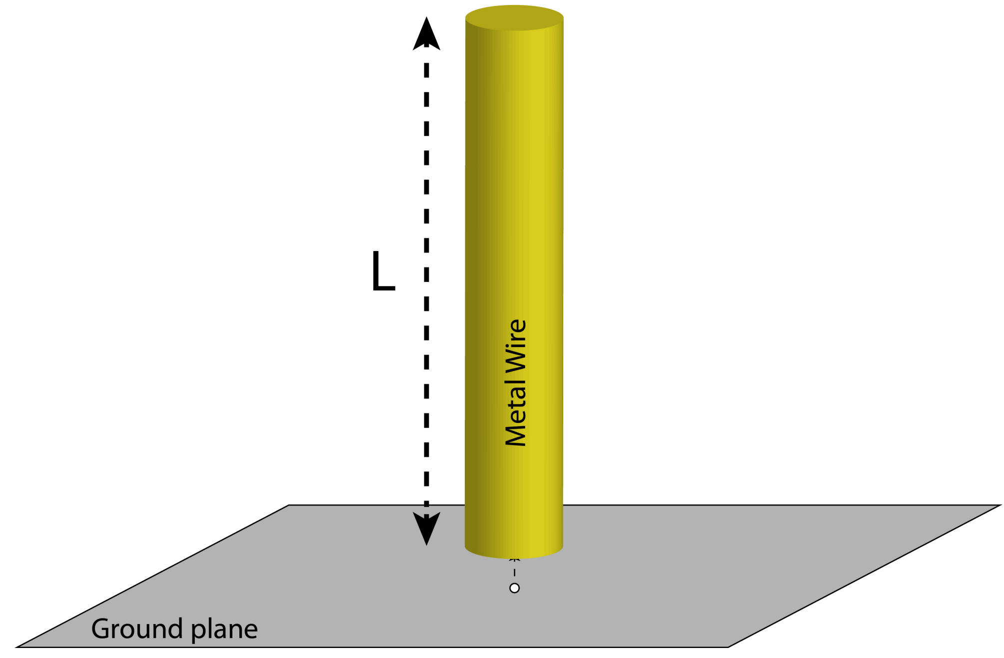

Figure 120: Monopole antenna with a length L standing above a ground plane.

The radiation pattern of a monopole antenna is perfectly isotropic except in the antenna direction as we can see on the Figure 121. The gain is twice the gain of a dipole antenna and ranges between 2 and 6 dBi. A monopole antenna has a high aspect ratio between the length and the radius. For example, an antenna working at 40 GHz has a length of 1.6 mm and a radius of 100 µm. On Figure 121, the simulation was done with a gold monopole antenna working at 40 GHz standing above a ground plane. The length of the monopole was 1.6 mm and the diameter was 100 µm [180]. Both parameters were defined using the antenna designer kit on HFSS.

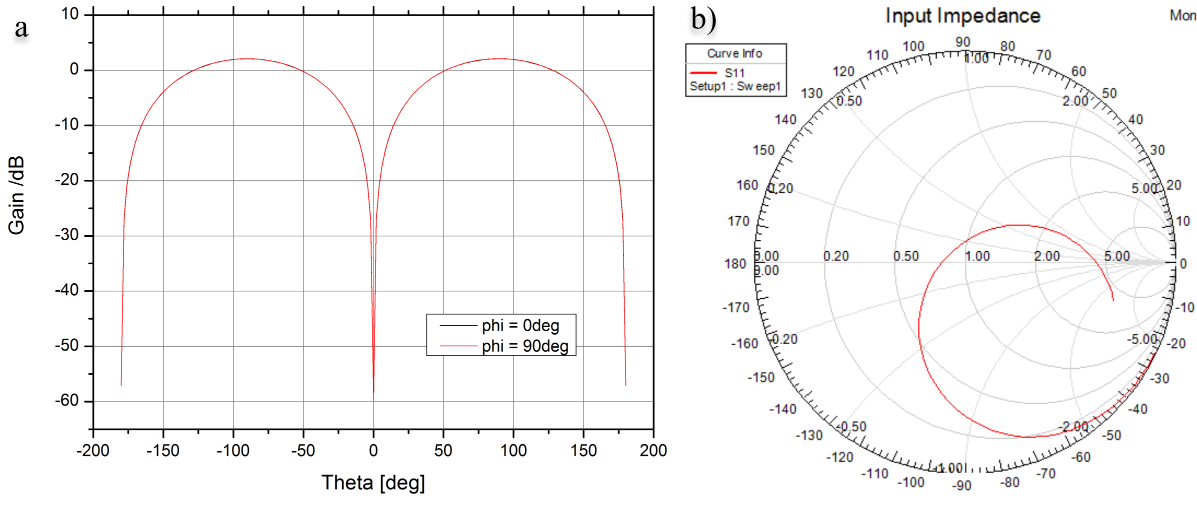

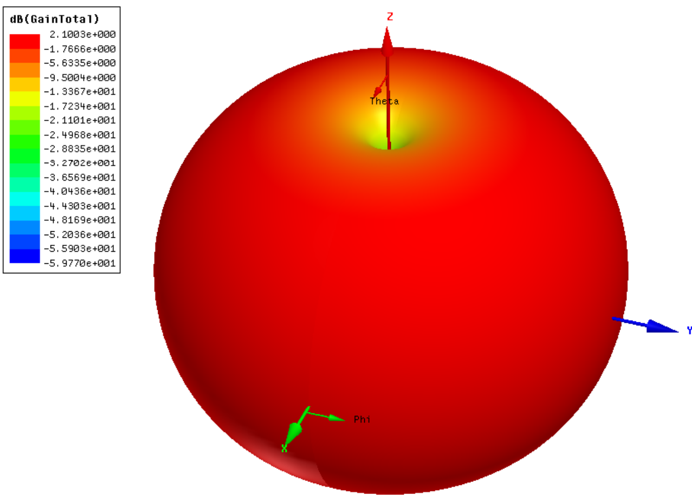

Figure 121: On (b), Input impedance of the monopole antenna. On (a), 2-D (on (a) at phi = 0 and 90°) and 3-D radiation patterns of a monopole antenna. Isotropic radiation except in the antenna direction is visible. Both represent the antenna gain.

Based on this high aspect ratio system, with a diameter of few nanometers and a length of hundreds of microns, carbon nanotubes (CNTs) are the perfect candidate to make a monopole antenna at high frequencies [175, 181, 182]. As we already know, CNT can be assimilating as a hollow cylinder composed of carbon atoms in a hexagonal arrangement. Moreover, as already explained in the chapter I, a single-wall carbon nanotube (SWCNT) is a 1-dimension structure, with quantum behaviors such as the kinetic inductance L_K that is 4 times bigger than the magnetic inductance L_M [69] (see section "Modeling of a single-wall carbon nanotube (SWCNT) on page (62)"). With this unique property, propagation velocity 50-100 times lower than that of light in vacuum can be reached [84]. Indeed, in a RLC circuit representing the SWCNT model, the resonance frequency is directed by the equation: $LCw^2=1$, with L the total inductance, C the total capacitance and $w=2\pi f$ the pulsation. With C constant (C_Q will be negligible as explain on the next part) and an inductance L_k 10^4 times bigger than L_M, $f=1/(2\pi\sqrt{(LC)})$, the resonance frequency will be 100 times lower with L_k. In the case of a bulk material, such as gold, the magnetic inductance directs the equation $f=1/(2\pi\sqrt{(LC)})$, we call it a geometrical resonance of the monopole. Instead, in the case of CNTs, the kinetic inductance directs the resonance frequency and that's why we call it a "quantum" resonance of the monopole. Thus, at a given working frequency, a size reduction of an antenna made by CNTs becomes possible. However, the DC resistances of a SWCNT (see chapter I, section "Analytical modeling of carbon nanotube for DC on page (57)"), which is also called the quantum resistances R_{CNT} and R_Q, are high (about 6.4 kΩ/µm or more for R_{CNT} and 6.4 kΩ for R_Q) [69].

b) Principle of the monopole antenna based on CNTs

Accordingly, in order to decrease the equivalent resistance, CNTs need to be placed in parallel to form a bundle following the principle we have used in the second chapter. As mentioned, in the CNT transmission line model for high frequency (chapter I, section "Modeling of a single-wall carbon nanotube (SWCNT) on page (62)"), the kinetic inductance L_k, the quantum resistance R_Q, the distributed CNT resistance R_{CNT}, the quantum C_Q and electrostatic C_{ES} capacitances exist. The number of CNTs aligned in parallel will divide the equivalent resistance evenly. While the equivalent bundle resistance decreases with the increase of the total number of CNT, the "quantum" effects also decrease due to the decrease of L_k and we lose the advantage of propagation velocity reduction. Thus, a balance between the equivalent bundle resistance and the equivalent kinetic inductance is important to get a high size reduction effect as well as good performance. We also have C_{ES} smaller than C_Q since the diameter of the monopole will remain low (below 10 µm). With C_{ES} in parallels with C_Q, the quantum capacitance C_Q will become negligible.

Thus, we have developed a circuit model on ADS in order to give an idea of the resonance frequency of our CNT monopole interconnection. As explained, this model is based on a RLC circuit with all the components described above. In all the simulations that will be presented later, we consider the contact resistance negligible because of the high number of CNTs (1000 minimum) and the quantum resistances R_Q and R_{CNT} that will be always higher than the contact resistance with this range of CNT length (between 100 µm and 1.6 mm). The circuit schematic on ADS is shown on Figure 122 and simulations are conducted from 1 to 500 GHz in order to design monopole working up to 300 GHz. The input port of our simulation is 50 Ω, so we will consider all our monopole with a characteristic impedance of 50 Ω.

The RLC circuit is a model of the CNT monopole with a circuit approach that can tell us the resonance frequency of the monopole based on CNTs. Indeed, by using the same RLC circuit presented in the "Modeling of a single-wall carbon nanotube (SWCNT) on page (62)" part in chapter II, and by adding two 50-Ω lumped ports at each access of the RLC circuit, we are able to extract the resonance frequency of the RLC circuit modeling the SWCNT bundle.

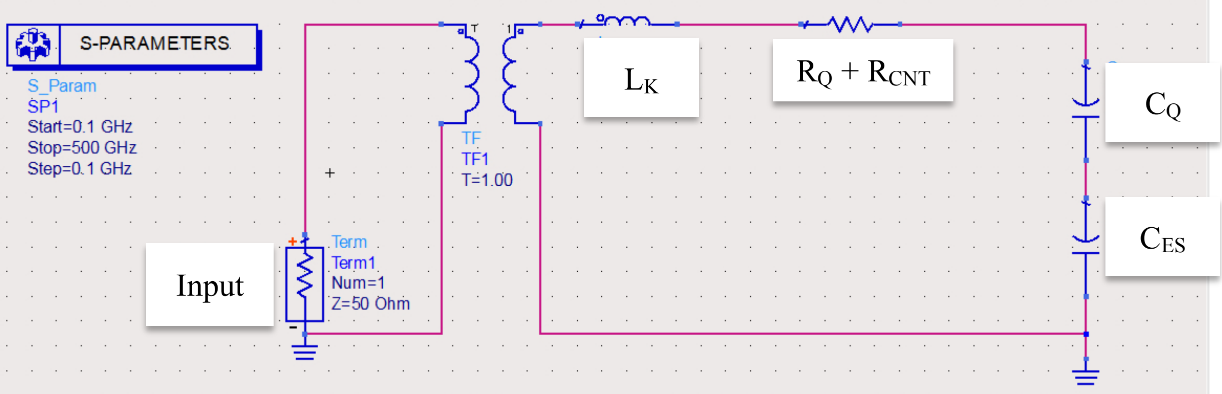

Figure 122: Schematic of the RLC circuit modeling the CNT monopole interconnection on ADS.

In this case, we are using SWCNT, hence the number of conducting channel will be N_i=2 (see section "Modeling of a single-wall carbon nanotube (SWCNT) on page (62)"). The use of SWCNTs instead of MWCNTs is due to the kinetic inductance effect L_k. L_k is higher in SWCNTs than MWCNTs because of the lower number of conducting channels. For L_K, C_Q, R_Q and R_{CNT}, we use the equations (22-25) with l the length of the monopole and N_{SWCNT} the number of CNTs in the bundle. For C_{ES}, we use the equation (26) with d the length of the monopole, which represents the distance from the monopole to the ground plane, a the monopole radius and ε= 11.7 for the silicon.

Thus, based on this circuit model, we design several configurations from 40 to 300 GHz with several CNT densities. The CNT densities are defined by searching the desired resonance frequency and a 50-Ω impedance matching. The monopole working at 40 GHz was designed in order to check the Hanson postulate saying no "quantum" resonance could appear with SWCNT below a frequency of 53 GHz as we already discussed earlier [83]. Next to the 40-GHz monopole, we increased the working frequency to 300 GHz with a step of 100 GHz in order to validate the effect of the kinetic inductance L_k with the increase of the frequency. These monopoles will be used on the next parts in order to realize more realistic designs that we will be able to characterize. The monopole radius is determined by the maximum CNT density we are able to grow in our laboratory by thermal CVD, which is approximately 1.10^{14} m^{-2} (see Table 7). Thus, from the density and the number of CNTs, we are able to calculate the corresponding monopole radius. The return loss (S_{11} parameters) of all the configurations are shown on the Figure 123 and the dimensions of the monopoles are given on the Table 19.

Table 19: Monopole configurations using SWCNTs.

<table>
<tr><th>Configuration</th><th>Number of SWCNTs N_{SWCNTs}</th><th>Monopole length</th><th>Monopole radius</th><th>Monopole dimensions using gold (length/diameter)</th></tr>
<tr><td>40 GHz</td><td>3.10^6</td><td>1.6 mm</td><td>100 µm</td><td>1.6 mm/100 µm</td></tr>
<tr><td>100 GHz</td><td>6000</td><td>600 µm</td><td>6 µm</td><td rowspan="2">760 µm/24 µm</td></tr>
<tr><td>100 GHz</td><td>1000</td><td>300 µm</td><td>2 µm</td></tr>
<tr><td>200 GHz</td><td>1000</td><td>150 µm</td><td>2 µm</td><td>325 µm/11 µm</td></tr>
<tr><td>300 GHz</td><td>1000</td><td>100 µm</td><td>2 µm</td><td>239 µm/6 µm</td></tr>
</table>

Thus, as we can see on the 100-GHz monopoles (green curve and red dash curve), with the increase of N_{SWCNT}, we decrease the effect of the kinetic inductance L_k and so the size reduction of the interconnection. However, with more CNTs in the bundle, we increase the 50-Ω adaptation of the monopole (red dash curve). Also, with the increase of the frequency, we decrease the monopole length (blue curve) and so we decrease the effect of R_{CNT}. With less loss, we increase the monopole adaption. Thus, we need to work at higher frequency in order to compensate for the "quantum" resistances in CNTs in order to be able to reduce the number of CNTs and consequently increase the effect of the kinetic inductance L_k [84, 183, 184]. All these observations will be confirmed again on the next parts of our studies on the monopole with more realistic designs. Thus, each part will focus on one configuration.

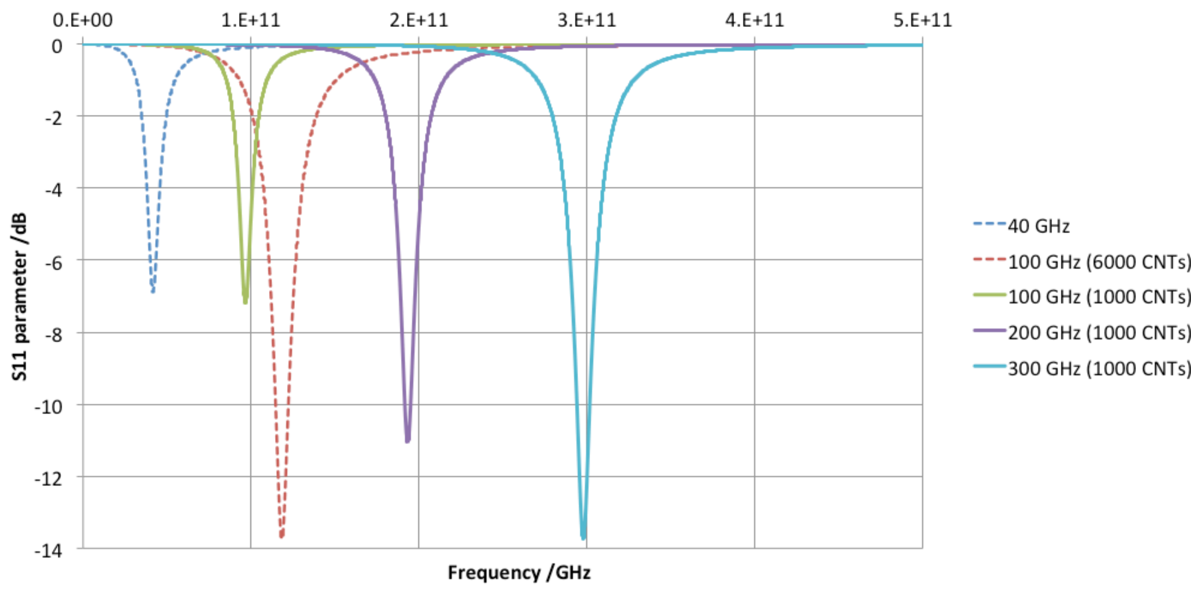

Figure 123: Return loss S_{11} of the RLC circuit modeling a CNT monopole (Figure 122).

With the increase of the monopole diameter without changing the number of CNTs, we increase the capacitance C_{ES} while the inductance L_k remains the same. Thus, as shown on the Figure 124, we decrease the resonance frequency of the monopole. At the opposite, with the decrease of the diameter, we increase the resonance frequency.

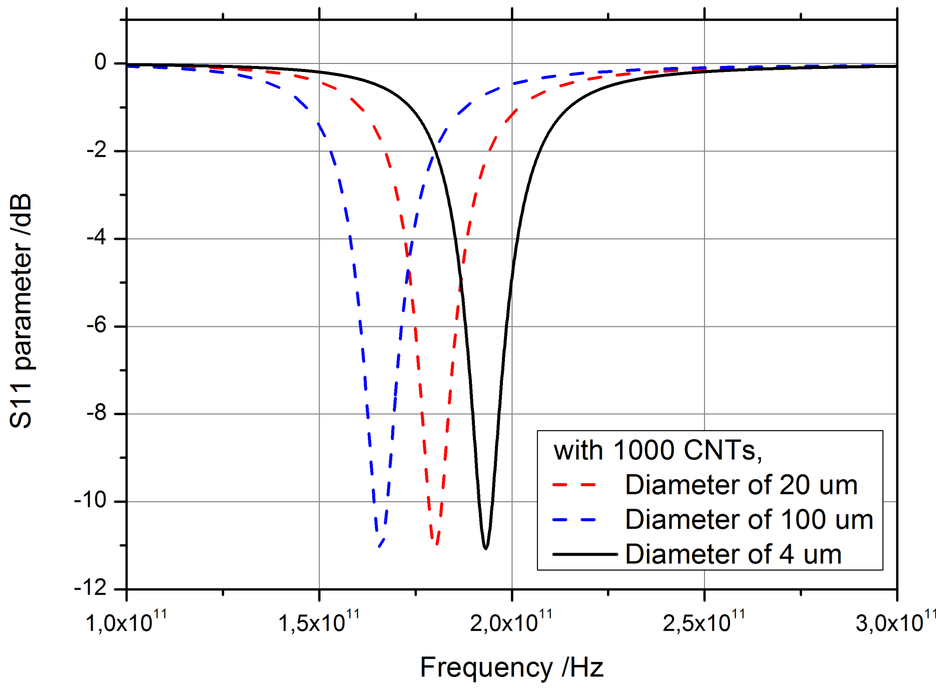

Figure 124: Variation of the monopole diameter with a fixed number of CNTs.

With the increase of the CNT density without changing the diameter, we decrease the kinetic inductance L_k while the capacitance C_{ES} remains the same. Thus, as shown on the Figure 125, we increase the resonance frequency of the monopole. At the opposite, with the decrease of the diameter, we decrease the resonance frequency. We can also observe that with a lower number of CNTs, we have a lower return loss.

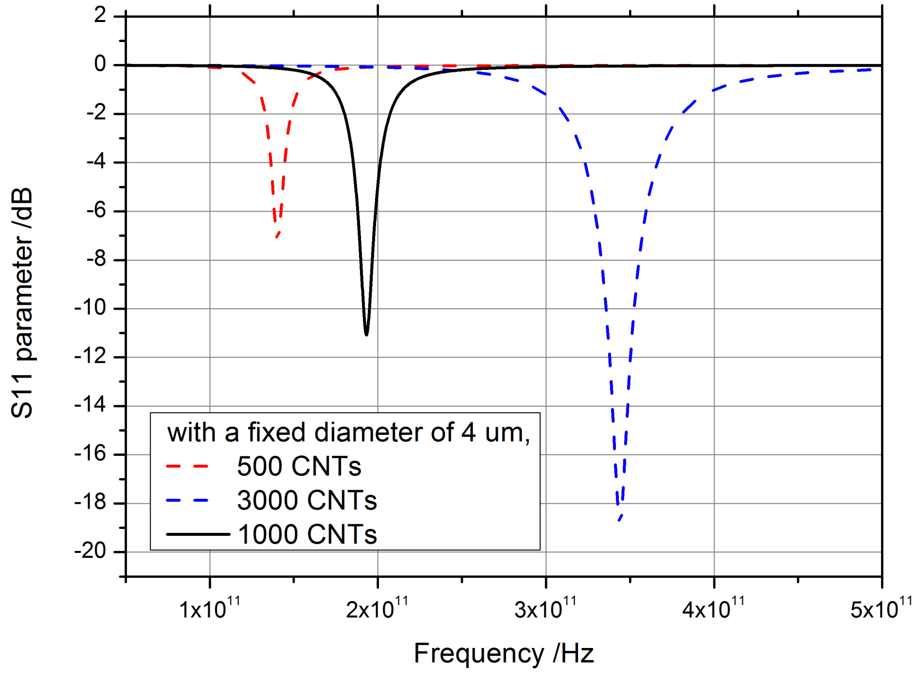

Figure 125: Variation of the CNT density with a fixed monopole diameter.

B. First prototype working at 40 GHz

a) Design of the monopole interconnection using a KOH etching

The first prototype is designed at a “low” frequency in order to be able to measure it in our laboratory but also, as explained previously, to verify we are able to achieve “quantum” resonance from the kinetic inductance L_k below 53 GHz. Thus, a frequency of 40 GHz is chosen. We also use gold as material for the monopole interconnection in order to compare the performance and the monopole characteristics with the CNT monopole. Hence, at 40 GHz, the metal wire is 1.6 mm length with a diameter of 100 µm. These dimensions are extracted from the antenna design kit from HFSS.

As you can see on the Figure 126, we dispose the metal wire vertically at the middle of our silicon substrate (permittivity of 11.7 and loss tangent about 0.002) and we feed the monopole with a normal microstrip line (50 Ω). A 50-Ω-lumped port is placed as excitation at the input of the microstrip line. In order to reduce the distance between the ground plane and the bottom of the metal wire, we realize a KOH etching (Figure 127). Thus, by reducing the substrate thickness, we are able to reduce also the width of the microtrip line, and so be compatible with the SWCNT-bundle diameter. This is a well-known technique using heated potassium hydroxide (KOH), which will etch the silicon substrate with a known angle (35°).

Normal rates are about 1 µm per minutes. Thus, with a thickness of 400 µm, the silicon substrate is etched to reach a thickness of 100 µm locally below the metal wire (Figure 126). Perfect conductor coats the back face of the silicon substrate in order to act as a ground plane either for the interconnection and the microstrip line. To compensate for the reduction of the silicon thickness, the width of the microstrip line is optimized in order to keep 50-Ω characteristic impedance in high frequency up to 40 GHz (Figure 126) and a transition is made where the silicon thickness decreases. All dimensions are given on the Figure 126.

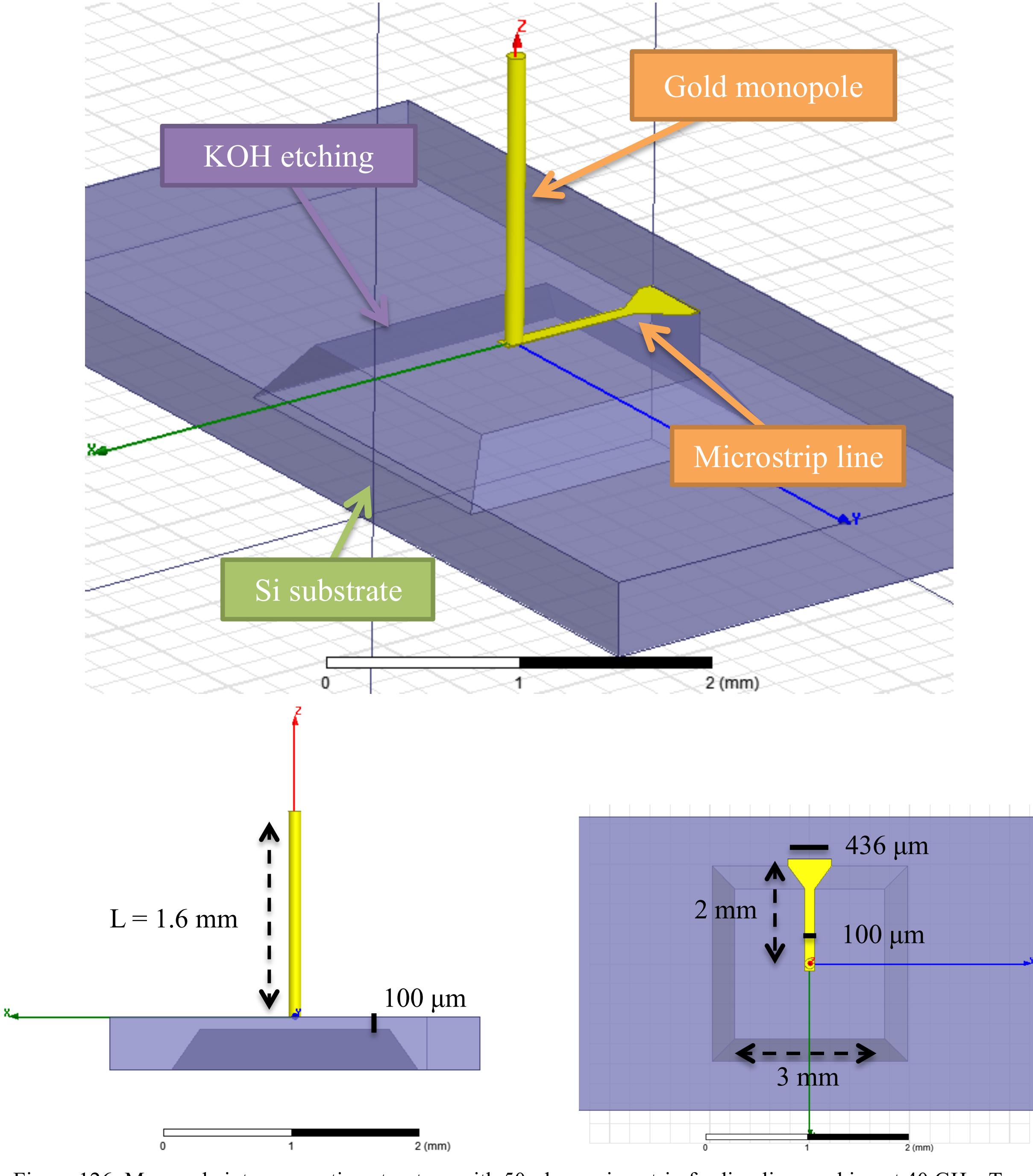

Figure 126: Monopole interconnection structure with 50-ohms microstrip feeding line working at 40 GHz. Top and side views.

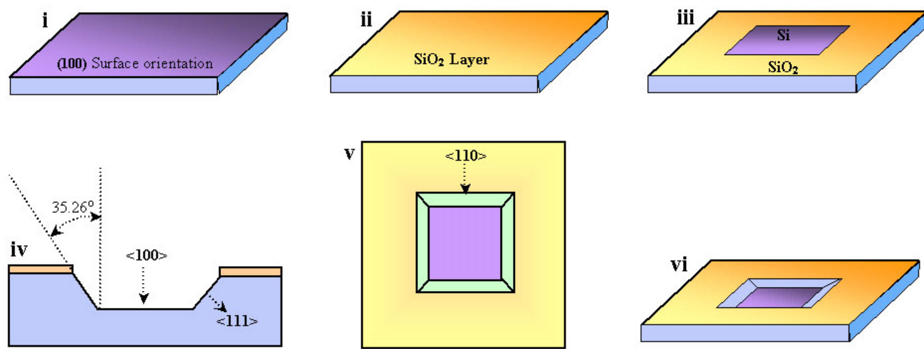

Figure 127: KOH etching principle and process flow.

i. Simulation results at 40 GHz

- Monopole material: Gold

The structure is simulated using HFSS software from Ansoft between 20 GHz and 60 GHz with gold material for the monopole. A frequency resonance is obtained at 43 GHz with return loss of -17.8 dB as you can see on the graph showing the S_{11} parameter (Figure 128). We suspect the feeding part composed by the 2-mm-length microstrip line to decrease the performance, and affect and parasitize the wireless interconnection. Moreover, some losses can be assigned to the microstrip line transition where the KOH etching has been done. However, by looking at the radiation patterns of the structure, we can easily admit that the behavior of a monopole antenna has correctly been obtained. A 2-dBi gain is also achieved. Thus, we theoretically prove the feasibility of our design using gold wire as the interconnection. Now, we will try to replace this metal wire by a bundle of carbon nanotubes vertically aligned.

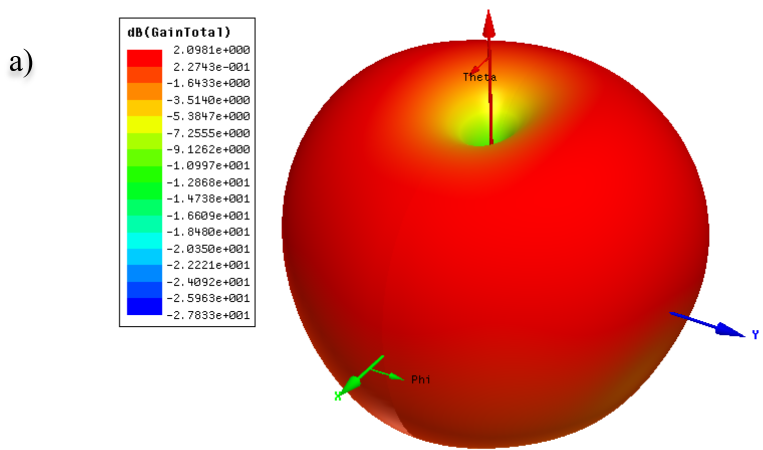

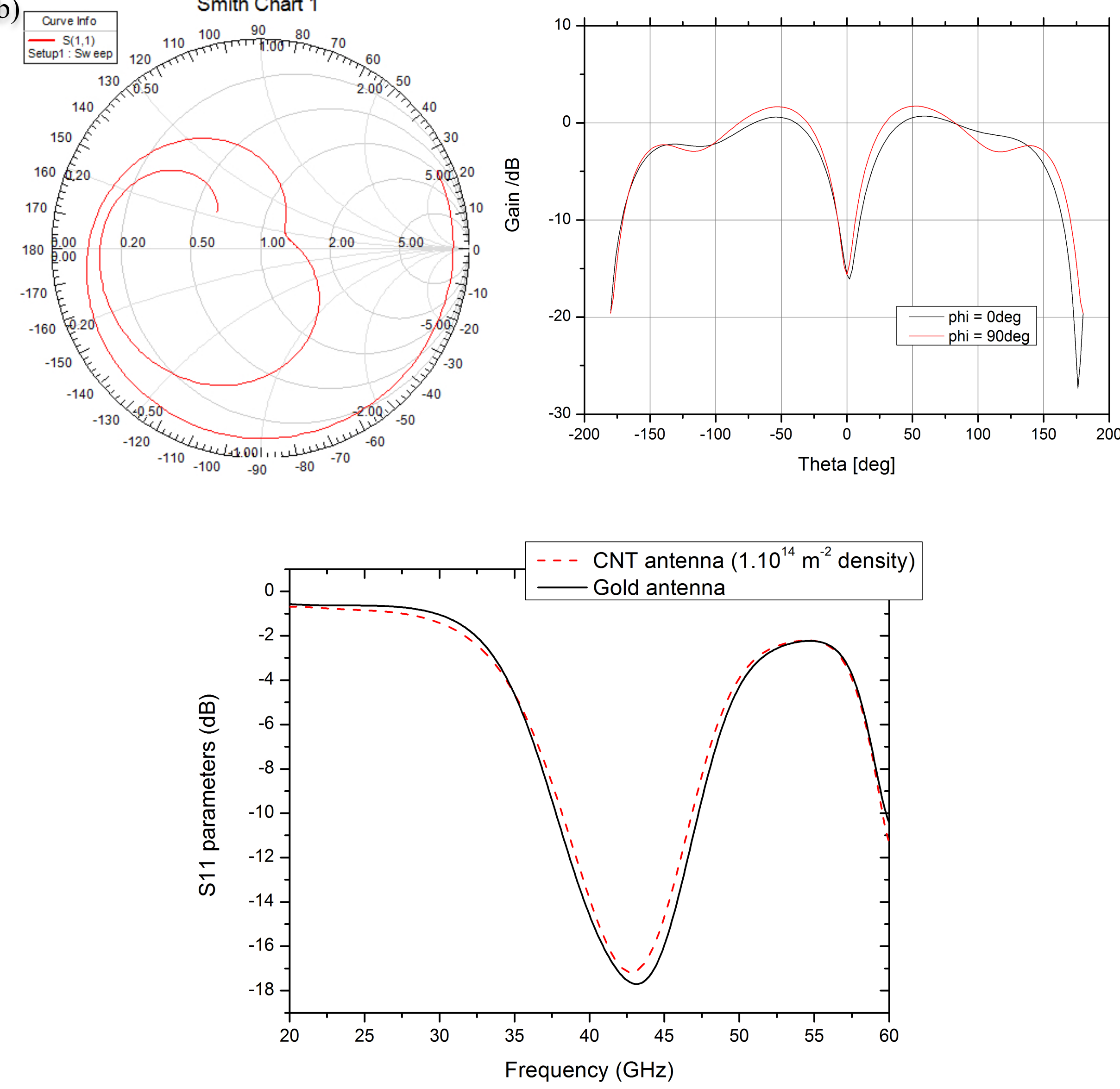

Figure 128: On (a), 3-D and 2-D radiation patterns (representing the gain) of the monopole interconnection structure using gold material working at 40 GHz. On (b), simulated return loss and input impedance of the device simulated from 20 to 60 GHz.

- Monopole material: SWCNTs-bundle

To model the bundle of CNTs as our wireless interconnection, we used the bulk CNT model that had been presented in the first chapter section "Bundle with an unlimited number of SWCNTs on page (88)". This model is only composed by metallic SWCNTs disposed in pararellels (homogeneous distance between CNTs and constant SWCNT diameter in the bundle). We applied the bulk CNT anysotropic conductivity along the z axis (equations (61) and (62)) on the cylinder and we kept the exact same structure geometry.

$$\sigma_{CNTarray(z)} = \begin{pmatrix} \sigma_{Tx} & 0 & 0 \\ 0 & \sigma_{Ty} & 0 \\ 0 & 0 & \sigma_{axial} \end{pmatrix} \quad (61)$$

$$\sigma_{axial} = \frac{8e^2 v_F}{h(v - jw)} \times D_{NT} \quad (62)$$

where w is the angular frequency, e = $1.602.10^{19}$ C is the elementary charge, h = $6.626.10^{34}$ J.s is the Plank constant, ν = T^{-1} is the relaxation frequency and v_F is the Fermi velocity in CNTs [84]. D_{CNT} is the density of nanotube (number of nanotube per unit area).

Then, by using HFSS, we simulated the structure with several CNT density. The bundle of CNTs was still 1.6 mm long with a diameter of 100 µm. We observed that below a CNT density of 1.10^{14} m^{-2}, the antenna performance was degraded (see Figure 129). However, above this density, we obtained similar result and performance than the metal-based wireless interconnection as shown on Figure 128. Indeed, the frequency resonance remained the same (about 43 GHz) and only the return loss and the gain were a bit reduced. Return loss was -16.5 dB instead of -17.5 dB (Figure 128) and the gain was 1.65 dBi instead of 2 dBi with the metal-based wire.

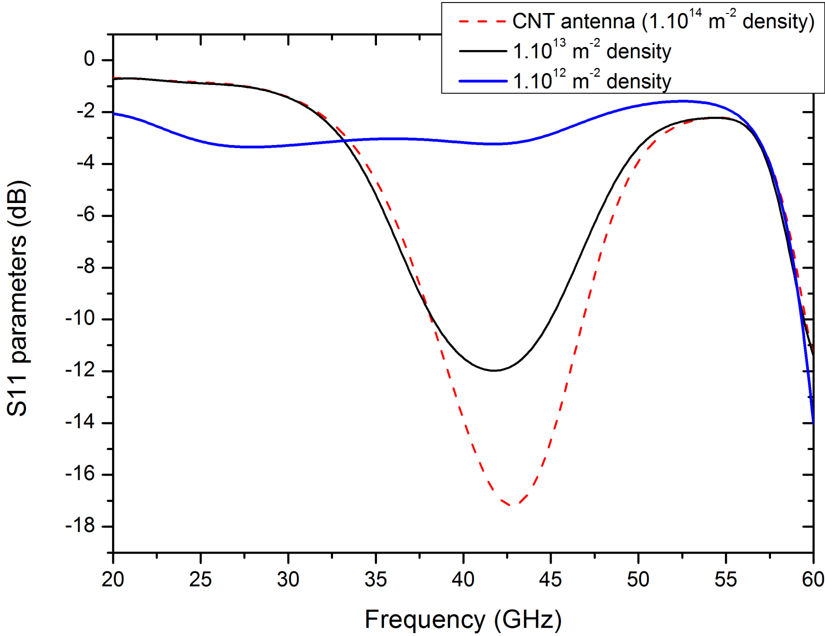

Figure 129: S_{11} parameter of the CNT monopole with several CNT densities.

Thus, from this first study and prototype, we can make several observations:

First, it proves the bulk model is coherent with what we expected: by increasing the CNT density in the bundle, we increase the performance of the monopole until we reach the performance of the metal-based one. Indeed, by increasing the CNT density, we decrease the resistance of the all bundle, and consequently, we bring the performance of the CNT-based interconnection closer to the metal-based one.

Secondly, as we already explained, Hanson said that no "quantum" resonance can appear below a frequency of 53 GHz because of the too high distribitued resistance of CNTs. With 1.6 mm length CNTs, the resistance in each CNT will be very high (10 MΩ). So, as we can observe here, we obtained a resonance only with a large enough number of CNTs in parallels. Thus, with a large number of CNTs, the kinetic inductance L_k becomes negligible, and so, no size reduction can be achieved at this frequency. We hence verify that at lower frequencies than 53 GHz, we can only achieved a geometrical resonance of the CNT bundle. Then, the performance of the resonance and the antenna will depends on the electrical conductivity of the CNT bundle, which directly depends on the number of CNTs in the bundle.

Therefore, for the next prototype, we need to go higher in frequency (higher than 53 GHz) in order to highlight the "quantum" resonance of our wireless interconnection made by bundle of CNTs. Also because our methods of fabrication, as presented in chapter I and II and Table 7, don't allow fabricating a 1.6-mm-high-vertical CNT bundle with a small diameter of 100 µm.

C. Second prototype working at 200 GHz

a) Monopole interconnection alone

Based on the same idea than our previous wireless interconnection working at 40 GHz, we design a new prototype working this time at 200 GHz in order to verify the size reduction effect of the monopole. With metal, a length of 325 µm and a radius of 11 µm are necessary to create a quarter-wavelength monopole interconnection working at 200 GHz. These dimension are found with the antenna design kit from HFSS. With a monopole length of 150 µm, a radius of 2 µm and a SWCNT population of 1000, we can observe the same resonance frequency at 200 GHz using the RLC circuit model we presented previously. We first model the monopole interconnection alone, standing above a silicon substrate (permittivity of 11.7

and tangent loss of 0.002), without the feeding parts and the KOH etching. Thus, we are able to check the dimensions of the monopoles we defined with the RLC circuit model (see section “Principle of the monopole antenna based on CNTs on page (191)”).

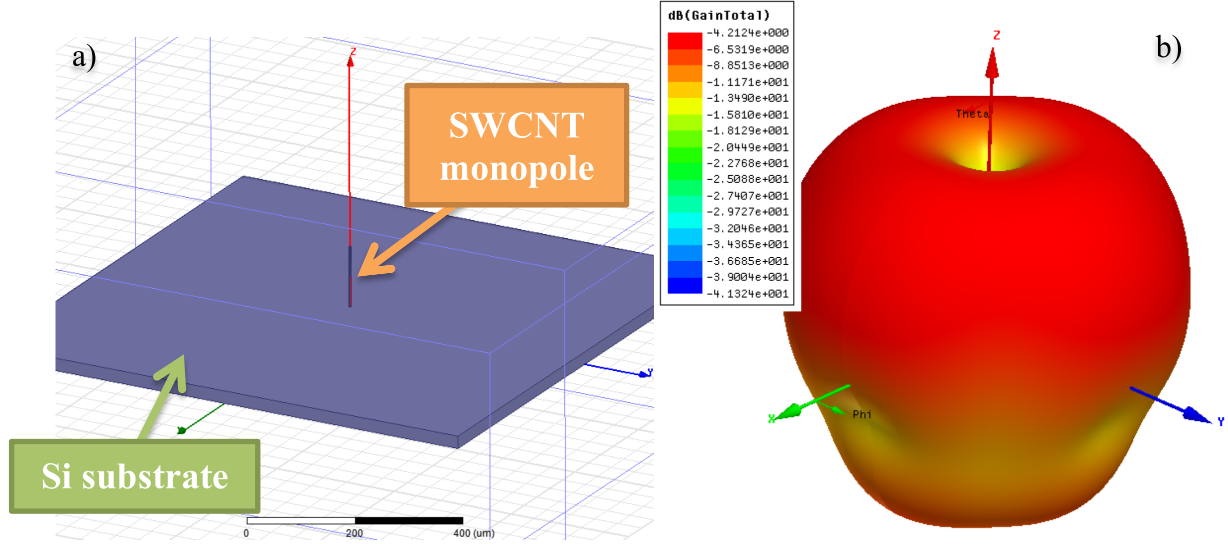

Figure 130: On (a), schematic of the monopole interconnection made by SWCNT bundle. On (b), 3-D radiation pattern (representing the gain) of the monopole interconnection.

On Figure 130, the schematic of the wireless interconnection alone is visible and on Figure 131, we can see the return loss S-parameter of the corresponding device. We also compare the S_{11} parameter we obtain with HFSS and the one we obtained with the RLC model presented previously. As we can observe, we have a good agreement between the two simulations, and so, we will use our RLC circuit model uniquely in order to define the dimensions of our monopoles for the next parts of this chapter. A gain of - 4 dBi is obtained. Isotropic radiation except in the antenna direction is visible with little perturbations. The low gain of the monopole is due to the low number of CNTs in the bundle. Thus, the bundle resistance is too high (6.4 kΩ/µm x 150µm /1000 = 1 kΩ) for the monopole and the performance (gain) are reduced.

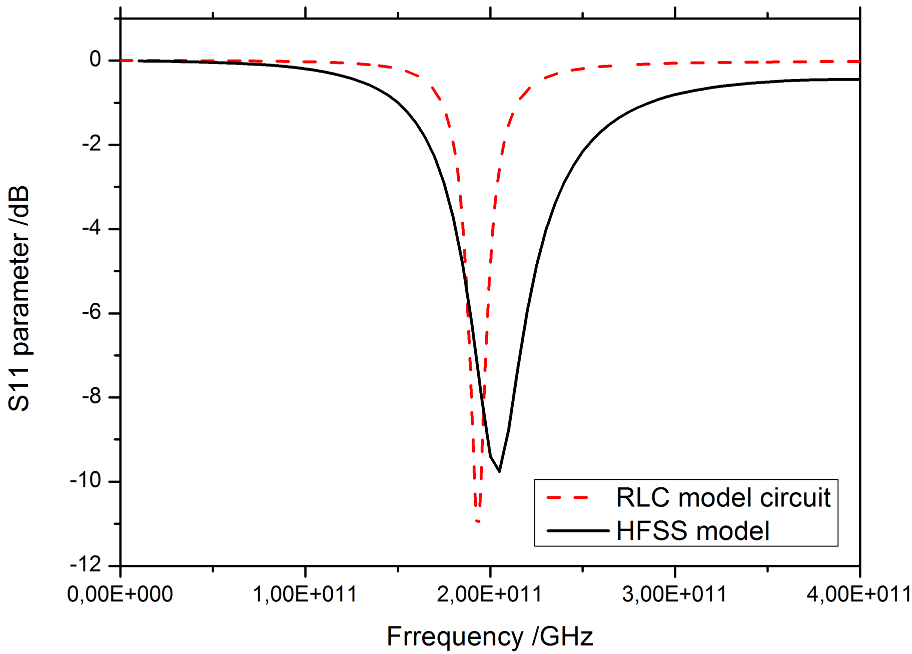

Figure 131: Simulated return loss of the monopole interconnection from 1 GHz to 400 GHz.

b) Final design of the monopole interconnection

However, because of the higher frequency (200 GHz), the microstrip lines presented in our previous design as our feeding part were not anymore compatible. The microstrip line was influencing our results and most of the time, the line was resonating instead of the vertical monopole. Indeed, with the increase of the working frequency, the wavelength becomes shorter and all metallic components composing the device likely to become to influence the monopole interconnection resonance. We choose to add a transition CPW-microstrip at the input of the feeding part. The CPW is 50-Ω and as you can see on the Figure 132, the transition between the CPW and the microstrip line is designed in order to avoid important losses and impedance mismatches. The dimensions of the transmission have been optimized using HFSS and simulations of the transition alone. The advantage of having a CPW instead a microstrip line is that we will be able to measure the return loss of our device more easily by using a probe station connected to a VNA. Vias are connecting the CPW ground with the ground plane coated below the silicon substrate.

Again, a KOH etching is considered in order to reduce the distance between the monopole interconnection and the ground plane. This time, as we precised previously, 10 µm are separating the bottom of the monopole and the ground plane (Figure 132). All other dimensions are given on the Figure 132.

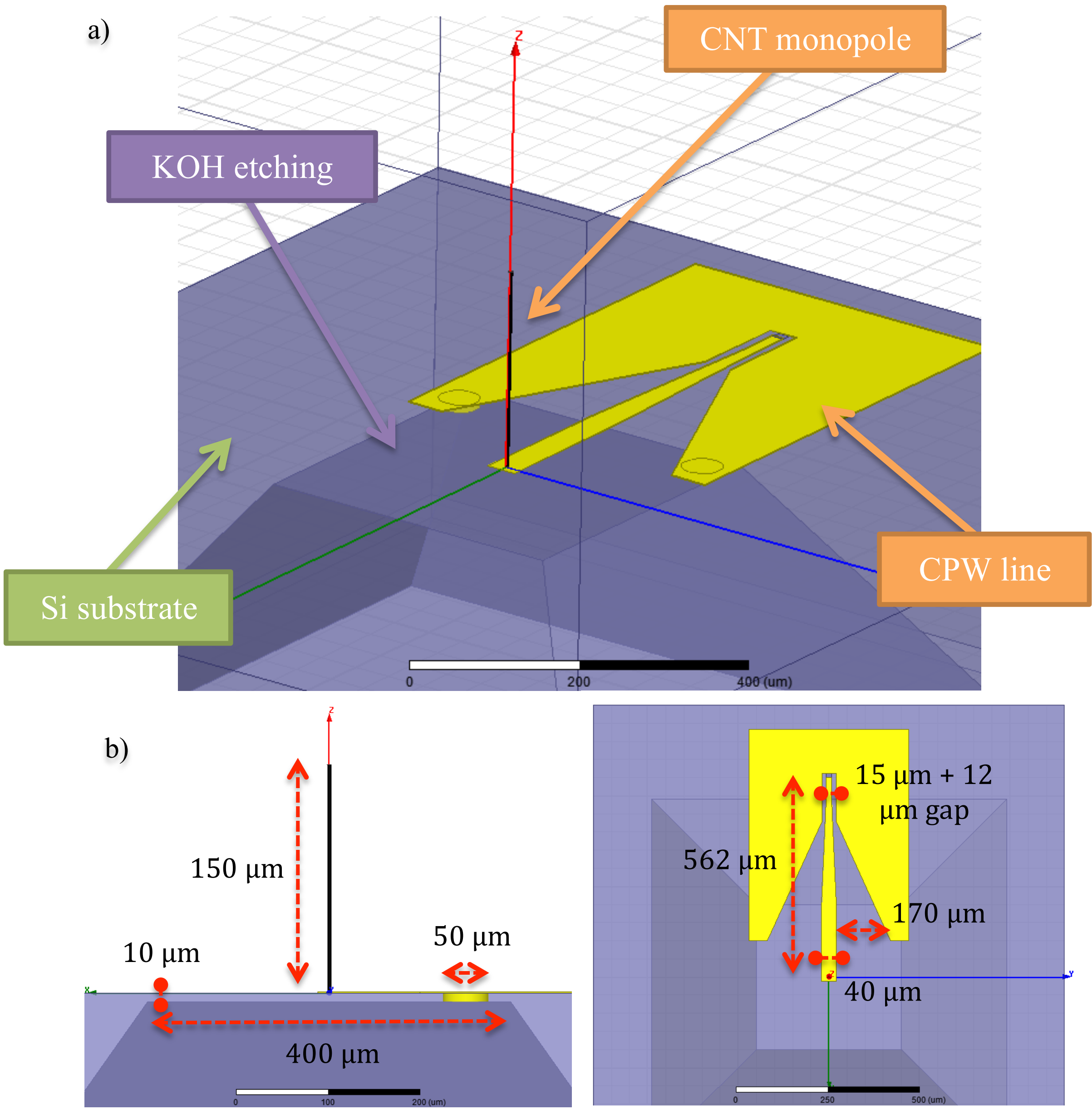

Figure 132: On (a), monopole interconnection structure using CNT bundle with 50-ohms CPW feeding line working at 200 GHz. On (b), side view and top views of the monopole interconnection structure working at 40 GHz.

c) Final design simulation results at 200 GHz

We simulated our device with HFSS software from 100 to 350 GHz, and after optimization of the feeding parts by simulating the CPW-microstrip transition alone, we obtain a resonance frequency at 235 GHz with return loss of -24.5 dB (Figure 133 red curve). On Figure 133, the red curve represents the return loss of the CNT monopole with 1000 SWCNTs in the bundle, a 150-µm length and a 2-µm radius. The blue curve represents the return loss of the monopole with the same dimensions using gold material instead of CNTs. Black curve represents the return loss of the structure without monopole (CPW-microstrip transition alone). As we can observe, due to the effects of the feeding parts, a 30-GHz shift of

the resonance frequency occurs. Indeed, because we add some gold structures to feed the monopole, we overlap the ground plan below the monopole. This overlapping might decrease the value of C_{ES}, the capacitance coupling between the monopole and the ground plan, and so by the equation $f=1/(2\pi\sqrt{(LC)})$ presented previously, the frequency resonance increases. The monopole gain is still - 4dBi and a familiar shape of an isotropic 3-D radiation pattern are obtained (Figure 135a). The feeding parts of the monopole interconnection disrupt the 3-D radiation pattern.

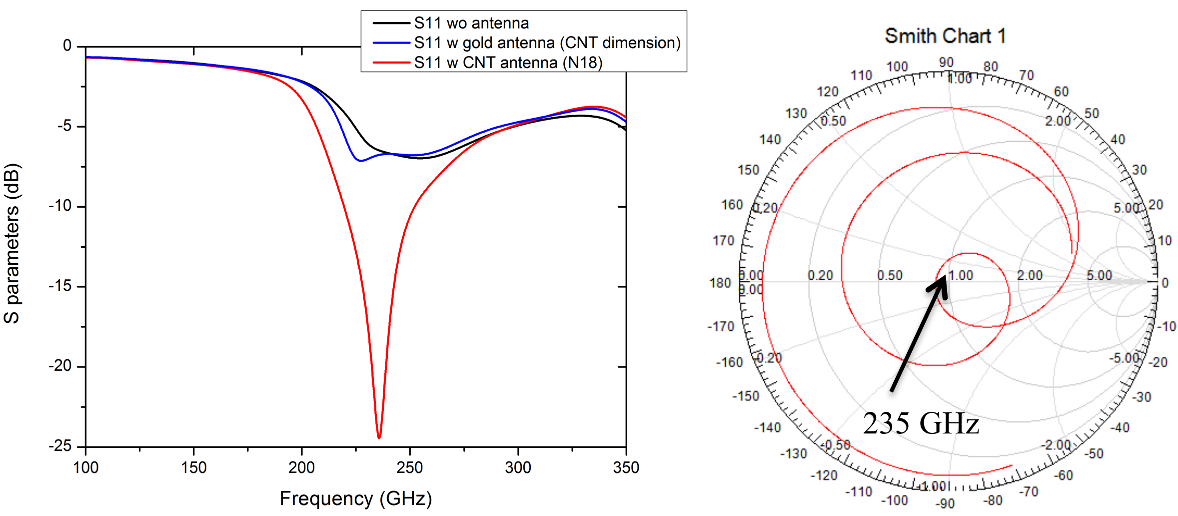

Figure 133: Simulated return loss of the monopole antenna device presented in Figure 132. Input impedance of the CNT monopole.

To verify if the resonance is due to the monopole interconnection, we replace the CNT bulk material by a simple gold material (conductivity of $4.1.10^7$ S/m) and keep the exact same monopole dimensions. As you can see on the Figure 133 (blue curve), no resonance appears. When the feeding part without the monopole is simulated, also no resonance appears. Thus, we prove that we achieve a “quantum” resonance from SWCNT bundles. Indeed, this “quantum” resonance comes from the kinetic inductance effect instead of the magnetic inductance L_M.

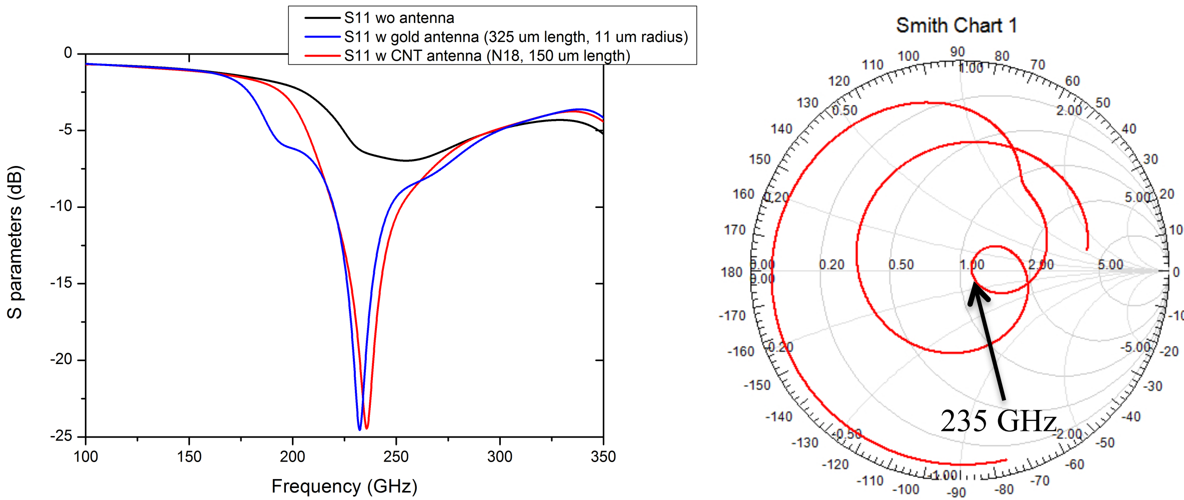

Figure 134: Simulated return loss of the monopole antenna device presented in Figure 132. Input impedance of the gold monopole.

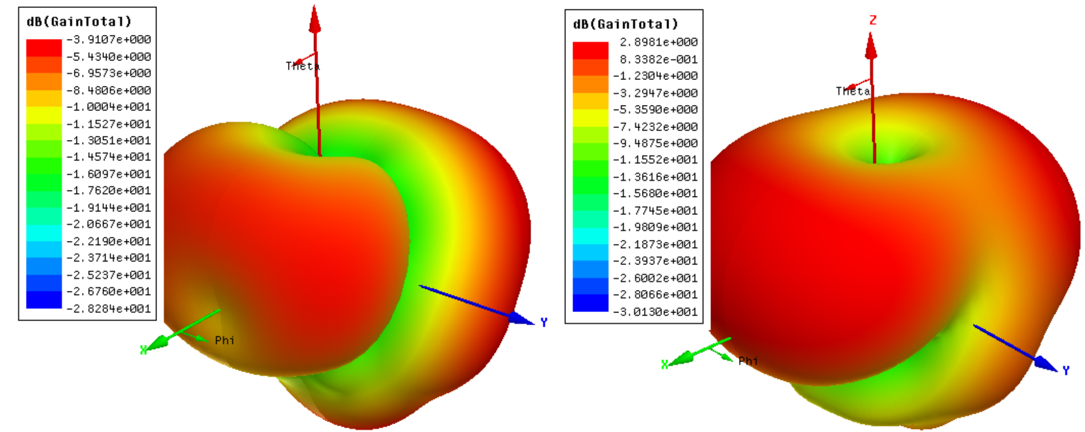

Figure 135: 3-D radiation pattern (representing the gain) of the monopole interconnection composed by CNTs (a) and gold material (b) at 200 GHz.

In a second time, we replace the CNT bundle monopole by a 50-Ω quarter-wavelength metal wire with the correct dimensions to resonate at 235 GHz. We need a 325-µm length and a diameter of 22 µm. These dimensions have been extracted from the antenna design kit of HFSS. On Figure 134, the red curve represents the return loss of the CNT monopole with 1000 SWCNTs in the bundle, a 150-µm length and a 2-µm radius. The blue curve represents the return loss of the monopole with using gold material with a 325-µm length and 11-µm radius. Black curve represents the return loss of the structure without monopole.

As you can see on the Figure 134 (blue curve), we obtain a resonance frequency at 235 GHz with the same return loss than the CNT monopole. However, if we take a look on the 3-D radiation pattern (Figure 135b), we achieved a cleaner radiation. We also increased the gain and obtained 2.8 dBi. The higher CNT bundle resistance (6.4 kΩ/µm x 150µm /1000 = 1 kΩ) and the shorter length of the CNT monopole are the reasons of the degradation obtained on

the 3-D radiation pattern. Thus, by using SWCNTs instead of metal for the monopole material, we achieved a size reduction factor of 2.2 on the length and 5 on the diameter.

We decided to do not fabricate the device due to the difficulties of aligning the KOH etching with our metallic parts and the fabrication of the vias. The third and last prototype will give answers to the previous issue.

D. Third prototype working from 100 to 300 GHz

a) Design and principle of the monopole interconnection using a single-plane

Based on our successfully results form the second prototype simulations, we decide to simplify the device in order to be able to fabricate it more easily. Thus, in the design shown on Figure 136, a transition from a coplanar waveguide (CPW) to a vertical monopole antenna is defined. This design is defined in the reference [180] where a new approach that offers the potential to create surface micro-machined vertical radiating structures with higher potential performance than other conventional printed-circuit patch antennas. In their work, they designed a monopole antenna working at 85 GHz with -16 dB return loss. A 50-Ω coplanar waveguide feed the antenna while gold ground plane is coated all around the monopole. This ground plane also serves as the monopole antenna ground. The KOH etching is hence abandoned. This special disposition permits to have the ground on the same plane than the bottom of the antenna. In order to get better monopole performance, the CPW gap and dimensions of the surface below the antenna have been optimized by simulating them alone (Table 20, Table 21 and Table 22). G stands for the CPW gap, W is the CPW width, while G2 and R2 respectively are the dimensions of the metal gap on the surface around the antenna and the radius of the gold surface below the antenna (Figure 136). The substrate use in this configuration is silicon (Si) with a permittivity of ε_r = 11.7 and a loss tangent of 0.002. Finally, the metallic wire stands vertically in the middle of the structure with a radius R1 and a length L. The monopole structures are analyzed using Ansoft HFSS software from 60 to 110 GHz, 160 to 260 GHz and 250 to 350 GHz. Our first simulations are done with a gold wire in order to verify our design and the feasibility of our new prototype.

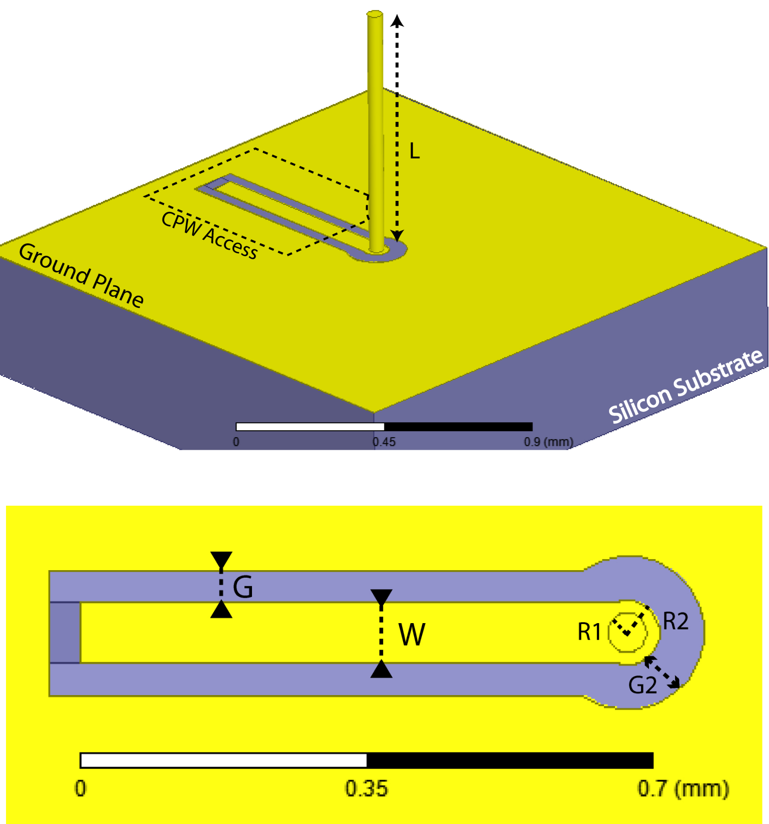

Figure 136: Schematic of the monopole interconnection with gold wire mounted on a CPW line. Metal ground plane surrounds the monopole. Side and top views are visible.

b) Wireless interconnection at 100 GHz

For the first antenna working at 96 GHz, with the optimized dimensions given in Table 20 and Figure 136, a return loss of -28.7 dB at 96.6 GHz are obtained for the gold monopole interconnection (Figure 137). A gain of 1.32 dBi is also obtained (Figure 138).

To compare this result with the state of the art, in the work of Yong-Kyu Yoon [180], a monopole antenna with the same topology was simulated and fabricated both on silicon and sapphire substrates. With a monopole length of 800 µm, operating frequency was found at 85 GHz with a -15 dB return loss and a theoretical gain of 1.7 dBi (simulation by HFSS). Instead of our 50-Ω input impedance, this antenna has 36.5 Ω impedance at resonance.

Table 20: The three-monopole interconnection configurations dimensions at 100 GHz.

Monopole material	**G /µm**	**W /µm**	**G2 /µm**	**R2 /µm**	**R1 /µm**	**L /µm**	**Ratio: L/(2R1)**
Gold	40	75	55	40	24	760	15.8
1000 SWCNTs	60	70	70	40	2	300	68.2
6000 SWCNTs	60	70	70	40	6	600	52.6

Using the bulk CNT model, the gold material monopole antenna was replaced by a CNT bundle with different number of SWCNTs (Table 20). We want to test two configurations with a very different number of CNTs in the monopole in order to highlight the consequences on the results obtained (resonance frequency, size reduction factor, return loss and gain). Thus, two configurations are considered: about 1000 and 6000 tubes. Each time, the objective is to reach 50-Ω impedance. In Table 20, bundles of CNTs dimensions are presented. As explained in the introduction, more the number of CNT in the bundle is important, the lower the bundle resistance is, but the global "quantum" effects such as the kinetic inductance L_k also decreases. So, with 6000 tubes and the 96-GHz-monopole interconnection, the size reduction is only of 1.27 whereas a size reduction of 2.5 is obtained compared with the reference monopole (1000 tubes). On Figure 137, the gold monopole is represented on the red solid lines, the grey solid lines represent the monopole with 1000-CNTs bundle and dark grey solid lines represent the monopole with 6000-CNTs bundle. Finally, the simulated return loss of the equivalent structures without the monopole is represented on dash lines. As shown on Figure 137, the return loss is better (-13 dB) for the configuration with 6000 tubes than the ones with 1000 tubes (-5 dB and -10 dB) because of the lower bundle resistance with 6000 CNTs.

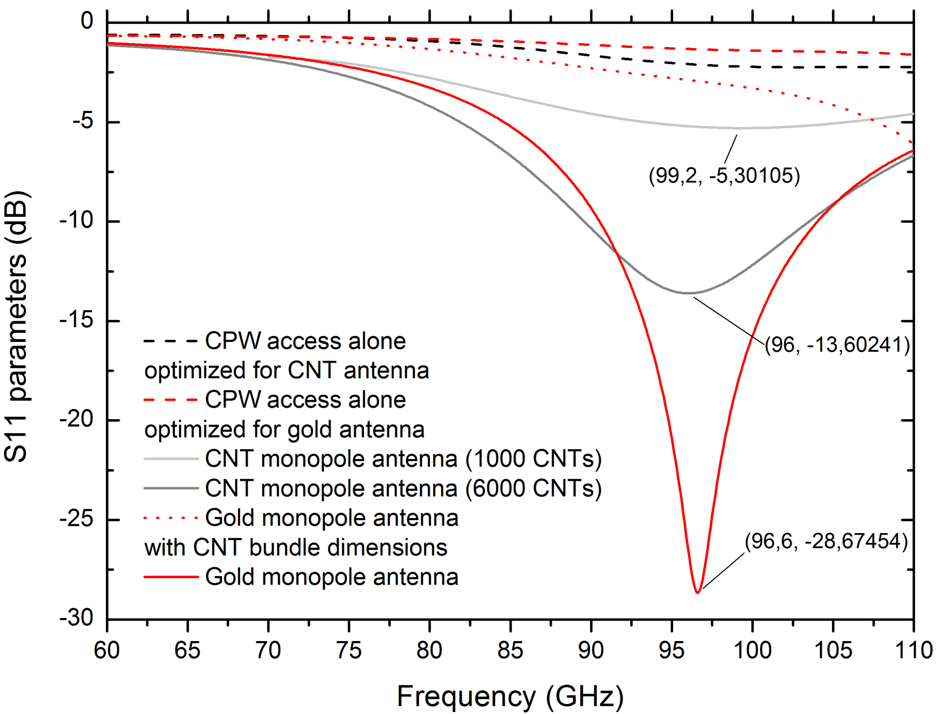

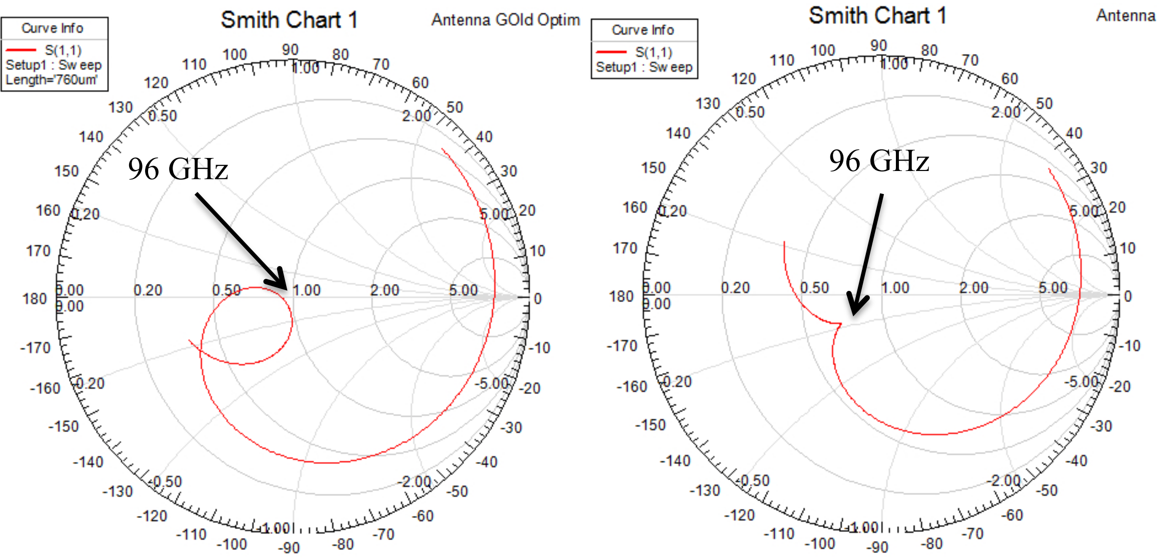

Figure 137: Simulated return loss for the monopole configuration working at 100 GHz. Smith charts of the gold monopole (left figure) and the 6000-CNTs monopole (right figure).

However, very low gains are obtained with CNT monopole interconnections even if the familiar isotropic shape of the radiation pattern is achieved all the time. Indeed, the gains are always below 0 and ranged between -3 and -6 dBi using CNTs (Figure 138b). The low gain in CNT monopole may come from two reasons:

- the higher resistance of the monopole because of the higher resistance of the CNT material (with a CNT density of 1.10^{14} m^{-2}) compared to a gold monopole with the same size.

- the shorter size of the antenna. Indeed, it is already known that shorter is an antenna, lower is the efficiency [83]. The problem is by reducing the height of the monopole, we decrease the radiation resistance and increase the dielectric loss due to the substrate. Thus, the solution might be to make larger CNT monopole with lower CNT density in order to keep the same number of CNTs [185]. Larger antenna would increase the capacitance effects and so increase the radiation resistance and consequently the monopole efficiency. However, since it is difficult to modify the CNT density with our TCVD process, we didn't realize that case.

To verify if the resonance of CNTs is due to the "quantum" effects, gold monopole interconnection with CNT monopole dimensions was simulated (Figure 137). The gold monopole antenna with CNT bundle dimensions (radius R1 = 6 µm and length L = 600 µm) is represented on dot lines. As shown on the graph, no resonance appears at frequencies around 100 GHz, quantum resonance by CNTs is so confirmed.

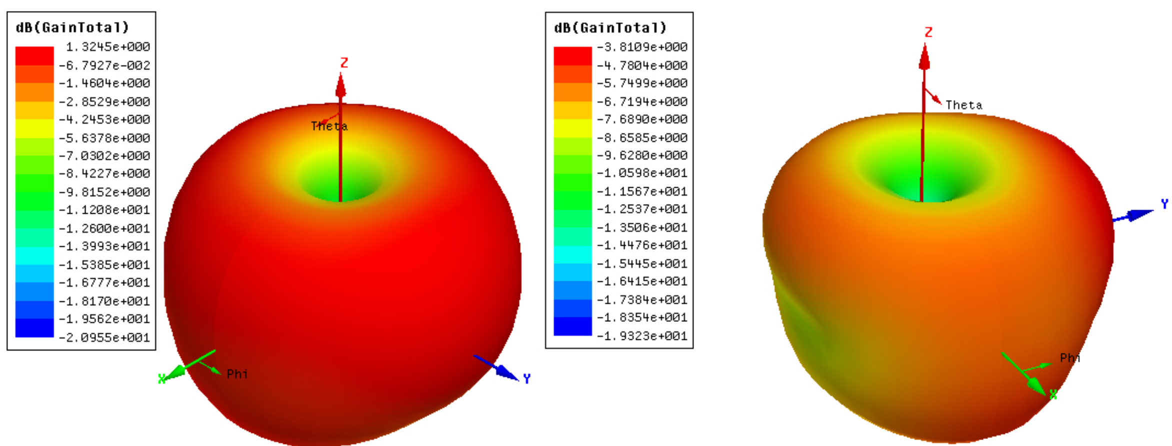

Figure 138: Simulated 3-D radiation patterns for the two configurations: gold monopole (left), 6000 CNTs bundle (right) working at 100 GHz.

The next step will be to go higher in frequency in order to reduce the length of the monopole. With shorter monopole, we can expect better return loss for the interconnection made by CNTs. Unfortunately, as we will observe, the monopole efficiency will be still reduced.

c) Wireless interconnection at 200 GHz

The second antenna working at 200 GHz, with dimension shown on Table 21 and Figure 139, returns a S_{11} parameter of -52 dB and a gain of 3.4 dbi (Figure 140b) using gold material. This designed monopole topologies have demonstrated performances similar to

existing antennas with a gain at 4 dBi and an isotropic radiation (Figure 141). Again, we replace the gold material by a bundle of SWCNTs with the dimensions given on Table 21. A population of 1000 tubes is used again in order to be able to compare our results with the monopole at 100 GHz. We found that this number of CNTs is a good trade-off between the total bundle resistance and the total value of the kinetic inductance. Indeed, with 1000 CNTs, we can still observe a correct adaptation on the return loss and a size reduction of the antenna higher than 2. With the 216 GHz monopole using 1000 CNTs, a size reduction of 2.3 is obtained.

Table 21: The two-monopole interconnection configurations dimensions at 200 GHz.

Monopole material	G /µm	W /µm	G2 /µm	R2 /µm	R1 /µm	L /µm	Ratio: L/(2R1)
Gold	5	16	26	15	11	350	15.8
1000 SWCNTs	5	30	50	15	2	150	37.5

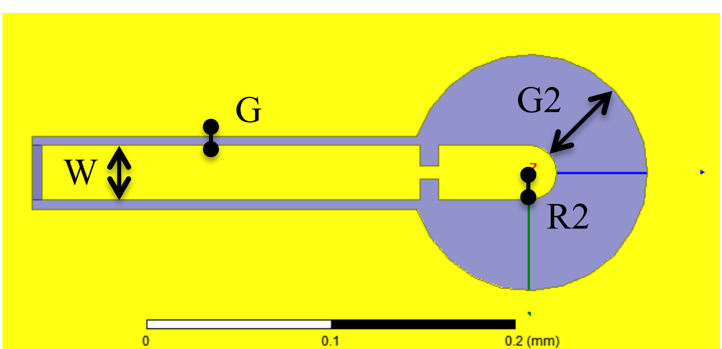

Figure 139: Top view of the monopole configuration working at 200 GHz.

As we can see on the Figure 140, a reduction of the line width has been proposed to improve the return loss and the matching of the monopole interconnection. The red solid lines represent the gold monopole and the black solid lines with dots represent the monopole with 1000-CNTs bundle. Indeed, if we take a look on the smith chart on Figure 140b, we can see that the 50-Ω impedance matching is respected at the resonance frequency. Moreover, as we were expecting, the return loss is better for the 216 GHz monopole than the 96 GHz one with the same number of CNTs (1000 CNTs) because the antenna is shorter at higher frequency, and so the monopole resistance decreases with the decrease of its length.

However, a gain still below 0 dBi is obtained with CNTs (Figure 141). The monopole using 1000 CNTs at 200 GHz is twice shorter than the one working at 100 GHz with the same number of CNTs, and we obtain a gain about 3 dBi lower with the monopole at 200 GHz. Thus, since we have the exact same number of CNTs in the bundle but a different gain, it could confirm that the size of the antenna plays an important role in its efficiency. So, we can imagine it will be difficult to achieve high gain monopole interconnection with an important size reduction since we need to increase the working frequency and decrease the length. As explained in the previous chapter, only an increase of the monopole diameter and by keeping the same number of CNTs could increase the monopole efficiency.

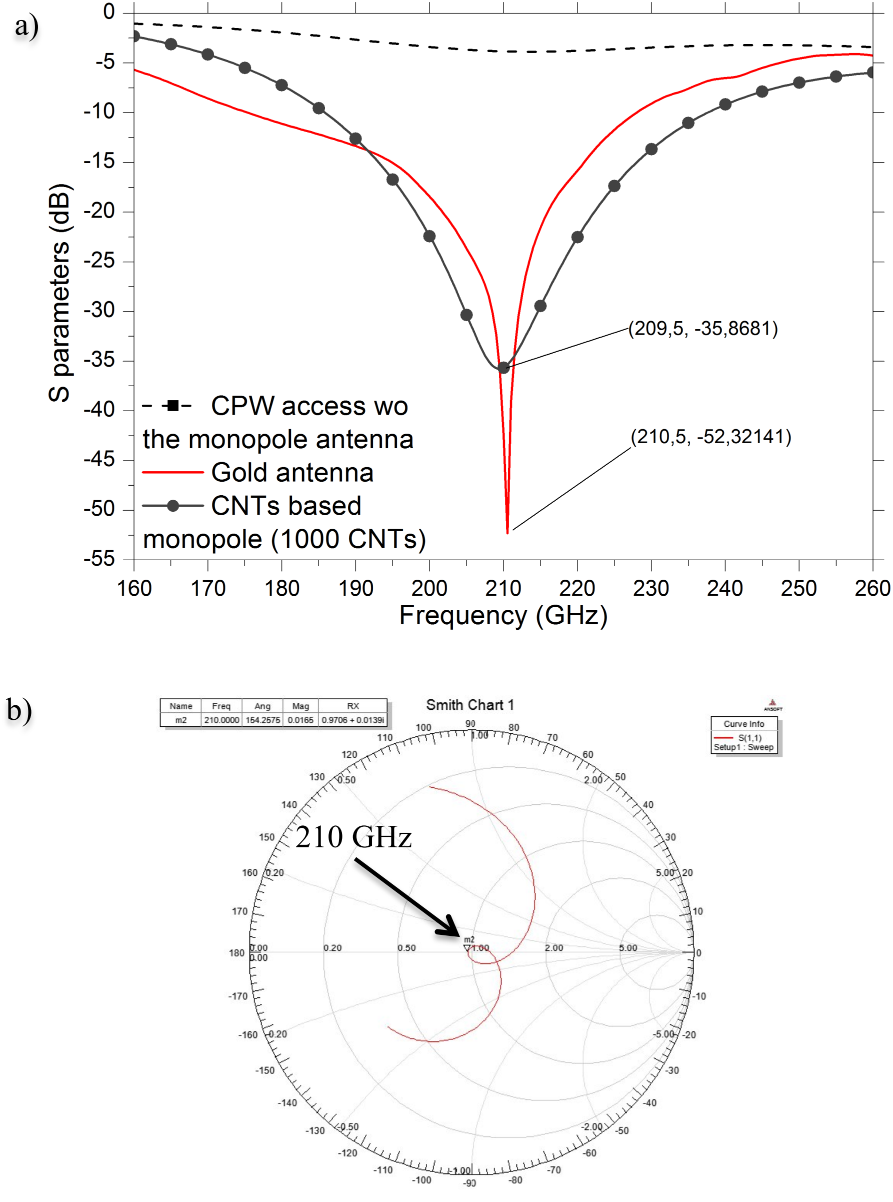

Figure 140: In (a), simulated return loss for the monopole configuration working at 200 GHz. In (b), corresponding simulated smith chart of the structure working at 200 GHz using CNT monopole.

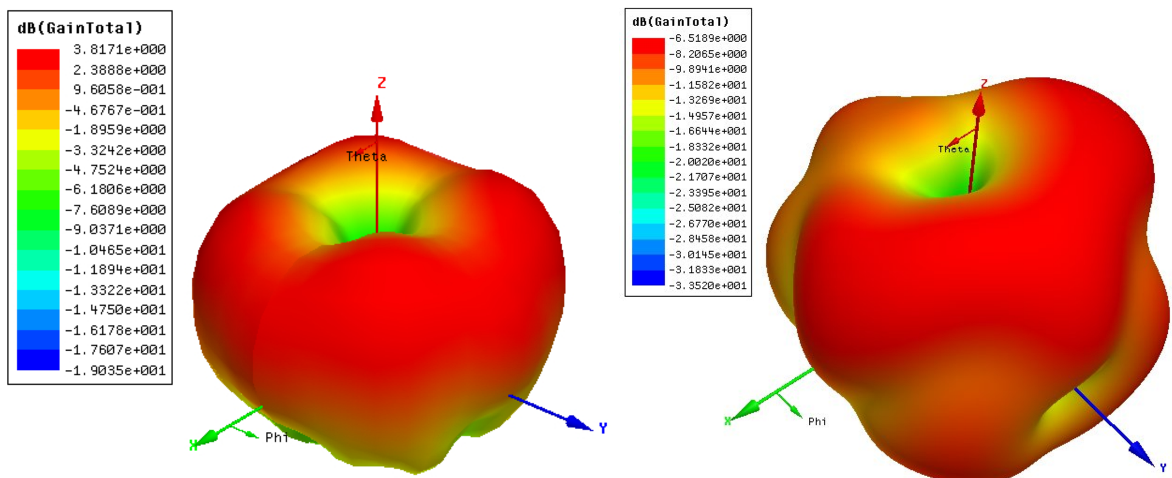

Figure 141: Simulated 3-D radiation patterns for the two configurations: gold monopole (left), 1000 CNTs bundle (right) working at 200 GHz.

Finally, a simulation is done without the monopole to verify the resonance is not due to the CPW itself. The dash line represents the return loss of the equivalent structure without the monopole. As we can see on Figure 140(dash line), there is no resonance and the return loss stays above -3 dB, which confirm that our monopole interconnection is working fine with both metal and CNT materials. Again, the next step will be to reach even higher frequency in order to increase our performance and to shorten the length of the antenna. With shorter antenna, we will also simplify the fabrication process of the structure.

d) Wireless interconnection at 300 GHz

We finally proposed a monopole working at 300 GHz, which is the monopole CNT length we are able to fabricate with a certain control of the verticality, as we will see later in this chapter (see also Table 7). Again, the same design is used and all the dimensions are given on the Table 22 and Figure 142. As we can observe on the same Figure 142, the circle without metal around the antenna, which is used to improve the monopole adaptation, gets bigger as we increase the working frequency. Indeed, with the increase of the frequency, the CPW will affect more the monopole radiation because of higher couplings. Thus, to reduce this parasitic effect, we needed to increase the size of the circle (represented by G2+R2). The width of the line at the input of the device has been adapted in order to be able to dispose the probe compatible at this frequency (minimum pad size of 25x35 µm).

Table 22: The monopole interconnection configuration dimensions at 300 GHz.

Monopole material	**G /µm**	**W /µm**	**G2 /µm**	**R2 /µm**	**R1 /µm**	**L /µm**	**Ratio: L/(2R1)**
1000 SWCNTs	10	15	55	5	2	100	25

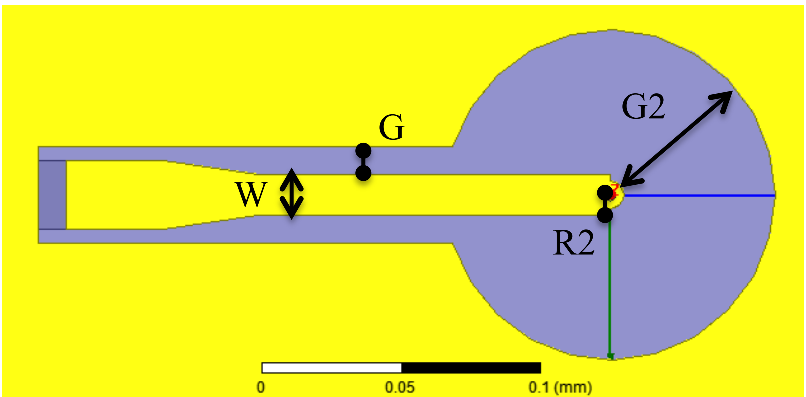

Figure 142: Top view of the monopole configuration working at 300 GHz.

On the Figure 143, we observe a resonance frequency at 302 GHz with return loss of -64 dB using again 1000 SWCNTs monopole with a diameter of 2 µm and a length of 100 µm. Moreover, if we take a look on the 3-D radiation pattern (Figure 144b), we observe a gain near 0 (-0.7 dB) and a shape very perturbed compared to the original isotropic shape (Figure 128). Also on the smith chart (Figure 144a), we reach 50-Ω impedance but with a lot of perturbations. If we compare these results with our previous observations, we can conclude that the monopole interconnection here is highly perturbed by the CPW lines. Indeed, instead of having a resonance by the monopole itself, we have here a resonance from the couple monopole + CPW. With this configuration, a higher gain is obtained and a better return loss is achieved. However, as we just said, the radiation pattern won't have an isotropic shape.

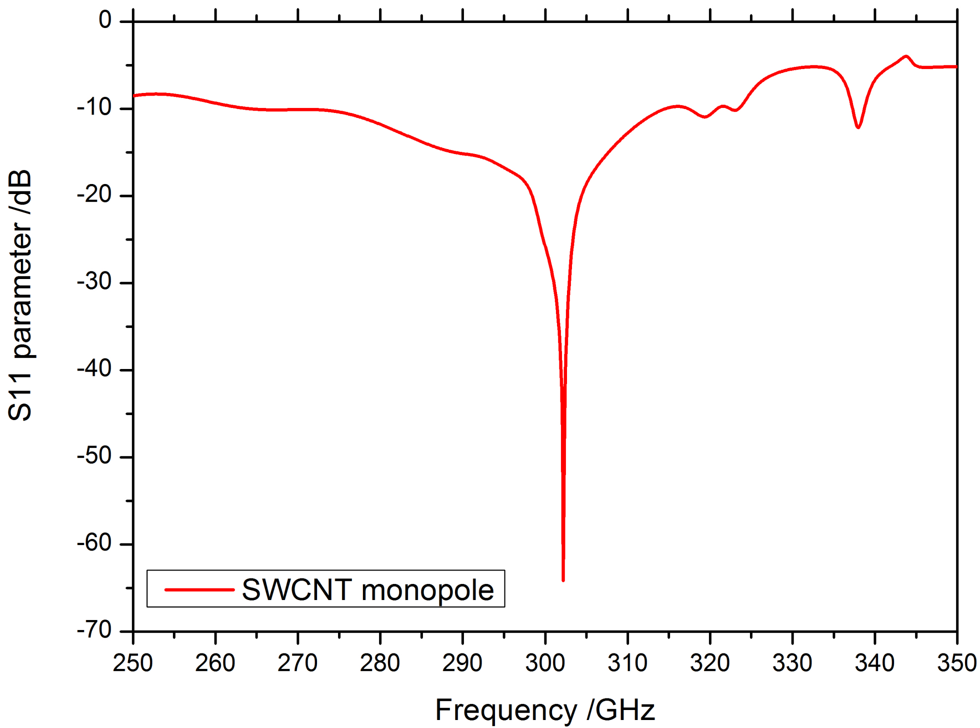

Figure 143: Simulated return loss for the monopole configuration working at 300 GHz using 1000 CNTs bundle.

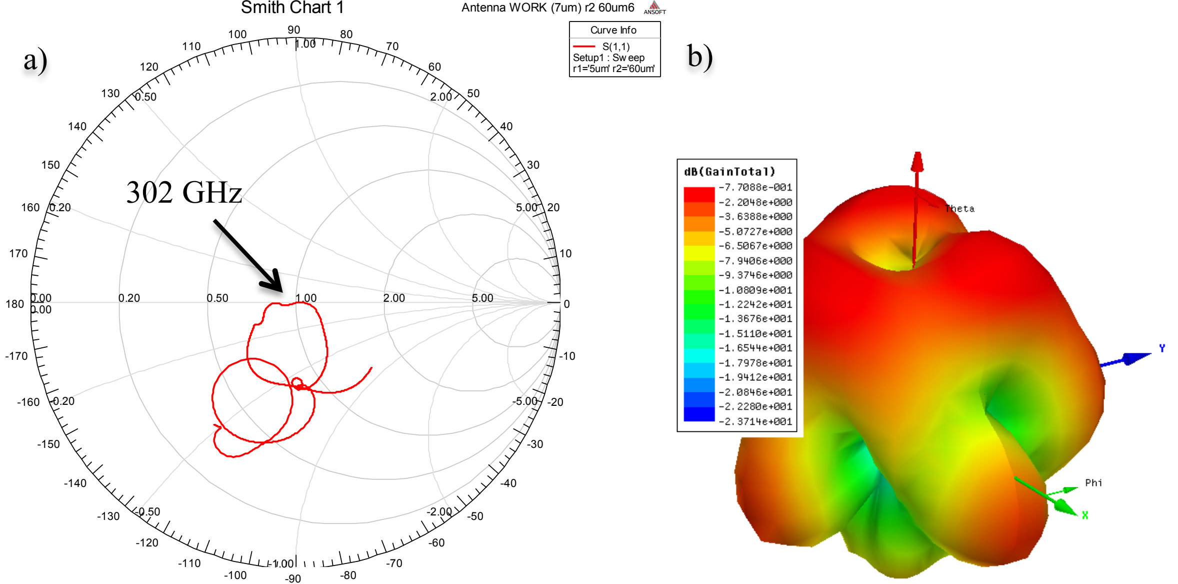

Figure 144: In (a), corresponding simulated smith chart of the structure working at 300 GHz using 1000 CNTs bundle monopole. In (b), Simulated 3-D radiation pattern for the configuration using working at 300 GHz.

However, it could be an alternative to overcome the low efficiency of the wireless interconnection made by carbon nanotubes. Indeed, by making a hybrid monopole with metal and carbon nanotubes (Figure 145), we will be able to achieve a size reduction of the interconnection and to reach higher gain. Further investigations must be achieved.

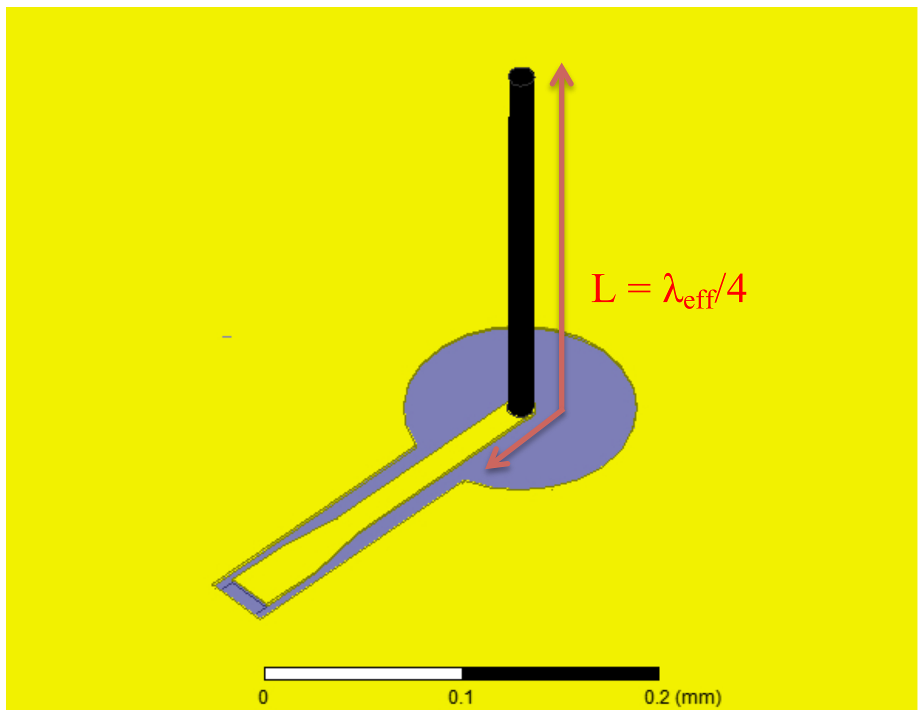

Figure 145: Hybrid gold/CNTs monopole.

e) Conclusions and observations

In conclusion, the best trade-off is to increase the working frequency of the monopole in order to decrease its length. With a shorter antenna length, the bundle resistance will decrease. On the same time, decrease the number of CNTs will increase the "quantum effect" such as the kinetic inductance L_k, which increases the size reduction of the monopole. Thus, we create an abacus showing the resonance frequency of a SWCNT-monopole as function as the monopole length and the number of CNTs (Figure 146). The impedance matching is chosen at 50 Ω. By modifying the number of CNTs for a fixed frequency and a fixed length will modify the 50-Ω impedance matching. As we can observe and as already explained previously, with the increase of the number of CNTs, we increase the resonance frequency. At the opposite, with the increase of the monopole length, we decrease the resonance frequency. Since we are only able to grow 200-µm high CNTs, it is quite hard to achieve CNT monopoles with resonance frequency lower than 200 GHz with good performance (good return loss). The yellow triangle on Figure 146 represents when the CNT monopole return losses are higher than - 10 dB with our RLC circuit model.

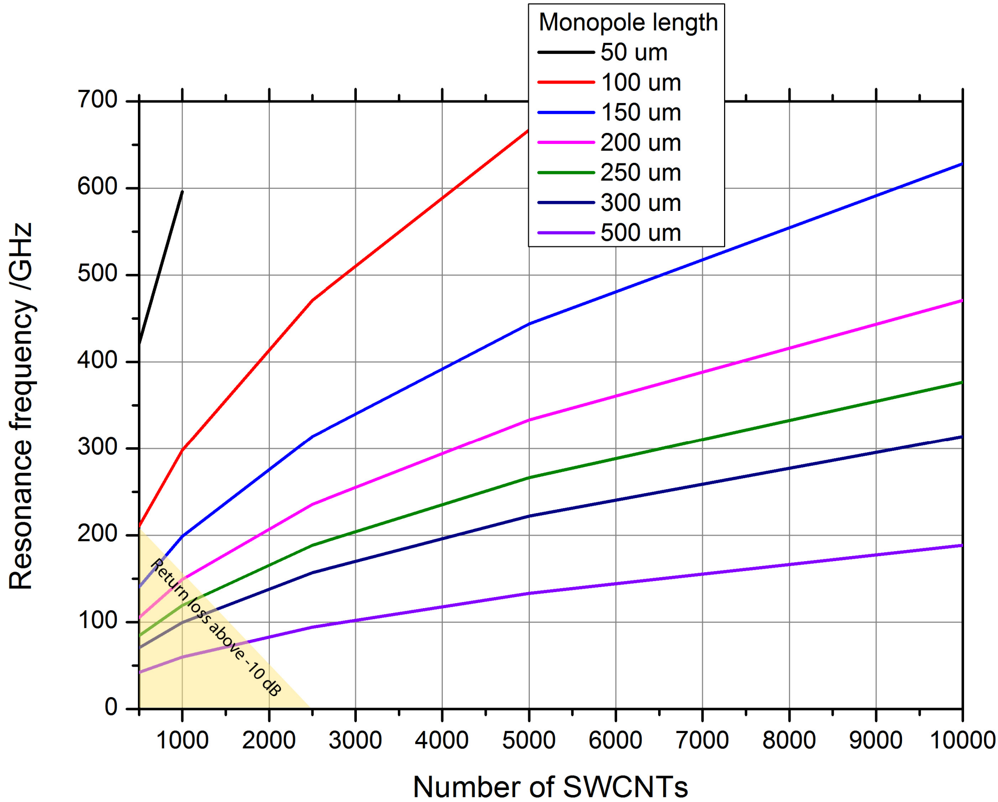

Figure 146: SWCNT monopole abacus as function as the number of CNTs and the monopole length.

On the first two cases (Figure 137 and Figure 140), return losses are not as good as the gold-based monopole interconnections (-28 dB and -52 dB). If we now compare the monopole gains and 3-D radiation patterns, all configurations have an omnidirectional radiation pattern with little more perturbations for the CNTs-based monopole interconnections. Gains are lower than 0 for all antennas with CNT bundle, respectively equal to -6.5 dBi and -3.8 dBi for 1000 and 6000 tubes at 96 GHz, -6.5 dBi for 1000 tubes at 216 GHz and -0.77 dBi at 302 GHz with the same number of CNTs. The CNT monopole gains stay low compared to metal wire antennas [186]. We showed that the increase of the monopole diameter could be a solution to increase the efficiency. One way would be to work with another monopole impedance than 50 Ω. Thus, for example, with lower impedance, a bigger number of CNTs is necessary and so, the monopole diameter can be increase easily compared to the same monopole working with 50- Ω impedance. More investigations need to be realized on that point.

However, CNT material to make interconnection is more compatible and sensitive with ’single electron’ devices and can be a solution to overcome the high resistance we have observed between carbon nanotubes and metal materials (see chapter I, section “Carbon

nanotubes modeling on page (56)") [83]. And as we have seen with the prototype working at 300 GHz, a hybrid structure using CNTs with metal could have higher efficiency and performance.

f) Transmission simulation tests

In the first part of this chapter, we demonstrated monopole interconnections using carbon nanotube bundle working with a large range of frequency from 40 GHz to 300 GHz. From these studies, we choose to model our monopole interconnections in a transmission configuration.

i. First approach

We derive our design from Figure 142 working at 300 GHz with a bundle of 1000 SWCNTs to study the transmission between two SWCNT-based monopoles (Figure 147). For this study, we consider the proposed antenna structure working at 300 GHz side-to-side and extract from HFSS simulations the S_{21} transmission between the monopoles at several spacing between the interconnections. The distance between the interconnections ranges between 80 and 1200 µm (Figure 147). As shown on Figure 148 and Table 23, we obtain a transmission by the carbon nanotube interconnections from -15 dB to -32 dB at 300 GHz.

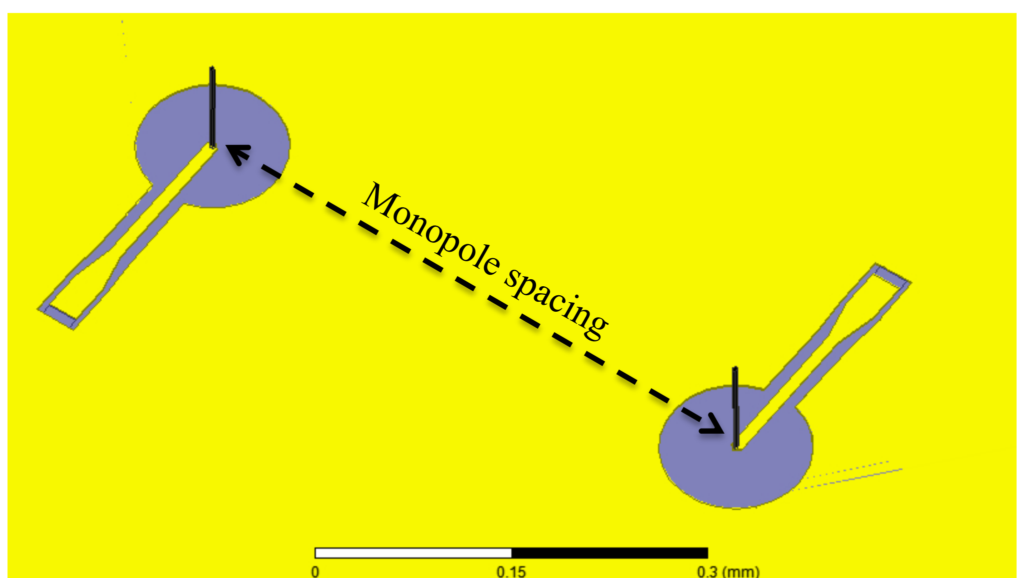

Figure 147: Schematic of the antenna monopoles transmission with monopole spacing between 80 to 1200 µm.

We simulate the same transmission configuration by replacing the SWCNT-based monopoles by gold-based monopole with the correct dimensions in order to obtain a

resonance about 300 GHz. Thus, the gold monopole has a radius of 6.7 µm and a length of 239 µm. As shown on the Table 23 and Figure 148, a transmission higher by at least 10 dB is achieved using the gold monopole. Similar to the CNT monopole results presented previously, the transmission levels are too low to make a viable replacement of usual metal-based interconnects. And as we can observe on the Figure 148, simulations are also done without monopoles (black curve). Thus, only with a distance between the CNT monopoles higher than 200 µm, we can have an improvement in transmission between the two monopoles. However, this topology presents the advantage of keeping a 50-Ω characteristic impedance (Figure 149) and thus to seamlessly integrate with current carbon nanotube-based devices.

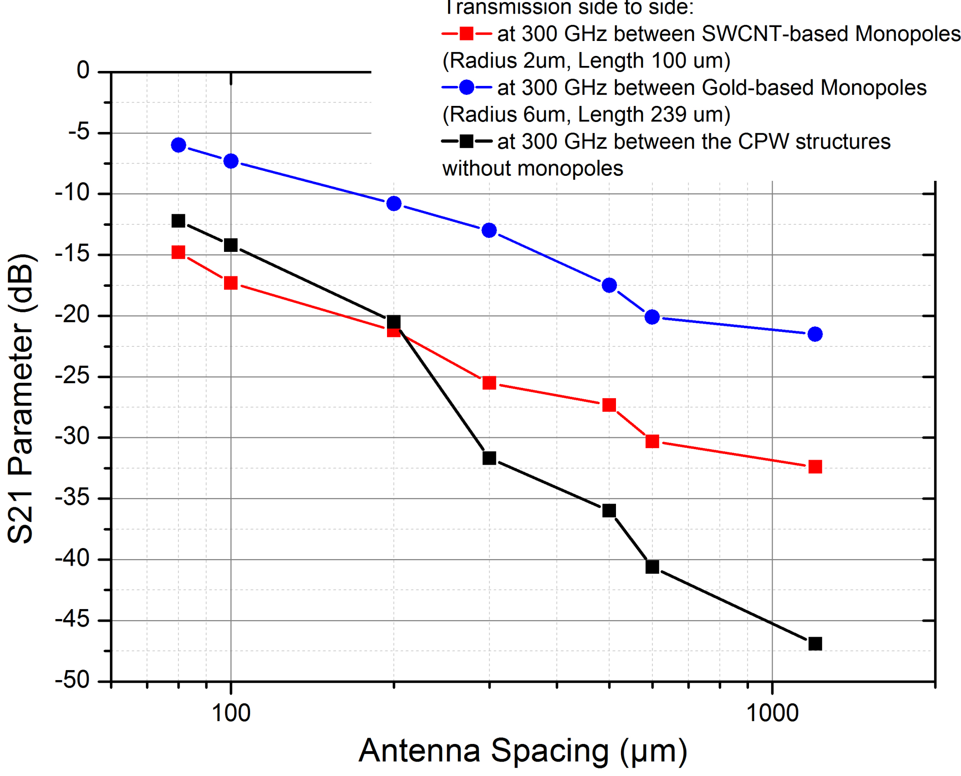

Figure 148: Simulated monopole-to-monopole transmission (S_{21} parameter) for two CNT-based monopoles (red curve), two gold-based monopoles (blue curve) and no monopoles (black curve).

Table 23: S_{21} parameters monopole-to-monopole transmission.

Distance between the monopoles /µm	**80**	**100**	**200**	**300**	**500**	**600**	**1200**
S_{21} /dB CNT-CNT	- 14.8	-17.3	-21.2	-25.5	-27.3	-30.3	-32.4
S_{21} /dB Gold-Gold	- 6	- 7.3	- 10.8	- 13	-17.9	-20.1	-21.5
S_{21} /dB No monopoles	-12.2	-14.2	-20.5	-31.7	-36	-40.6	-46.9

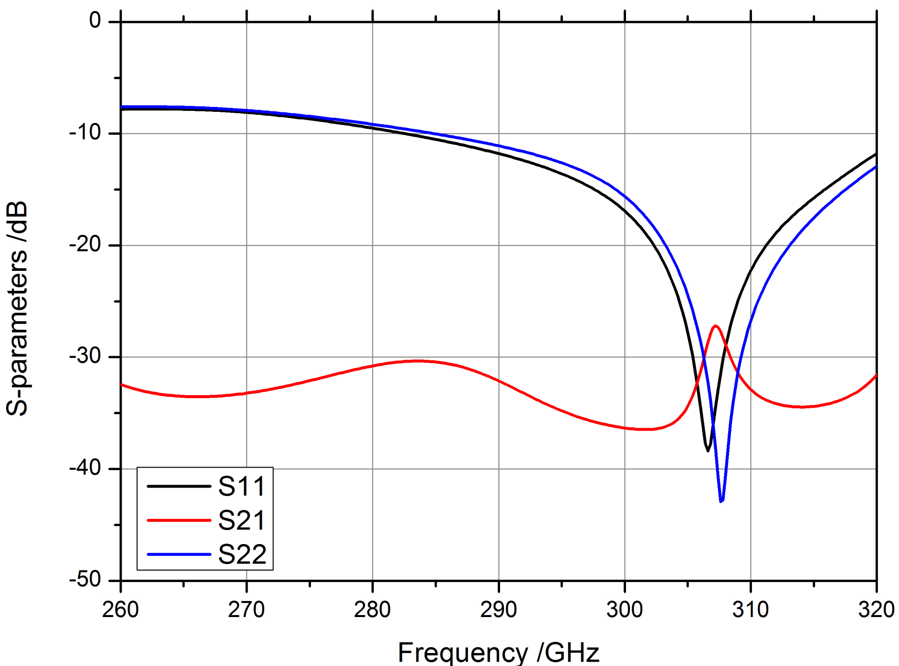

Figure 149: On left, simulated monopole-to-monopole transmission (S parameters) for two CNT-based monopoles with a distance of 500 µm working at 300 GHz.

Finally, to create an interface between the micro-electronics and nanoscale components is still challenging and the solution might come from these CNT interconnection structures. Indeed, decreasing the distance between the interconnections or having a more directive interconnection can solve the losses due to the antenna transmission.

ii. Second approach with reflectors

The second approach consists of adding a reflector around the monopole in order to direct the radiations. We propose two reflector shapes: a circular one and a parabolic one. A 200-µm distance between the monopoles is fixed for all the following simulations. Simulations are done between 250 and 350 GHz.

The circular reflector has its center located at the monopole location. The Figure 150 is showing the proposed configuration. We also propose two materials for the reflector: gold and bundle of vertically aligned CNTs (density of 1.10^{14} m^{-2}). Thus, the height of the reflector is chosen in order to be able to fabricate it, we chose 300-µm-high bundle of CNTs (as detailed in Table 7). However, after simulation of the device composed by circular reflector, no improvements in transmission have been identified either with gold or CNTs. We can imagine that the low gain of our monopole interconnections is the reason of the low performance in transmission even with the reflector.

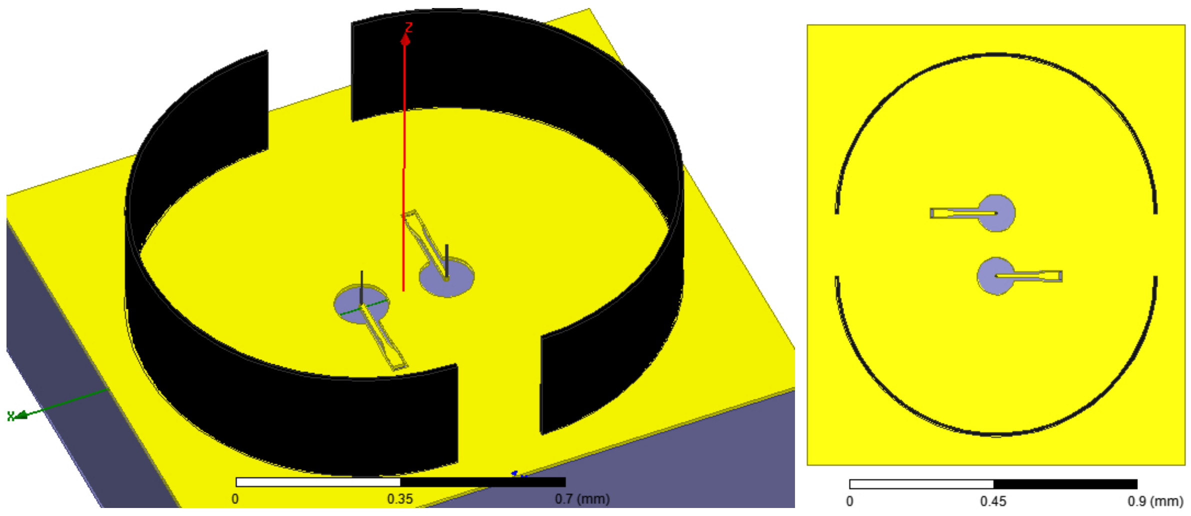

Figure 150: Transmission system between two monopoles placed side to side with circular reflectors. The distance between the two monopoles is 200 µm. Working frequency is 300 GHz.

In the second case, the circular reflector is replaced by a parabolic shape using the parabolic equation $Y = 500X^2$ (figure 149). The focal point of the parable corresponded to the monopole location. The monopole interconnection dimensions and the distance between the two monopoles (200 µm) are unchanged. After simulations (with gold and CNTs materials), again, no improvements have been observed on the S_{21} transmission between the two monopoles.

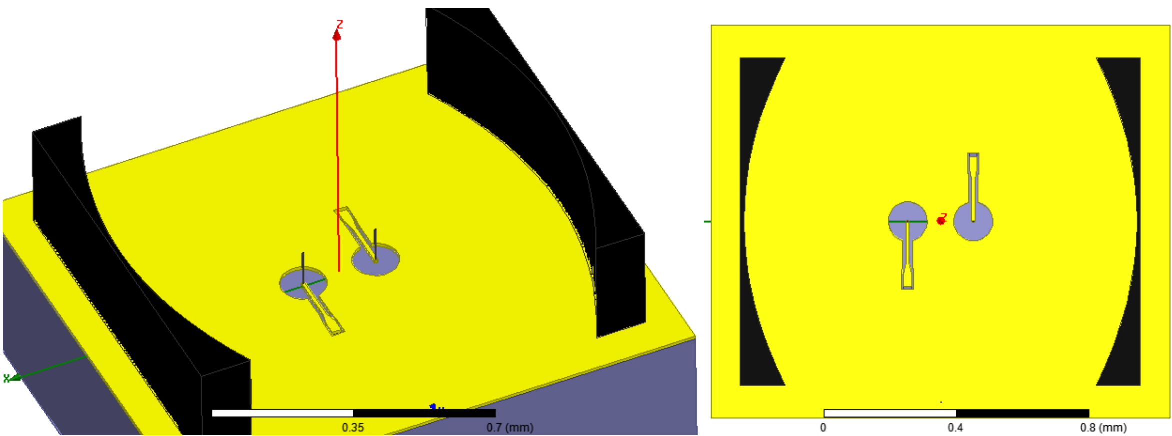

Figure 151: Transmission system between two monopoles placed side to side with parabolic reflectors. The distance between the two monopoles is 200 µm. Working frequency is 300 GHz.

Thus, we conclude the reflectors are not useful to significantly improve the performance and the efficiency of the transmission between the CNT monopoles. As we explained earlier, other solutions must be investigated in order to improve the gain of the CNT monopole interconnections. One idea is to form a hybrid couple CNT/metal to design

our wireless interconnection. The metal will act as an efficient material for the monopole gain whereas the CNT bundle will permit to decrease the size of the interconnection using their unique “quantum” properties.

g) Fabrication of the device

After we complete the simulation part presented previously, we decide to fabricate the transmission structures at CINTRA/NTU with the help of Yap Chin Chong, Chow Wai Leong, Pierre Franck and Tan Chong Wei. We choose to fabricate first the design working at 300 GHz since the bundle length is less important than the ones at lower frequencies. Using the same photolithography process we explained in the chapter II based on the flip-chip, we deposite our metallic parts (500 nm of Pt) by ebeam (Figure 152). An Al_2O_3 barrier layer (10 nm) is then deposited to avoid the diffusion of the Pt on the catalyst layer during the CNT growth. Catalyst layer (1.1 nm of Fe) is finally deposited and a thermal CVD process was run between 5 and 30 minutes at 625 °C.

As we can see on the Figure 152, carbon nanotubes bundles, mainly composed by DWCNTs and triple-wall CNTs, have grown following the cylinder shape of our monopole interconnections. Indeed, as a first fabrication test, the growth of DWCNTs is easier than the growth of SWCNTs. The growth of SWCNTs requires a fine control of the catalyst layer deposition and thickness. This control can be difficult in our case with small patterns (from few microns to 10 microns). Moreover, as we already explained in the section “Double-wall carbon nanotube on page (14)”, the electrical properties between SWCNTs and DWCNTs are quite similar. As we can see on close views on Figure 152d and f, a high CNT density is achieved using the thermal CVD process. The CNT density is previously estimated to be about 1.10^{14} m^{-2}. Unfortunately, as shown on the Figure 152a-b and e, the CNT bundles didn’t stand vertically on the device and, most of the time, fall in a random direction. However, few SEM images showing the monopole interconnections almost standing vertically has been captured. The lengths of the monopoles are approximately about 100 µm after 5 mins growth and 300 µm after 30 mins growth. An improvement in term of bundle length and bundle orientation is expecting in future works. However, a high ratio between CNT bundle length and diameter has been reach, which is already an important breakthrough for the rest of our project.

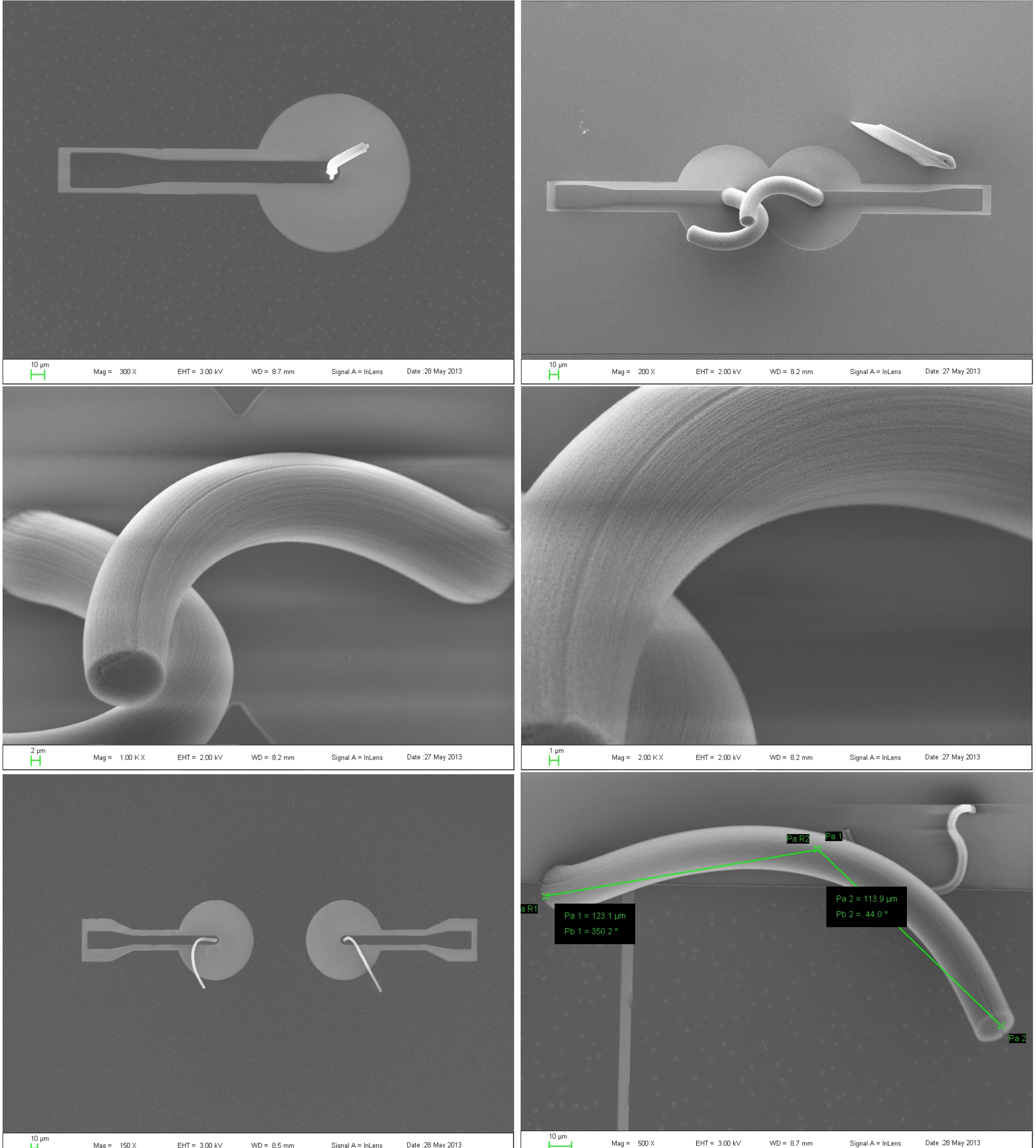

Figure 152: Carbon nanotubes monopoles fabricated by TCVD within a transmission configuration. On (a, b and e), bundles of aligned CNTs were visible following a cylinder shape. On the close view (c and d), alignment of CNTs and CNT density were visible. A height greater than 300 µm was obtained on f.

On going works plan to measure the monopole up to 500 GHz with the appropriate setup.

h) Conclusion

In conclusion, CNT-based monopole interconnections have been demonstrated at 96 GHz, 216 GHz and 302 GHz using electromagnetic simulations based on a bulk bundle model

of SWCNT. Performances have been compared with classical gold monopole antenna. A size reduction greater than two on the interconnection length becomes possible by using "quantum" effects existing in CNTs. Lower cost and better compactness of CNT monopole interconnections open a new domain of investigations in high frequency. From the technological point of view, the proposed CNT based monopole will follow the process already developed and described in the chapter II with flip-chip devices. It offers the advantage of simpler and more straightforward fabrication process, compared to [180]. Thus, we were able to initiate the monopole fabrication with very encouraging and impressive results in terms of breakthrough on the high ratio CNT bundle fabrication. Unfortunately, the high frequency measurements up to 170 GHz didn't return any good results. Finally, the performance of CNT monopole interconnection will strongly depends on the CNT quality, the number of CNTs in the bundle, their diameter and their length [182].

Conclusion and outlook

Carbon nanotubes exhibited unique electrical, thermal and mechanical properties compared to classical materials used for electronic applications. Thus, since their discovery, a lot of applications on electronic components based on carbon nanotubes have been studied. We can denote: transistors, sensors, RF switches, radios, radiators, antennas and interconnections.

In this PhD work, we focused on RF nanopackaging and we mainly studied two specific applications: CNT based flip-chip bonding and CNT based wireless interconnects.

We first designed interconnections made by bundle of vertically aligned carbon nanotubes (MWCNTs) for flip-chip technology. These bundles were grown by PECVD on the two parts and then interconnected each others using the electrostatic and Van der Waals forces. An electrical bond was hence created and we have proved for the first time, after fabrication of the device, a high frequency transmission through the CNT interconnections. The performance obtained were quite good for a first prototype and leave us a strong believe on the feasibility and potential that can be achieved with this innovative device using CNTs. A full modeling of the device with two approaches (full-EM and hybrid EM/analytical modeling) was done with a very good agreement with measurements, which gives us a full understanding of our flip-chip device using CNT-based interconnections. The contact resistance was extracted and a high value about 300 kΩ was found. That gave us advices and the points to focus in order to improve the performance of the device: an increase of the CNT density. Thus, new designs of flip-chip had been proposed in order to give answers and solutions to our previous issues. The fabrication of these new designs is still under progress and primary DC results showed encouraging performance.

Thus, on the CNT-based flip-chip, showing promising results, several points need to be improved to become, one day, a reality for industry.

Hence, a lower temperature needs to be reached in order to become CMOS compatible. Further investigation on the CNT growth process has been presented in the manuscript in order to find new catalyst heat approaches. Heating the catalyst layer from the top could decrease the CNT growth process temperature. A CNT growth temperature lower than 350 °C needs to be reached. However, with lower growth temperature, the level of

impurities in CNTs is increased. Thus, we need to work on three aspects in the same time: the growth temperature, the quality of CNTs and the good control of CNT uniformity. To summarize, most of the work need to focus on the CNT growth in order to reach an unprecedented level of control. With a better control of CNT growth, more and more complex devices for high frequency such as the one presented in this manuscript could be imagine. With better CNT quality, verticality and a perfect control of the CNT density, the flip-chip working up to 110 GHz with small 20-µm-bundle size will outperform the possibility offered by the same device made by metal-based bumps.

Secondly, we also studied wireless interconnections for chip-to-chip communication based on carbon nanotubes monopole. We demonstrated the interests of using CNTs for these architectures. Indeed, using the kinetic inductance in CNTs and its effect on the wave velocity showed a size reduction of the monopole. Several designs based on this principle were defined at several frequencies between 40 and 300 GHz. For each configuration, we explained and defined the behavior of our CNT-based monopole interconnections. The observations showed by these studies demonstrated that higher is the monopole frequency, shorter is the monopole length, and so the number of CNTs in the monopole can be reduced. By decreasing the number of CNTs, the size reduction factor of the monopole can be increase. However, with shorter monopoles, their efficiency is also reduced. Thus, a trade-off needs to be found between the size reduction factor and the wireless interconnection performance. Several options have been proposed in order to find solutions for the monopole efficiency. Indeed, working with lower characteristics impedance or lower CNT density would increase the monopole diameter, and compensate for the low monopole efficiency. Secondly, a hybrid metal/CNT monopole could be achieved in order to get the efficiency advantage of the metal and the size reduction advantage of the CNTs. Finally, the monopole interconnections were fabricated using a CVD principle and high frequency measurements are under progress.

After showing the unique possibilities offered by the SWCNT properties for resonant systems such as the monopole interconnection, we realized again that the control of the CNT growth would be the major point to focus on. Indeed, to make a CNT monopole with the desired characteristics, we need to growth a bundle of SWCNTs with a small diameter of few microns, a perfect verticality up to 100 µm and a perfect SWCNT uniformity in term of diameter and quality. The method to grow 100 % metallic SWCNTs in a bundle needs also to be developed. The challenge is very high but not impossible. Indeed, in this PhD work, we

have demonstrated in a first run, the growth of such CNT monopole with a promising control of the bundle parameters. Making CNT based resonant circuits can decrease the size of classical resonant circuits. Hence, we can imagine the fabrication of smaller filters and antennas.

This PhD work showed the first study of new applications using CNTs for RF nanopackaging, and we hope that more works will be conducted on these ideas in order to concretize, on day, the principles that we have tried to bring to the reality.

List of publications

Journals

- **Yap, C. C., D. Tan, Christophe Brun, HONG Li, Edwin Hang TONG Teo, Dominique BAILLARGEAT, B. K. TAY.**
"Impact of the CNT growth process on gold metallization dedicated to RF interconnect applications."
International Journal of Microwave and Wireless Technologies, 2010.

- **Chin Chong YAP, Christophe BRUN, Dunlin TAN, HONG Li, Edwin Hang TONG Teo, Dominique BAILLARGEAT and Beng Kang TAY.**
"Carbon nanotubes bumps for flip chip packaging system."
Nanoscale Research Letters 2012, 7:105 - Published: 7 February 2012.

- **Christophe BRUN, Chin Chong YAP, Dunlin TAN, Stephane Bila, Sebastien Pacchini, Dominique BAILLARGEAT and Beng Kang TAY.**
"Flip-Chip Based on Carbon Nanotube – Carbon Nanotube Interconnected Bumps for High Frequency Applications."
IEEE transaction on Nanotechnology – 2013.

International conferences

- **Christophe BRUN, C. YAP, D. TAN, E. TEO, Stéphane BILA, Serge VERDEYME, Dominique BAILLARGEAT, B. TAY.**
"Study of carbon nanotube flip-chip methodology for interconnect technology bia electromagnetic and circuit model approach."
IEEE MTT-S, IMS 2011, THPR-2, Baltimore, USA, June 5-10, 2011.

- **Christophe BRUN, Pierre FRANCK, C. C. YAP, D. TAN, E. H. TONG, Stéphane BILA, Dominique BAILLARGEAT, B. K. TAY.**
"Hybrid EM/Circuit Modeling for Carbon Nanotubes based Interconnects."
13th Electronics Packaging Technology Conference, 2011, Singapore.

- **C. C. Yap, Christophe BRUN, D. TAN, E. H. TONG, J. WEI, Dominique BAILLARGEAT, B. K. TAY.**
"Characterization of novel CNT to CNT joining interconnections implemented for 1st level flip chip packaging."
13th Electronics Packaging Technology Conference, 2011, Singapore.

- **Pierre FRANCK, Christophe BRUN, C. C. YAP, D. TAN, E. H. TONG, Stéphane BILA, Dominique BAILLARGEAT, B. K. TAY.**
"Plasmonic Resonances of Carbon-nanotube-based Dipole Antennas for Nano-Interconnects."
13th Electronics Packaging Technology Conference, 2011, Singapore.

- **Christophe Brun, Chin Chong Yap, Dunlin Tan, Dominique Baillargeat, Beng Kang Tay.**
"Electrical Properties of Flip Chip Bonding Using Carbon Nanotube Bundles for Rf Applications."
International Conference of Young Researchers on Advanced Materials (ICYRAM), Singapore, 2012.

- **W.L. Chow, C.C. Yap , D. Tan, M. Shakerzadeh, M.K. Samani, C. Brun, E.H.T. Teo, D. Baillargeat and B.K. Tay.**
"RF Nanopackaging based on Carbon-Nanostructures."
International Topical Symposium on RF Nanotechnology, Singapore, 2012.

- **W.L. Chow, C.C. Yap, D. Tan, M. Shakerzadeh, M.K. Samani, C. Brun, E.H.T. Teo, D. Baillargeat and B.K. Tay.**
"Carbon based multi-functional materials towards 3D system integration. Application to thermal and interconnect management."
IEEE MTT-S, IMS 2012, Montreal, Canada, June 17-22, 2012.

- **Christophe Brun, Pierre Franck, Philippe Coquet, Dominique Baillargeat, and Beng Kang Tay.**
"Monopole antenna based on carbon nanotubes."
Microwave Symposium Digest (MTT), EEE MTT-S International, Seattle, USA, 2013.

- **Christophe Brun, Ching Chong Yap, Philippe Coquet, Dominique Baillargeat, and Beng Kang Tay.**
"Measurement and Modeling of Carbon Nanotubes-based Flip-Chip RF Device."
Microwave Symposium Digest (MTT), EEE MTT-S International, Seattle, USA, 2013.

- **Pierre FRANCK, Christophe BRUN, C. C. YAP, Waileong CHOW, Cong Xiang LU, Dunlin TAN, Hong LI, Dominique BAILLARGEAT, Beng Kang TAY.**
"Applications of a Mesoscopic Electromagnetic Model for Carbon Nanotubes Arrays."
International Conference on Material for Advanced Technologies, ICMAT 2013, Singapore.

- **Chin Chong YAP, Dunlin TAN, Christophe BRUN, Jun WEI, Dominique BAILLARGEAT, Edwin Hang Tong TEO, Beng Kang TAY.**
"Improving the Performance of CNT to CNT Bumps for Flip Chip Applications."
International Conference on Material for Advanced Technologies, ICMAT 2013, Singapore.

- **P. Franck, C.C. Yap, C. Brun, S. Pacchini, W.L. Chow, H. Li, D. Baillargeat, B.K. Tay.**
"Carbon-nanotube-based RF components with multiple applications."
IEEE MTT-S International Wireless Symposium, Beijing China, 2013.

- **C. Brun, P. Franck, W.L. Chow, P. Coquet, D. Baillargeat and B.K. Tay.**
"Horizontal and vertical carbon-nanotube-array-based antenna designs."
European Microwave Week 2013 Nuremberg, Germany, October 2013.

National conferences

- **Christophe Brun, Yap Chin Chong, Edwin Hang Tong , Stéphane Bila , Dominique Baillargeat , Beng Kang Tay.**

“Modèle hyperfréquence de nanotubes de carbone appliqués en connectique.”
17èmes Journées Nationales Microondes, Brest 2011.

- **Christophe Brun, Yap Chin Chong, Stéphane Bila, Dominique Baillargeat, Beng Kang Tay.**
"Interconnexion Haute Fréquence à base de Nanotubes de Carbone."
18èmes Journées Nationales Microondes, Paris, 14-17 mai 2013.

- **Christophe Brun, Philippe Coquet, Pierre Franck, Dominique Baillargeat, Beng Kang Tay.**
"Antennes Monopoles à base de Nanotubes de Carbone"
18èmes Journées Nationales Microondes, Paris, 14-17 mai 2013.

Bibliography

[1] S. Iijima, *Nature,* vol. 354, 1991.

[2] L. Hong, X. Chuan, N. Srivastava, and K. Banerjee, "Carbon Nanomaterials for Next-Generation Interconnects and Passives: Physics, Status, and Prospects," *Electron Devices, IEEE Transactions on,* vol. 56, pp. 1799-1821, 2009.

[3] C. Rutherglen and P. Burke, "Nanoelectromagnetics: Circuit and Electromagnetic Properties of Carbon Nanotubes," *Small,* vol. 5, pp. 884-906, 2009.

[4] T. Wang, "Towards Carbon Nanotube-based on-Chip Interconnects," 2009.

[5] W. Xueshen, L. I. Qunqing, X. I. E. Jing, J. I. N. Zhong, W. Jinyong, L. I. Yan*, et al.*, "Fabrication of Ultralong and Electrically Uniform Single-Walled Carbon Nanotubes on Clean Substrates," vol. 9, ed. Washington, DC, ETATS-UNIS: American Chemical Society, 2009, p. 5.

[6] L. Hong, N. Srivastava, M. Jun-Fa, Y. Wen-Yan, and K. Banerjee, "Carbon Nanotube Vias: Does Ballistic Electron–Phonon Transport Imply Improved Performance and Reliability?," *Electron Devices, IEEE Transactions on,* vol. 58, pp. 2689-2701, 2011.

[7] K. Banerjee, L. Hong, and N. Srivastava, "Current Status and Future Perspectives of Carbon Nanotube Interconnects," in *Nanotechnology, 2008. NANO '08. 8th IEEE Conference on*, 2008, pp. 432-436.

[8] Y. Li, D. Mann, M. Rolandi, W. Kim, A. Ural, S. Hung*, et al.*, "Preferential Growth of Semiconducting Single-Walled Carbon Nanotubes by a Plasma Enhanced CVD Method," *Nano Letters,* vol. 4, pp. 317-321, 2004/02/01 2004.

[9] L. Ding, A. Tselev, J. Wang, D. Yuan, H. Chu, T. P. McNicholas*, et al.*, "Selective Growth of Well-Aligned Semiconducting Single-Walled Carbon Nanotubes," *Nano Letters,* vol. 9, pp. 800-805, 2009/02/11 2009.

[10] R. Saito, G. Dresselhaus, and M. S. Dresselhaus, *Physical Properties of Carbon Nanotube*: Imperial College Press, 1998.

[11] L. Hong, Y. Wen-Yan, K. Banerjee, and M. Jun-Fa, "Circuit Modeling and Performance Analysis of Multi-Walled Carbon Nanotube Interconnects," *Electron Devices, IEEE Transactions on,* vol. 55, pp. 1328-1337, 2008.

[12] C. T. White and J. W. Mintmire, "Fundamental Properties of Single-Wall Carbon Nanotubes," *The Journal of Physical Chemistry B,* vol. 109, pp. 52-65, 2005/01/01 2004.

[13] KOCIAK, #160, M., SUENAGA, #160, K.*, et al.*, *Linking chiral indices and transport properties of double-walled carbon nanotubes* vol. 89. Ridge, NY, ETATS-UNIS: American Physical Society, 2002.

[14] A. Cassell and J. Li, "Carbon Nanotube Based Interconnect Technology: Opportunities and Challenges," ed, 2007, pp. A181-A204.

[15] M. Meyyappan, "A review of plasma enhanced chemical vapour deposition of carbon nanotubes," *Journal of Physics D: Applied Physics,* vol. 42, p. 213001, 2009.

[16] N. Rouhi, D. Jain, and P. J. Burke, "Nanoscale Devices for Large-Scale Applications," *Microwave Magazine, IEEE,* vol. 11, pp. 72-80, 2010.

[17] J. W. Beck, "Isotope Junctions Created in Carbon Nanotubes for Spintronic Applications," 2011.

[18] E. Titus, M. K. Singh, G. Cabral, V. Paserin, P. R. Babu, W. J. Blau, *et al.*, "Fabrication of vertically aligned carbon nanotubes for spintronic device applications," *Journal of Materials Chemistry,* vol. 19, pp. 7216-7221, 2009.

[19] H. Mehrez, J. Taylor, H. Guo, J. Wang, and C. Roland, "Carbon Nanotube Based Magnetic Tunnel Junctions," *Physical Review Letters,* vol. 84, pp. 2682-2685, 03/20/ 2000.

[20] "http://en.wikipedia.org/wiki/Electron_mobility," ed.

[21] "http://en.wikipedia.org/wiki/Ballistic_conduction," ed.

[22] H. J. Li, W. G. Lu, J. J. Li, X. D. Bai, and C. Z. Gu, "Multichannel Ballistic Transport in Multiwall Carbon Nanotubes," *Physical Review Letters,* vol. 95, p. 086601, 08/15/ 2005.

[23] C. T. White and T. N. Todorov, "Carbon nanotubes as long ballistic conductors," *Nature,* vol. 393, pp. 240-242, 05/21/print 1998.

[24] J. Jiang, J. Dong, H. T. Yang, and D. Y. Xing, "Universal expression for localization length in metallic carbon nanotubes," *Physical Review B,* vol. 64, p. 045409, 07/02/ 2001.

[25] R. Stephan, J. Jie, E. F. F. T. Luis, and S. Riichiro, "Charge transport in carbon nanotubes: quantum effects of electron–phonon coupling," *Journal of Physics: Condensed Matter,* vol. 19, p. 183203, 2007.

[26] C. Yang, S. Minghui, X. Zhiyong, L. Yuan, Z. Min, and P. C. H. Chan, "Pursuit of Future Interconnect Technology with Aligned Carbon Nanotube Arrays [Nanopackaging]," *Nanotechnology Magazine, IEEE,* vol. 5, pp. 22-26, 2011.

[27] B. Q. Wei, R. Vajtai, and P. M. Ajayan, "Reliability and current carrying capacity of carbon nanotubes," *Applied Physics Letters,* vol. 79, pp. 1172-1174, 2001.

[28] C. Ren, W. Zhang, Z. Xu, Z. Zhu, and P. Huai, "Thermal Conductivity of Single-Walled Carbon Nanotubes under Axial Stress," *The Journal of Physical Chemistry C,* vol. 114, pp. 5786-5791, 2010/04/08 2010.

[29] T. Yamamoto, K. Watanabe, and E. Hernández, "Mechanical Properties, Thermal Stability and Heat Transport in Carbon Nanotubes," in *Carbon Nanotubes*. vol. 111, ed: Springer Berlin Heidelberg, 2008, pp. 165-194.

[30] E. Pop, D. Mann, Q. Wang, K. Goodson, and H. Dai, "Thermal Conductance of an Individual Single-Wall Carbon Nanotube above Room Temperature," *Nano Letters,* vol. 6, pp. 96-100, 2006/01/01 2005.

[31] P. Kim, L. Shi, A. Majumdar, and P. L. McEuen, "Thermal Transport Measurements of Individual Multiwalled Nanotubes," *Physical Review Letters,* vol. 87, p. 215502, 10/31/ 2001.

[32] **Wikipedia, "Carbon nanotube."**

[33] **T. Iwai, H. Shioya, D. Kondo, S. Hirose, A. Kawabata, S. Sato*, et al.*, "Thermal and source bumps utilizing carbon nanotubes for flip-chip high power amplifiers," in *Electron Devices Meeting, 2005. IEDM Technical Digest. IEEE International*, 2005, pp. 257-260.**

[34] **C. Yang, X. Zhiyong, and C. H. C. Philip, "Horizontally aligned carbon nanotube bundles for interconnect application: diameter-dependent contact resistance and mean free path," *Nanotechnology,* vol. 21, p. 235705, 2010.**

[35] **J. B. K. Law, C. K. Koo, and J. T. L. Thong, "Horizontally directed growth of carbon nanotubes utilizing self-generated electric field from plasma induced surface charging," *Applied Physics Letters,* vol. 91, pp. 243108-243108-3, 2007.**

[36] **Y. Hayashi, B. Jang, T. Iijima, T. Tokunaga, R. A. Afre, M. Tanemura*, et al.*, "Direct growth of horizontally aligned carbon nanotubes between electrodes and its application to field-effect transistors," in *Nanoelectronics Conference (INEC), 2010 3rd International*, 2010, pp. 215-216.**

[37] **Y. Saito, "Preparation and properties of carbon nanotubes," in *Micromechatronics and Human Science, 1999. MHS '99. Proceedings of 1999 International Symposium on*, 1999, pp. 43-49.**

[38] **B. RUELLE, "Functionalization of carbon nanotubes via plasma post-discharge surface treatment: Implication as nanofiller in polymeric matrices," 2009.**

[39] **J. Bernholc, D. Brenner, M. Buongiorno Nardelli, V. Meunier, and C. Roland, "Mechanical and electrical properties of nanotubes," *Annual Review of Materials Research,* vol. 32, pp. 347-375, 2002.**

[40] **S. Demoustier, E. Minoux, M. Le Baillif, M. Charles, and A. Ziaei, "Review of two microwave applications of carbon nanotubes: nano-antennas and nano-switches," *Comptes Rendus Physique,* vol. 9, pp. 53-66, 2008.**

[41] **S. Iijima, "Helical microtubules of graphitic carbon," *Nature,* vol. 354, pp. 56-58, 11/07/print 1991.**

[42] **T. Guo, P. Nikolaev, A. Thess, D. T. Colbert, and R. E. Smalley, "Catalytic growth of single-walled nanotubes by laser vaporization," *Chemical Physics Letters,* vol. 243, pp. 49-54, // 1995.**

[43] **M. Jose-Yacaman, M. Miki-Yoshida, L. Rendon, and J. G. Santiesteban, "Catalytic growth of carbon microtubules with fullerene structure," *Applied Physics Letters,* vol. 62, pp. 202-204, 01/11/ 1993.**

[44] **L. Delzeit, C. V. Nguyen, B. Chen, R. Stevens, A. Cassell, J. Han*, et al.*, "Multiwalled Carbon Nanotubes by Chemical Vapor Deposition Using Multilayered Metal Catalysts," *The Journal of Physical Chemistry B,* vol. 106, pp. 5629-5635, 2002/06/01 2002.**

[45] **R. E. Morjan, O. A. Nerushev, M. Sveningsson, F. Rohmund, L. K. L. Falk, and E. E. B. Campbell, "Growth of carbon nanotubes from C60," *Applied Physics A,* vol. 78, pp. 253-261, 2004/02/01 2004.**

[46] **Y. Kumar M Fau - Ando and Y. Ando, "Chemical vapor deposition of carbon nanotubes: a review on growth mechanism and mass production," 20100401 DCOM- 20100503.**

[47] **M. Kumar, *Carbon Nanotube Synthesis and Growth Mechanism*, 2011.**

[48] S. Xuhui, L. Ke, W. Wen, T. Saito, and C. Y. Yang, "Effect of catalyst and underlayer metal on PECVD growth of vertically aligned carbon nanotubes," in *Nanotechnology Materials and Devices Conference, 2009. NMDC '09. IEEE*, 2009, pp. 1-2.

[49] S. Joydip and J. Chacko, "The effect of Fe and Ni catalysts on the growth of multiwalled carbon nanotubes using chemical vapor deposition," *Journal of Nanoparticle Research,* 2009.

[50] M. Meyyappan, D. Lance, C. Alan, and H. David, "Carbon nanotube growth by PECVD: a review," *Plasma Sources Science and Technology,* vol. 12, p. 205, 2003.

[51] A. V. Melechko, V. I. Merkulov, T. E. McKnight, M. A. Guillorn, K. L. Klein, D. H. Lowndes*, et al.*, "Vertically aligned carbon nanofibers and related structures: Controlled synthesis and directed assembly," *Journal of Applied Physics,* vol. 97, pp. 041301-39, 02/15/ 2005.

[52] A. Kawabata, S. Sato, T. Nozue, T. Hyakushima, M. Norimatsu, M. Mishima*, et al.*, "Robustness of CNT Via Interconnect Fabricated by Low Temperature Process over a High-Density Current," in *Interconnect Technology Conference, 2008. IITC 2008. International*, 2008, pp. 237-239.

[53] M. Fayolle, J. F. Lugand, R. Kachtouli, H. Okuno, J. Dijon, P. Gautier*, et al.*, "Integration of dense CNTs in vias on 200mm diameter wafers: Study of post CNT growth processes," in *Interconnect Technology Conference and 2011 Materials for Advanced Metallization (IITC/MAM), 2011 IEEE International*, 2011, pp. 1-3.

[54] G. Y. Chen, B. Jensen, V. Stolojan, and S. R. P. Silva, "Growth of carbon nanotubes at temperatures compatible with integrated circuit technologies," *Carbon,* vol. 49, pp. 280-285, 1// 2011.

[55] J. Dijon, H. Okuno, M. Fayolle, T. Vo, J. Pontcharra, D. Acquaviva*, et al.*, "Ultra-high density carbon nanotubes on Al-Cu for advanced vias," in *Electron Devices Meeting (IEDM), 2010 IEEE International*, 2010, pp. 33.4.1-33.4.4.

[56] C. Bower, O. Zhou, W. Zhu, D. J. Werder, and S. Jin, "Nucleation and growth of carbon nanotubes by microwave plasma chemical vapor deposition," *Applied Physics Letters,* vol. 77, pp. 2767-2769, 10/23/ 2000.

[57] "http://en.wikipedia.org/wiki/Matter_wave," ed.

[58] K. Asaka, M. Karita, and Y. Saito, "Modification of interface structure and contact resistance between a carbon nanotube and a gold electrode by local melting," *Applied Surface Science,* vol. 257, pp. 2850-2853, 2011.

[59] I. V. e. Alla, "Fabrication techniques of electrode arrays for carbon nanotubes," *Physics-Uspekhi,* vol. 52, p. 225, 2009.

[60] L. Chun, S. Pornsak, B. A. Placidus, S. F. Timothy, X. Xianfan, and G. R. Ronald, "Measurement of metal/carbon nanotube contact resistance by adjusting contact length using laser ablation," *Nanotechnology,* vol. 19, p. 125703, 2008.

[61] S. C. Lim, J. H. Jang, D. J. Bae, G. H. Han, S. Lee, I.-S. Yeo*, et al.*, "Contact resistance between metal and carbon nanotube interconnects: Effect of work function and wettability," *Applied Physics Letters,* vol. 95, pp. 264103-3, 2009.

[62] F. Wakaya, K. Katayama, and K. Gamo, "Contact resistance of multiwall carbon nanotubes," *Microelectronic Engineering,* vol. 67–68, pp. 853-857, 2003.

[63] S. Xuhui, L. Ke, R. Wu, P. Wilhite, and C. Y. Yang, "Contact resistances of carbon nanotubes grown under various conditions," in *Nanotechnology Materials and Devices Conference (NMDC), 2010 IEEE*, 2010, pp. 332-333.

[64] C. A. Santini, A. Volodin, C. Van Haesendonck, S. De Gendt, G. Groeseneken, and P. M. Vereecken, "Carbon nanotube–carbon nanotube contacts as an alternative towards low resistance horizontal interconnects," *Carbon,* vol. 49, pp. 4004-4012, 2011.

[65] J. J. Plombon, K. P. Obrien, F. Gstrein, V. M. Dubin, and Y. Jiao, "High-frequency electrical properties of individual and bundled carbon nanotubes," *Applied Physics Letters,* vol. 90, pp. 063106-063106-3, 2007.

[66] S. Xuhui, L. Ke, W. Wen, P. Wilhite, T. Saito, and C. Y. Yang, "Contact resistances of carbon nanotube via interconnects," in *Electron Devices and Solid-State Circuits, 2009. EDSSC 2009. IEEE International Conference of*, 2009, pp. 131-135.

[67] J.-Y. Park, S. Rosenblatt, Y. Yaish, V. Sazonova, H. Üstünel, S. Braig*, et al.*, "Electron−Phonon Scattering in Metallic Single-Walled Carbon Nanotubes," *Nano Letters,* vol. 4, pp. 517-520, 2004/03/01 2004.

[68] H. Stahl, J. Appenzeller, R. Martel, P. Avouris, and B. Lengeler, "Intertube Coupling in Ropes of Single-Wall Carbon Nanotubes," *Physical Review Letters,* vol. 85, pp. 5186-5189, 12/11/ 2000.

[69] P. J. Burke, "Luttinger liquid theory as a model of the gigahertz electrical properties of carbon nanotubes," *Nanotechnology, IEEE Transactions on,* vol. 1, pp. 129-144, 2002.

[70] M. S. Sarto and A. Tamburrano, "Single-Conductor Transmission-Line Model of Multiwall Carbon Nanotubes," *Nanotechnology, IEEE Transactions on,* vol. 9, pp. 82-92, 2010.

[71] "http://fr.wikipedia.org/wiki/Inductance," ed.

[72] "http://en.wikipedia.org/wiki/Capacitance," ed.

[73] M. W. Bockrath, "Carbon nanotubes: electrons in one dimension," University of California, 1999.

[74] M. P. Anantram and F. Léonard, "Physics of carbon nanotube electronic devices," *Reports on Progress in Physics,* vol. 69, p. 507, 2006.

[75] S. Salahuddin, M. Lundstrom, and S. Datta, "Transport effects on signal propagation in quantum wires," *Electron Devices, IEEE Transactions on,* vol. 52, pp. 1734-1742, 2005.

[76] L. Hong and K. Banerjee, "High-Frequency Analysis of Carbon Nanotube Interconnects and Implications for On-Chip Inductor Design," *Electron Devices, IEEE Transactions on,* vol. 56, pp. 2202-2214, 2009.

[77] P. Collins and P. Avouris, "Multishell conduction in multiwalled carbon nanotubes," *Applied Physics A,* vol. 74, pp. 329-332, 2002.

[78] Y.-G. Yoon, P. Delaney, and S. G. Louie, "Quantum conductance of multiwall carbon nanotubes," *Physical Review B,* vol. 66, p. 073407, 08/02/ 2002.

[79] B. Bourlon, C. Miko, L. Forró, D. C. Glattli, and A. Bachtold, "Determination of the Intershell Conductance in Multiwalled Carbon Nanotubes," *Physical Review Letters,* vol. 93, p. 176806, 10/21/ 2004.

[80] T. Chee Wee and M. Jianmin, "Transmission Line Characteristics of a CNT-based Vertical Interconnect Scheme," in *Electronic Components and Technology Conference, 2007. ECTC '07. Proceedings. 57th*, 2007, pp. 1936-1941.

[81] S. Minghui, X. Zhiyong, C. Yang, L. Yuan, and P. C. H. Chan, "Inductance Properties of In Situ-Grown Horizontally Aligned Carbon Nanotubes," *Electron Devices, IEEE Transactions on,* vol. 58, pp. 229-235, 2011.

[82] M. S. Sarto, A. Tamburrano, and M. D'Amore, "New Electron-Waveguide-Based Modeling for Carbon Nanotube Interconnects," *Nanotechnology, IEEE Transactions on,* vol. 8, pp. 214-225, 2009.

[83] G. W. Hanson, "Fundamental transmitting properties of carbon nanotube antennas," *Antennas and Propagation, IEEE Transactions on,* vol. 53, pp. 3426-3435, 2005.

[84] P. Franck, D. Baillargeat, and T. Beng Kang, "Mesoscopic Model for the Electromagnetic Properties of Arrays of Nanotubes and Nanowires: A Bulk Equivalent Approach," *Nanotechnology, IEEE Transactions on,* vol. 11, pp. 964-974, 2012.

[85] A. D. Franklin, M. Luisier, S.-J. Han, G. Tulevski, C. M. Breslin, L. Gignac*, et al.*, "Sub-10 nm Carbon Nanotube Transistor," *Nano Letters,* vol. 12, pp. 758-762, 2012/02/08 2012.

[86] A. Javey, J. Guo, Q. Wang, M. Lundstrom, and H. Dai, "Ballistic carbon nanotube field-effect transistors," *Nature,* vol. 424, pp. 654-657, 08/07/print 2003.

[87] H. Li and Q. Zhang, "Tunable ambipolar Coulomb blockade characteristics in carbon nanotubes-gated carbon nanotube field-effect transistors," *Applied Physics Letters,* vol. 94, pp. 022101-3, 01/12/ 2009.

[88] M. Dragoman, D. Neculoiu, D. Dragoman, G. Deligeorgis, G. Konstantinidis, A. Cismaru*, et al.*, "Graphene for Microwaves," *Microwave Magazine, IEEE,* vol. 11, pp. 81-86, 2010.

[89] P. Avouris, "Molecular Electronics with Carbon Nanotubes," *Accounts of Chemical Research,* vol. 35, pp. 1026-1034, 2002.

[90] P. Bondavalli, P. Legagneux, and D. Pribat, "Carbon nanotubes based transistors as gas sensors: State of the art and critical review," *Sensors and Actuators B: Chemical,* vol. 140, pp. 304-318, 6/18/ 2009.

[91] Y. Wang and J. T. Yeow, "A review of carbon nanotubes-based gas sensors," *Journal of Sensors,* vol. 2009, 2009.

[92] K. Kordas, G. Toth, P. Moilanen, M. Kumpumaki, J. Vahakangas, A. Uusimaki*, et al.*, "Chip cooling with integrated carbon nanotube microfin architectures," *Applied Physics Letters,* vol. 90, pp. 123105-3, 03/19/ 2007.

[93] J. Dijon, "Ultra High density carbon nanotubes for advanced interconnects and thermal management," Nano packaging workshop 2013.

[94] H. Bajwa, P. Patra, A. A. Ikram, and J. Mirza, "Nanostructured conformable patch antenna array," in *Information and Emerging Technologies (ICIET), 2010 International Conference on*, 2010, pp. 1-4.

[95] A. C. Patel, M. P. Vaghela, H. Bajwa, and H. Seddik, "Conformable patch antenna design for remote health monitoring," in *Applications and Technology Conference (LISAT), 2010 Long Island Systems*, 2010, pp. 1-6.

[96] Z. Yijun, Y. Bayram, D. Feng, D. Liming, and J. L. Volakis, "Polymer-Carbon Nanotube Sheets for Conformal Load Bearing Antennas," *Antennas and Propagation, IEEE Transactions on,* vol. 58, pp. 2169-2175, 2010.

[97] J. Weldon, K. Jensen, and A. Zettl, "Nanomechanical radio transmitter," *physica status solidi (b),* vol. 245, pp. 2323-2325, 2008.

[98] K. Jensen, J. Weldon, H. Garcia, and A. Zettl, "Nanotube Radio," *Nano Letters,* vol. 7, pp. 3508-3511, 2007/11/01 2007.

[99] C. B. Sébastien Pacchini, Emmanuel Flahaut, Dominique Baillargeat, Tay Beng Kang, "Fabrication developing and impact of CNTs inks on RF Resonator on paper," *MRS (not published yet),* 2013.

[100] L. Hoseon, G. Shaker, K. Naishadham, S. Xiaojuan, M. McKinley, B. Wagner*, et al.*, "Carbon-Nanotube Loaded Antenna-Based Ammonia Gas Sensor," *Microwave Theory and Techniques, IEEE Transactions on,* vol. 59, pp. 2665-2673, 2011.

[101] A. Naeemi and J. D. Meindl, "Performance Modeling for Single- and Multiwall Carbon Nanotubes as Signal and Power Interconnects in Gigascale Systems," *Electron Devices, IEEE Transactions on,* vol. 55, pp. 2574-2582, 2008.

[102] P. Saraswat, "http://www.stanford.edu/class/ee311/NOTES/Interconnect_Scaling.pdf," ed.

[103] Y. Awano, S. Sato, M. Nihei, T. Sakai, Y. Ohno, and T. Mizutani, "Carbon Nanotubes for VLSI: Interconnect and Transistor Applications," *Proceedings of the IEEE,* vol. 98, pp. 2015-2031, 2010.

[104] A. K. Mizuhisa Nihei, Motonobu Sato, Tatsuhiro Nozue, Takashi Hyakushima, Daiyu Kondo, Mari Ohfuti, Shintaro Sato and Yuji Awano *Carbon Nanotube Interconnect Technologies for Future LSIs, Solid State Circuits Technologies,*, 2010.

[105] L. Zhengchun, C. Lijie, S. Kar, P. M. Ajayan, and L. Jian-Qiang, "Fabrication and Electrical Characterization of Densified Carbon Nanotube Micropillars for IC Interconnection," *Nanotechnology, IEEE Transactions on,* vol. 8, pp. 196-203, 2009.

[106] D. Jiang, T. Wang, S. Chen, L. Ye, and J. Liu, "Paper-mediated controlled densification and low temperature transfer of carbon nanotube forests for electronic interconnect application," *Microelectron. Eng.,* vol. 103, pp. 177-180, 2013.

[107] A. Ceyhan and A. Naeemi, "Cu Interconnect Limitations and Opportunities for SWNT Interconnects at the End of the Roadmap," *Electron Devices, IEEE Transactions on,* vol. 60, pp. 374-382, 2013.

[108] W. Wen, S. Krishnan, L. Ke, S. Xuhui, R. Wu, T. Yamada*, et al.*, "Extracting Resistances of Carbon Nanostructures in Vias," in *Microelectronic Test Structures, 2009. ICMTS 2009. IEEE International Conference on*, 2009, pp. 27-30.

[109] J.-H. Ting, C.-C. Chiu, and F.-Y. Huang, "Carbon nanotube array vias for interconnect applications," *Journal of Vacuum Science & Technology B: Microelectronics and Nanometer Structures,* vol. 27, pp. 1086-1092, 2009.

[110] S. Sangsub, K. Youngmin, M. Jimin, L. Heeseok, K. Youngwoo, and S. Kwang-Seok, "A Millimeter-Wave System-on-Package Technology Using a Thin-Film Substrate With a Flip-Chip Interconnection," *Advanced Packaging, IEEE Transactions on,* vol. 32, pp. 101-108, 2009.

[111] L. H. Hsu, C. W. Oh, W. C. Wu, E. Y. Chang, H. Zirath, C. T. Wang*, et al.*, "Design, Fabrication, and Reliability of Low-Cost Flip-Chip-On-Board Package for Commercial Applications up to 50 GHz," *Components, Packaging and Manufacturing Technology, IEEE Transactions on,* vol. PP, pp. 1-1, 2012.

[112] W. Heinrich, "The flip-chip approach for millimeter wave packaging," *Microwave Magazine, IEEE,* vol. 6, pp. 36-45, 2005.

[113] R. Tummala, *Microsystem Packaging*, 2001.

[114] N. Jae-Woong, C. Kai, J. O. Suh, and K. N. Tu, "Electromigration Study in Flip Chip Solder Joints," in *Electronic Components and Technology Conference, 2007. ECTC '07. Proceedings. 57th*, 2007, pp. 1450-1455.

[115] M. Chhowalla, K. B. K. Teo, C. Ducati, N. L. Rupesinghe, G. A. J. Amaratunga, A. C. Ferrari*, et al.*, "Growth process conditions of vertically aligned carbon nanotubes using plasma enhanced chemical vapor deposition," *Journal of Applied Physics,* vol. 90, pp. 5308-5317, 2001.

[116] . *International Technology Roadmap for Semiconductors - Assembly & Packaging*. Available: http://www.itrs.net/Links/2009ITRS/2009Chapters_2009Tables/2009_Assembly.pdf

[117] R. Tummala, C. P. Wong, and P. Markondeya Raj, "Nanopackaging research at Georgia Tech," *Nanotechnology Magazine, IEEE,* vol. 3, pp. 20-25, 2009.

[118] S. Hermann, B. Pahl, R. Ecke, S. E. Schulz, and T. Gessner, "Carbon nanotubes for nanoscale low temperature flip chip connections," *Microelectronic Engineering,* vol. 87, pp. 438-442, 2010.

[119] A. Jentzsch and W. Heinrich, "Theory and measurements of flip-chip interconnects for frequencies up to 100 GHz," *Microwave Theory and Techniques, IEEE Transactions on,* vol. 49, pp. 871-878, 2001.

[120] I. Soga, D. Kondo, Y. Yamaguchi, T. Iwai, M. Mizukoshi, Y. Awano*, et al.*, "Carbon nanotube bumps for LSI interconnect," in *Electronic Components and Technology Conference, 2008. ECTC 2008. 58th*, 2008, pp. 1390-1394.

[121] S. Fan, M. G. Chapline, N. R. Franklin, T. W. Tombler, A. M. Cassell, and H. Dai, "Self-Oriented Regular Arrays of Carbon Nanotubes and Their Field Emission Properties," *Science,* vol. 283, pp. 512-514, January 22, 1999 1999.

[122] H. Jun and C. WonBong, "Controlled growth and electrical characterization of bent single-walled carbon nanotubes," *Nanotechnology,* vol. 19, p. 505601, 2008.

[123] A. Kumar, V. L. Pushparaj, S. Kar, O. Nalamasu, P. M. Ajayan, and R. Baskaran, "Contact transfer of aligned carbon nanotube arrays onto conducting substrates," *Applied Physics Letters,* vol. 89, pp. 163120-3, 2006.

[124] K. P. Yung, J. Wei, and B. K. Tay, "Formation and assembly of carbon nanotube bumps for interconnection applications," ***Diamond and Related Materials,*** **vol. 18, pp. 1109-1113, 2009.**

[125] M. Glickman, P. Tseng, J. Harrison, I. B. Goldberg, P. Johnson, P. Smeys*, et al.*, "CMOS-compatible back-end process for in-plane actuating ferromagnetic MEMS," in ***Solid-State Sensors, Actuators and Microsystems Conference, 2009. TRANSDUCERS 2009. International*****, 2009.**

[126] P. L. McEuen, M. S. Fuhrer, and H. Park, "Single-walled carbon nanotube electronics," ***Nanotechnology, IEEE Transactions on,*** **vol. 1, pp. 78-85, 2002.**

[127] S. Hofmann, C. Ducati, J. Robertson, and B. Kleinsorge, "Low-temperature growth of carbon nanotubes by plasma-enhanced chemical vapor deposition," ***Applied Physics Letters,*** **vol. 83, pp. 135-137, 07/07/ 2003.**

[128] M. Nessim Gd Fau - Seita, K. P. Seita M Fau - O'Brien, A. J. O'Brien Kp Fau - Hart, R. K. Hart Aj Fau - Bonaparte, R. R. Bonaparte Rk Fau - Mitchell, C. V. Mitchell Rr Fau - Thompson*, et al.*, "Low temperature synthesis of vertically aligned carbon nanotubes with electrical contact to metallic substrates enabled by thermal decomposition of the carbon feedstock," 20091014 DCOM- 20091222.

[129] B. Wang, X. Liu, H. Liu, D. Wu, H. Wang, J. Jiang*, et al.*, "Controllable preparation of patterns of aligned carbon nanotubes on metals and metal-coated silicon substrates," ***Journal of Materials Chemistry,*** **vol. 13, pp. 1124-1126, 2003.**

[130] B. K. TAY, Z. F. WANG, K. P. YUNG, and J. WEI, "EFFECTS OF UNDER CNT METALLIZATION LAYERS ON CARBON NANOTUBES GROWTH," ***Modern Physics Letters B,*** **vol. 22, pp. 1827-1836, 2008.**

[131] J. García-Céspedes, S. Thomasson, K. B. K. Teo, I. A. Kinloch, W. I. Milne, E. Pascual*, et al.*, "Efficient diffusion barrier layers for the catalytic growth of carbon nanotubes on copper substrates," ***Carbon,*** **vol. 47, pp. 613-621, 3// 2009.**

[132] N. Bertrand, B. Drevillon, A. Gheorghiu, C. Senemaud, L. Martinu, and J. E. Klemberg-Sapieha, "Adhesion improvement of plasma-deposited silica thin films on stainless steel substrate studied by x-ray photoemission spectroscopy and in situ infrared ellipsometry," ***Journal of Vacuum Science & Technology A: Vacuum, Surfaces, and Films,*** **vol. 16, pp. 6-12, 01/00/ 1998.**

[133] V. L. De Los Santos, D. Lee, J. Seo, F. L. Leon, D. A. Bustamante, S. Suzuki*, et al.*, "Crystallization and surface morphology of Au/SiO2 thin films following furnace and flame annealing," ***Surface Science,*** **vol. 603, pp. 2978-2985, 10/1/ 2009.**

[134] P. Wißmann and H.-U. Finzel, "The Effect of Annealing on the Electrical Resistivity of Thin Gold Films," in ***Electrical Resistivity of Thin Metal Films*****. vol. 223, ed: Springer Berlin Heidelberg, 2007, pp. 35-52.**

[135] V. L. von Arnim, J. Fessmann, and L. Psotta, "Plasma treatment of thin gold surfaces for wire bond applications," ***Surface and Coatings Technology,*** **vol. 116–119, pp. 517-523, 9// 1999.**

[136] D. Basa, "Plasma treatment studies of MIS devices," ***Central European Journal of Physics,*** **vol. 8, pp. 400-407, 2010/06/01 2010.**

[137] D. Takagi, Y. Homma, H. Hibino, S. Suzuki, and Y. Kobayashi, "Single-Walled Carbon Nanotube Growth from Highly Activated Metal Nanoparticles," ***Nano Letters,*** **vol. 6, pp. 2642-2645, 2006/12/01 2006.**

[138] A. Cao, X. Zhang, C. Xu, J. Liang, D. Wu, and B. Wei, "Synthesis of well-aligned carbon nanotube network on a gold-patterned quartz substrate," ***Applied Surface Science,*** **vol. 181, pp. 234-238, 9/21/ 2001.**

[139] S. Bhaviripudi, E. Mile, S. A. Steiner, A. T. Zare, M. S. Dresselhaus, A. M. Belcher*, et al.*, "CVD Synthesis of Single-Walled Carbon Nanotubes from Gold Nanoparticle Catalysts," ***Journal of the American Chemical Society,*** **vol. 129, pp. 1516-1517, 2007/02/01 2007.**

[140] Y. ZHANG, R. LI, H. LIU, X. SUN, MEREL, #160*, et al.*, ***Integration and characterization of aligned carbon nanotubes on metal/silicon substrates and effects of water*** **vol. 255. Amsterdam, PAYS-BAS: Elsevier, 2009.**

[141] M. S. Dresselhaus, G. Dresselhaus, R. Saito, and A. Jorio, "Raman spectroscopy of carbon nanotubes," ***Physics Reports,*** **vol. 409, pp. 47-99, 2005.**

[142] K. Sun X Fau - Li, R. Li K Fau - Wu, P. Wu R Fau - Wilhite, T. Wilhite P Fau - Saito, J. Saito T Fau - Gao, C. Y. Gao J Fau - Yang*, et al.*, "The effect of catalysts and underlayer metals on the properties of PECVD-grown carbon nanostructures," 20091221 DCOM- 20100225.

[143] G. D. Nessim, D. Acquaviva, M. Seita, K. P. O'Brien, and C. V. Thompson, "The Critical Role of the Underlayer Material and Thickness in Growing Vertically Aligned Carbon Nanotubes and Nanofibers on Metallic Substrates by Chemical Vapor Deposition," ***Advanced Functional Materials,*** **vol. 20, pp. 1306-1312, 2010.**

[144] S. Fan and Y. Chan, "Effect of misalignment on electrical characteristics of ACF joints for flip chip on flex applications," ***Microelectronics Reliability,*** **vol. 42, pp. 1081-1090, 2002.**

[145] J.-B. Kim, S.-J. Kong, S.-Y. Lee, J.-H. Kim, H.-R. Lee, C.-D. Kim*, et al.*, "Characteristics of nitrogen-doped carbon nanotubes synthesized by using PECVD and Thermal CVD," ***Journal of the Korean Physical Society,*** **vol. 60, pp. 1124-1128, 2012/04/01 2012.**

[146] T. Susi, A. Kaskela, Z. Zhu, P. Ayala, R. Arenal, Y. Tian*, et al.*, "Nitrogen-Doped Single-Walled Carbon Nanotube Thin Films Exhibiting Anomalous Sheet Resistances," ***Chemistry of Materials,*** **vol. 23, pp. 2201-2208, 2011/04/26 2011.**

[147] C. C. Yap, D. Tan, C. Brun, E. H. T. Teo, J. Wei, D. Baillargeat*, et al.*, "Characterization of Novel CNT to CNT Joining Interconnections Implemented for 1st Level Flip Chip Packaging " presented at the Electronics Packaging Technology Conference, Singapore, 2011.

[148] G.-H. Jeong, N. Olofsson, L. K. L. Falk, and E. E. B. Campbell, "Effect of catalyst pattern geometry on the growth of vertically aligned carbon nanotube arrays," ***Carbon,*** **vol. 47, pp. 696-704, 3// 2009.**

[149] BERBER, #160, Savas, KWON, #160, Young-Kyun*, et al.*, ***Bonding and energy dissipation in a nanohook assembly*** **vol. 91. Ridge, NY, ETATS-UNIS: American Physical Society, 2003.**

[150] M. S. Fuhrer, J. Nygård, L. Shih, M. Forero, Y.-G. Yoon, M. S. C. Mazzoni*, et al.*, "Crossed Nanotube Junctions," ***Science,*** **vol. 288, pp. 494-497, April 21, 2000 2000.**

[151] H. Li, L. Wan Khai, Q. Zhang, and S. F. Yoon, "Physical device modeling of carbon nanotube/GaAs photovoltaic cells," ***Applied Physics Letters,*** **vol. 96, pp. 043501-043501-3, 2010.**

[152] A. Bachtold, C. Strunk, J.-P. Salvetat, J.-M. Bonard, L. Forro, T. Nussbaumer*, et al.*, "Aharonov-Bohm oscillations in carbon nanotubes," ***Nature,*** **vol. 397, pp. 673-675, 02/25/print 1999.**

[153] H. Li, Q. Zhang, and J. Li, "Interpretation of Coulomb oscillations in carbon-nanotube-based field-effect transistors," *Physical Review B,* vol. 73, p. 235431, 06/27/ 2006.

[154] M. Nihei, A. Kawabata, D. Kondo, M. Horibe, S. Sato, and Y. Awano, "Electrical properties of carbon nanotube bundles for future via interconnects," *Japanese journal of applied physics,* vol. 44, p. 1626, 2005.

[155] W. Wei-Cheng, E. Y. Chang, H. Ruey-Bing, H. Li-Han, H. Chen-Hua, C. Karnfelt*, et al.*, "Design, Fabrication, and Characterization of Novel Vertical Coaxial Transitions for Flip-Chip Interconnects," *Advanced Packaging, IEEE Transactions on,* vol. 32, pp. 362-371, 2009.

[156] C. C. Yap, D. Tan, C. Brun, H. Li, E. H. T. Teo, D. Baillargeat*, et al.*, "Impact of the CNT growth process on gold metallization dedicated to RF interconnect applications," *International Journal of Microwave and Wireless Technologies,* vol. FirstView, pp. 1-7, 2010.

[157] C. Brun, P. Franck, C. Yap Chin, T. Dunlin, E. T. H. Tong, S. Bila*, et al.*, "Hybrid EM/circuit modeling for carbon nanotubes based interconnects," in *Electronics Packaging Technology Conference (EPTC), 2011 IEEE 13th*, 2011, pp. 158-162.

[158] K. Hocheol, K. Haixin, T. Hubing, and L. Byoung Hwa, "Inductance calculations for advanced packaging in high-performance computing," in *Electromagnetic Compatibility, 2008. EMC 2008. IEEE International Symposium on*, 2008, pp. 1-4.

[159] D. Marc, S. V. Rotkin, and N. R. Aluru, "Calculation of pull-in voltages for carbon-nanotube-based nanoelectromechanical switches," *Nanotechnology,* vol. 13, p. 120, 2002.

[160] T. Ricart, *Etude de nano-systèmes électro-mécaniques (NEMS) à base de nanotubes de carbone pour applications hyperfréquences*, 2008.

[161] J. Lennard-Jones, "Perturbation problems in quantum mechanics," *Proceedings of the Royal Society of London. Series A,* vol. 129, pp. 598-615, 1930.

[162] L. Girifalco, M. Hodak, and R. S. Lee, "Carbon nanotubes, buckyballs, ropes, and a universal graphitic potential," *Physical Review B,* vol. 62, p. 13104, 2000.

[163] J. D. Jackson and R. F. Fox, "Classical electrodynamics," *American Journal of Physics,* vol. 67, p. 841, 1999.

[164] K. Boustedt, "GHz flip chip-an overview," in *Electronic Components & Technology Conference, 1998. 48th IEEE*, 1998, pp. 297-302.

[165] S. Beer, B. Ripka, S. Diebold, H. Gulan, C. Rusch, P. Pahl*, et al.*, "Design and measurement of matched wire bond and flip chip interconnects for D-band system-in-package applications," in *Microwave Symposium Digest (MTT), 2011 IEEE MTT-S International*, 2011, pp. 1-4.

[166] A. Nojeh, P. Pande, A. Ganguly, S. Sheikhaei, B. Belzer, and A. Ivanov, "Reliability of wireless on-chip interconnects based on carbon nanotube antennas," in *Mixed-Signals, Sensors, and Systems Test Workshop, 2008. IMS3TW 2008. IEEE 14th International*, 2008, pp. 1-6.

[167] A. W. Topol, D. C. L. Tulipe, L. Shi, D. J. Frank, K. Bernstein, S. E. Steen*, et al.*, "Three-dimensional integrated circuits," *IBM Journal of Research and Development,* vol. 50, pp. 491-506, 2006.

[168] **Y. Wang, Q. Wu, W. Shi, X. He, X. Sun, and T. Gui, "Radiation Properties of Carbon Nanotubes Antenna at Terahertz/Infrared Range,"** ***International Journal of Infrared and Millimeter Waves,*** **vol. 29, pp. 35-42, 2008/01/01 2008.**

[169] **MAKSIMENKO, #160, S. A., SLEPYAN, #160, G. Ya.,** ***et al.*****,** ***Carbon nanotube antenna : Far-field, near-field and thermal-noise properties*****. Amsterdam, PAYS-BAS: Elsevier, 2008.**

[170] **K. Kempa, J. Rybczynski, Z. Huang, K. Gregorczyk, A. Vidan, B. Kimball,** ***et al.*****, "Carbon Nanotubes as Optical Antennae,"** ***Advanced Materials,*** **vol. 19, pp. 421-426, 2007.**

[171] **Y. Wang, K. Kempa, B. Kimball, J. B. Carlson, G. Benham, W. Z. Li,** ***et al.*****, "Receiving and transmitting light-like radio waves: Antenna effect in arrays of aligned carbon nanotubes,"** ***Applied Physics Letters,*** **vol. 85, pp. 2607-2609, 2004.**

[172] **A. Nojeh and A. Ivanov, "Wireless Interconnect and the Potential for Carbon Nanotubes,"** ***Design & Test of Computers, IEEE,*** **vol. 27, pp. 44-53, 2010.**

[173] **G. Y. Slepyan, M. V. Shuba, S. A. Maksimenko, and A. Lakhtakia, "Theory of optical scattering by achiral carbon nanotubes and their potential as optical nanoantennas,"** ***Physical Review B,*** **vol. 73, p. 195416, 05/18/ 2006.**

[174] **M. C. F. Chang, V. P. Roychowdhury, Z. Liyang, S. Hyunchol, and Q. Yongxi, "RF/wireless interconnect for inter- and intra-chip communications,"** ***Proceedings of the IEEE,*** **vol. 89, pp. 456-466, 2001.**

[175] **G. W. Hanson, "A Common Electromagnetic Framework for Carbon Nanotubes and Solid Nanowires—Spatially Dispersive Conductivity, Generalized Ohm's Law, Distributed Impedance, and Transmission Line Model,"** ***Microwave Theory and Techniques, IEEE Transactions on,*** **vol. 59, pp. 9-20, 2011.**

[176] **P. J. Burke, L. Shengdong, and Y. Zhen, "Quantitative theory of nanowire and nanotube antenna performance,"** ***Nanotechnology, IEEE Transactions on,*** **vol. 5, pp. 314-334, 2006.**

[177] **G. W. Hanson, "Current on an infinitely-long carbon nanotube antenna excited by a gap generator,"** ***Antennas and Propagation, IEEE Transactions on,*** **vol. 54, pp. 76-81, 2006.**

[178] **P. F. C. Brun, L. Hong, P. Coquet, D. Baillargeat and B. K. Tay, "Monopole Antenna based on Carbon Nanotubes," presented at the Microwave Symposium Digest (MTT), Seattle, USA, 2013, 2013.**

[179] **Y. Liping and G. Hanson, "Wave propagation channels for intra-chip wireless communication systems," in** ***Antennas and Propagation Society International Symposium, 2009. APSURSI '09. IEEE*****, 2009, pp. 1-4.**

[180] **Yong-Kyu Yoon, Bo Pan, Peter Kirby, John Papapolymerou, Manos Tentzeris, and M. G. Allen, "Surface micromachined electromagnetically radiating RF MEMS," presented at the Tech. Dig. Solid-State Sensor, Actuator, and MicrosystemsWorkshop (Hilton Head 2004), June 2004. .**

[181] **C. Sangjo and K. Sarabandi, "Performance Assessment of Bundled Carbon Nanotube for Antenna Applications at Terahertz Frequencies and Higher,"** ***Antennas and Propagation, IEEE Transactions on,*** **vol. 59, pp. 802-809, 2011.**

[182] **H. Yi, Y. Wen-Yan, and L. Qing Huo, "Performance Prediction of Carbon Nanotube Bundle Dipole Antennas,"** ***Nanotechnology, IEEE Transactions on,*** **vol. 7, pp. 331-337, 2008.**

[183] P. Franck, D. Baillargeat, and B. K. Tay, "Trade-offs in designing antennas from bundled carbon nanotubes," in *Microwave Symposium Digest (MTT), 2012 IEEE MTT-S International*, 2012, pp. 1-3.

[184] P. Franck, D. Baillargeat, and B. K. Tay, "Performance assessment of optimized carbon-nanotube-based wireless on-chip communication," pp. 84620B-84620B, 2012.

[185] C. E. Smith and E. M. Johnson, "Performance of Short Antennas," *Proceedings of the IRE,* vol. 35, pp. 1026-1038, 1947.

[186] P. Bo, Y. Yoon, J. Papapolymerou, M. M. Tentzeris, and M. G. Allen, "Design and fabrication of substrate-independent integrated antennas utilizing surface micromachining technology," in *Microwave Conference Proceedings, 2005. APMC 2005. Asia-Pacific Conference Proceedings*, 2005, p. 4 pp.

Appendix

Matlab code for the determination of the bump inductance and capacitance:

```
%Constantes

mu0 = 1.25663706E-6;
vF = 9.7E5;
e = 1.60217646E-19;
h = 6.626068E-34;

haut = 20E-6;
NCNT = 135000;
sigmaAu = 4.1E7;

Lk = h./(2.*e.*e.*vF);

%Calcul distance entre bump signal et ground en fonction du rayon

    r = 1:0.1:100;
    S = 163E-6 + (75-r).*1E-6;

    %BUMP EN OR

        %Calcul de Resistance R et Inductance Lm du bump

        R = 2.*haut./(sigmaAu.*pi.*r.*1E-6.*r.*1E-6);
        Lm = ((mu0)./(2.*pi)) .* log (S./(r.*1E-6));

    %BUMP CNT

    LkCNT = Lk.*haut./NCNT;

    RC = zeros(1,20);

        for i=1:1:20

        RCNT = 20E3.*haut.*1E6./NCNT;
        RC(1,i) = RCNT;

        subplot (2,1,2), plot(r,RCNT);
        hold all

        NCNT=NCNT + 1E5;

        end

%Graphs

subplot (2,1,2),plot(r,R);
title ('Resistance')

subplot (2,1,1), plot(r,Lm, 'LineWidth',4);
hold all
subplot (2,1,1), plot(r,LkCNT,'LineWidth',4);
title ('Inductance')
```

Appendix 1

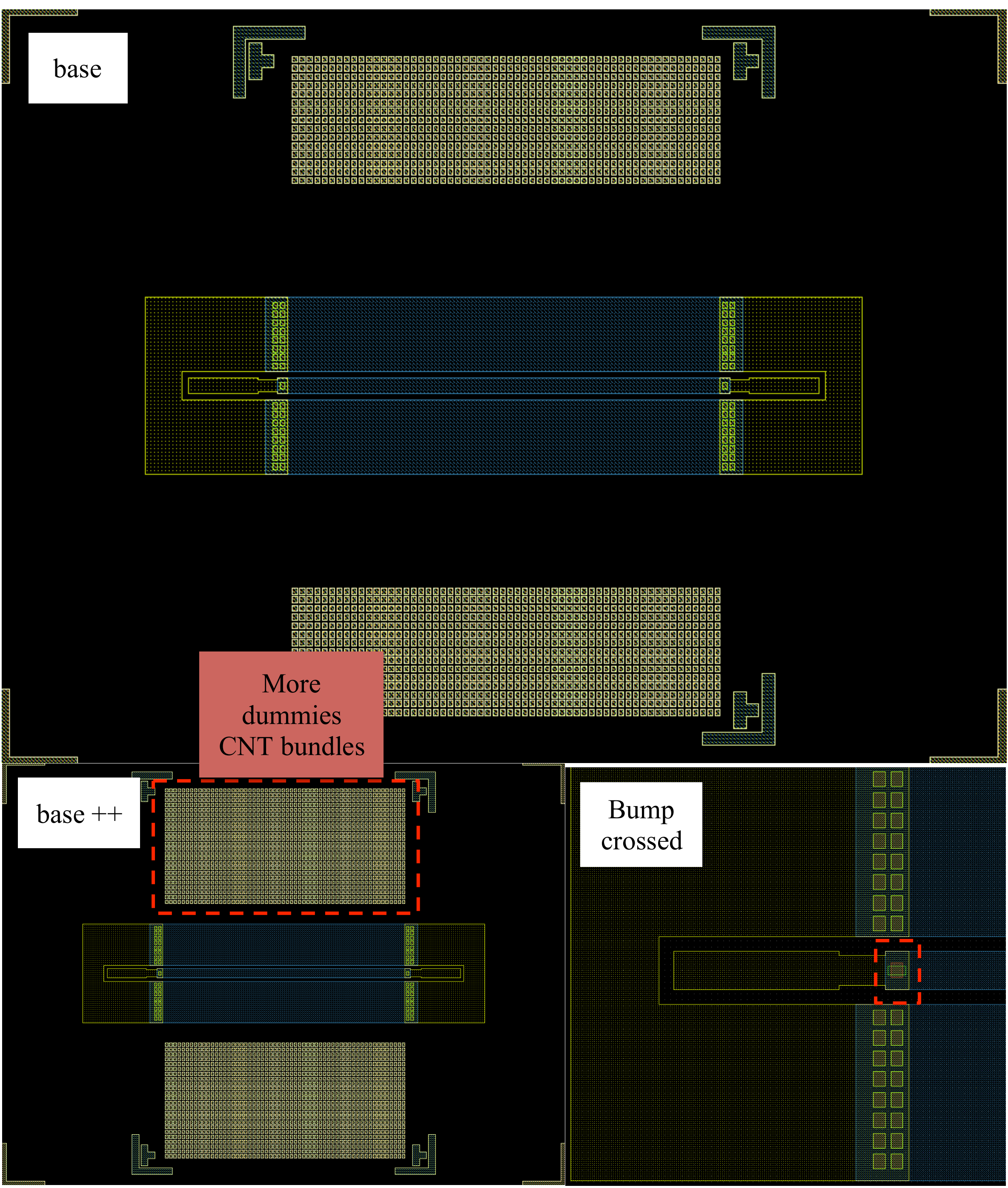

(a) Top view of the flip-chip device composed by 20 µm CNT bundle size. The yellow parts represent the PCB and the blue parts represent the chip. All other colors parts are on the two sides of the flip-chip. (b) is the same flip-chip configuration with more dummies CNT bundles on each sides. (c) shows the crossed bundles configuration with a zoom in the interconnections.

Appendix 2

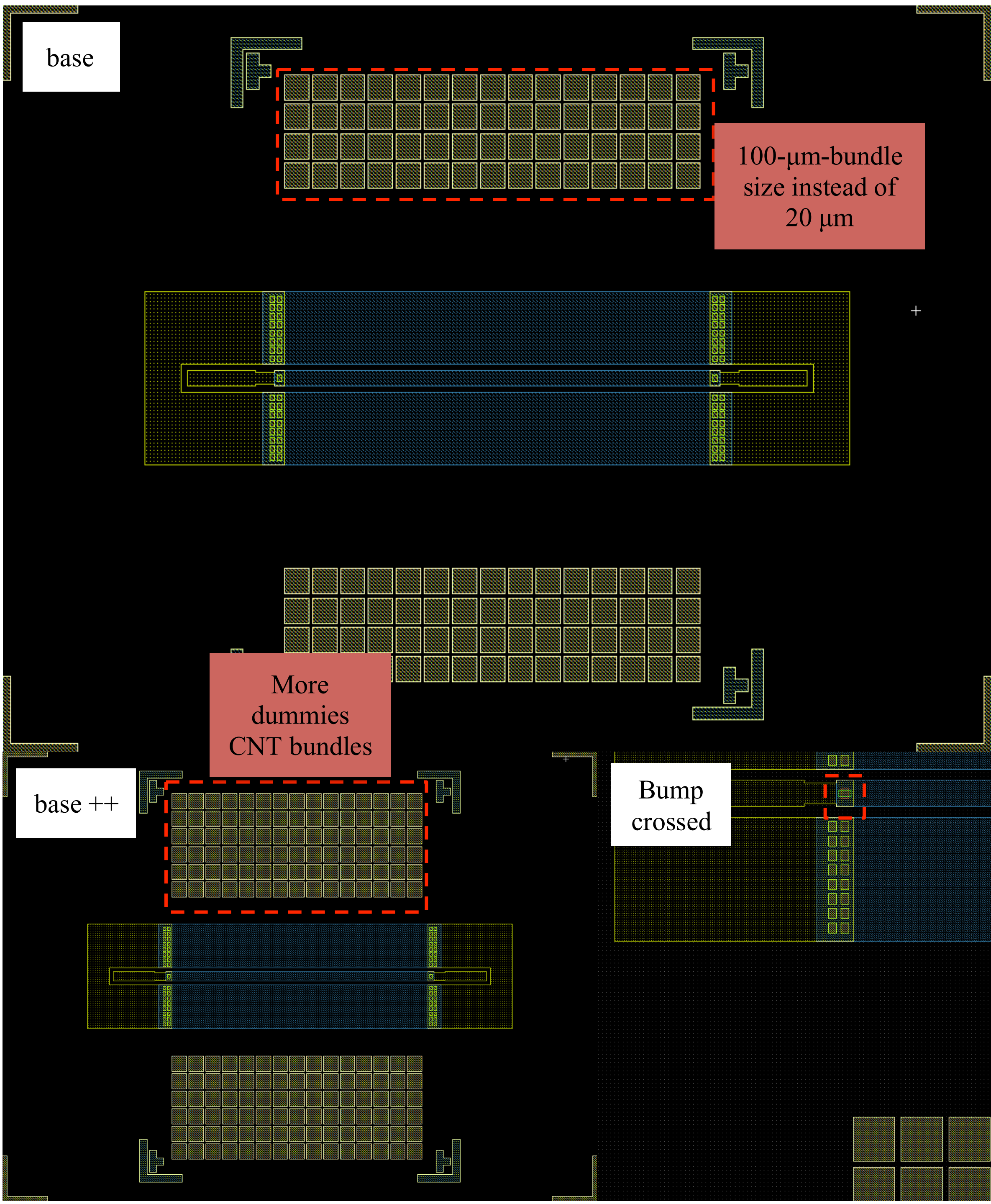

(a) Top view of the flip-chip device composed by 20 µm CNT bundle size for signal and ground and 100 µm CNT bundle size for dummies in order to increase the mechanical strength between the two parts. The yellow parts represent the PCB and the blue parts represent the chip. All other colors parts are on the two sides of the flip-chip. (b) is the same flip-chip configuration with more dummies CNT bundles on each sides. (c) shows the crossed bundles configuration with a zoom in the interconnections.

Appendix 3

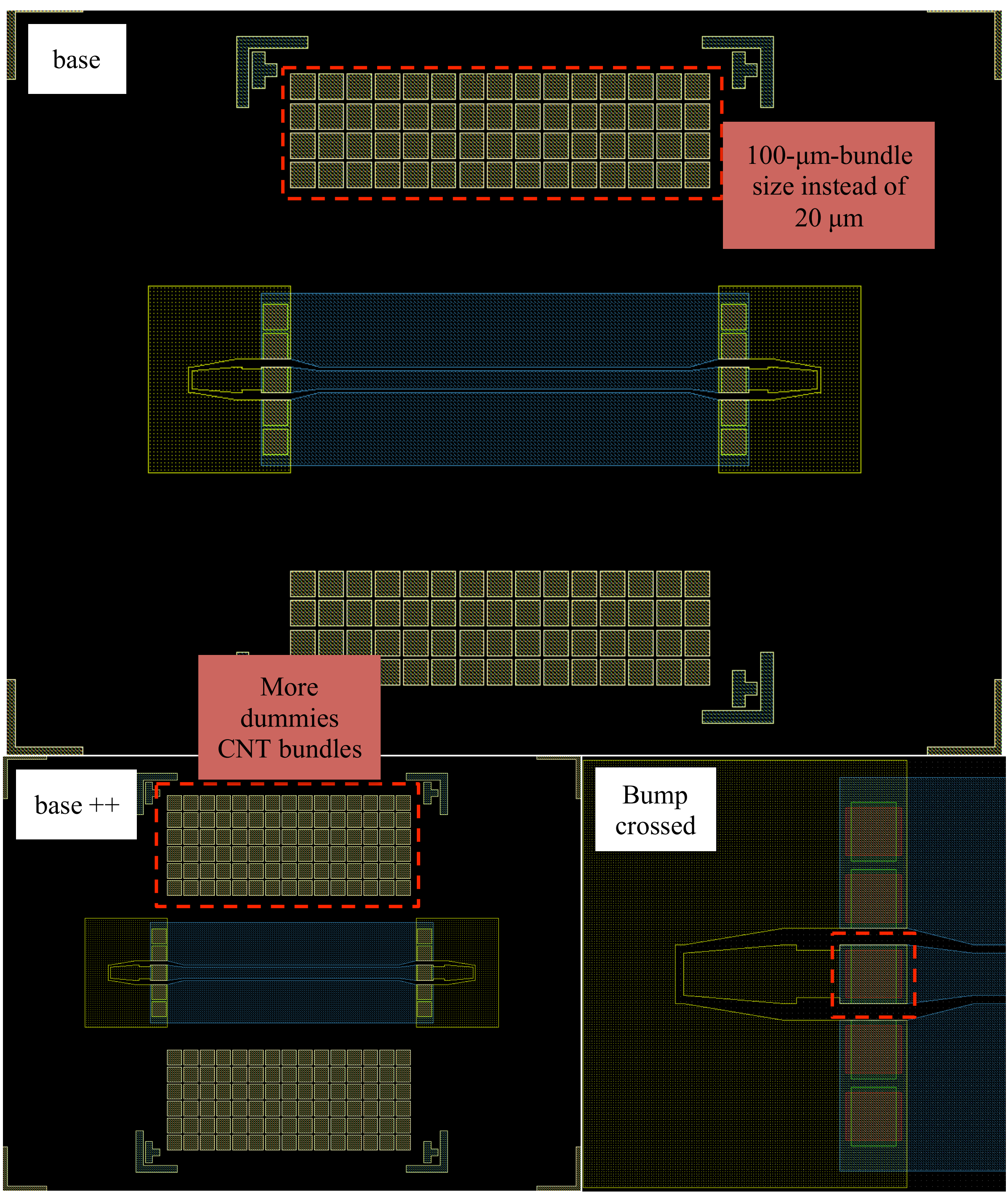

(a) Top view of the flip-chip device composed by 100 µm CNT bundle size. The yellow parts represent the PCB and the blue parts represent the chip. All other colors parts are on the two sides of the flip-chip. Matching parts are also visible. (b) is the same flip-chip configuration with more dummies CNT bundles on each sides. (c) shows the crossed bundles configuration with a zoom in the interconnections.

Appendix 4

Matlab code for the determination of the Van der Waals and electrostatic forces:

```
%Definition des variables

    %Rayon du nanotube
    Rin = 25;
    Rout = 50;
    R = Rout;

    %Longueur du nanotube
    L = 20e-6;

    %Nombre de bundle
    Nbundle = 58;

    %Voltage
    voltage = 0.1;

%Definition des constantes
    C6 = 15.2e-6;
    sig = 38;
    eps0 = 8.854e-3;

%----------------------------------

%Calcul de la force de VDW

i=2;
V = zeros (1000, 20);
E = zeros (1000, 20);

for Nconnection = 10000:10000:500000;
%for Nconnection = 1:1:20;

NCNT = Nconnection*Nbundle;
V(1,i) = NCNT;
E(1,i) = NCNT;

n = 2;

    for d = 1:1:1000;

        %Calcul de la force de VDW

        F = 
((C6*sig.^2*pi.^2*R.*sqrt(d.*(d+2*R))).*(8.*d.^4+32*R.*d.^3+72*R.^2.*d.^2+8
0*R.^3.*d+35*R.^4))./(2.*d.^5.*(d+2*R).^5);

        FV = F*NCNT*L;

        V(n,1) = d;
        V(n,i) = FV;

        %Calcul de la force electrostatique
```

```
        F = 
(pi*eps0*voltage.^2)/(R*sqrt((d.*(d+2*R)/R.^2).*(log(1+d./R+sqrt((d.*(d+2*R
)/R.^2)))).^2));

        FE = F*NCNT*L;

        E(n,1) = d;
        E(n,i) = FE;

        n = n+1;

    end

i = i+1;

end

%Poids du systeme


g = 9.81;
masse = 16.5E-6;

P = masse*g;

%Graphiques

loglog(E(2:1001,1),E(2:1001,2));
hold all
loglog(V(2:1001,1),V(2:1001,2));
loglog(V(2:1001,1),V(2:1001,2)+E(2:1001,2));
loglog(V(2:1001,1),V(2:1001,11)+E(2:1001,11));
loglog(E(2:1001,1),P);
```

Table of figures

Figure 1: carbon allotropes: diamond (a), graphite (b), lonsdaleite (c), fullerenes (C60 (d), C540 (e), C70 (f)), amorphous carbon (g), carbon nanotube (h). 9
Figure 2: The different allotropes structures from carbon atoms. Different dimensionalities can be obtained from 1-D structure such as (d) and (e) to 3-D with (a) and (b). (c) is 2-D and (f) is 0-D. (a) is the diamond, (b) is the graphite, (c) is the graphene, (d) is a single-wall carbon nanotube and (e) is a nanoribbon. Source: [2].. 15
Figure 3: On (a), definition of the chirality vector Ch represented on a graphene mesh structure. On (b), the three different configurations, which can be encountered: "A" represents the armchair configuration, "B" the zig-zag configuration and "C" a random chiral configuration. Source: [4] 16
Figure 4: SWCNT with a (6,0) chirality. 18
Figure 5: On left, E-k dispersion diagram of a metallic CNT. On right, E-k dispersion diagram of a SC CNT with a visible band gap between the conduction and valance bands. Source: [2] 19
Figure 6: On the left, a representation of a single-wall carbon nanotube and a multi-wall NT. Transmission electron microscope (TEM) image of MWCNTs with several numbers of shell. Source: [1] 20
Figure 7: Representation of the periodical boundaries in carbon nanotubes with the hexagonal arrangement of carbon atoms. E-k dispersion diagram is also represented. 21
Figure 8: Band structure of a multi-wall carbon nanotube. Source: [11]................................ 22
Figure 9: Number of conducting channel in function of the CNT diameter. With SWCNTs with diameter always below 10 nm, the number of conducting channel remains 2 (see equation (5)). 23
Figure 10: TEM images of DWCNTs fabricated at CINTRA by Chow Wai Leong.............. 24
Figure 11: MWCNF versus MWCNT according to the delta angle representing the angle between carbon nanotube shells. Source: [15] 24
Figure 12: The two possible spin states for an electron (spin up and spin down). Magnetic field direction is changing with the spin. 26
Figure 13: On top, the diffusive electron conduction in a 3-D material and the corresponding material electrical resistance definition. Below, the anisotropic ballistic transport of the electron existing in 1-D material such as carbon nanotube. In this case, the equation of R is still unknown. R is the material resistance, L is the material length, W is the material width and ρ is the material electrical resistivity. Source: [3] 27
Figure 14: Single-wall carbon nanotube bended at 0, 30, 45 and 60°. We can see the deformation of the structure, which decreases the electrical performance of the carbon nanotube. Source: [37] 31
Figure 15: Arc discharge method principle to grow CNTs.. 32
Figure 16: Laser ablation method principle to grow CNTs. 34
Figure 17: Chemical Vapor Deposition (CVD) process principle. The central tube, which is surrounded by a furnace, is the CNT growth location. 36
Figure 18: Melting points of several metallic particles (Fe, Ni, Au and Ag) in function of their diameter. Iron presents the higher melting point with particle diameter above 30 nm. Source: [46] 38
Figure 19: Ebeam principle for metal deposition on substrate... 39
Figure 20: Effects of the catalyst layer roughness on the CNT growth by CVD. Source: [48]41

Figure 21: Top (a) and bottom (b) carbon nanotube growth mechanisms. The carbon atoms diffusion into the catalyst adopts a different path according to the type of CNT growth. Source: [46] 42
Figure 22: On left, bamboo type of CNT with intermediate layer of carbon nanotubes along the carbon nanotube. On right, straight-like CNT with particles of catalyst inside the CNT structure. Source: [49] 43
Figure 23: Bottom and top growth of carbon nanotube. Source: [15] 44
Figure 24: Representation of the surface diffusion of carbon atoms on a catalyst particle. On (i), the single carbon atoms diffuse on the surface in order to form the carbon nanotube network in a hexagonal arrangement (ii and iii). Source: [46] 47
Figure 25: Bundle of MWCNTs grown by thermal CVD in CINTRA/Nanyang Technological University associated to the group of Prof Tay Beng Kang composed by Li Hong, Chow Wai Leong, Yap Chin Chong and Dunlin Tan. 48
Figure 26: Schematic of the PECVD setup. Source: [15] 50
Figure 27: Bundle of carbon nanotubes grown by PECVD. The CNTs are vertically aligned in the direction of the plasma. Source: [15] 51
Figure 28: Vertically aligned MWCNT bundle fabricated by PECVD in CINTRA/Nanyang Technological University associated to the group of Prof Tay Beng Kang composed by Li Hong, Chow Wai Leong, Yap Chin Chong and Dunlin Tan. 53
Figure 29: Schematic circuit of a carbon nanotube model in DC. 58
Figure 30: Contact resistance Rc in function of the CNT diameter. Source: [63, 66] 59
Figure 31: Transmission line model of a single-wall carbon nanotube in parallel above a ground plane. The model is composed by distributed RLC components. 62
Figure 32: MWCNT circuit model based on RLC transmission line models. Additional coupling effects between MWCNT shells are considered. Source: [11] 65
Figure 33: MWCNT bundle grown by PECVD process at CINTRA. CNTs appear to be quite uniform in term of length and diameter. 66
Figure 34: Schematic illustrating the process flow from the synthesis of CNTs to the fabricated CPW GSG structures. (a) Patterned deposition of catalyst and barrier layer line array. (b) Growth of VACNTs line array by TCVD process. (c) Realization of ultra-dense HACNTs film by planarization using IPA. (d) Patterning of ultra-dense HACNTs film by O_2 plasma etching. (e) Patterned metallization for final CPW GSG structures. 69
Figure 35: (a) Schematic of CPW GSG structure with 125 nm thick HACNTs film with variation in length and width. (b) Typical SEM image of CPW GSG structure with 20-µm HACNTs film width, inset shows that overlap between metal-to-CNTs is well defined. 70
Figure 36: DC resistance vs. length of CNTs for three different widths of HACNTs film. 71
Figure 37: ADS schematic of the GSG structure presented in Figure 35 and composed by HACNTs. Each box models 1-µm length bundle of DWCNTs as detailed on Figure 38. 73
Figure 38: Circuit model of the bundle of CNT. A distributed RLC circuit with quantum components as the kinetic inductance L_k and the quantum capacitance C_Q compose this model. On both side, a contact resistance R_C in parallel with a contact capacitance C_C models the CNT/metal contacts. 73
Figure 39: S parameters of HACNT structure (presented in Figure 35 and in the asset (top view)) for a 20-µm-width bundle of CNT. By increasing the gap between electrodes, S_{21} transmission is decreasing. 74
Figure 40: Carbon nanotube in a transmission line configuration. L is the CNT length and h' the distance between the SWCNT and the ground plane. The SWCNT is considered with a circular shape. 77
Figure 41: S-parameters of 10 and 20 µm length single-wall carbon nanotube in transmission line configuration. 79

Figure 42: DWCNT design on HFSS. A metallic box links the two DWCNT shells at the extremities. 79
Figure 43: The three bundle configurations (in 2D on the first schematic and in 3D in the others) composed by 3 SWCNTs with a 10-μm length........ 81
Figure 44: Circuit representations of the three configurations L1, L2 and L3. C_{SS} represents the coupling capacitance between carbon nanotubes. (No analytical modeling or simulation have been done for this study)........ 82
Figure 45: S_{21} parameters of 10 μm length single-wall carbon nanotube bundle in transmission line configuration with different distance between CNTs (1, 10 and 20 nm). S-parameters results for the 3 configurations L1, L2 and L3........ 84
Figure 46: On a), EM model of the bundle composed by 21 SWCNTs. On b), equivalent circuit model of the SWCNT bundle with coupling capacitance between nanotubes; each box is a 1-μm single-wall carbon nanotube transmission line (see Figure 31) as represented in the assets below. Only the first row has an electrostatic capacitance C_{ES} between the CNT and the ground plane. 86
Figure 47: S parameters of 1 μm length bundle of single-wall carbon nanotube in transmission line configuration. Solid lines: Circuit model – Dash lines: EM model. 87
Figure 48: (Left) Schematic representation of a top-gated CNTFET. (Right) Room-temperature output electrical characteristics of a 300-nm-long, top-gated CNTFET. Source: [89] 92
Figure 49: Sensing (gas) based on CNT FET transistor. Source: [90, 91]........ 92
Figure 50: Electromechanical switch devices consisting of three MWCNTs. Source: [40]........ 94
Figure 51: Level 1 and level 0 of interconnections. As we can see, level 1 connects the entire chip while the level 0 interconnections are smaller and only bond unique components together such as transistor. 96
Figure 52: Interconnections electrical conductivity as function of the length. Copper and CNTs based interconnections are compared. W is the width of the interconnection made by copper and D is the diameter of CNTs. Sources: [2, 7] 99
Figure 53: SEM images of each level of interconnections. Global interconnections are the biggest whereas local ones are the smallest. 100
Figure 54: Three interconnection configurations using carbon nanotube materials. On left, we have CNTs embedded in metal bump. Next, we have a combination of horizontally and vertically aligned CNT bundle. On right, a 160 nm diameter CNT bundle in via is presented. Source: [104] 101
Figure 55: The densification process steps and principle is visible on the top asset. Others SEM images show the effect of the densification process on carbon nanotubes bundles according to their size. On the bottom images, we can also see the effect of the solvent with several depth of penetration into the carbon nanotube bundle. Source: [105] 102
Figure 56: Wire bonding made by gold. 104
Figure 57: Schematic of a hot via interconnection........ 104
Figure 58: Growth of CNT bundles in vias. As we can see, the depth of the via is quite low (below 1 μm on the right SEM image) and CNTs growth is not really suitable for interconnect applications (images on the left). Source: [109] 105
Figure 59: On left, cross sectional schematic of CNTs via. Ni is used as catalyst and only 500 nm high via is expected. On right, CNT growth in via. Source: [109] 105
Figure 60: On the left SEM images, vias filled by CNT bundle before and after a densification process. On the right graph, a 4-probe measurements for 1 μm via filled by CNTs. A 10-kΩ resistance was found. Source: [55]........ 106
Figure 61: On left, a schematic of the current flip chip bumps made by metal. On right, a SEM image of these metal bumps. Source: [113] 107

Figure 62: On left, concept of a flip chip using carbon nanotube interconnections for thermal management. On right, SEM images of the corresponding CNT bundles. A high CNT density is observed. Source: [33] 109
Figure 63: Schematic of coplanar waveguides (CPW) test structure used (not drawn to scale). Left shows the top view of the CPW with a length of 0.7 mm for signal and 1.2 mm for ground. The dark circles indicate the locations of the CNT interconnects. Right shows the cross-section view indicating different layers of the test structure. Note that the 50 nm barrier layer is not shown in this figure. 113
Figure 64: SEM micrographs of the Au metallization at different stages of CNT growth. (a) As-deposited film was smooth with no crack-lines. The circular islands were formed during the deposition of Au metallization by e-beam evaporation process. (b) After annealing for 2 min at 800 °C in ambient NH_3 and crack-lines were observed. (c) After subjecting to C_2H_2 and plasma treatment for 15 min in a PECVD chamber, the Au film formed a hill-like morphology. 114
Figure 65: S-parameters of the two test structures A and B: (a) return loss of structure A, (b) return loss of structure B, (c) insertion loss of structure A, and (d) insertion loss of structure B. Note that the peaks at 1 GHz in each S-parameter results above are due to the calibration process for the probe station. The calibration shows no successful results at this frequency. 116
Figure 66: SEM image of the test structure with three Au lines on a silicon oxide surface. The catalyst used for CNT growth is patterned in the circular bumps. The roughness on the Au lines is the result of agglomeration during the PECVD growth process. 117
Figure 67: SEM micrographs of CNTs grown using PECVD approach using different barrier layers on underlying Au metallization: (a) TiN, (b) Ti, (c) Cr, and (d) on the Au surface. ... 117
Figure 68: Raman spectrum of the CNT grown on different barrier layers normalized to their G maximum intensity. 118
Figure 69: shows the schematic of the flip chip structure been fabricated to test for both DC and RF functionality. (a) the final flip chip after the chip is flipped and combine with the carrier, (b) carrier design which comprises of an 'open' coplanar line structure, (c) chip design which comprises of coplanar line, (d) shows the variation of the size of 3 flip chip test structure. 121
Figure 70: Picture of the plastic mask with carrier line patterns presented in the first paragraph. 123
Figure 71: Side view of the deposited layers after two consecutive photolithography followed by ebeam processes. Gold is 1 μm in order to avoid skin depth losses at high frequency. Ti or TiN are used as a barrier layer and Ni as the catalyst for the CNT growth by PECVD. 124
Figure 72: Photolithography, ebeam and PECVD steps to deposit pattern of catalyst material before CNT growth by PECVD. (1) shows the UV illumination of the photo resist using a shadow mask. (2) shows the development of the photo resist in order to remove non-wanted patterns. (3) is the deposition of the barrier layer and catalyst on the all sample by ebeam. Finally, in 4, CNTs are grown by PECVD and all the photo resist is removed in order to keep only the remaining bundle of CNTs. 125
Figure 73: On (a), the low magnification view of the CNT bumps formed on the Au metal lines. On (b), SEM image of a CNT bump grown using PECVD approach. The grown CNTs were vertically aligned and their length was approximately 20 μm. 126
Figure 74: Principle of the flip-chip using interconnected bundle of carbon nanotubes. Top part (chip or die) is rotated at 180° above the bottom part (PCB or carrier) and a downward force is applied on it. CNTs will stick together by the electrostatic and Van der Waals forces. 127

Figure 75: Interconnection length regarding the force applied: no load (a), 0.03 g (b) and 3 kg (c). At 3 kg, the interconnection length is maximal. Source: [124] 127
Figure 76: illustrates the CNT bumps on Au electrode with 3 different pitches. The smallest pitch designed is 80 µm in this work. The dimension of each CNT bump in (a) Structure 1 is 170 µm by 150 µm, (b) Structure 2 is 120 µm by 100 µm, and (c) Structure 3 is 70 µm by 50 µm. The scale bar at the bottom right of each image represents 100 µm. 128
Figure 77: Schematic view of the assembled final flip-chip device. 129
Figure 78: SEM images of the CNT interconnection bumps demonstrated using a flip chip concept (a-f). The dimensions of CNT bumps were 100 µm by 100 µm for all images. (a) Die attached to carrier at a tilted angle of 75˚, (b) magnified view of 2 CNT interconnection bumps, (c-d) show the distance separating the two parts of the flip-chip, (e) CNTs from bottom carrier were observed to be touching the die substrate indicative of the connections made and (f) shows the CNTs touching each others. 130
Figure 79: SEM images of the CNT bumps morphology after top die removal. (a) CNT bumps on the carrier, (b) CNT bumps on the chip joined to the carrier bump in (a) and (c) a magnified view of the bump. The remaining vertical alignments of the CNTs show the mechanical flexibility of CNTs. 132
Figure 80: I-V measurements from the input to the output signal line for 3 samples. On blue curve (device *a*), a resistance of 12.5 Ω was extracted. Other devices returned a resistance between 98 Ω (device *b*) and 500 Ω (device *c*). 133
Figure 81: On (a), schematic of the four-point-probe measurement set-up. On (b), the corresponding DC measurements fro 4 penetrations forces (0.00003, 1, 2 and 3 kg respectively corresponding to a penetration length of 3.6, 7.3, 11.1 and 15 um). Source: [124] 134
Figure 82: Two-point probe DC measurement across two interconnection bumps measured across the input and output of the carrier substrate. The CNT bumps dimension were 150 µm by 150 µm. 135
Figure 83: S-parameters measurements of the flip chip device *a* (solid lines) and device *b* (dash lines) between carrier input and output. 137
Figure 84: S_{21} parameters of device a and b between 6 and 40 GHz. HF transmission is increased by 1 dB at low frequency between device *b* and *a*... 138
Figure 85: S-parameters measurements of the flip chip device *c* between carrier input and output.. 138
Figure 86: S-parameters measurements of the CPW transmission lines placed on the die before and after PECVD process. 139
Figure 87: Top side view of the flip-chip device with the top scale. 140
Figure 88: S_{21} and S_{11} parameters measurements of the CPW transmission lines placed on the die before and after PECVD process (black lines) and the flip-chip measurements from the input to the output (see Figure 87). 141
Figure 89: On (a), side view of the flip chip structure and the corresponding equivalent electrical circuit with a breakdown of the bump resistances. On (b), details on Rbump corresponding of the all bump resistance for two interconnected MWCNTs according to (a) schematic. 144
Figure 90: S-parameters measurements (solid lines) of the flip chip device a between carrier input and output of structure 1 (Figure 77) and EM simulations (dash lines) corresponding to the same structure with CNT bumps replaced by a material with a 142 S/m electrical conductivity. 145
Figure 91: S_{21} parameters of device a between 1 and 40 GHz (solid line). EM simulation (dash line) corresponding to the same structure with gold bump (150 × 150 µm bump size and 25 µm high). EM simulations (lines and symbols) corresponding to the same structure with

CNT bumps replaced by a material with respectively a 142, 200, 300 and 1000 S/m electrical conductivity. 147
Figure 92: Details on R_{bump} corresponding of the all bump resistance for two interconnected MWCNTs according to Figure 89(a) schematic. 148
Figure 93: Top view of the schematic of the flip chip structure. 150
Figure 94: Diagram of the hybrid flip chip structure model. 151
Figure 95: S-parameters of the flip chip structure measured between Port 1 and Port 2. Solid lines correspond to the measurements while dash lines show the hybrid EM/circuit simulation results. 153
Figure 96: Schematic of the full-EM flip-chip simulation without bumps. 154
Figure 97: S-parameters of the full-EM simulation of the flip-chip structure without bumps according to the schematic in Figure 96. 155
Figure 98: S_{21} parameter of the hybrid EM/analytical flip-chip simulation with a parametric study on the CNT resistance R_{CNT}. 156
Figure 99: S_{21} parameter of the hybrid EM/analytical flip-chip simulation with a parametric study on the CNT contact resistance $R_{CNT-CNT}$. 157
Figure 100: S_{21} parameter of the hybrid EM/analytical flip-chip simulation with a parametric study on the CNT density. 158
Figure 101: On (a), total inductance of a gold bump and a CNT bundle according to the bump radius. On (b), total resistance of a gold bump and a CNT bundle according to the bump radius. In gold bumps, electromigration effects appear with a radius below 10 µm. 161
Figure 102: Top view of the 150-µm-bump size (structure 1) flip-chip device composed by the PCB (left asset) and the chip (right asset). In this structure, we can observe a total number of 58 bundles of CNTs. 163
Figure 103: Electrostatic and Van der Waals forces of a given number of CNTs as function as the distance between two carbon nanotubes. 164
Figure 104: An overview of all patterns existing on the mask and representing the different new flip-chip configurations that they will be presented later. References are on the right and the size of the CNT bundles below the reference. 167
Figure 105: Side view (a), top view (b) and zoom in on the interconnections (c) of the first new flip-chip configuration (FC1). 168
Figure 106: Electrostatic and Van der Waals forces of a given number of CNTs as function as the distance between them (the carbon nanotubes). On solid curves, we have the addition of these two forces. The dash orange curve represents the weight of the top flip-chip with the new configuration (FC1 and FC2). 169
Figure 107: On (a), simulated S-parameters from 80 to 120 GHz of the first new flip-chip configuration (FC1) and a comparison with the hybrid EM/analytical simulations for 0 MWCNTs and 100000 MWCNTs per bumps. On (b), corresponding S_{21} parameters with several densities of MWCNTs (from 2400 to 500000 MWCNTs). 171
Figure 108: De-embedding parts of the flip chip devices composed by six structures: Thru (input and output connected), reflect (short) and line (quarter wavelength lines) disposed respectively before and after the interconnections. 173
Figure 109: Side view (a), top view (b) and zoom in o the interconnections (c) of the first new flip-chip configuration (FC2). 174
Figure 110: On (a), simulated S-parameters from 80 to 120 GHz of the second new flip-chip configuration (FC2) and a comparison with the hybrid EM/analytical simulations for 0 MWCNTs and 60000 MWCNTs per bumps. On (b), corresponding S_{21} parameters with several densities of MWCNTs (from 60000 to 1000000 MWCNTs). 176
Figure 111: De-embedding parts of the flip chip devices composed by six structures: Thru (input and output connected), reflect (short) and line (quarter wavelength lines) disposed

respectively before and after the interconnections. A high frequency measurement of these structures will allow us to extract the CNT bundles S-parameters. 178
Figure 112: High-density CNT bundle interconnected. 178
Figure 113: Top views of the flip-chips composed by high density bundles of CNTs. Square shapes are on the left figure and cross shapes are on the right figure. 179
Figure 114: Schematic of the high density interconnected bundles of CNTs following the square shape. 179
Figure 115: Schematic of the high density interconnected bundles of CNTs following the cross shape.. 180
Figure 116: Polarization effect. Reflected, normalized light intensity vs polarization angle Θ for the sample shown in the insets. Circles represent the light intensity from the random array of nanotubes, and squares from the metallic film. Left inset: sample viewed with the polarization plane parallel to nanotubes (p-polarization), Θ=0. Right inset: sample viewed through polarizer with the polarization plane perpendicular to nanotubes (s-polarization), Θ=90°. Scale bars, 1 cm. Source: [171] 184
Figure 117: Schematic representation of a transmitter (top figure) and a receiver (bottom figure) using a nanotube antenna. Source: [172, 174].. 185
Figure 118: Dipole antenna concepts using carbon nanotube materials from Burke's works. Source: [176] 186
Figure 119: Potential solution to connect the micro-electronics word with the nano-electronics one using wireless interconnections. These wireless interconnections can be done with carbon nanotube antennas. Source: [176] 187
Figure 120: Monopole antenna with a length L standing above a ground plane. 189
Figure 121: On (b), Input impedance of the monopole antenna. On (a), 2-D (on (a) at phi = 0 and 90°) and 3-D radiation patterns of a monopole antenna. Isotropic radiation except in the antenna direction is visible. Both represent the antenna gain. 190
Figure 122: Schematic of the RLC circuit modeling the CNT monopole interconnection on ADS. 192
Figure 123: Return loss S_{11} of the RLC circuit modeling a CNT monopole (Figure 122). ... 193
Figure 124: Variation of the monopole diameter with a fixed number of CNTs. 194
Figure 125: Variation of the CNT density with a fixed monopole diameter. 195
Figure 126: Monopole interconnection structure with 50-ohms microstrip feeding line working at 40 GHz. Top and side views. 196
Figure 127: KOH etching principle and process flow... 197
Figure 128: On (a), 3-D and 2-D radiation patterns (representing the gain) of the monopole interconnection structure using gold material working at 40 GHz. On (b), simulated return loss and input impedance of the device simulated from 20 to 60 GHz............................... 198
Figure 129: S_{11} parameter of the CNT monopole with several CNT densities. 199
Figure 130: On (a), schematic of the monopole interconnection made by SWCNT bundle. On (b), 3-D radiation pattern (representing the gain) of the monopole interconnection. 201
Figure 131: Simulated return loss of the monopole interconnection from 1 GHz to 400 GHz. 202
Figure 132: On (a), monopole interconnection structure using CNT bundle with 50-ohms CPW feeding line working at 200 GHz. On (b), side view and top views of the monopole interconnection structure working at 40 GHz. 203
Figure 133: Simulated return loss of the monopole antenna device presented in Figure 132. Input impedance of the CNT monopole. 204
Figure 134: Simulated return loss of the monopole antenna device presented in Figure 132. Input impedance of the gold monopole. 205

Figure 135: 3-D radiation pattern (representing the gain) of the monopole interconnection composed by CNTs (a) and gold material (b) at 200 GHz. 205
Figure 136: Schematic of the monopole interconnection with gold wire mounted on a CPW line. Metal ground plane surrounds the monopole. Side and top views are visible. 207
Figure 137: Simulated return loss for the monopole configuration working at 100 GHz. Smith charts of the gold monopole (left figure) and the 6000-CNTs monopole (right figure). 209
Figure 138: Simulated 3-D radiation patterns for the two configurations: gold monopole (left), 6000 CNTs bundle (right) working at 100 GHz. 210
Figure 139: Top view of the monopole configuration working at 200 GHz. 211
Figure 140: In (a), simulated return loss for the monopole configuration working at 200 GHz. In (b), corresponding simulated smith chart of the structure working at 200 GHz using CNT monopole. 212
Figure 141: Simulated 3-D radiation patterns for the two configurations: gold monopole (left), 1000 CNTs bundle (right) working at 200 GHz. 213
Figure 142: Top view of the monopole configuration working at 300 GHz. 214
Figure 143: Simulated return loss for the monopole configuration working at 300 GHz using 1000 CNTs bundle. 215
Figure 144: In (a), corresponding simulated smith chart of the structure working at 300 GHz using 1000 CNTs bundle monopole. In (b), Simulated 3-D radiation pattern for the configuration using working at 300 GHz. 215
Figure 145: Hybrid gold/CNTs monopole. 216
Figure 146: SWCNT monopole abacus as function as the number of CNTs and the monopole length. 217
Figure 147: Schematic of the antenna monopoles transmission with monopole spacing between 80 to 1200 µm. 218
Figure 148: Simulated monopole-to-monopole transmission (S_{21} parameter) for two CNT-based monopoles (red curve), two gold-based monopoles (blue curve) and no monopoles (black curve). 219
Figure 149: On left, simulated monopole-to-monopole transmission (S parameters) for two CNT-based monopoles with a distance of 500 µm working at 300 GHz. 220
Figure 150: Transmission system between two monopoles placed side to side with circular reflectors. The distance between the two monopoles is 200 µm. Working frequency is 300 GHz. 221
Figure 151: Transmission system between two monopoles placed side to side with parabolic reflectors. The distance between the two monopoles is 200 µm. Working frequency is 300 GHz. 221
Figure 152: Carbon nanotubes monopoles fabricated by TCVD within a transmission configuration. On (a, b and e), bundles of aligned CNTs were visible following a cylinder shape. On the close view (c and d), alignment of CNTs and CNT density were visible. A height greater than 300 µm was obtained on f. 223

Tables

Table 1: Carbon nanotube general properties compared to gold and copper materials. Best performances are highlight in red. 29
Table 2: Summary of pros and cons of using arc discharge method to grow CNTs. 33
Table 3: Summary of pros and cons of using laser ablation method to grow CNTs. 34
Table 4: Summary of pros and cons of using thermal CVD method to grow CNTs. 48
Table 5: Summary of pros and cons of using thermal PECVD method to grow CNTs. 52
Table 6: Carbon nanotubes growth methods summary: Pros and Cons 54
Table 7: CINTRA/NTU (with the group of Professor Tay Beng Kang) CNT growth capabilities 55
Table 8 – Values of circuit components for each bundle of CNT width. 75
Table 9 – Comparison of circuit components values obtained by our previous extracted values and Minghui gap's work. The device is a 20-µm gap coplanar waveguides working up to 40 GHz. 76
Table 10: Positions of D and G peaks, calculated I_D/I_G of Raman spectra of CNTs grown on different barrier layer. 119
Table 11: Process flow summary of the device fabrication including CNT growth. 120
Table 12: CNT bundle components values. 152
Table 13: Comparison of the two flip-chip configurations FC0 and FC1. 169
Table 14: CNT bundle components values. 170
Table 15: Comparison of the two flip-chip configurations FC1 "base" and FC1 "base ++". 172
Table 16: Comparison of the two flip-chip configurations FC0 and FC2. 174
Table 17: CNT bundle components values. 175
Table 18: Comparison of the two flip-chip configurations FC2 "base" and FC2 "base ++". 177
Table 19: Monopole configurations using SWCNTs. 193
Table 20: The three-monopole interconnection configurations dimensions at 100 GHz. 208
Table 21: The two-monopole interconnection configurations dimensions at 200 GHz. 211
Table 22: The monopole interconnection configuration dimensions at 300 GHz. 214
Table 23: S_{21} parameters monopole-to-monopole transmission. 219

Abstract :
Nanoelectronics applications will face limits imposed by physics laws, material properties, circuits and systems characteristics, assembly and packaging conditions. In this context, packaging will play a major role by providing an effective capability of complementing the nanometric device features to the circuit boards. Interconnecting the nanometric devices will be a major problem, especially on the global level. Assembly approaches are moving toward the system-level integration paradigm and new packaging technologies are proposed (3D system integration, wafer-level packaging, electro/optical integration). The conventional materials used in the classical packaging are expected to be inadequate in terms of thermal, mechanical and electrical performances. A possibility under investigation is the use of new materials in nanopackaging such as carbon nanotubes (CNTs), nanowires, nanoparticules and graphene (monoatomic layer of graphite). In this manuscript, CNTs (rolled-up sheets of graphene) are studied and revealed unique physical, electrical and thermal properties, which make them extremely attractive for many applications in the area of nanoelectronics. This new field of research concerns the use of nanomaterials applied to the packaging of electronics or photonic components. That can be for interconnect, thermal, mechanical, etc managements. In this manuscript, we will mainly focused on two main applications: interconnections based on CNTs for flip-chip technology and wireless interconnections using CNT monopole.

Keywords: Interconnections, carbon nanotubes, high frequency, modeling, flip-chip, monopole.

Nanopackaging à base de nanotubes de carbone pour des interconnections innovantes aux hautes fréquences.

Résumé :
A échelle nanométrique, les applications électroniques vont devoir faire face à des difficultés imposées par les lois physiques, les propriétés des matériaux, les caractéristiques des circuits et systèmes, l'assemblage et le conditionnement. Dans ce contexte, le packaging jouera un rôle majeur en fournissant les performances et l'efficacité nécessaires combinés aux composant nanométriques reliés à la carte mère. Les techniques d'assemblage se concentrent sur l'intégration au niveau système et de nouvelles technologies sont proposées (système 3D, packaging de substrats, intégration electro/optique). Les matériaux conventionnels utilisés pour le packaging seront ainsi inadaptés en terme de performances thermiques, mécaniques et électriques. Une des solutions actuellement à l'étude concerne l'utilisation de matériaux innovants tels que les nanotubes de carbone (NTCs), les nano-fils, les nanoparticules ou le graphène (monocouche de graphite). Dans ce manuscrit, les NTCs (feuille de graphène enroulée) vont être étudiés et vont révéler des propriétés physiques, électriques et thermiques uniques, ce qui leur apportent un certain intérêt pour le champ d'applications de l'électronique nanométrique. Ce nouveau champ de recherche concerne l'utilisation de nanomatériaux appliqués au packaging des composants électroniques et photoniques. Les applications sont diverses et variées entre les interconnections, la gestion thermique ou même mécanique. Dans ce manuscrit, nous nous concentrerons sur deux applications : les interconnections à base de nanotube de carbone utilisant la technologie flip-chip et les interconnections sans fils à base de monopoles composés de nanotubes de carbone.

Mots clés: Interconnections, nanotubes de carbone, haute fréquence, modélisation, flip-chip, monopole.